UNIVERSITÀ DI PISA

DIPARTIMENTO DI INGEGNERIA CIVILE E INDUSTRIALE

UNIVERSITY OF ILLINOIS AT URBANA-CHAMPAIGN

DEPARTMENT OF NUCLEAR, PLASMA AND RADIOLOGICAL ENGINEERING

MASTER OF SCIENCE IN NUCLEAR ENGINEERING

Design, Development and Investigations of a Novel X-ray Fluorescence and X-ray Luminescence Computed Tomography System for Theranostic Applications

Supervisors:

Prof. Ing. Francesco D'ERRICO

Prof. Ling-Jian MENG

Ing. Valerio GIUSTI

Student:

Luca GIANNONI

Academic year 2015 – 2016

ABSTRACT

A novel and advanced design for an experimental imaging system, combining x-ray fluorescence and x-ray luminescence computed tomography (XFCT/XLCT) has been proposed, developed, built and finally tested, during this thesis work. The main target of such design, and of the entire thesis project, was to create a fully working state-of-the-art XFCT and XLCT benchtop setup, in order to investigate on potential theranostic applications of such technology, i.e. the combination of therapeutic delivery against cancer and simultaneous molecular imaging and monitoring of such treatment.

X-ray fluorescence (XF) and x-ray luminescence (XL) are based on selective excitation with an x-ray beam of specific materials within a biological target, which in turn emits characteristic x-rays (for XF) and/or optical photons (XL) to be used as detectable signal for 3D imaging and as direct activators of therapeutic effects. The major types of therapies that have been envisioned for the proposed XFCT/XLCT system were: (1) X-ray Photodynamic Therapy (XPDT), where the light produced during XLCT is used to generate cytotoxic effect in cancerous tissues; (2) Auger Therapy, where low energy electrons produced during x-ray stimulation can directly kill tumor cells; (3) radiosensitization and radiation dose enhancement of conventional chemotherapy (mainly with Cisplatin). Metal-based nanomaterials have been selected as main agents for such theranostics applications, in particular LaF_3:Tb, Y_2O_3:Eu(III) and HfO_2 nanoparticles, due to their size-dependent unique properties.

The XFCT/XLCT system was built using commercial and custom-modified instrumentation. The main components are: (1) two x-ray sources, a monochromatic one and a polychromatic x-ray tube; (2) an x-ray CCD camera; (3) an optical EMCCD camera coupled with a demagnifier (DM) tube; (4) a CdTe x-ray spectroscope; (5) a hybrid x-ray sCMOS camera and a flat panel for transmission CT imaging.

Specific optimized geometries, using particular beam shapes and collimation of the emitted signals, were implemented and a single-slit collimator has been designed and built for such purposes. A geometric calibration model of the XFCT part of the system has been also developed and verified, after proper 3D modeling of the entire setup. A processing code for the analysis and correction of the XL signal data has also been implemented for final XLCT imaging and XL signal quantification.

Finally, a quantification study has been conducted to evaluate both the XF and XL signals produced by some of the chosen nanoparticles and to assess the best excitation strategies for theranostics XFCT and XLCT with the system. Best energy efficiencies were found with Y_2O_3:Eu(III), using

low energies (12-14 keV) to maximize XL, and K-edge excitation for XF. In addition, two imaging studies for both XFCT, XLCT and a multimodal combination of the twos were performed using the setup. The results of these studies demonstrated excellent 200-μm spatial resolution, 300 μg/mL sensitivity and capability of multiplexed imaging for monitoring and delivering XPDT and other therapies.

TABLE OF CONTENTS

TABLE OF FIGURES

1. Introduction to X-ray Fluorescence and X-ray Luminescence Computed Tomography

Diagnostics and therapy in current medicine and healthcare are moving increasingly towards a preemptive approach to the treatment of diseases and disorders, in order to achieve a broader and deeper understanding of their mechanisms and causes. This could potentially allow the detection and cure of such conditions in human body before the occurrence of revelatory symptoms, which usually manifest when the pathology may have already reached a critical and severe status. Concerning non-invasive diagnostic methods, one of the most promising and rapidly emerging preclinical research discipline nowadays is *molecular imaging*. It is unanimously considered a novel multidisciplinary field that aims to visualize, quantify and characterize *in vivo* biological processes and body functions at cellular and sub-cellular level [1] [2] [3]. While current imaging modalities investigate and capture primarily macroscopic physiological and metabolic variations in human body, for correlating them with potential abnormal and pathological conditions, molecular imaging techniques focus on the identification and determination of specific molecular events responsible for diseases.

In addition, the recent development of groundbreaking nanotechnologies for imaging and pharmaceutical applications has opened to the possibility of combining molecular diagnosis with therapy in a new discipline, called "*theranostics*". Such novel approach represents a promising propeller towards a future of personalized and highly specific medicine [4].

Innovative and advanced imaging systems and instrumentation are thus required for the accomplishment of the goals and purposes these cutting-edge research fields are addressing. In particular, among the most valuable characteristics necessary for *in vivo* molecular imaging modalities and theranostic applications are the following, reported in the list:

1) Non-invasiveness (or minimal invasiveness) of the procedure, both for preclinical and potential clinical applications;
2) High spatial resolution, generally at sub-millimeter (<mm) and micrometer scale (μm), as to visualize graphic details and features at cellular and molecular level (Figure 1.1);
3) High sensitivity, in terms of nanomoles per liter (nmol/L) or picomoles per liter (pmol/L), to detect very small concentrations of molecular agents or probes;
4) High temporal resolution, preferably in the range of seconds to minutes, for small image acquisition times and rapid responsiveness of the imaging system to any rates of changes in the biological processes and in the subject;
5) Large, or even potentially limitless, imaging depth and penetration in any biological tissue;

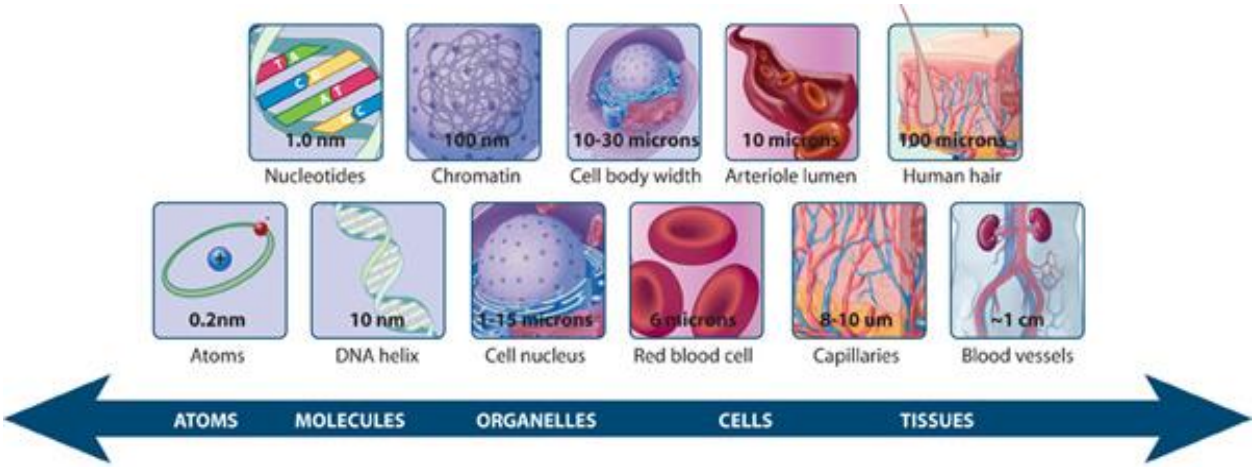

Figure 1.1: Biological scale as reference for spatial resolution required in molecular imaging [5].

6) Capability of providing quantitative information of biological phenomena, such as biodistribution, concentrations in the specific analyzed area or tissue and molecular composition;
7) Capability of providing volumetric information through tomographic imaging assays and computational three-dimensional reconstruction;
8) Possibility to couple the molecular and functional information with anatomical and structural details, potentially in a single system or device;
9) Capability of multiplexed and multicolored imaging, in order to simultaneously visualize and characterize different biological processes, events or objects;
10) Miniaturization and compatible system dimensions and size for benchtop preclinical applications, small animal studies and prospective future clinical transition;
11) Competitive cost and economy of the system, the instrumentation and the procedures, especially in the context of potential clinical applications;

Although it appears extremely challenging to combine all these advantageous features in a single imaging system, which could also be used for theranostics and medical therapy, several candidates have been tested and investigated in the last decades and are still highly researched and developed in order to optimize and improve their current state-of-the-art [1] [2].

Computed tomography (CT) technologies based on x-ray stimulated emission represent one of the possible innovative and emerging systems for the abovementioned theranostic and molecular imaging applications. They rely on different physical phenomena rather than x-ray attenuation used in conventional radiography and CT, which provide good quality anatomical information, but are not suitable for achieving molecular sensitivity and contrast. In x-ray stimulated emission CT techniques, an external x-ray excitation source is used to interact with specific targets within the imaged sample, in order to generate detectable secondary radiation, which constitutes the signal to build the image on. Depending on the nature of this secondary radiation, it is possible to distinguish between X-ray Fluorescence Computed Tomography (XFCT), if characteristic x-rays (or fluores-

cence x-rays) compose the secondary radiation, and X-ray Luminescence Computed Tomography (XLCT), when the secondary emission consists of visible light. The excited target can be endogenous (naturally occurring metal or phosphors) or exogenous (contrast agents, imaging probes or therapeutic agents). The detection of the emitted radiation and its subsequent processing for image reconstruction can result in the quantification of the three-dimensional distribution of the target in the sample and its characterization. Such modalities can also provide a real-time mapping of the biodistribution of the mentioned targets, as to extract critically needed information about biological processes, metabolic functions and molecular pathways in a specific tissue or organism [3].

The most attractive characteristics of these two x-ray stimulated emission imaging modalities reside in their high spatial resolution and good sensitivity, coupled with the relevant capability to perform multiplexed and multicolored imaging. Furthermore, these techniques can be combined with conventional computed tomography or state-of-the-art micro-CT, in order to merge anatomical information from x-ray attenuation with the complementary molecular and functional information provided by the excited emission signal.

Finally, as it will be described in Paragraph 1.4, there is also the significant potential to employ selective x-ray excitation and fluorescence/luminescence emission for therapeutic applications, in particular with high atomic number (Z) materials and metal-loaded nanoparticles. Such utilization regards primarily the treatment of localized tumors and targeted cancers, while at the same time the 3D imaging capabilities of the modalities can perform real-time monitoring of the therapy and its activation, as an exemplary realization of the previously described theranostic approach.

1.1. X-ray Fluorescence Computed Tomography (XFCT)

X-ray Fluorescence Computed Tomography (XFCT) is a tomographic imaging modality based on the external stimulation with x-rays of specific elements and target materials in the body, in order to trigger a secondary radiation emission, in the form of x-ray fluorescence (XF, for short), that can be detected as signal for volumetric reconstruction of the distribution of the target. The physical phenomenon of x-ray fluorescence originates from the interaction between an incoming external x-ray photon, from the stimulating source, and an electron of the inner shells of the atoms in the target material. Through photoelectric effect, the x-ray photon excites the shell electron by depositing all its energy. When the energy is equal or higher than the binding energy of the given orbital, the electron is ejected from the shell. Afterwards, the vacancy left in the inner shell by the ejected electron is filled by another electron from one of the outer shells in the atom. In the transition from a higher energy orbital to a lower energy one, the excess energy of such electron is converted in an x-ray photon and emitted from the atom of the target material. Such type of radiation is called characteristic x-ray. As the name implies, its discrete energy varies from element to

element, according to the difference in the energies of its orbitals, and thus can be considered a typical signature or "footprint" of the material itself [6] [8]. This provides a very useful tool for the identification of the elemental and chemical composition of the target, as commonly used in X-ray Fluorescence Spectroscopy for inorganic material analysis. Moreover, the energy of the characteristic x-rays (or fluorescence x-rays) depends also on the following aspects: (1) in which inner orbital the photoelectric interaction has occurred; (2) from which outer electronic shell the filling secondary electron comes from. In the first case, the energy of the characteristic x-ray photon decreases as the photoelectric interaction occurs in orbitals farther from the nucleus. Therefore, it is possible to distinguish between so-called K x-rays (when the interaction occurs in the first orbital, or K-shell), L x-rays (when the interaction occurs in the second orbital, or L-shell), then M x-rays (when the interaction occurs in the third orbital, or M-shell), and so on. This process is described in a diagram in Figure 1.2 [6] [8]. In the second case, as the filling electron comes from a more distant orbital than the one containing the vacancy, then the energy transition will be larger and the energy of the emitted characteristic x-ray will be higher. When the electron transition takes place between the L-shell and the K-shell, the characteristic x-ray is named K-alpha (K_α), while if it occurs between the M-shell and the K-shell, the characteristic x-ray is named K-beta (K_β). The same notation is applied for the outer shells. Figure 1.3 shows a simplified depiction of such phenomenon. It must also be noted that, due to difference in the azimuthal quantum number (which determines the shape of an orbital) of a given electron shell (K, L, M…), another slight variation in the energy of the characteristic x-rays can be present, as well. Such difference is expressed by the notation $K_{\alpha 1}$, $K_{\alpha 2}$, $K_{\beta 1}$, $K_{\beta 2}$ and so on also for the outer shells, accordingly to the azimuthal quantum number of the orbital from where the filling

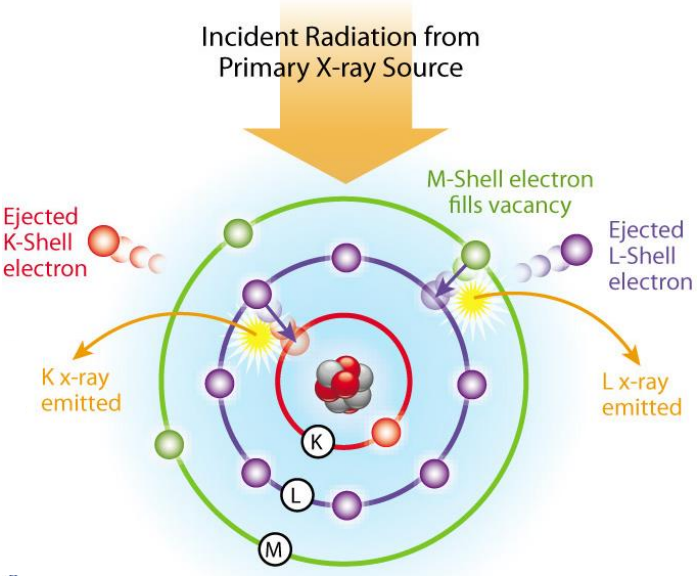

Figure 1.2: Characteristic x-ray emission (x-ray fluorescence) from different electron shells.

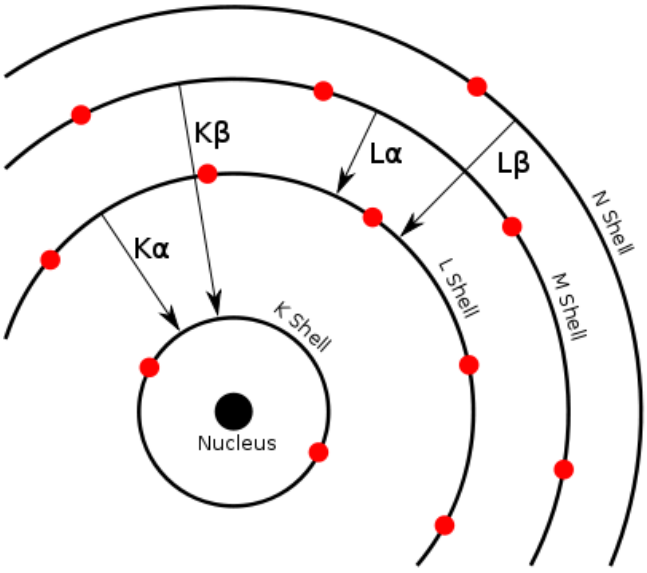

Figure 1.3: Characteristic x-ray emission (x-ray fluorescence) for different energy level transitions.

electron comes from (for outer electrons also a γ notation is possible) [6] [7] [8].

The x-ray absorption due to photoelectric effect in the target atoms, for creating x-ray fluorescence, strictly depends on the energy E_x of the stimulating x-ray photons and on the atomic number Z of the target. Generally, the probability of photoelectric effect per unit path length in a given material, expressed by its linear attenuation coefficient τ, can be approximately assumed as [8]:

$$\tau \propto \frac{Z^{4\div5}}{(E_x)^{3.5}} \quad (1)$$

Therefore, relatively high-Z elements and materials, such as heavy metals and rare earths, are usually considered as the main targets for XFCT and can be utilized as basis for contrast agents and imaging probes [2]. In addition, significant importance is given to the phenomenon known as "absorption edge", which consists in sharp, discrete and discontinuous increases in the photoelectric absorption of x-rays at specific energies, corresponding to the electron binding energies of the orbitals of the target atoms. Thus, it is possible to identify different edges, according to the various shells, such as the K-edge, the L-edge and the M-edge [6] [8]. The trend of the total mass attenuation coefficient with absorption edges is shown in Figure 1.4 for different given materials.

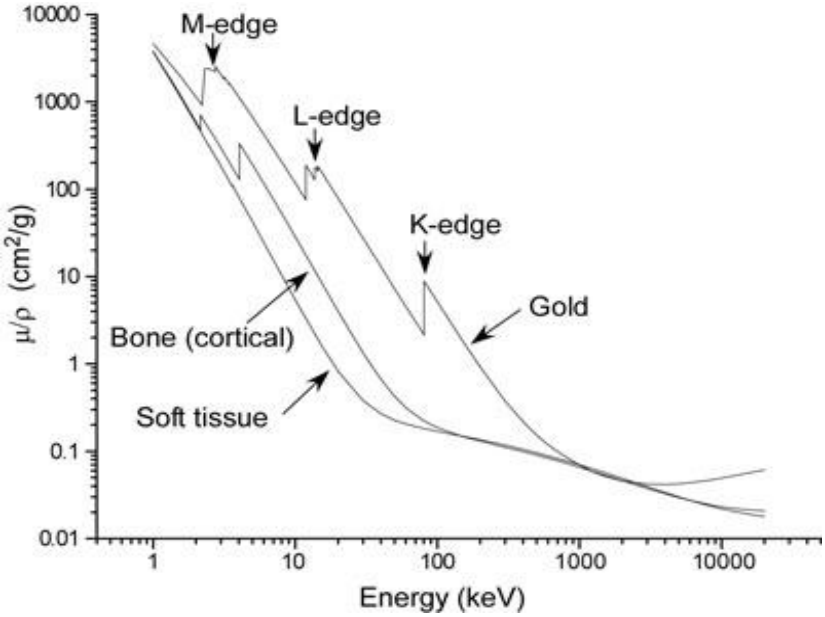

Figure 1.4: Total mass attenuation coefficient for different materials, showing the absorption edges for the K, L and M shells of gold.

In XFCT, the energy of the exciting x-ray beam can be tuned to match the absorption edges of the target material, in order to maximize the absorption of the x-ray photons and thus increase the production of XF signal. Above all, the K-edges of high atomic number materials are particularly suited for medical applications, being close or often higher than the x-ray energies required to penetrate organic tissues, in order to provide enough penetration depth for the output signal [2].

XFCT systems commonly require high intensity, highly collimated and monoenergetic x-ray beams, as to provide the best spatial resolution and sensitivity achievable, to maximize the output

fluorescence signal per unit area of the irradiated material and to tune the stimulating source to the K-edge of the target [2] [9]. A practical correlation for the required excitation x-ray fluence Φ (in terms of photons per unit area) is the following [9] [10]:

$$\Phi \propto \frac{1}{f\Omega\omega\tau(E)}\left(\frac{D}{\mathrm{d}}\right)^3 \qquad (2)$$

where D is the diameter of an hypothetic cylindrical target, d is the size of the x-ray beam (which can be used to estimate of the achievable spatial resolution), f is the concentration (atoms/atom) of the imaged element in the object, Ω is the geometric detection efficiency (i.e. the solid angle between the source and the used detector, ω is the x-ray fluorescence yield and $\tau(E)$ the photoelectric absorption probability at the energy E of the excitation x-rays.

For these reasons, the first medical investigations on XFCT, during the late 1980's, were mainly conducted at synchrotron facilities [10] [19]. From 2000's, improvements in the instrumentation and decreases in the cost of the equipment have permitted the development of desktop XFCT system for small laboratories, using commercial micro-focused x-ray tubes, opening towards application of such modality to routine preclinical research and medical imaging [2] [20].

The most frequent and experimented procedure for XFCT imaging involves the scanning of the entire imaged object with a focused pencil beam, line by line (LBL) and at different rotation angles around the target axis. This permits to acquire tomographic information of the object from sequential projections, which can be reconstructed to obtain the volumetric distribution of the fluorescent compounds in the subject. The x-ray fluorescence signal is detected and recorded using radiation detectors located outside the excitation beam. These detectors need to be designed for x-ray spectroscopy and photon-counting, in order to discriminate between x-ray fluorescence photons with different energies, which belongs to different scanned elements [2] [11]. The standard line-by-line setup for XFCT is depicted in Figure 1.5. Nevertheless, such mechanical scanning procedure has the disadvantage of requiring long image acquisition times for a complete three-dimensional imaging study. The lengthy scanning time can lead to relatively high and not-negligible doses of x-rays to the imaged target, which may limit any potential clinical transition. A number of approaches have been proposed to overcome this complication, such using converging aperture systems (Chukalina *et al.* [12]) or a confocal

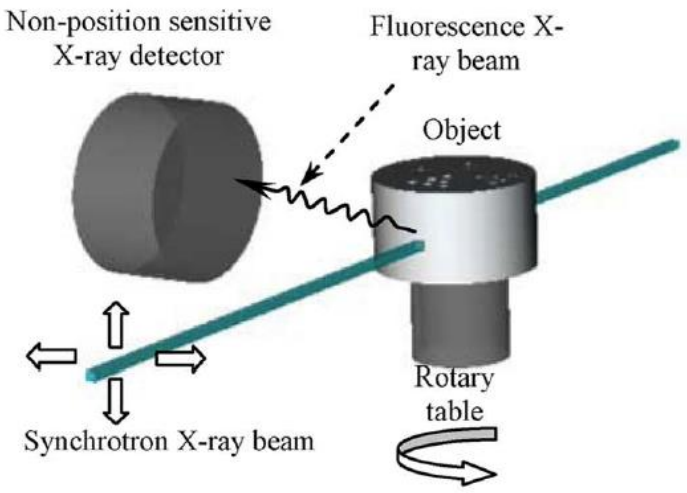

Figure 1.5: Diagram of the geometry of a standard line-by-line (LBL) setup for XFCT [11].

collimation geometry (Vekemans *et al*. [13]). Meng *et al*. [11] has investigated an alternative solution, based on image formation methods similar to those used in nuclear medicine and emission tomography, which they called "*X-ray Fluorescence Emission Tomography*" (XFET). The XFET approach involves the use of a pencil beam of x-rays to irradiate the object, line by line, and of a detection system composed by position-sensitive photon-counting detectors coupled to multiple-slits collimated apertures. At the price of a reduced geometric detection efficiency, due to the use of collimators, the XFET method provides a greater imagining information per detected photon, thus increasing the acquisition speed. In principle, no rotation of the object is required, simplifying the scanning procedure, thanks to the capability to offer more information content per detected photon. This is because each detected photon, having passed through the slit collimation, is associated to a smaller average number of potential source voxel in the object. Moreover, the use of micro-focused x-ray beam and very narrow slit (with widths in the order of the tenths or hundreds of micrometers) allows the achievement of excellent spatial resolution for molecular imaging applications [11]. A schematic representation of the XFET approach using slit collimation is illustrated in Figure 1.6 [16].

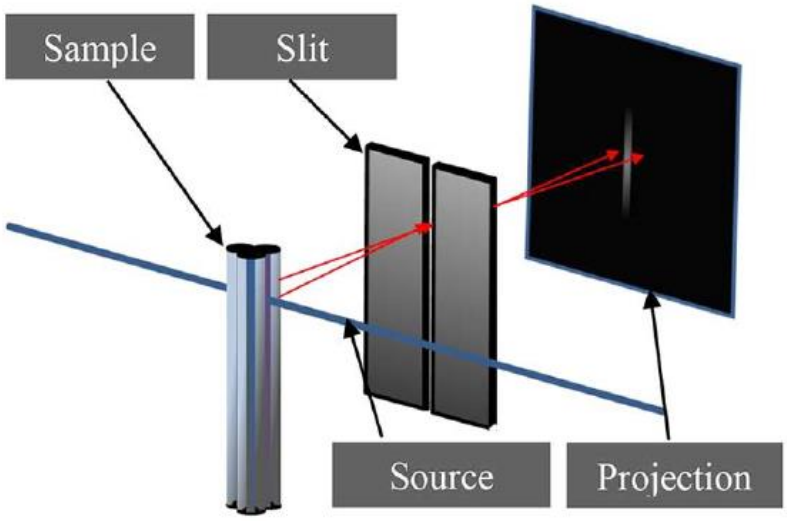

Figure 1.6: Configuration of the collimation geometry in XFET using narrow slit aperture. Photons are only geometrically limited in the horizontal direction and are free to project anywhere along the vertical direction [16].

Correction for the attenuation of both the primary x-rays and the fluorescence x-rays, through the object thickness, is always required during image reconstruction, because it can reduce image contrast of features deep inside the target [2] [11] [16].

Several studies and investigations performed in the last ten years have proved and established the strengths and the potentials of XFCT as a promising molecular imaging modality [2] [11] [14] [15] [16] [20]. It was shown, both theoretically and experimentally, that XFCT provides higher sensitivity than x-ray transmission CT, at the same radiation dose [15], with an excellent spatial resolution, in the range of 100 to 300 μm [11]. Moreover, one of the main advantages of XFCT is its

limitless depth of penetration due to the involvement of x-rays with energy usually above 5-10 keV (in comparison with optical molecular imaging modalities, for example).

The use of small-pixelated detector, with pixel size lower than 25 μm, could furtherly improve the spatial resolution limit. The dimensions of the stimulating x-ray beam and the size of the collimation system play also a fundamental role in establishing the spatial resolution performances of this modality. Newer methods for focusing high intensity beams, while maintaining a relatively strong photon flux, are currently required for energies of the x-rays above 30 keV in benchtop applications [2].

On the other hand, the application of high-energy resolution detectors (such as solid-state semiconductor detectors) would offer greater detection efficiencies and increase the sensitivity performances of XFCT [11]. One of the key factor limiting the sensitivity of XFCT regards Compton scattering of primary x-ray photons from the excitation beam, which could reach the detector and interfere or overlap with the fluorescence signal. Such interaction could occur in the target, both in the background tissue or in the imaged element, and in the surrounding media. Due to the difficulty to discriminate the energy of these scattered x.-ray photons from the real fluorescence ones, the overall sensitivity and image contrast can be worsened because of the poorer signal-to-noise ratio (SNR) [2] [17]. An estimate of the SNR of an XFCT system can be assumed as:

$$\mathrm{SNR} \cong \frac{\mathrm{N}_{XF}}{\sqrt{\mathrm{N}_{XF} + \mathrm{N}_{CS}}} \tag{3}$$

where N_{XF} is the number of x-ray fluorescence photons detected and N_{SC} is the number of Compton scattered x-ray photons detected, which cannot be discriminated from the real signal [17]. Many Compton scatter correction strategies have been tested an implemented for XFCT image reconstruction [17] [18], most of them concerning the acquisition of prior information about the shape, the intensity and distribution of the Compton scattering background and accurate modeling of it, in order to reduce its noise contribution. Mechanical reduction of Compton scattering can also be implemented, via shielding and using particular collimation geometries in front of the detection system, or even by varying the incidence angle of the emitted x-rays with the detector focal plane (backscattering detection geometries has also been tested [17]). Anyway, both these two possible approaches may also generate a decrease in the geometric efficiency of the system.

Current research in XFCT are primarily concentrated in optimizing the characteristics of the imaging system and to further leverage the performances of such modality, for current applications in preclinical and small animal research and future prospective in whole-body clinical molecular imaging. Substantial efforts are also spent in trying to combine XFCT with micro-CT for multimodal imaging applications [21], in order to merge anatomical and morphological information from transmission x-ray with the molecular and functional information from x-ray fluorescence.

1.2. X-ray Luminescence Computed Tomography (XLCT)

X-ray Luminescence Computed Tomography (XFCT) is another emission tomographic imaging modality based on x-ray stimulation of target materials. Differently from XFCT, as described in the previous paragraph, in XLCT the excitation via x-ray photons produces optical emission, in the form of a secondary radiation that is usually visible light. In other cases, it can also be near infrared (NIR) or ultraviolet (UV) light. The physical phenomenon on which XFCT is based is called x-ray luminescence, also commonly known as radio-luminescence or scintillation [2] [8] [22]. Such process is long established and has been widely used (and still applied largely nowadays) in radiation detection and conventional imaging. In these fields, luminescence is primarily a form of intermediate or conversion signal, while in XFCT luminescence photons generated by x-ray scintillation compose the principal detected signal for image formation.

Scintillation occurs after interaction of x-ray photons with the scintillating material. The photons deposit all or part of their energy in the target, primarily through photoelectric effect and Compton scattering (depending on the energy of the x-rays), thus creating a number of lower-energy secondary electrons (in the keV range). These secondary particles can furtherly produce other downstream ionization events, resulting in an electromagnetic shower of ionized low-energy electrons. If the target medium is an inorganic crystal doped with an activator, which could be either intrinsic (impurities or defect in the crystal lattice) or extrinsic (generally, doping ions), a secondary electron from the shower can migrate to a luminescence center in the crystal lattice. This luminescence centers, originated from the activators, are excited states between the valence band and the conduction band of the bulk crystal. By trapping one of the free electrons created by the stimulating ionizing radiation, this temporary excited electronic states can decay and release their energy as an optical photon with few eV of energy. Being the luminescence center located in the forbidden energy band of the crystal, the optical photon can avoid reabsorption by the lattice or photoionization of another center. Moreover, the energy level of the luminescence center determines the wavelength of the emitted optical photon. [8] [22]. The scintillation process is briefly summarized as a diagram in Figure 1.7.

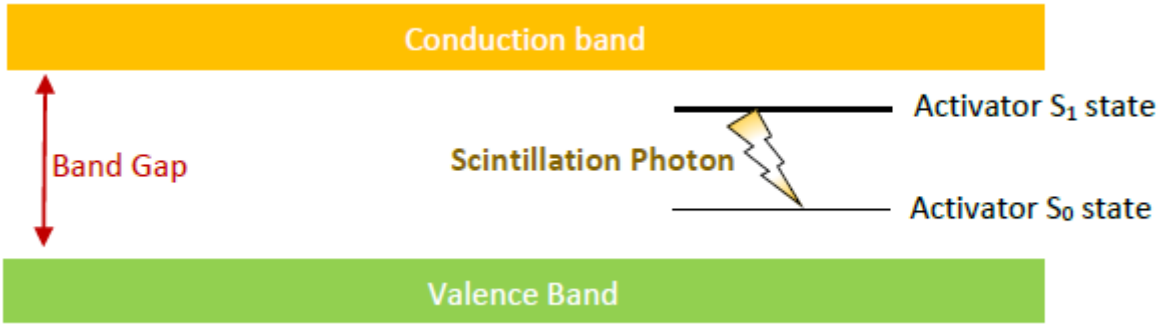

Figure 1.7: Depiction of the scintillation process in inorganic crystal materials. The mechanism is the physical foundation of x-ray luminescence for XLCT.

The typical decay times of the excited electron states in the scintillation process are generally of the order of 30 to 500 nanoseconds [8] [22]. It must also be noted that competitive processes exist along the previously described scintillation one. Among them, the so-called "phosphorescence" (or "afterglow") occurs when the excited configuration, produced by the trapping of the secondary electron in a luminesce center, needs additional energy for the transition to the ground state. A possible source for this extra energy is often provided by thermal excitation. This effect generates a delay in the light production and results in a slow component of the optical emission, which is called phosphorescence photon. Other alternative processes to scintillation are represented by radiationless de-excitations from the activator center, which are commonly grouped under the umbrella term of "quenching" [8].

The XLCT modality involves the combination of the just described x-ray luminescence mechanism with the basic principles of tomographic image acquisition. As for XFCT, a target is commonly scanned, line by line (LBL), by a very narrow and focused beam of x-ray photons, in order to excite the scintillating materials within the irradiated voxel. Then, such materials will produce visible light through the scintillation process and one or more photo-detectors, which are generally located outside the stimulating beam, can detect the optical emission signal. The object must be scanned entirely and rotated, in order to acquire enough information for its complete three-dimensional reconstruction. A scheme of such imaging procedure for XLCT is visible in Figure 1.8 [23].

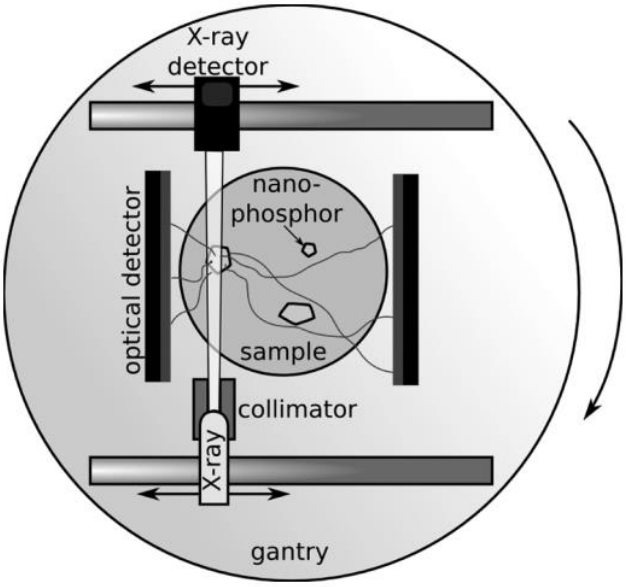

Figure 1.8: Depiction of the most common XLCT system geometry for image acquisition [23].

The total measured flux of optical photons detected by the photo-sensors can be correlated, after data processing and correction, to the summation of the amounts of scintillating materials in the path of the x-ray beam, thus enabling quantification of the concentration of the agents within the irradiated volume [2] [23]. Knowing that the measured optical photons must be created somewhere within the narrow path of the stimulating x-ray beam, the optical detector does not generally need to be spatial-resolving [23]. Nevertheless, the scattering and diffusion of the optical photons in the thickness of the imaged object must be taken into account. In fact, tissue penetration of the emitted light and optical scattering represent issues for this technique in relatively thick tissues (several millimeters), primarily regarding sensitivity. The design of target phosphors producing near infrared (NIR) light after scintillation can

cope with such problematic, thanks to the lower attenuation in tissues provided by such low frequencies of optical radiation [2] [24].

Simulation studies have proved the feasibility of XLCT at depth in mouse-sized subjects, with nanophosphors concentration of the order of µg/mL (with a total radiation dose to tissue estimated between 1 and 10 cGy) [23]. However, experimental studies has still failed to reach such ideal sensitivity, demonstrating only detectability of concentrations in the range of mg/mL of nanophosphors [25]. One of the main problems limiting sensitivity is also related to non-negligible x-ray scattering in tissue, which can cause undesired excitation of the target scintillators outside the primary beam path, thus decreasing image contrast and introducing noise [2]. Another important source of noise in XLCT, which can contribute to degrade its sensitivity performances, is represented by intrinsic background luminescence from endogenous phosphors naturally occurring in tissues (mainly water, hemoglobin and aromatic amino acids) or by air scintillation in the surrounding environment (from excited nitrogen in the atmosphere). Such undesired noisy contribution to the detected XL signal can be avoided using optical filters in front of the detectors, in order to select only specific wavelengths coming directly from the target phosphors [2].

Compared to other optical imaging modalities for preclinical applications, such as optical fluorescence, XLCT has the great advantage of higher spatial resolution, especially at depth in biological tissues. This is due to the specific localization of the emitted XL signal only in the selective area of the target volume irradiated by the x-ray excitation beam [2]. As for XFCT, the spatial resolution of XFCT is predominantly set by the collimation of the stimulation beam. Moreover, being the XL signal localized in a very small volume of the imaged sample, spatial information can be resolved just with a relatively limited number of optical photons detected. This is because each luminescence photon carries a larger amount of imaging information due to selective excitation [2].

As for XFCT, long tomographic image acquisition time is required also in the case of XLCT and represents a criticality for large field-of-view and whole-body imaging that are typical in human clinical imaging. Several novel irradiation geometries, such as cone beam geometry [26] as in Figure 1.9, or specifically engineered reconstruction algorithm, such as single-view XLCT reconstruction methods [27], have been proposed as possible solutions for decreasing the scanning time and the total imaging time. XFET methods [11] [16], such as those described in the previous paragraph for XFCT can also be implemented systematically in XLCT to reduce acquisition time and maintain,

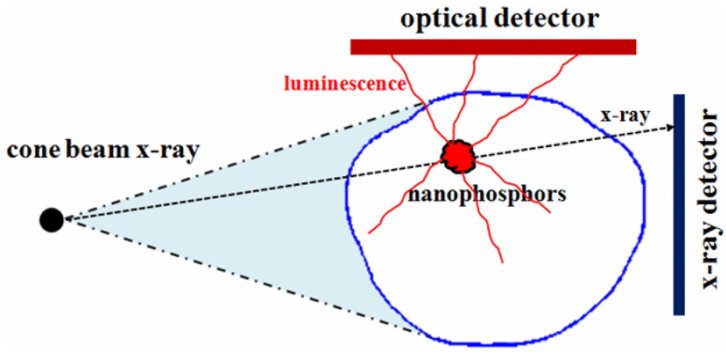

Figure 1.9: Schematic illustration of the irradiation geometry of cone beam XLCT [26].

at the same time, good spatial resolution capabilities with fields of view (FOV) suitable for small animal preclinical imaging.

Finally, it must be reported that active research and investigations are currently focusing on developing XLCT image reconstruction methods for derivation of the distribution of internal radioluminescence sources in the target, given the measured optical emission intensities at the surface of the imaged object. Uncertainties in such relative intensities may complicate the reconstruction and reduce sensitivity, again due to optical scattering and absorption. Therefore, reliable and subject-specific physical models of light propagation in the imaged target are necessary for optimal reconstruction and light attenuation correction. Such models can be inferred from *a priori* image knowledge or from concurrent structural imaging (using conventional CT or MRI, for example).

1.3. Comparison of XFCT and XLCT with other imaging modalities

As described in the previous two paragraphs, both XFCT and XLCT demonstrate interesting characteristics and qualities that could potentially make them suitable for novel molecular imaging applications. Among their most remarkable capabilities, they show excellent spatial resolution with deep tissue penetration (due to selective and highly focused x-ray excitation), good sensitivity for detection of trace quantities of target agents, the capacity of quantifying such concentrations in the subject and the ability to achieve multiplexed and multimodal 3D imaging. It must also be added to these strength points, the fact that both such modalities may be combined in a single compact system, which allows their simultaneous functioning. This is permitted, in principle, by the use of the same excitation and irradiation mean, i.e. a particular x-ray beam, which is used to trigger both the x-ray fluorescence and the x-ray luminescence phenomena. Such combination of the two techniques, whose feasibility and overall outcomes is one of the main objective of the system described here and of this reported thesis project as well, has the potential to exploit all the single benefits of XFCT and XLCT and to enable new and advanced theranostic applications (as it will be described in the next Paragraph).

At this point, a comparison of XFCT and XLCT with well-established state-of-the-art imaging modalities (either clinically adopted or presently under investigation) is important and useful to evaluate their respective performances and features in the specific context of molecular imaging, precisely referring to those particular characteristics explained at the beginning of this chapter.

Starting with conventional nuclear medicine techniques, including Positron Emission Tomography (PET) and Single Photon Emission Tomography (SPECT), which are the most widespread clinical molecular imaging modalities currently available, it can be noted that both XFCT and XLCT have the capability to achieve higher spatial resolution, also deep in tissue, as described multiple times previously. Spatial resolution in XFCT and XLCT is only limited by the size of the stimulating x-

ray beam and by the dimensions of the pixels of the camera used to detect the signal. Experimental imaging results showing 100-μm resolution have been reported in literature for XFCT [28]. On the other hand, clinical PET and SPECT for human imaging are currently capable of achieving spatial resolution in the range of 1-2 millimeters [1][29], while preclinical systems for small-animal PET and SPECT imaging have demonstrated spatial resolutions ranging from 350 to 800 μm [30] [31]. Limitations of spatial resolution in these modalities are mainly due to physical constrains in focusing and detecting high-energy gamma rays. In particular, for PET, finite positron range and non-collinearity of annihilation photons greatly contribute to degrade its overall spatial resolution performances [29].

However, the main advantage and strength of nuclear medicine modalities, such as PET and SPECT, is represented by their exceptional sensitivity, being able to detect up to pmol/mL concentrations of radiopharmaceutical probes in tissues [1][29]. Sensitivity in XFCT and XLCT, as described in the previous paragraphs, is currently restricted by scattering contribution of both primary and secondary photons, and ideal concentrations of few nmol/mL have been demonstrated by simulations for both the two emission techniques [17] [25]. Nonetheless, experimental imaging studies have not reached such values yet, reporting one or two orders of magnitude less in the detected concentrations [14] [15] [23] [25]. Background signal from tissue is a minor issue in PET and SPECT, due to very low attenuation of gamma rays in tissues [29].

Finally, it must be noted that, while PET and SPECT rely on radioactive agents that cannot be selectively trigger by the imaging procedure itself and usually have unwanted half lives, both XFCT and XLCT benefit of the capability to directly trigger the signal emission through the x-ray stimulation. Such important factor has several repercussion, such as limiting radiation dose only to the area selectively excited by the beam and excluding any noise contribution from undesired zones where the probe may have diffused (as it happens in PET and SPECT).

Optical imaging modalities, such as Diffuse Optical Tomography (DOT), Optical Coherence Tomography (OCT), Fluorescence Optical Imaging, Bioluminescence Optical Imaging and others [24], are currently under strong and wide investigation and research for molecular imaging, thanks to their high sensitivity and the high specificity of the optical probes used in such techniques [2]. "Smart" probes design, which can target particular molecular processes or functions are more achievable for optical imaging modalities. Moreover, such as for XFCT and XLCT, signal generation can be triggered directly during imaging and furtherly for some optical techniques such phenomenon can also be enhanced and optimized by the biochemistry of the probes themselves [2]. All these features contribute together to the excellent image contrast of these modalities against background tissues, thus enabling detection of very small concentrations of the probes in the range of nmol/mL to almost pmol/mL [1].

Nevertheless, spatial resolution capabilities of optical imaging modalities are limited by the depth of penetration of optical photons, both in the case of the stimulating source and the detectable signal. Regarding this, XFCT with energies of the fluorescence x-rays higher than 20 keV does not show this criticality (as well as for PET and SPECT), while XLCT could be constrained only in the emitted luminescence signal. Spatial resolution in mouse-sized subjects for optical imaging modalities is typically poor, only reaching between 1 to 10 millimeters [1] [24].

Although not extensively investigated for molecular imaging applications, MRI and CT can also be compared with XFCT and XLCT in terms of their main features, when they are used in combination with specific contrast agents. Spatial resolution for both MRI and CT modalities are among the best achievable in current clinical and preclinical imaging, ranging between 25-100 μm for MRI and 50-200 μm for CT [1]. However, because of the physical principles on which they are based, their sensitivity is greatly limited, allowing the detection of only relatively large concentrations of target agents, up to μmol/mL for both [1] [2].

Finally, regarding acoustic-based imaging modalities, primarily including ultrasounds (US) and photoacoustic imaging (PAT), it has been demonstrated how such techniques can be characterized by excellent spatial resolution (between 50 and 500 μm) when high frequency soundwaves are used. In addition, good time resolution for *in vivo* capturing of blood circulation and cardiac functioning can be achieved by these modalities for fast real-time imaging. However, spatial resolution in high-frequency US and PAT is limited, as for optical imaging, by tissue penetration of few centimeters (with decreasing spatial resolution) [1]. Anyway, the two abovementioned modalities are currently less established in molecular imaging and active research has started recently [2].

A last point for an effective comparison between different molecular imaging modalities (achieved and potential) and XFCT/XLCT needs to include also the cost of all these techniques, even if it is difficult to make an actual estimate of the prices of both the instrumentation and the probes involved. For XFCT and XLCT based on commercial detection device and sources, it can be assumed a lower expenditure rather than more expensive modalities such as PET, SPECT and MRI. Even so, CT and acoustic-based techniques can be considered cheaper, while most optical imaging modalities have been shown to be the least costly [1].

A qualitative summary of all the compared features here discussed is outlined in Table 1.1.

Imaging modality	**Spatial resolution**	**Imaging depth**	**Sensitivity**	**Quantitative degree**	**Temporal resolution**	**Cost**	**Type of probes**
XFCT	+++	++++	++	+++	++	$$$	Activatable
XLCT	+++	++	++	+++	+++	$$$	Activatable
PET	+	++++	++++	+++	+++	$$$$	Not activ.
SPECT	+	++++	++++	++	++	$$$$	Not activ.

Optical	++	+	+++	++	++++	$	Activatable
MRI	++++	++++	+	+	+	$$$	Limited activ.
CT	++++	++++	+	++	++	$$	Limited activ.
PAT/US	+++	++	++	+	++++	$$	Limited activ.

Table 1.1: Qualitative comparison between XFCT/XLCT and other molecular imaging modalities.

1.4. Potential theranostic applications of XFCT and XLCT systems

In the previous paragraphs, a detailed description of the characteristics and performances of XFCT and XLCT for functional and molecular imaging has been introduced, also comparing such features with those of other conventional and/or state-of-the-art imaging modalities. Nevertheless, one of the most interesting and promising aspects of XFCT and XLCT techniques is represented, as mentioned previously, by their capability and potential to be applied even for radiation-mediated therapy. Thus, with these techniques a therapeutic effect to the body and the tissues (mainly against cancer and tumors) can be delivered and the treatment can be simultaneously monitored with their primary imaging functions. Such combination of therapy and diagnostic, called theranostic (as explained before), exemplifies a unique and novel multidisciplinary and multitask approach to both medicine and the nuclear and radiological technology related to it [4].

The potential theranostic applications of a novel XFCT and XLCT system, described in this thesis work, and their investigation and feasibility are among the primary and most important targets and objectives of this project. In particular, a relevant importance and interest is stressed towards the use of nanotechnology as the primary form of contrast and therapeutic agents for this type of applications, due to the outstanding emergence of such field and its advantageous characteristics for medical purposes, specifically for theranostics.

Nanotechnology is commonly defined as the study and manipulation of matter and related physical phenomena at nanoscale, from about 1 to 100 nanometers. Most applications of nanotechnology in medicine, also those on which this work is focused, are related to the distinctive physical and chemical properties of matter at this scale, compared to bulk and macroscopic materials. Above all, the large surface-to-volume ratio and the possibility to manipulate and tune the absorption and scattering cross-sections of nanomaterials, when interacting with radiation, are the most exploited and researched. Moreover, from a perspective of cancer imaging and therapy, nanoparticles and nanomaterials are greatly suitable for accessing tumor cells and tissues in the presence of leaky, undeveloped and chaotic blood vessels. Hence, accumulation of small nanoparticles in the desired diseased regions is favorable, due to enhanced permeability and retention (EPR) effect [4] [32].

Considering all the aspects mentioned until now, it can be stated that nanoparticle-mediated and x-ray-stimulated anticancer therapies are the types of treatments on which the applications of a

novel XFCT/XLCT system described in this thesis project, are predominantly focused. An advanced XFCT/XLCT system designed with these applications in mind can provide an incredibly flexible, smart and specific tool for delivering targeted therapeutic effects with minimal invasiveness and high-precision, thanks to the use of highly focused and micro-collimated beams of x-rays to stimulate particular nanoparticle agents in cancer tissues. Furthermore, the stimulation through x-rays, which is the basis of XFCT and XLCT modalities, permits a selective and localized therapeutic action only in the desired area. Such action can be triggered only when the x-ray irradiation is present. In addition, the use of stimulating x-ray photons with relatively high energies, such as beyond 10 keV, would allow to achieve almost limitless tissue penetration, thus permitting to reach regions that are either very deep within the body (such as the brain) or surrounded by very dense areas (such as bone tissues and structures).

The emission of either ionizing radiation in the form of x-ray photons, through x–ray fluorescence, or optical light, via x-ray luminescence, is the fundamental and core process on which this kind of therapies relies on, as the primary activator of the treatment. Therefore, an active and switchable therapy can be delivered, minimizing in such way the amount of undue dose to surrounding healthy tissues and to other undesired areas where the nanoparticles may have diffused spontaneously.

Finally, due to the possibility of detecting x-ray fluorescence and x-ray luminescence for imaging, the therapeutic effects created with the x-ray stimulation can be monitored and tracked over the entire treatment with high performances typical of molecular and functional imaging, as those described in the previous paragraphs. Both therapy and imaging are thus performed by the same system, in a single setup and with the same instrumentation, providing great compactness, convenience and the possibility to save a lot of precious time in such way [33] [34].

The primary nanoparticle-mediated and x-ray-stimulated antitumor therapy, which has been investigated with the XFCT/XLCT system proposed and designed in this thesis work, is the so-called *X-ray Photodynamic Therapy* (XPDT). It involves the use of particular scintillating metal-based nanoparticles doped with activators, like the probes used in XLCT (as described in Paragraph 2.2), as the core therapeutic agents, usually conjugated with different shell membranes for protection and organic ligands for specific targeting of cancer cells. Such agents can be selectively stimulated with x-ray photons, in order to produce optical radiation (generally visible light or NIR) via x-ray luminescence, in the same way as in XLCT. Then, the emitted luminescence photons can either activate specific molecules incorporated in the nanoparticle shell, called *photosensitizers*, which in the presence of molecular oxygen O_2 produce singlet oxygen $^1O_2$ or other reactive oxygen species (ROS), or directly create these ROS in cellular aqueous solution via water radiolysis. Singlet oxygen and ROS are known to be powerful cytotoxic agents that can produce multiple damages to cancer cells, such as cellular membrane disruption, apoptosis or DNA double-strand break,

which ultimately lead to the death of the diseased cell [35] [36] [37]. The use of specifically engineered nanoparticles for XPDT, which incorporates metal-based scintillators, will also allow the simultaneous production of x-ray fluorescence with relevant photon energies. Hence, this radiation can easily penetrate the tissues and can be detected by the proposed system for XFCT. Simultaneous XFCT imaging of the XPDT treatment can be used to check the outcomes of the therapy, the correct radio-activation of the nanoparticles and their biodistribution in the body. Alternatively, also x-ray luminescence signal not involved in the direct production of ROS can be detected, either for XLCT or just to quantify the therapeutic effect. A scheme of the processes involved in nanoparticle-mediated XPDT is depicted in Figure 1.10 [38].

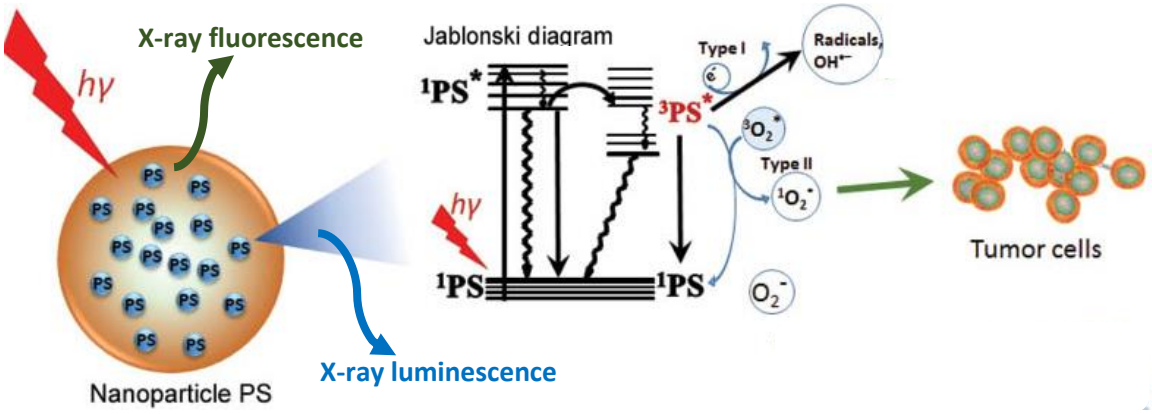

Figure 1.10: Schematic depiction of nanoparticle-mediated XPDT mechanisms of action [38].

Among the metal-based nanoparticles that are particularly suited for XPDT, those investigated in this thesis works are the following two types:

1) Lanthanum trifluoride nanoparticles doped with terbium, or LaF_3:Tb. The core material for x-ray fluorescence in these nanoparticles, Lanthanum (La), is a relatively high-Z (57) rare earth and it has a K-edge at 38.92 keV and an L-edge at 6.27 keV. It can produce multiple K-fluorescence, with $K_{\alpha 1}$ at 33.43 keV, and L-fluorescence, ranging around 5 keV. The complete XF energy spectrum of pure lanthanum (99%) is provided in Figure 1.11 [39]. The doping with terbium (Tb) gives to these nanoparticles scintillating properties, with principal emission wavelengths at

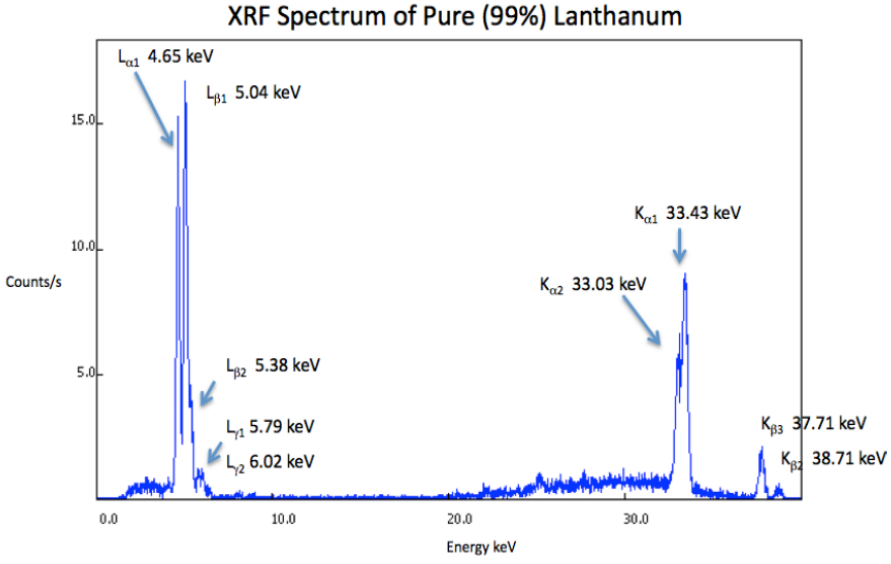

Figure 1.11: X-ray fluorescence spectrum of pure La (99%) taken at 40 kVp of tube voltage and 24 µA of tube current [39].

about 482 nm and 535 nm (typical of bluish light). The x-ray luminescence emission spectra of LaF_3:Tb is shown in Figure 1.12, for different dopant concentrations [40].

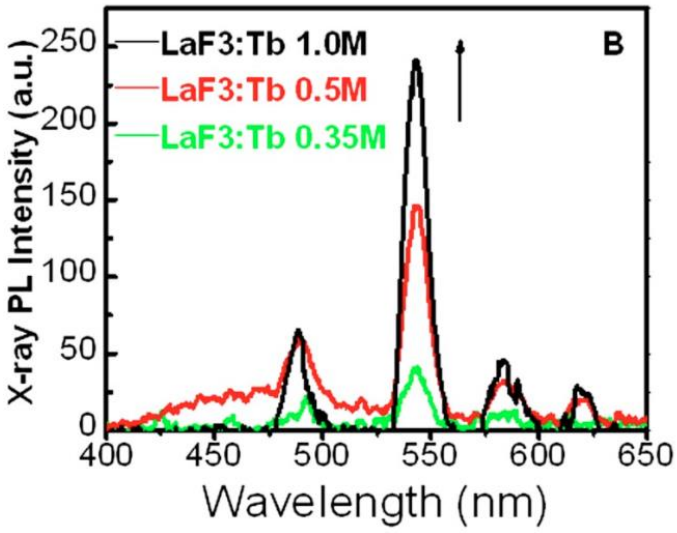

Figure 1.12: X-ray luminescence emission spectrum of LaF_3:Tb nanoparticles at different concentrations of the dopant [40].

2) Yttrium oxide nanoparticles doped with europium (III), or Y_2O_3:Eu(III). The main metal component of such compound is yttrium (Z=39), which has a K-edge at 17.03 keV. L-edge is negligible, due to corresponding energies too low for such applications. Yttrium (Y) can generate K-edge fluorescence at 14.96 keV ($K_{\alpha 1}$) and at 16.74 keV ($K_{\beta 1}$). The typical XF energy spectrum is also provided for pure yttrium (99%), in Figure 1.13 [39].

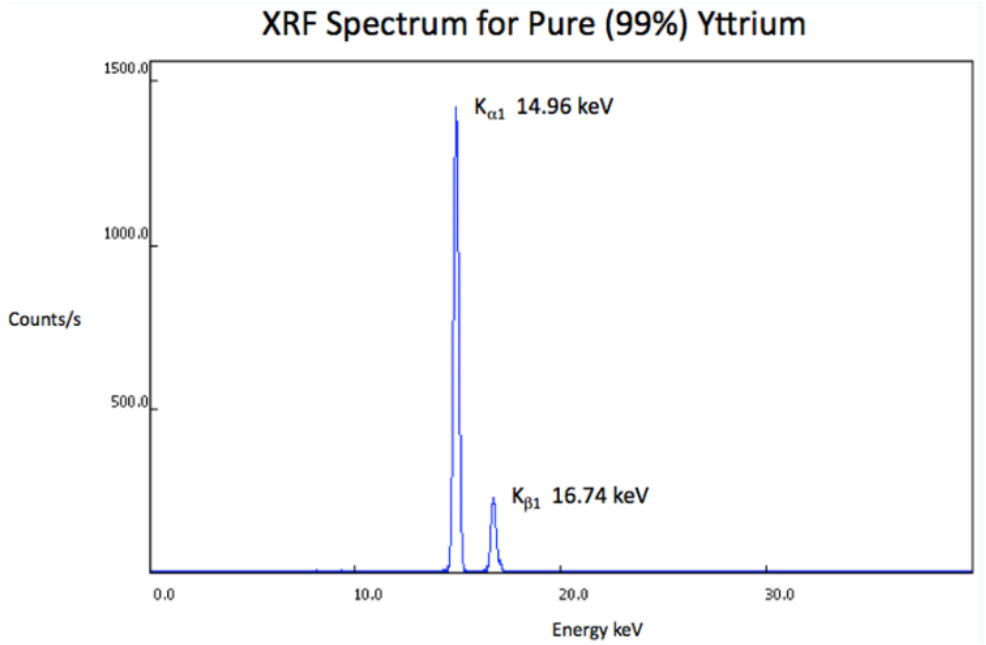

Figure 1.13: X-ray fluorescence spectrum of pure Y (99%) taken at 40 kVp of tube voltage and 24 μA of tube current [39].

Furthermore, Y_2O_3:Eu(III) can also produce radio-luminescence under x-ray excitation with emission wavelength equal to 611 nm (red light). This is due to the presence of europium (III) as dopant activator (as explained in Paragraph 2.2). The corresponding XL emis-

sion spectrum from Y_2O_3:Eu(III) is then visible in Figure 1.14 [41].

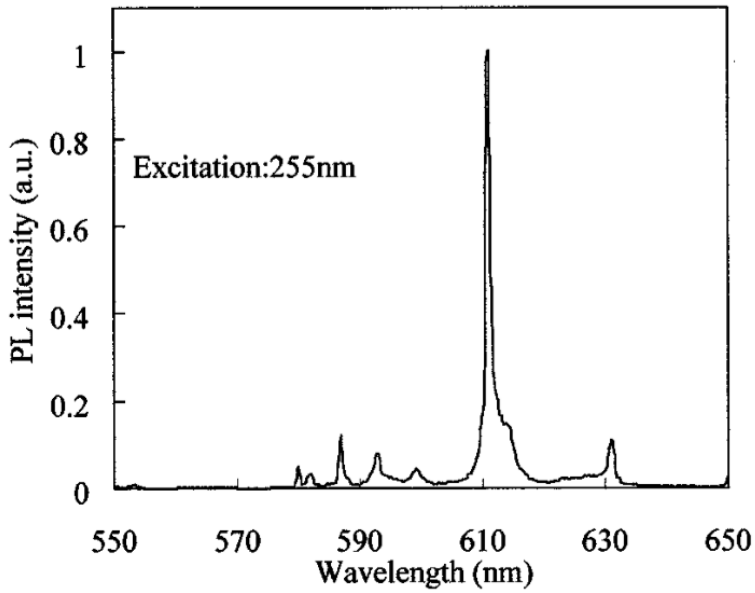

Figure 1.14: X-ray luminescence emission spectrum of Y_2O_3:Eu(III) [41].

Both the two nanoparticles just described have been chosen primarily for their relatively high K-edge (also L-edge for lanthanum) energies, which perfectly match the typical ones involved in the medical use of x-rays. Moreover, they are optimally suited for both the two types of x-ray sources that are used in the proposed XFCT/XLCT system, as it will be described in the next Chapter.

Another relevant theranostic application, which has been experimentally investigated with the XFCT/XLCT setup described in this work (see Chapter 4 and Chapter 5), is generally called *X-ray Auger Therapy*, also known sometimes as *Photoactivation Therapy* (PAT). Such therapeutic treatment involves the x-ray excitation of metal-based compounds and nanoparticles with high atomic number, in order to produce a particular form of secondary radiation, i.e. Auger electrons [42]. These electrons are produced during a process complementary to x-ray fluorescence, when, in atoms, the de-excitation energy from the filling of an electron vacancy due to photoelectric effect, is not emitted as a characteristic x-ray, but instead is transferred to an electron in the outer shell. Being such energy usually greater than the binding energy of that electron, this particle is thus ejected from the given atom and becomes a low-energy free electron, called Auger electron [6] [8]. Such process is schematized in Figure 1.15, also showing x-ray fluorescence.

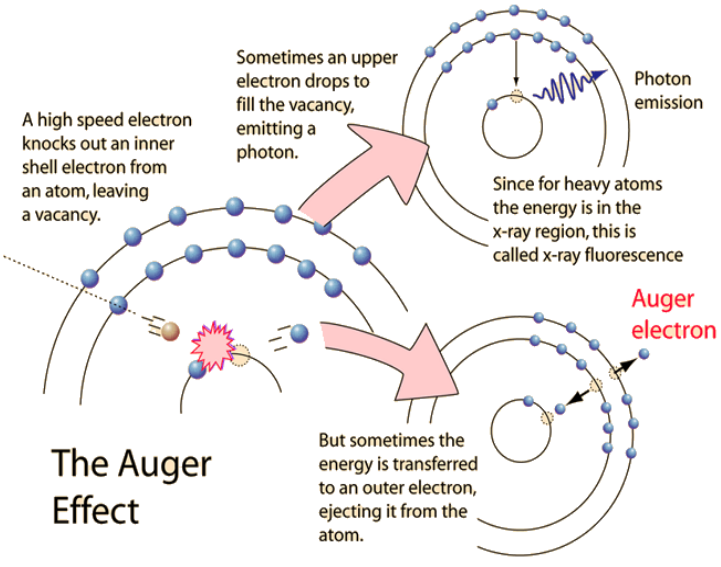

Figure 1.15: The process of Auger electron emission, in comparison with x-ray fluorescence.

The usefulness in cancer therapy of these Auger electrons, having low kinetic energy (from hundreds of eV to few keV), comes from their high linear energy transfer (LET), defined as the amount of energy deposited per unit path length travelled by such particlew in tissues. Therefore, Auger electrons can release all their energy in a very short range, thus being able to create a very localized cytotoxic effect in cancer cells, by either creating free radicals via water radiolysis or directly damaging the DNA. Hence, x-ray induced Auger therapy consists in the creation of a large number of these Auger electrons from metal-based compounds accumulated in cancer tissues, after proper excitation via x-ray beam [42] [43]. The mechanisms of Auger therapy with selective x-ray stimulation of metal-based nanoparticles are shown in a diagram in Figure 1.16.

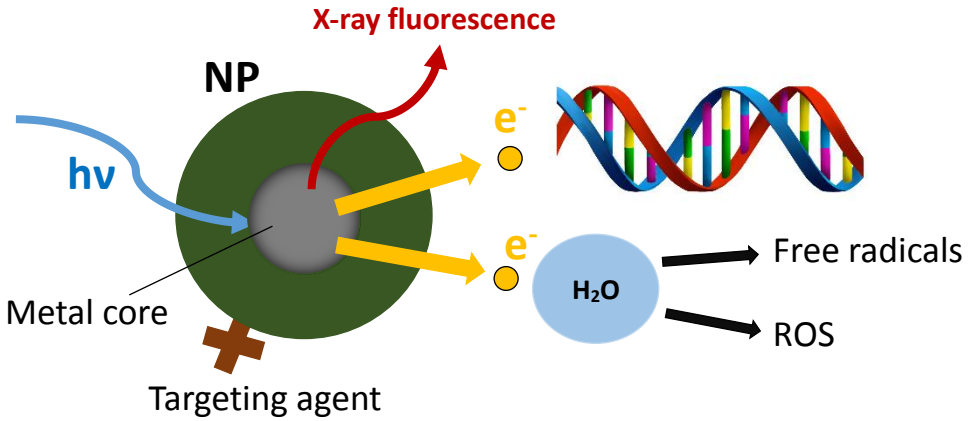

Figure 1.16: X-ray induced Auger therapy mediated with metal-core nanoparticles.

The use of nanoparticles with a metal core is particularly favorable for this kind of therapeutic application, because nanoscale materials can absorb a large amount of x-ray photons within a small volume. This is thanks to their high atomic density and large surface-to-volume ratio [42]. Therefore, in the experimental investigations with the proposed XFCT/XLCT system, hafnium dioxide nanoparticles (HfO_2) have been used and tested, with x-ray induced Auger therapy in mind as primary target application. An image taken with Scanning Electron Microscopy (SEM), showing the nanoscale structure of these nanoparticles, is visible in Figure 1.17 [44]. The metal core composing this type of nanoparticles, i.e. hafnium (Hf), has a very high atomic number (Z=72) and a high density ($\rho = 13.32$ g/cm^3), which make it perfectly suited for absorbing x-rays through photoelectric effect. Moreover, both its K-edge, at 65.34 keV, and L-edge, at 11.26 keV, match in a good way those energies required to penetrate several centimeters of tissue. In addition to that, HfO_2 can also produce x-ray fluorescence photons with K-fluorescence around 65 keV and L-

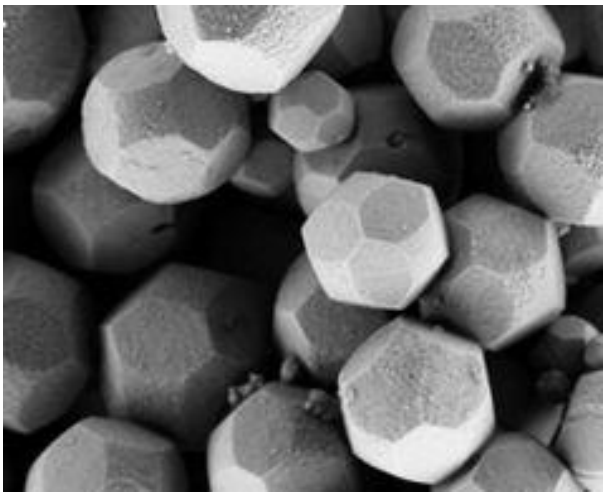

Figure 1.17: SEM image of HfO_2 nanoparticles [44].

fluorescence ranging between 7 to 9 keV. The XF energy spectrum for the L-fluorescence of pure hafnium (99.7%) is depicted in Figure 1.18.

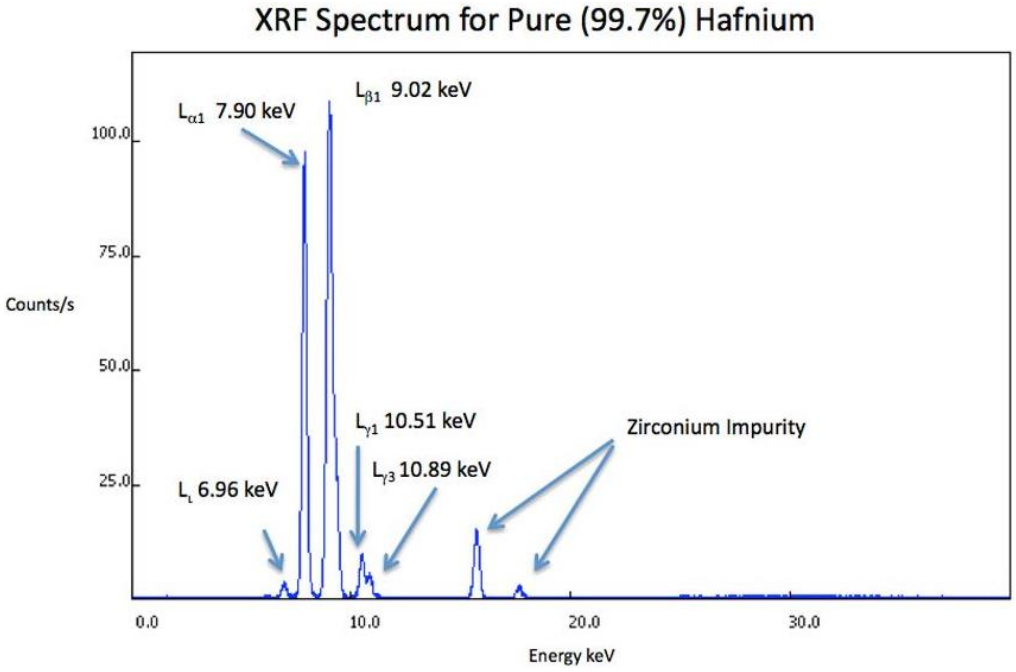

Figure 1.18: X-ray fluorescence spectrum of pure Hf (99.7%) taken at 40 kVp of tube voltage and 24 µA of tube current [39].

As for XPDT, also X-ray induced Auger therapy with HfO_2 nanoparticles can be actively monitored by detecting x-ray fluorescence produced by hafnium and use it to perform XFCT imaging. This is possible because, as explained previously, x-ray fluorescence is a competitive and complementary process with Auger electron emission and both are generated from the same physical trigger action, i.e. the selective excitation with x-rays [6].

Finally, it has to be mentioned a third type of radiation therapy that can be combined with the previously mentioned x-ray-induced Auger therapy. Such treatment consists in the radiosensitization and radiation dose enhancement of tumor tissue, simultaneously with conventional chemotherapy. For example, the use of Auger electron emitting compounds in combination with chemically toxic agents can greatly increase the total net damage to cancer cells. Experimental investigations are currently active with the use of gold nanoparticles and chemotherapeutic drugs to produce such kind of effect, as shown in Figure 1.19 [45]. Nonetheless, the possibility to use metal-based chemotherapeutic

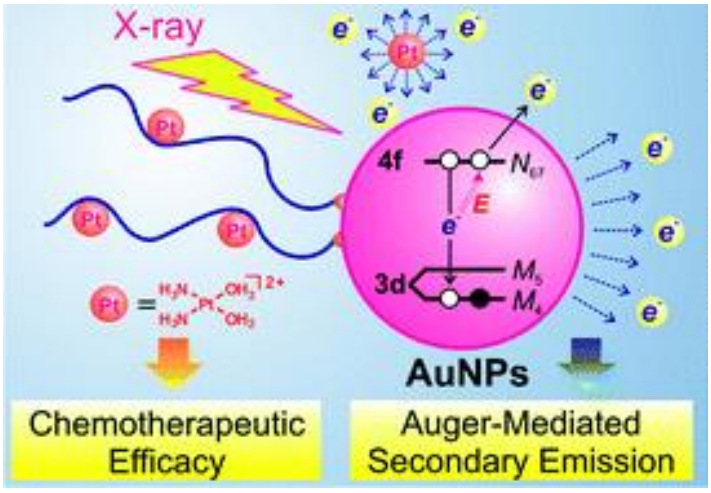

Figure 1.19: Diagram depicting the combination of Auger therapy with Au nanoparticles and chemotherapy, in order to produce radiosensitization of tumor tissue and radiation dose enhancement [45].

agents, such as Cisplatin, which is the only FDA approved drug for chemotherapy that incorporates metals, would greatly facilitate this type of therapeutic treatment, due to the use of only one type of agent, instead of multiples. Cisplatin, whose molecular structure is depicted in figure 1.20, has a metal core composed of atomic platinum (Pt), which has a very high Auger electron yield [45]. Moreover, platinum is also a very high-Z material (Z=78) and can be used for producing x-ray fluorescence for combined XFCT imaging with the therapeutic delivery. In fact, platinum has a K-edge at around 78.4 keV and an L-edge equal to about 13.88 keV, which are optimally suited energies for XFCT, deep within tissues. In particular, K-fluorescence of platinum has an energy of 77.88 keV, which has almost limitless penetration in every type of biological tissue, and an L-fluorescence ranging from 9 to 11 keV. The XF energy spectrum of pure platinum (99.9%) for its L-fluorescence can be seen in Figure 1.21.

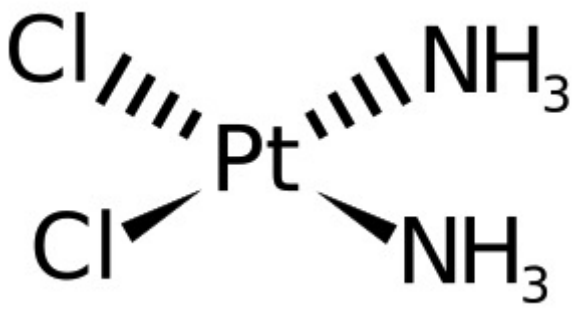

Figure 1.20: Molecular structure of cisplatin.

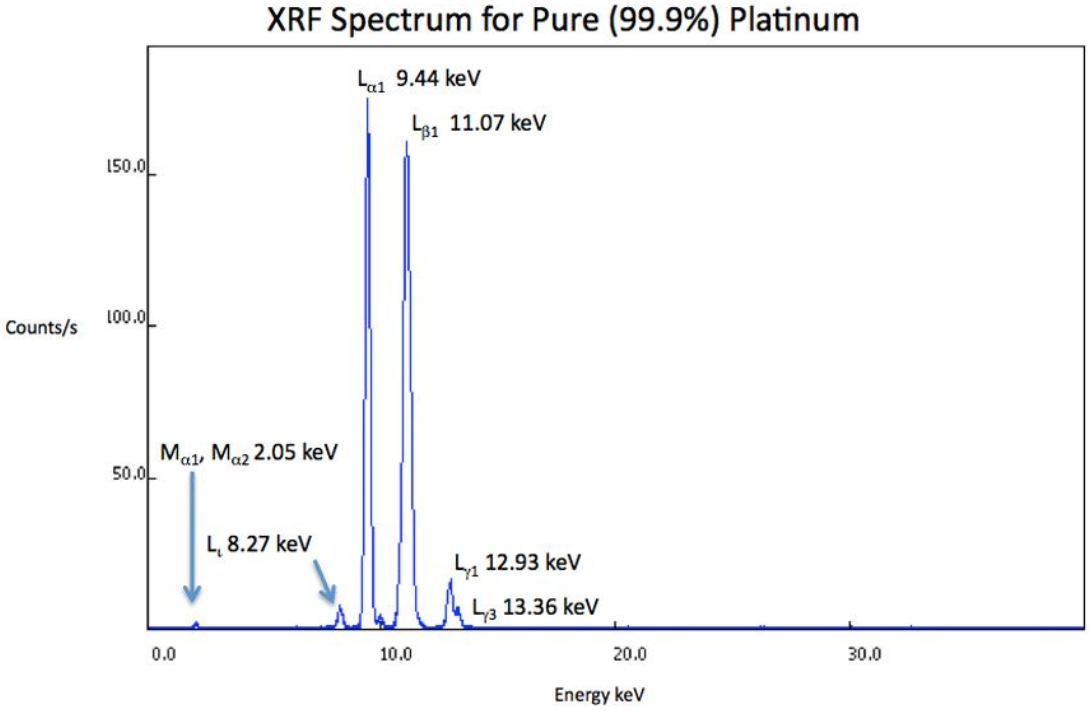

Figure 1.21: X-ray fluorescence spectrum of pure Pt (99.9%) taken at 40 kVp of tube voltage and 24 µA of tube current [39].

Other theranostics applications can also be potentially performed with the XFCT/XLCT system that will be described in details in the next Chapter. An example is represented by x-ray induced selective drug release, where x-ray stimulation is used on nanoparticles or compounds carrying antitumor drugs that could be released after such excitation [32]. However, such additional therapies have not been investigated in the current thesis works, but they can anyway be considered and researched in future studies and developments of the proposed system.

2. Design and development of a novel XFCT/XLCT system

A novel design for a benchtop combined X-ray Fluorescence and X-ray Luminescence Computed Tomography system (based on the premises introduced in Chapter 1) has been proposed, developed and built in the Radiation Detection and Imaging Group, at the University of Illinois at Urbana-Champaign (UIUC). The system uses state-of-the-art commercial and conventional x-ray sources, detectors and camers, stage motors, supports and custom-made apertures and collimators. The main goals of such system involve the testing and the investigations on the feasibility and the performances of desktop tri-modal XFCT, XLCT and micro-CT imaging, ultimately including the research on potential advanced theranostic applications of such techniques and technologies (as described in the previous chapter).

It must be mentioned that the creation of a working and well-characterized XFCT and XLCT laboratory setup, plus the demonstration of the practicability and achievability of its good imaging and therapeutic capabilities, has a substantial importance for future progressions of such technology towards preclinical or even clinical implementations. As an example, using conventional and less expensive x-ray sources, such as x-ray tubes or micro-focused sources that do not differ excessively from those required in daily diagnostic imaging, is necessary and inevitable, because of the impracticableness and unaffordability of synchrotron-based sources. The capability of scaling the system, such as for small animal imaging or human whole-body imaging, is also another fundamental factor that must be taken into account and analyzed in the same perspective. Anyway, the current system should be mainly considered as a preliminary project only for research and investigations on the aforementioned topics, though it could potentially lead to significant results for new, advanced and commercially focused designs in the future.

2.1 Materials, instrumentation and radiation detection devices

First and foremost, the XFCT/XLCT system to be described has been located and assembled inside a specifically designed box, which is made of a metallic structural frame and plasterboard walls. The purpose of such structure is twofold: (1) to shield the outer environment and personnel standing in the vicinity of the x-ray sources from harmful effects and excessive doses of ionizing radiation; (2) to obscure as much as possible the space inside the box and to prevent the entrance of ambient light. This second reason is of fundamental importance, in order for the luminescence background level to be reduced at the lowest value achievable during the detection of emitted optical light in XLCT and to prevent it to contaminate the x-ray luminescence signal. Moreover, to enhance such effect, the internal walls of the box has been blackened with black paper and black

tape and all the inner edges and corners of the box have been covered with black foam, as to prevent light leakages from outside. A system of fans has been also provided on the top, for ventilation and cooling of the inside of the box and for removing the heat generated by the instrumentation during functioning. The assembly of fans and the pipes connecting them with the inside of the box has been covered with black plastic bags, to further block light penetration through such system. Finally, a black thick tissue curtain has been mounted in front of the doors of the box to additionally cover potential chinks and spaces for light to enter the structure during experiments. Pictures of the box structure and its blackened internal walls are depicted in Figure 2.1.The curtain on the doors of the box and the covered ventilation system are clearly visible.

Figure 2.1: Box structure containing the XFCT/XLCT system (left) and blackened internal walls (right).

The box structure is aboveground and lays on an optical table with precision tunable damper (Newport Integrity 3 VCS Table System with 1 precision tuned damper [46]), where the instrumentation has been mounted and assembled. The damper-coupled optical table is primarily used to minimize and to attenuate potential vibrations of the surroundings from affecting the system and its performances, in particular to avoid undesired variations in the setup geometry during experiments. The optical table with damper is shown in Figure 2.2 [46].

Figure 2.2: Newport optical table with precision tuned damper supporting the box setup [46].

The optical table provides the working platform for the XFCT/XLCT system, where all the instrumentation and the devices of the setup, together with their supporting parts, are assembled. Regarding such constituents, the described system is composed of two separate commercial x-ray sources with different characteristics and purposes. One of them is a monochromatic x-ray tube (Xenocs GeniX^{3D} x-ray delivering system [47]) using a molybdenum target anode to produce a micro-focused pencil beam of 17.48 keV x-ray photons. The primary collimation and monochromatization of the beam is achieved by an aspheric multilayer optic (Xenocs FOX^{3D}) embedded in the source, with the capability of maintaining high brightness at low power. Hence, the photon flux of the source at the maximum operating settings (50 kVp of tube voltage and 1 mA of tube current) is approximately 25 million of photons per second ($25 \cdot 10^6$ ph/sec). The pencil beam diameter at the focal spot (23 cm away from the beryllium window of the tube) is about 130 µm with a divergence of about 5 mrad. The micro-focused x-ray beam can also be further collimated down to about 100 µm, using a vacuum-enhanced collimation system with different sizes of platinum pinholes. The vacuum inside the collimator is provided in order to eliminate scattering of photons in air and conserve the high photon flux. The source anode is water-cooled at ambient temperature with an external chiller, in order to prevent its potential overheating and melting during operation. A picture of the Genix^{3D} monochromatic source and its components is visible in Figure 2.3 [47].

Figure 2.3: Genix^{3D} monochromatic source system (left) and inside the setup with vacuum-enhanced collimation (right) [47].

The source is specifically suited for XFCT and XLCT applications, due to its high flux, size of the x-ray beam and monenergetic spectrum, as explained in the Chapter 1. In particular, the shape of the pencil beam can be used to scan line-by-line voxel regions of the imaged object as in conventional synchrotron setups (see Chapter 1). Furthermore, the energy of the source, coming from the Mo anode, is perfectly suited for excitation of the K-edge of nanoparticles such as Y_2O_3:Eu(III), and of the L-edge of compounds like platinum and hafnium.

The second source of the XFCT/XLCT system is a conventional high-flux, high-stability polychromatic x-ray tube (Oxford Instruments Apogee 5000 Series [48]) with a tungsten anode, delivering a cone beam with a focal spot size of about 35 µm and a total aperture angle of 22°. The polychromatic source can be operated from 10 to 50 kVp of tube voltage and between 0.01 and 1 mA of tube current (the maximum power achievable by the source is 50 W). The vacuum envelope of the x-ray tube has a beryllium window of 127-µm thickness. A remote-controlled shutter has been attached to the front of the source and it can be synchronized with the detector system. Cooling of the tube is provided through a double fan assembly mounted on two sides of the x-ray tube shielding. The polychromatic source and its place in the setup is shown in Figure 2.4 [48].

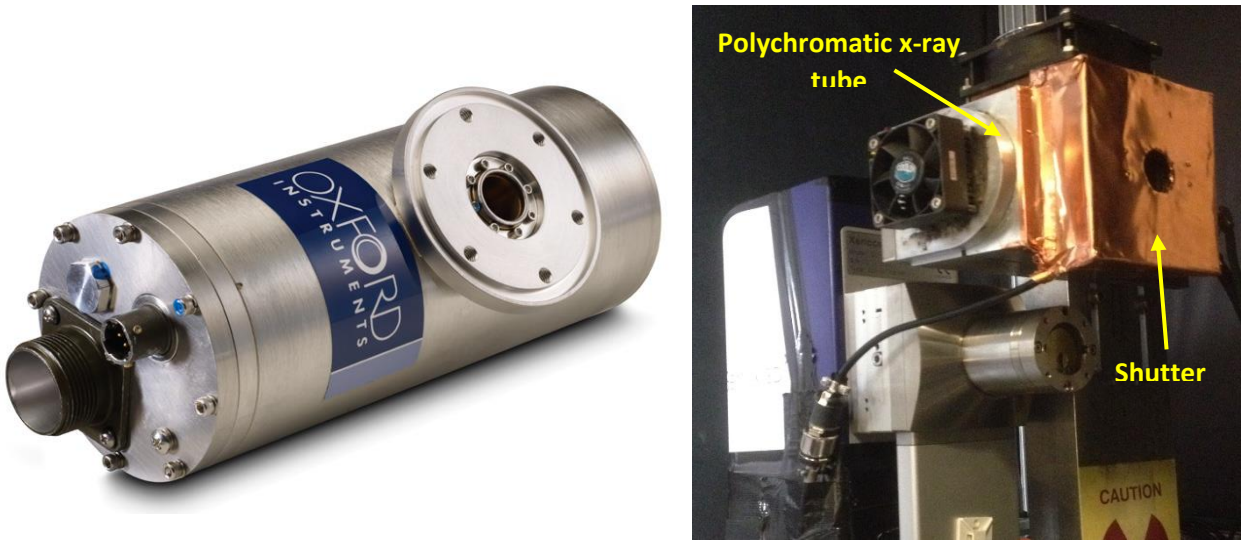

Figure 2.4: Apogee 5000 polychromatic source (left) and its place in the XFCT/XLCT setup above the Genix^{3D} monochromatic source (right) [48].

The polychromatic source has been chosen and implemented in the system for CT imaging, but it can also be used to perform XFCT. Its cone beam can entirely irradiate the object or it can be collimated using a XFET geometry (as described in Chapter 1), such as by using a single slit collimator to produce a thin sheet beam of x-rays for selective excitation [11].

The other important major part in the XFCT/XLCT system, besides the two sources assembly, is the radiation and optical detection system, which is composed by five different detectors, each with specific purposes and characteristics. The first detector is an x-ray CCD camera (Andor iKon-L DO936 [49] [50]) with a sensor containing an array of 2048 by 2048 square pixels with size equal to 13.5 µm. The total active area of the detector sensor is then 27.6 by 27.6 millimeters, providing a large field of view and excellent spatial resolution. The CCD camera has a 5-stage TE cooler, which enable operation at sensor temperatures down to -50° C. Cooling of the camera sensor permits high sensitivity and minimize dark current noise. Low-noise readout electronics is also incorporated in the camera and four different pixel readout rates are available (50 kHz, 1 MHz, 3MHz and 5 MHz) in a wide dynamic range. Pixel binnings equal to 1x1, 2x2, 4x4, 8x8 and

16x16 are also allowed with maximum frame speed up to 8.745 frames per second. The maximum quantum efficiency (QE) of the back-illuminated sensor of the CCD camera can reach more than 90% in an interval of photon energies between about 1 keV to 7-8 keV. Hence, Figure 2.5 [49] depicts the general variation of the QE of the CCD camera along the entire energy detection range (from few keV to around 20 keV).

Although the overall range of energies that can be detected by such CCD camera spans from around 1-2 eV (corresponding to NIR photons) up to 20 keV, the detector has been modified upon request to incorporate a 0.5 mm beryllium window in front of the sensor. This has been done in order to filter the lowest-energy photons and to allow detection only of x-rays.

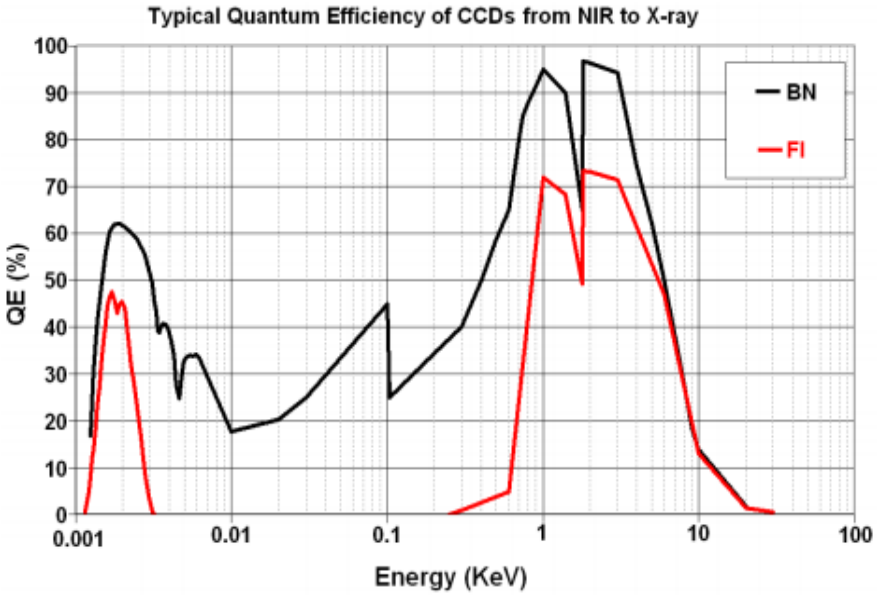

Figure 2.5: Typical QE trend of the Andor iKon-L CCD camera along the entire energy range [49].

In addition to that, a stainless steel flange has been designed and attached on the front surface of the detector, as to protect the fragile Be window and also to permit the mounting of apertures and collimators before the sensor. The commercial x-ray CCD camera is visible in Figure 2.6 [49], together with its modified version, which is currently used in the XFCT/XLCT setup, with the Be window and the stainless steel front flange.

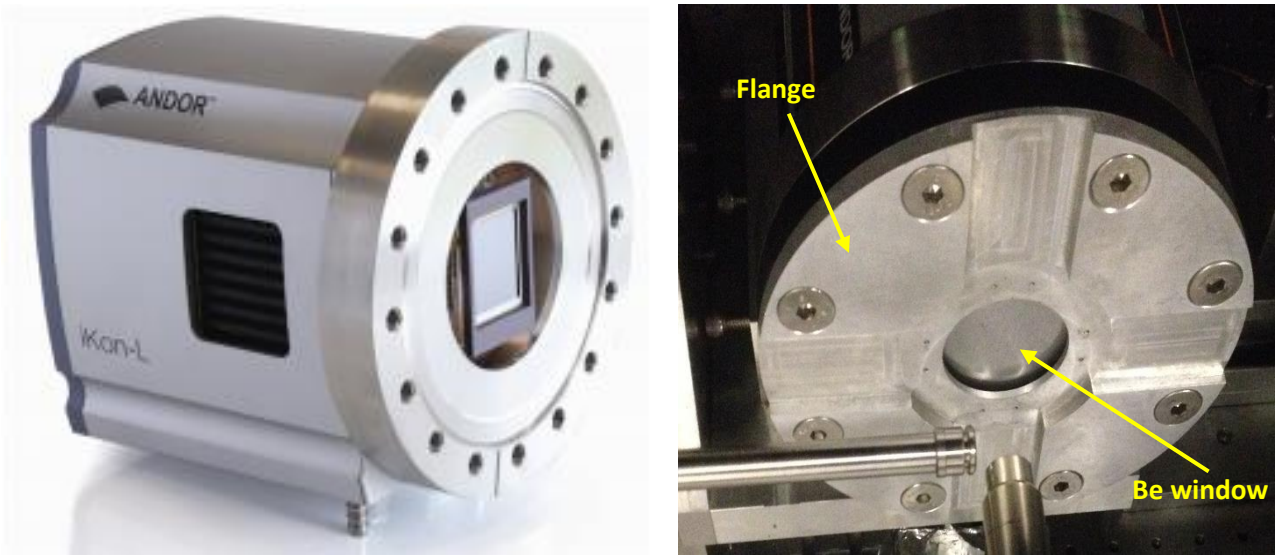

Figure 2.6: Andor iKon-L CCD camera in its original version (left) and in its modified version, inside the setup, with Be window and stainless steel flange (right) [49].

The modified x-ray CCD camera has been chosen and designed exactly for detection and imaging of x-ray fluorescence. The maximization of the QE of the sensor in a suitable energy range and the incorporation of the flange, where aperture and collimators can be mounted, are engineered examples of such purpose. The high-resolution and low-noise performances of the camera are also fundamental for performing XFCT with excellent spatial resolution and good sensitivity.

The second detector that has a primary role within the XFCT/XLCT signal is an electron-multiplying CCD (EMCCD) camera (Andor iXon3 [51]) for optical detection. The EMCCD camera is greatly similar in structure to a conventional CCD camera, except for the presence of a series of multiplying register added before the readout amplifier. Such registers amplify the charge signal with a gain of several thousands, through a process called "impact ionization". Such signal amplification permits very low-noise performances at high frame speed, compared to traditional CCD cameras. In particular, EMCCD cameras would allow a readout noise of less than one electron RMS per pixels at 20 MHz of readout speed, while a conventional CCD camera at the same rate would present a readout noise of 30 or more electrons [52]. The EMMCD camera in the XFCT/XLCT setup has a sensor composed of 512 by 512 square pixels with size equal to 16.5 µm. The active area of the sensor is therefore equal to about 8.45 by 8.45 millimeters. The EMCCD can be cooled by a 4-stage TE cooling system down to about -35°C, in order to furtherly reduce dark current noise. Moreover, the EMCCD has been coupled with a custom-made assembly comprising of an electrostatically focused demagnifying image intensifier (DM) tube (Phototek demagnifying image intensifier DM80 [53]) and relative electronics, mounted in front of the camera sensor through a specific case assembly to support it. A picture of the EMCCD and the DM tube assembly is provided in Figure 2.7.

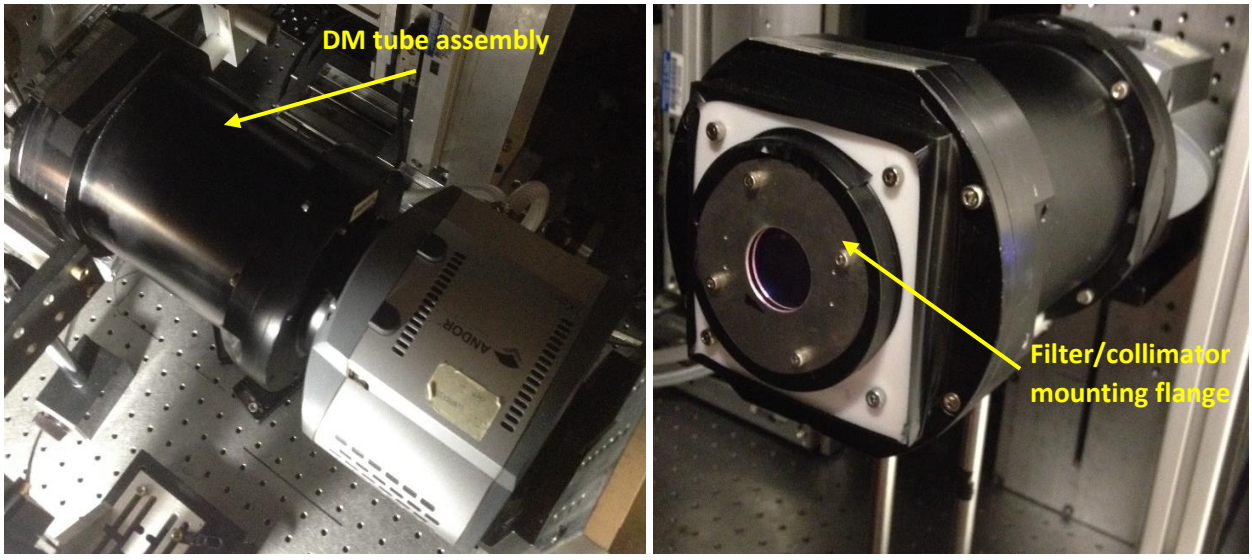

Figure 2.7: Andor iXon3 EMCCD with DM tube assembly (left) and support for mounting collimators and optical filters (right).

The DM tube is used mainly to furtherly improve signal-to-noise ratio, by focusing and amplifying

the incoming luminescence signal before transmitting it to the camera, thus providing an extra gain stage to the detection process. In addition, through its demagnification effect, such device works as an "electronic taper" to enlarge the active area of the camera [52]. In fact, the DM tube as an input window of 80 by 80 mm and an output window of 40 by 40 mm. Inside the support case, the output of the DM tube is coupled to the EMCCD sensor via a fiber-taper and a fiber-faceplate that have aspect ratios equal to 1.5:1 and 1:1, respectively [52] [54]. Finally, the DM tube case also incorporates a machined flange on the front, where it is possible to mount collimators and optical filters for imaging of x-ray luminescence signal with XFET geometries (see Chapter 1) and discrimination of desired optical wavelengths in the measured signal.

The third principal detector used in the XFCT/XLCT setup is a hybrid sCMOS camera (Andor Zyla 5.5 [55]) composed of an array of 2560 by 2160 square pixels of size equal to 6.5 µm. It has an active sensor area of 16.6 by 14.0 mm (21.8-mm diagonal) and can be operated at two different pixel readout rates: a slow rate at 200 MHz and a fast rate at 560 MHz. The sCMOS camera is air-cooled, down to 0°C for a mean dark current value of about 0.14 electron per pixel per second. However, it can also be operated at room temperature. Such device is originally designed for optical applications and light detection in a range of wavelengths between 400 nm and 1000 nm with a maximum QE of about 60%. Nevertheless, in the XFCT/XLCT system, this camera has been chosen for primary x-ray detection from the stimulating beams of the two sources. Therefore, the original version of the detector has been modified by coupling the sCMOS sensor with a cesium iodide (CsI) scintillation crystal, in order to detect ionizing radiation and convert it to visible light before transmitting it to the camera. The front surface of the CsI crystal facing the incoming beam is then shielded with a thin beryllium window for protection and to avoid humidity accumulation on the scintillator. Figure 2.8 [55] shows the original version of the Zyla sCMOS camera and modified one, inside the setup.

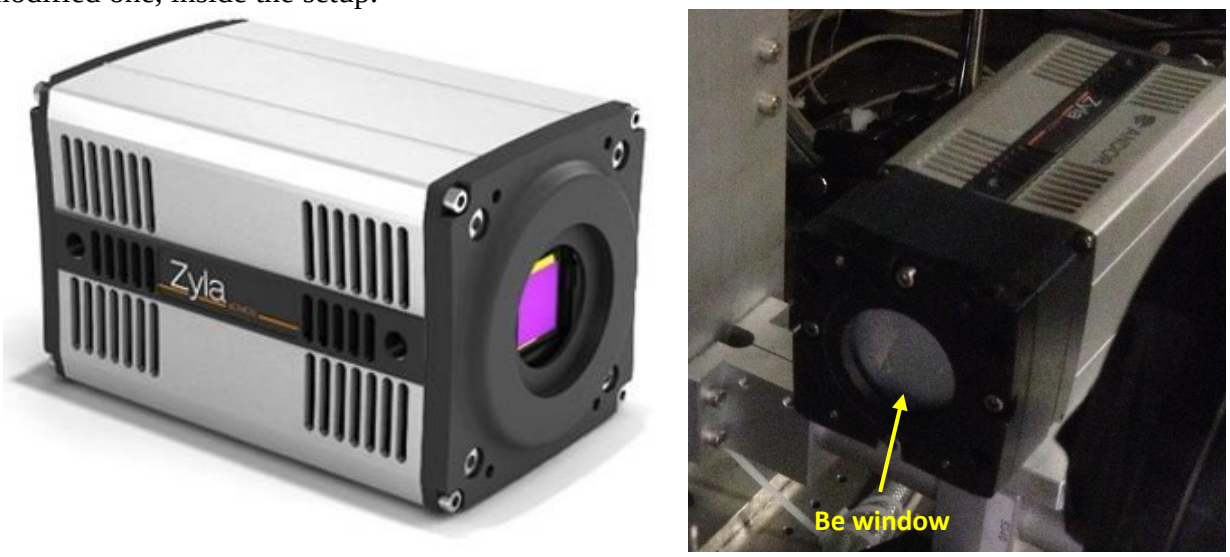

Figure 2.8: Andor Zyla 5.5 sCMOS camera (left) and modified version, inside the setup, with CsI scintillator and Be window (right) [55].

The main purpose of the Zyla sCMOS camera in the XFCT/XCLT setup is to perform high-resolution x-ray transmission micro-CT imaging, for relatively small objects and field-of views (due to the limited dimensions of its sensor area), with the cone beam of the polychromatic x-ray tube. It can also be used during XFCT and XLCT to measure the x-ray transmission of the primary excitation beam (from both the two sources) through the imaged target, for attenuation estimation and correction of the final XF or XL image. Finally, it is also useful in a practical way to help aligning a small pencil beam from the monochromatic source with the object, again by measuring its relative x-ray attenuation at different beam positions.

For x-ray transmission CT imaging of bigger objects and larger fields of view, a fourth detector is incorporated in the XFCT/XLCT providing a larger magnification. Such device is a digital flat panel (Varian Paxscan 1313 [56]) made of amorphous silicon for the receptor, coupled with direct deposit CsI crystal for the conversion screen (converting the x-ray signal in visible light). The flat panel has a 1024 by 1024 array of square pixel with 127-μm size, for a detection active area of 130 by 130 mm. The flat panel can be operated at room temperature with maximum readout frame rate of 30 frames per second. Figure 2.9 [56] illustrates such flat panel and its place inside the XFCT/XLCT setup.

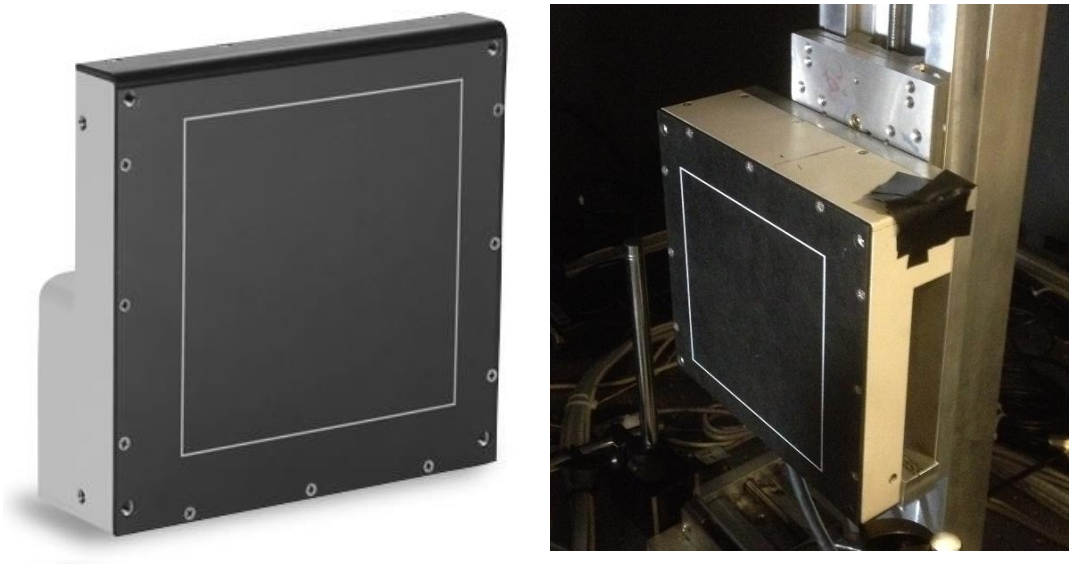

Figure 2.9: Varian Paxscan 1313 flat panel detector (left) and its position inside the XFCT/XLCT setup (right) [56].

Finally, the experimental XFCT/XLCT setup involves the use of a fifth and last detector, to complete its radiation detection system. This detector is a single-crystal semiconductor cadmium telluride (CdTe) spectroscope (Amptek XR-100T-CdTe [57]), using a 3 by 3 by 1 mm CdTe diode crystal mounted on a two stage TE cooler. The device also comprehends a charge sensitive preamplifier and operates under vacuum (using a 100- μm beryllium window) at a temperature as low as -30° C. The CdTe detector is optimum for x-ray spectroscopy, due to its large range of detectable photon energies (from few to even several hundreds of keV) and primarily for its high energy

resolution. In fact, for this spectroscope, the typical full width at half maximum (FWHM) at 122 keV is about 1.2 keV. For lower energy applications, as in the case of fluorescence x-rays ranging between 5 to 100 keV, the CdTe spectroscope can reach a minimum FWHM of about 390 eV. The detector can also be used to measure the flux of x-ray photons coming from the primary x-ray beam and to estimate the energy attenuated by the object during transmission. A picture of the Amptek CdTe spectroscope and an example of energy spectrum at low energies measured with such device are visible in Figure 2.10.

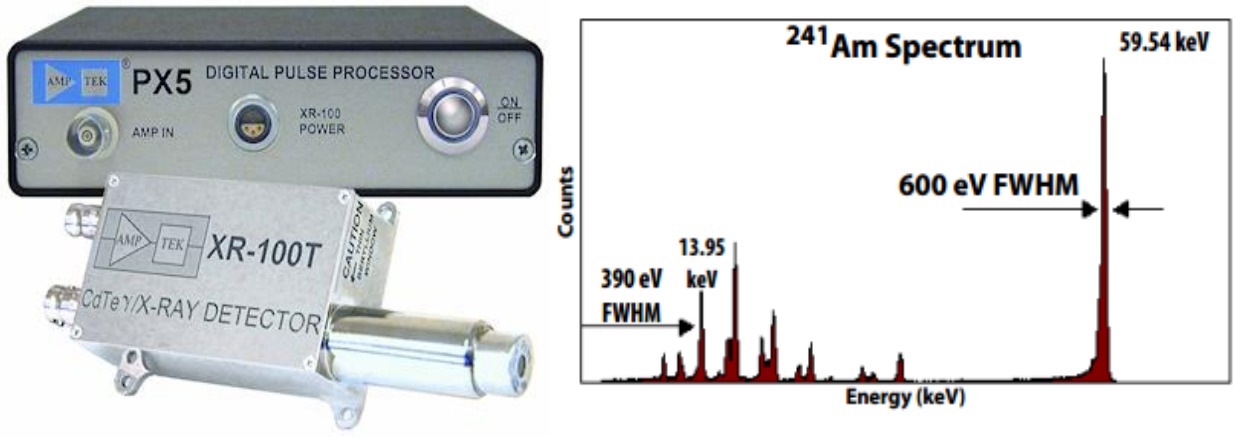

Figure 2.10: Amptek XR-100T-CdTe detector with digital pulse processor (left) and energy spectrum of ^{241}Am source measured with such device (right) [57].

To conclude the description on the instrumentation composing the XFCT/XLCT system, it must be reported that a mechanical arm connected with two linear stage motors is used as the principal stand for supporting any sample to be imaged and experimented in the setup. A high-precision micro-stage motor and a high-precision rotational motor with encoder are attached at one end of the arm, where the imaged object is mounted. Such assembly provides the capability of movement of the object in three directions (XYZ) with micrometer tolerance, plus allowing rotation of the sample up to 360° with great accuracy, in order to perform the scanning of the imaged sample and complete tomographic/volumetric information acquisition. A picture of the abovementioned support assembly with motors is illustrated in Figure 2.11. A box structure, made of multiple layers of copper and aluminum, wrapping the micro-stage linear motor is visible in the figure and it has been designed

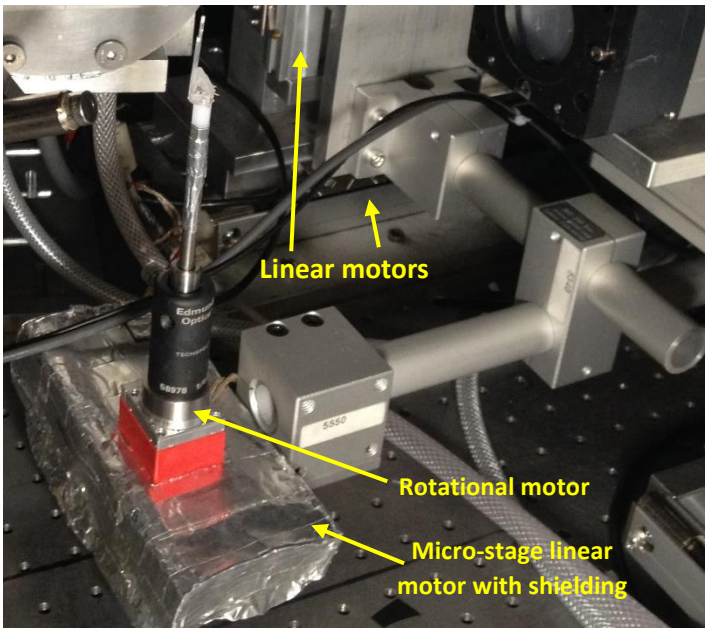

Figure 2.11: Support assembly with linear and rotational motors for movement of the sample in the setup.

to block NIR light coming from the optical switch of the device. This would prevent noisy contamination of the x-ray luminescence signal to the EMCCD camera.

2.2 Geometry of the system and modeling of the setup

The XFCT/XLCT system has been designed as a two-level setup, separating along the vertical direction the part concerning XFCT and XLCT from the part related to x-ray transmission CT. The upper level includes the polychromatic x-ray tube and the two detectors designated CT imaging, i.e. the Zyla sCMOS camera and the flat panel. These detectors are interchangeable and can be used one at a time by simply moving the Zyla camera in or out the way of the primary x-ray beam. A depiction of the geometry of the CT level is shown in Figure 2.12.

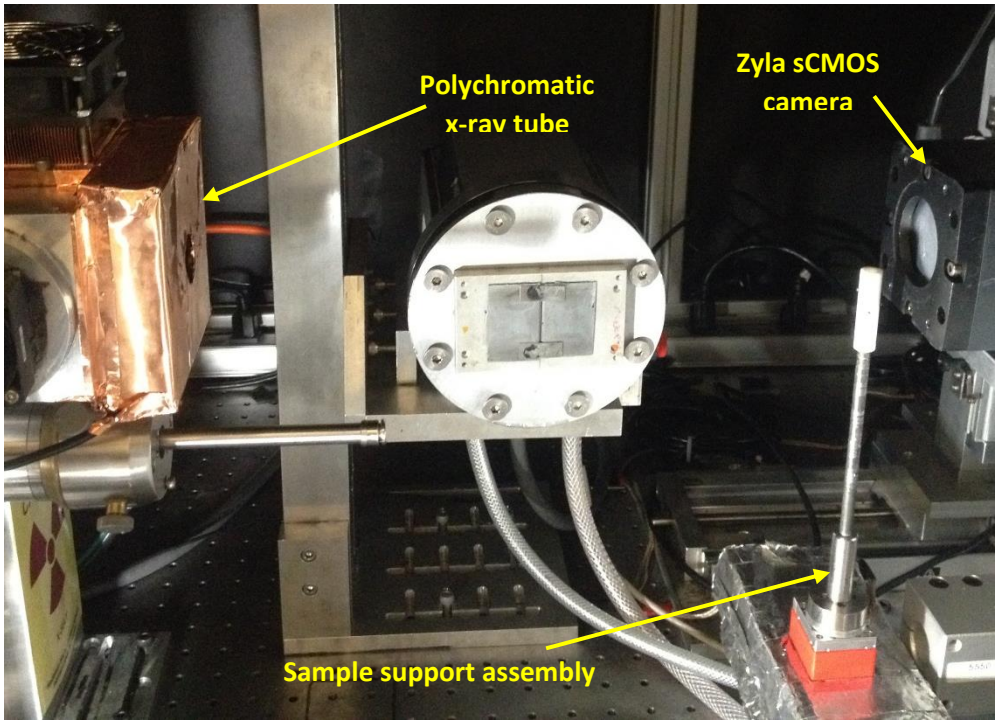

Figure 2.12: Upper level of the XFCT/XLCT system for x-ray CT imaging. The polychromatic source and the Zyla sCMOS camera are visible, while the flat panel is outside the picture.

The lower level consists of the XFCT/XLCT setup, comprising the monochromatic source, the x-ray CCD camera and EMCCD camera (on opposite sides facing the sample) and the CdTe spectroscope. The Zyla sCMOS camera can be translated, via a linear stage motor, along the vertical direction from the upper level to the lower level, where it can be used for aligning the primary x-ray beam. The CdTe spectroscope has a magnetic support, which allow it to be moved across the entire setup in different positions and configuration, according to the specific purpose. It can be directed towards the sample to measure the energy spectrum from the x-ray fluorescence at various angles, or it can be placed along the primary x-ray beam direction, in order to measure the transmission spectrum through the sample or the flux of x-ray source (when no sample is present in between). The EMCCD and the CCD cameras can be shifted as close as possible to the imaged

object, without hitting the primary x-ray beam. Such proximity to the target would maximize the geometric efficiency (i.e. the solid angle) of the two detectors, thus increasing the detection efficacy and the net measured XF or XL signal. Figure 2.13 shows different views of the XFCT/XLCT system and in particular of its lower level (as previously described), with all its main components.

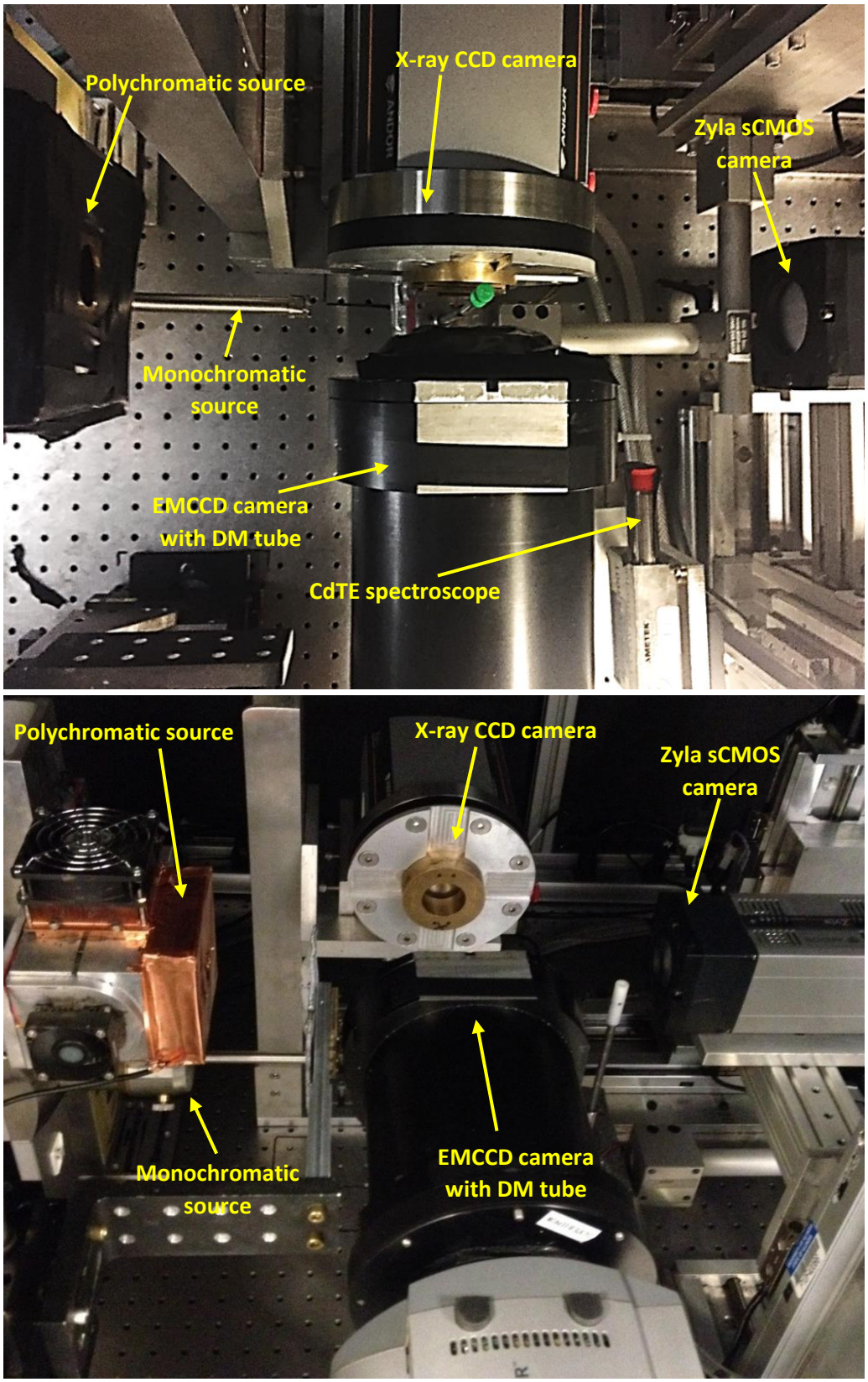

Figure 2.13: View from above of the entire XFCT/XLCT system with details of the lower level (top) and same view from a different angle (bottom).

A 3D drawing of the lower level of the XFCT/XLCT system is also reported, in Figure 2.14, for a better comprehension of the geometry of the setup.

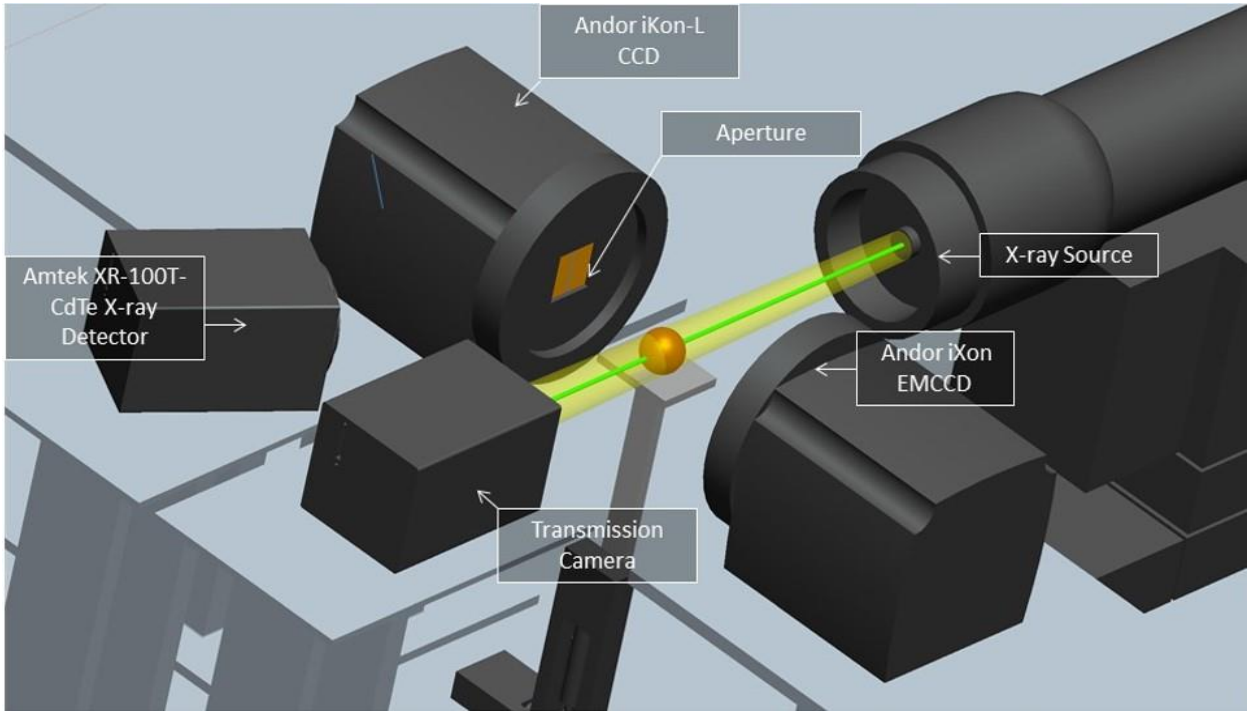

Figure 2.14: 3D drawing of the lower level of the XFCT/XLCT system.

The sample on its support assembly can be moved up and down using the corresponding linear stage motor, in order to switch from one level to the other. In this way, the geometry of the setup is preserved and no other components need to be relocated (except for the Zyla sCMOS camera, which has its own motors, as described previously). To further maintain the same geometric configuration and the relative distances between each part of the setup during an experiment, all the movable components (i.e. the sample support assembly and the Zyla sCMOS) are provided with micron-precision Bes Test dial indicators (Brown & Sharpe Bes Test dial indicator). These indicators measure whether such components would return in the exact position after being moved, with a precision of ±2.54 µm. Such precision is also required to preserve the geometry of the setup in the case of geometric calibration (as described in Paragraph 3.1). An example of the arrangement of the Bes Test indicators for the Zyla sCMOS camera is shown in Figure 2.15.

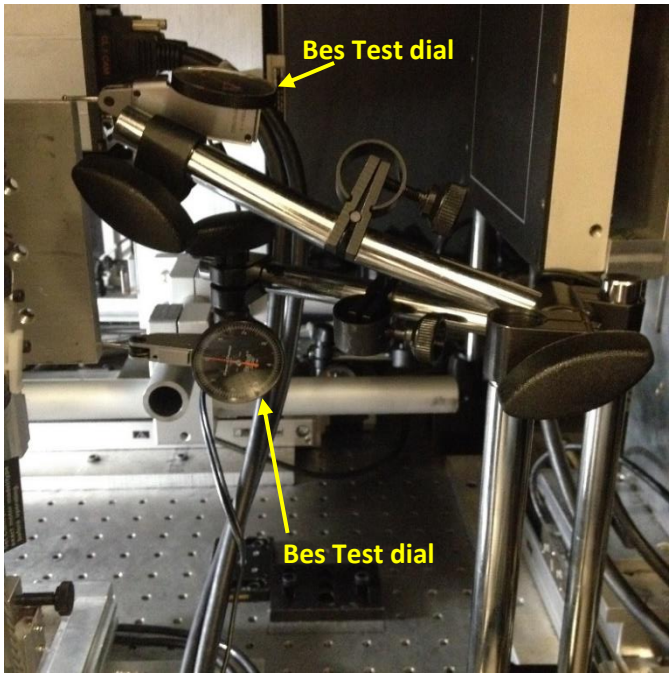

Figure 2.15: Bes Test dials for tracking the movement of the Zyla sCMOS camera.

A model of the geometry of the XFCT/XLCT system has been developed, establishing the main systems of coordinates and reference frames of the setup, together with the identification of its primary geometric parameters. Such modeling could be used as a base for future geometric calibrations of the entire setup (as in Paragraph 3.1) and/or Monte Carlo simulations of the system. The model of the XFCT/XLCT system is summarized in a diagram in Figure 2.16, showing and assessing the entire geometry of the setup.

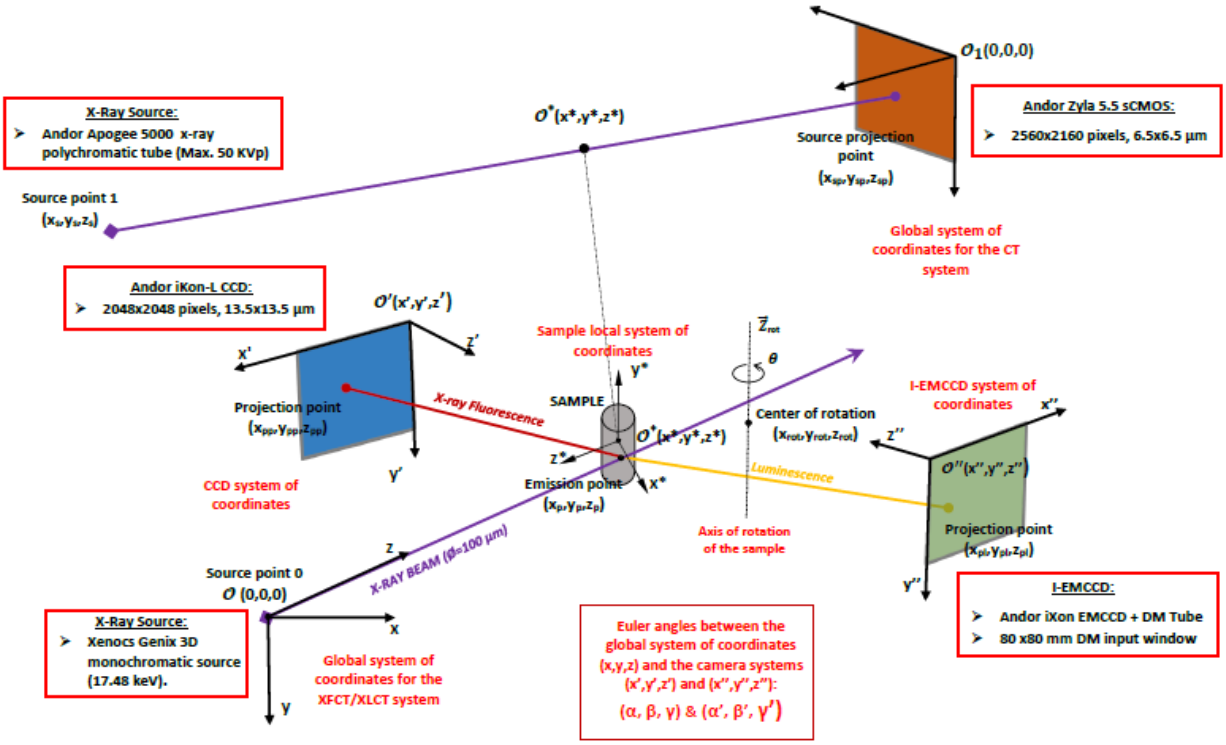

Figure 2.16: 3D modeling of the geometry of the XFCT/XLCT system.

In the model of the XFCT/XLCT system, the two levels (CT and XFCT/XLCT) are considered as separate units, with their own global reference frames and axes. The global system of coordinates for the lower level has been chosen to have its origin $\mathcal{O}(0,0,0)$ coincident with the source point of the central beam line of the primary x-rays emitted by the Genix^{3D} monochromatic source. It is a right-hand system of coordinates with the *z*-axis coming out of the source point and directed as the primary x-ray beam, while the *y*-axis is pointing downwards. Each one of the two detectors for XFCT/XLCT (both the x-ray CCD camera and the EMCCD camera plus DM tube) has its own local system of coordinates. For the CCD camera, such system has its *x'y'*-plane laying on the detector sensor surface, with the origin $\mathcal{O}'(x', y', z')$ on the top-right corner and the *z'*-axis pointing outward. The EMCCD plus DM tube assembly has a local system of coordinates with the *x''y''*-plane on the surface of the input window of the DM tube. Again, the origin $\mathcal{O}''(x'', y'', z'')$ of such system is located on the top-right corner and the *z''*-axis pointing outward. The two local systems of coordinates of the detectors (CCD and I-EMCCD) are related to the global one on the source emission point through the definition of two triplets of Euler angles, (α, β, γ) and $(\alpha', \beta', \gamma')$,

respectively. Such Euler angles establish the rotational transformations required to perform the change of coordinates from one of the local reference frames to the global one and vice versa.
Regarding the upper CT level of the XFCT/XLCT setup, the global system of coordinates is chosen on the Zyla sCMOS camera (or on the flat panel, depending on which detector is used in a particular situation). Its origin $\boldsymbol{O_1}(0,0,0)$ is located on the top-right corner of the sensor surface of the detector, which coincides with the *xy*-plane of such reference frame. Again, the *z*-axis of the system points outward and is direct to the x-ray tube central beam emission point.
Finally, a moving local system of coordinates is also determined for the sample, to which all the interaction points with the primary x-ray central beam (these points are also emission points for the subsequent x-ray fluorescence and/or x-ray luminescence) are referred. Such right-hand system has its own origin $\boldsymbol{O}^*(x^*, y^*, z^*)$ in the center of the sample volume. All the movements of the sample due to the linear stage motors and the rotational motor are tracked in the model by establishing a fixed axis of rotation $\vec{Z}_{\mathrm{rot}}$, outside the sample volume, and a center of rotation $(\mathrm{x_{rot}}, \mathrm{y_{rot}}, \mathrm{z_{rot}})$ belonging to such axis. Every change of position of the origin of the local reference frame of the sample can be quantified as a relative distance between the origin $\boldsymbol{O}^*(x^*, y^*, z^*)$ of the coordinate system and the center of rotation $(\mathrm{x_{rot}}, \mathrm{y_{rot}}, \mathrm{z_{rot}})$, while each rotation of the sample around the axis $\vec{Z}_{\mathrm{rot}}$ is determined by an angle of rotation θ. Moreover, the local system of coordinates represents also the geometric connection between the upper level and the lower level, with their own systems of coordinates. In fact, the origin $\boldsymbol{O}^*(x^*, y^*, z^*)$ of the sample reference frame would translate along a specific direction (corresponding to the linear stage motor translation direction up and down), shifting between on level and the other, without changing the overall geometry of the setup.

2.3 Design and sensitivity study of a single-slit aperture for XF imaging

The XFCT/XLCT system that is currently described here has been designed and developed to be used in combination with XFET imaging geometries and image acquisition configurations, as already illustrated in Chapter 1. They involve the collimation of the emitted radiation, mainly x-ray fluorescence, after stimulation with an x-ray beam of specific shape. However, as it will be seen in details in Paragraph 3.3, they can also be applied for XLCT imaging. Such geometries are primarily used in order to reduce image acquisition time and maximize the tradeoff between spatial resolution and geometric sensitivity. In particular, the use of a small pencil beam of excitation x-rays in combination with a slit collimator for the emitted x-ray fluorescence has been introduced, again Chapter 1, as a way to increase the amount of imaging information carried by each XF photon, by limiting the size of the source voxels within the field of view (FOV) of the slit collimator.

Considering such purposes, a single-slit aperture has been designed to be used in front the x-ray CCD camera of the XFCT/XLCT system for x-ray fluorescence imaging, using the abovementioned type of XFET geometry. The aperture design was conceived according to the specific geometry of the modified version of the CCD detector, in particular its size and all the relative distances between the CCD sensor, the beryllium window and also the focal distance where the imaged object is supposed to be located. All this specifications are reported in the blueprint of the CCD camera, as it can be seen in Figure 2.17.

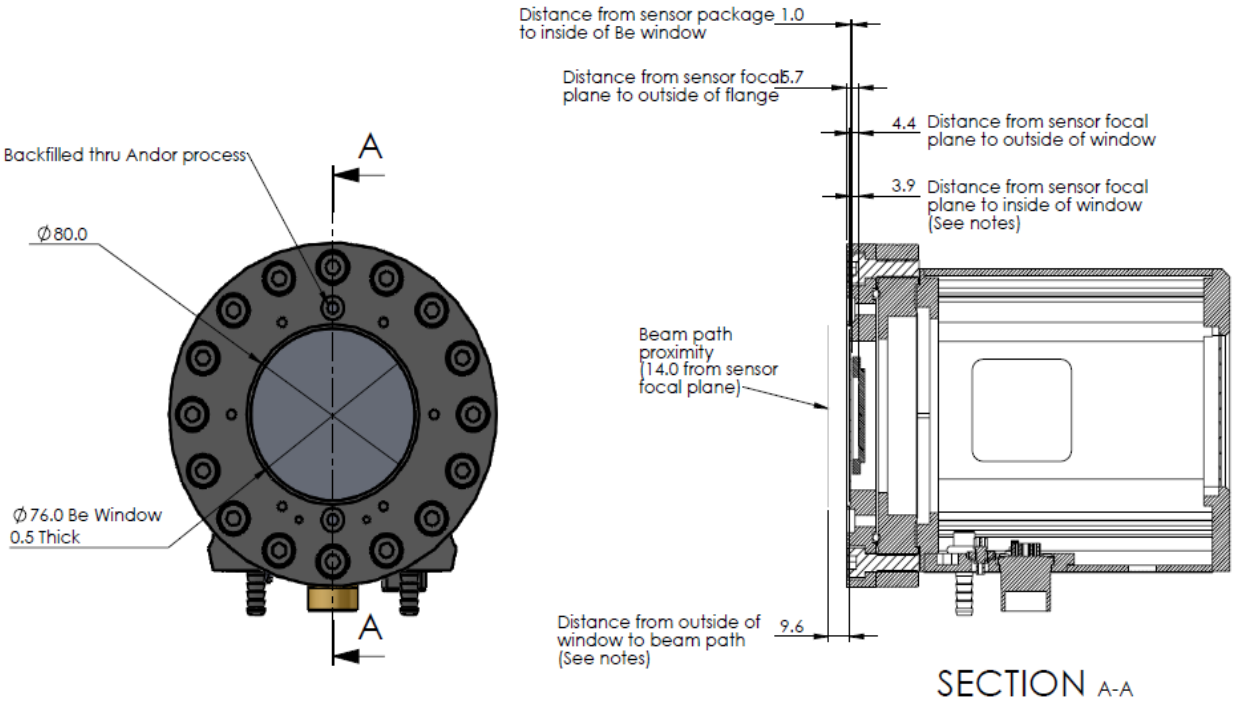

Figure 2.17: Blueprint of the design and geometry of the modified Andor iKon-L CCD camera and all its geometric specifications.

It can be seen from the figure that the distance $d_{\text{obj\_det}}$ between the pencil beam hitting the object and the focal sensor plane of the camera is 14 mm. Moreover, the distance $d_{\text{flange\_det}}$ between the outside of the stainless steel flange and the sensor focal plane is 5.7 mm. From that, it is possible to define the relative distances between the pencil beam, the central longitudinal section of the slit and the detector surface, considering that the aperture will be mounted on the flange (as described in the Paragraph 2.1). Regarding the aperture geometry, a width w equal to 100 µm has been chosen for the single slit, as to provide high spatial resolution for XF imaging. The material chosen for the slit is tungsten, because of its high density (ρ = 19.25 g/cm^3) and high atomic number (Z = 74), which permit strong attenuation of incoming fluorescence x-ray photons using a minimal thickness of material. The optimal thickness of the aperture has been calculated in order to block photon energies up to 100 keV and shield the CCD sensor from any fluorescence that is not passing directly through the slit. Being the mass attenuation coefficient μ/ρ of tungsten at 100 keV equal

to 4.438 cm^2/g [58], the mean free path λ (corresponding to the attenuation of about 33% of photons) in tungsten is:

$$\lambda = \frac{1}{\mu} = \frac{1}{\left(\mu/\rho\right) \cdot \rho} = \frac{1}{4.438\ \mathrm{cm^2/g} \cdot 19.25\ \mathrm{g/cm^3}} \approx 0.01171\ \mathrm{cm} \approx 0.1\ \mathrm{mm}$$

In order to maximize the attenuation (almost 0% photons transmitted), the thickness of the tungsten aperture has been chosen equal to five times the mean free path λ at 100 keV, i.e. equal to 0.5 mm. At this point, by knowing the thickness t of the aperture, it is possible to determine the distance from the pencil beam (and the object) to the aperture central longitudinal section, plus also the distance between the aperture central longitudinal section and the CCD camera sensor plane. Thus, the detector-to-aperture distance $d_{\mathrm{apt\_det}}$ is given by:

$$d_{\mathrm{apt\_det}} = d_{\mathrm{flange\_det}} + \frac{t}{2} = 5.7\ \mathrm{mm} + 0.25\ \mathrm{mm} = 5.95\ \mathrm{mm}$$

On the other hand, the object-to-aperture distance $d_{\mathrm{apt\_obj}}$ is calculated as:

$$d_{\mathrm{apt\_obj}} = d_{\mathrm{obj_{det}}} - d_{\mathrm{apt\_det}} = 14\ \mathrm{mm} - 5.95\ \mathrm{mm} = 8.05\ \mathrm{mm}$$

The position of the center of the slit has been established to be aligned with the center of the detector sensor. From all the previously calculated parameters, it is possible to model the geometry of the aperture system in order to complete the design of the single-slit collimator. Such model of the aperture system is depicted in Figure 2.18.

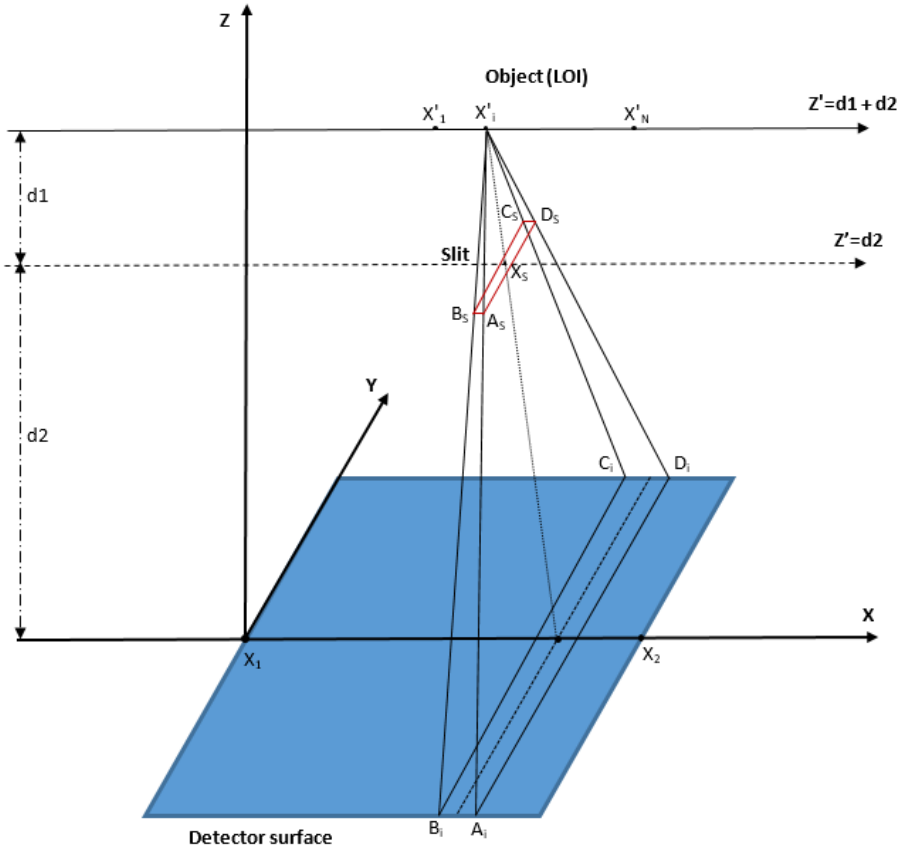

Figure 2.18: 3D modeling of the single-slit aperture system. The object line of interest (LOI) is visible, together with the slit longitudinal section (in red) and the CCD sensor surface (in blue). The projections of an arbitrary emission point of the FOV through the edges of the slit and on the detector surface are also depicted.

The model would allow the calculation of the geometric sensitivity profile of the slit, which provides the trend of the geometric efficiency of the CCD camera with the addition of the collimator. To perform such modeling and the geometric sensitivity calculation, the field of view of the slit has been chosen to be equal to 1 cm. Such FOV is perfectly suited for the imaging of organs (in particular, the brain) of small animals, such as mice.

In the model, a right-hand system of coordinates has been chosen with the *xy*-plane laying on the detector sensor surface and the *z*-axis pointing towards the aperture and the line of interest (LOI) of the object (i.e. the segment of the x-ray beam hitting the object within the FOV of 1 cm). The origin $\mathcal{O}(0,0,0)$ of such system is located on one side of the detector, at half its length, such that the detector area can be defined by the intervals $0 \leq x \leq 27.6$ mm and $-13.8 \leq y \leq 13.8$ mm. The slit center X_S is aligned with the center of the square sensor of the CCD at a distance $d_2 = d_{\text{apt\_det}}$, while the object LOI is direct along the *x*-axis, having its midpoint aligned with the center of the sensor area at a distance from the aperture equal to $d_1 = d_{\text{apt\_obj}}$. Each emission point X'_i from the object LOI is included in the FOV, ranging as $\mathrm{X'_1} \leq \mathrm{X'_i} \leq \mathrm{X'_N}$, for $i = 1, \ldots, N$. The projection lines from each of this emission points passing through the edges $\mathrm{A_S}$, $\mathrm{B_S}$, $\mathrm{C_S}$ and $\mathrm{D_S}$ of the slit intersect the detector surface at the projection points $\mathrm{A_i}$, $\mathrm{B_i}$, $\mathrm{C_i}$ and $\mathrm{D_i}$. Equally, the projection line from each emission point passing through the center of the slit X_S intersects the CCD sensor surface at the projection point $\mathrm{X_i}$.

Given the modeling of the aperture system and its parameters, it is possible to complete the design of the single-slit by calculating its length L. Such length must be long enough for the projections of the emission points through the slit to cover the entire size of the sensor (along the *y*-axis), but without extending beyond the detector area. Therefore, the length of the projected area $A_iB_iC_iD_i$ of each emission point must be equal to the size of the CCD sensor, thus: $\overline{\mathrm{A_iD_i}} = \overline{\mathrm{B_iC_i}} = 27.6$ mm. From Figure 2.19, it can be seen how to calculate the length L of the slit

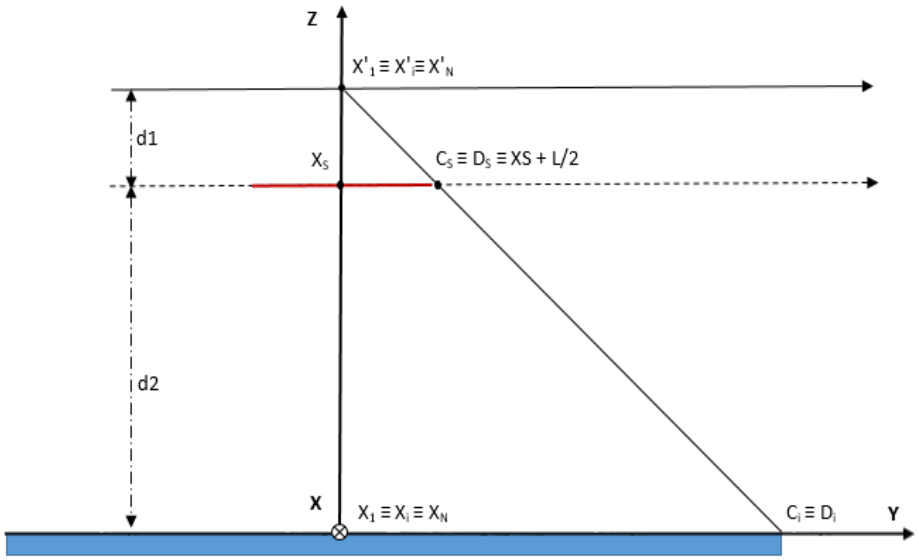

Figure 2.19: ZY view of the geometry of the single-slit aperture system. Only one half of the slit and of the detector is considered, for simplicity.

from the known parameters of the aperture geometry, using the similarity theorems of the triangles. Considering the two similar triangles (in figure), which are specifically $\Delta X_i D_i X'_i$ and $\Delta X_S D_S X_i$, it is possible to state from the similitudes that:

$$\frac{\overline{X_S D_S}}{\overline{X_\iota D_\iota}} = \frac{d_1}{d_1 + d_2} \tag{4}$$

Therefore, by resolving the previous equation for the length L:

$$\frac{L}{2} = \left(\frac{d_1}{d_1 + d_2}\right)\overline{X_\iota D_\iota} \tag{5}$$

Being $\overline{X_\iota D_\iota}$ equal to half the size of the CCD sensor (13.8 mm), then the length L of the slit designed in such a way is given by the following formula:

$$L = 2\left(\frac{5.95\text{ mm}}{14\text{ mm}}\right)13.8\text{ mm} = 11.73\text{ mm}$$

In the end, the dimensions of the designed single-slit are 0.1 mm by 11.73 mm by 0.5 mm.

After the calculation of the optimal dimensions of the slit, it is possible to calculate the position of the four edges A_S, B_S, C_S and D_S of the slit, as the following:

- $A_S = (X_S + w/2;\ X_S - L/2; d_2)$ = Bottom-right vertex of the slit;
- $B_S = (X_S - w/2;\ X_S - L/2; d_2)$ = Bottom-left vertex of the slit;
- $C_S = (X_S - w/2;\ X_S + L/2; d_2)$ = Top-left vertex of the slit;
- $D_S = (X_S + w/2;\ X_S + L/2; d_2)$ = Top-right vertex of the slit;

The knowledge of the edges of the slit allows to finalize the model of the aperture by calculating the projections A_i, B_i, C_i and D_i on the detector surface of each emission point X'_i. This can be performed by first calculating the parametric form of the equation of each projection line, (6) line passing through the given emission point and the corresponding edge of the slit. Thus:

$$P_A(t) = A_S + t(X'_i - A_S)$$
$$P_B(t) = B_S + t(X'_i - B_S)$$
$$P_C(t) = C_S + t(X'_i - C_S)$$
$$P_D(t) = D_S + t(X'_i - D_S)$$

Then, the projections A_i, B_i, C_i and D_i of each emission point on the detector surface can be calculated as the intersections of each of this lines with the CCD camera plane, that is the *xy*-plane (i.e. z = 0). Thus, by equaling the *z*-component of any of the previous parametric equations:

$$z = d_2 + t(d_1 + d_2 - d_2) = d_2 + t \cdot d_1 = 0 \tag{7}$$

From that, the parameter t that gives the projection points results as equal to:

$$t = -\frac{d_2}{d_1} \tag{8}$$

Finally, the projection points A_i, B_i, C_i and D_i on the detector surface are then equal to:

- $A_i = A_S - \left(d_2/d_1\right)(X'_i - A_S)$
- $C_i = C_S - \left(d_2/d_1\right)(X'_i - C_S)$
- $B_i = B_S - \left(d_2/d_1\right)(X'_i - B_S)$
- $D_i = D_S - \left(d_2/d_1\right)(X'_i - D_S)$

(9)

In addition, the projection X_i of each emission point through the center of the slit X_S can be calculated in the same way as the following:

$$X_i = X_S - \left(d_2/d_1\right)(X'_i - X_S) \tag{10}$$

The just-described model for the design of the single-slit aperture and the calculations of the projections from the object LOI through the slit has been implemented in a MATLAB code, in order to validate the previous mathematical framework and to obtain a 3D visualization of the entire geometry. The results from such code are reported in Figure 2.20.

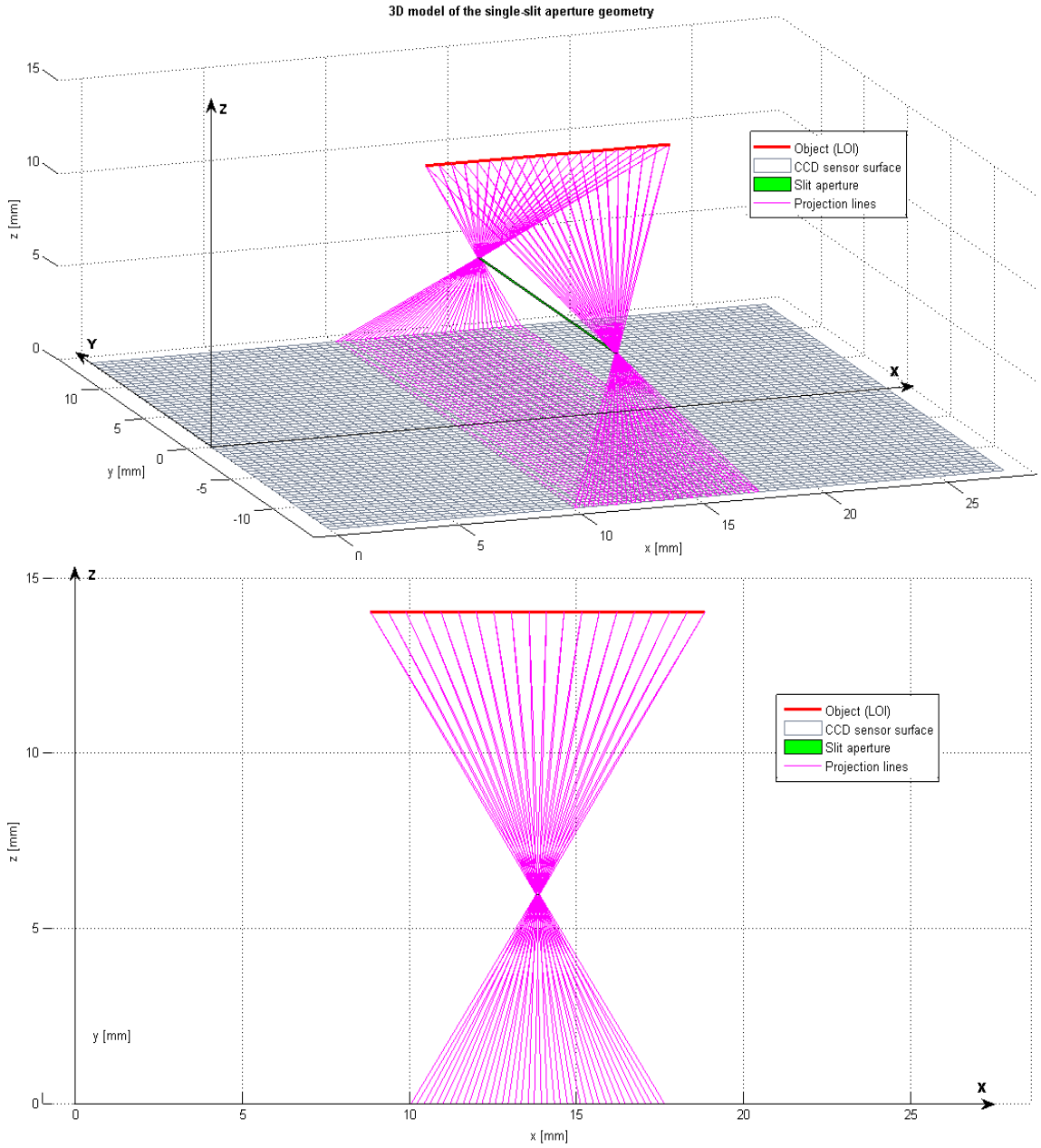

Figure 2.20: 3D visualization and validation of the mathematical and geometric model for the single-slit aperture system. The isometric view (top) and the *xz*-plane perspective (bottom) are coherent with the proposed geometry and thus verify the correctness of the abovementioned model.

As it can be seen from such figure, the 3D visualization of the aperture system is coherent with the expected geometry, thus it can be assumed that the mathematical structure of the model is correct and it can be considered validated. The figure also clearly shows the area covered by all the projections of the object LOI, passing through the slit, on the CCD camera sensor. As expected, the area is completely contained on the sensor, in order to maximize the detection efficiency.

A geometric sensitivity study of the calculated design of the single-slit aperture has also been performed, in order to evaluate the profile of the geometric efficiency of the proposed collimator. The geometric sensitivity ϵ_i for each emission point X'_i through the slit is defined as the total solid angle Ω_i between such points and the slit aperture normalized by 4π, thus:

$$\epsilon_i = \frac{\Omega_i}{4\pi} \tag{11}$$

The variation of the values of the geometric sensitivity ϵ_i along the FOV would give the geometric sensitivity profile of the aperture. Moreover, the mean value $\bar{\epsilon}$ of such profile can be evaluated as the average geometric sensitivity over the total number of emission points N. Thus, it is given by:

$$\bar{\epsilon} = \frac{1}{N}\sum_{i=1}^{N} \epsilon_i = \frac{1}{N}\sum_{i=1}^{N} \frac{\Omega_i}{4\pi} \tag{12}$$

The solid angle Ω_i between a given emission point X'_i and the slit aperture $A_S B_S C_S D_S$ can be obtained as the sum of two solid angles Ω_{i1} and Ω_{i2}, each one defined between the emission point and one of the triangles composing the halves of the rectangular slit (divided across one of its diagonals). Such triangles are, for example, $\Delta A_S B_S C_S$ and $\Delta C_S D_S A_S$. To calculate such solid angles, the Van Oosterom and Strackee formula [N] is applied, stating that:

$$\Omega = 2\tan^{-1}\left[\frac{\vec{R}_1 \cdot (\vec{R}_2 \times \vec{R}_3)}{R_1 R_2 R_3 + (\vec{R}_1 \cdot \vec{R}_2)R_3 + (\vec{R}_1 \cdot \vec{R}_3)R_2 + (\vec{R}_2 \cdot\times \vec{R}_3)R_1}\right] \tag{13}$$

Ω is the solid angle to be calculated, while $\vec{R}_1$, $\vec{R}_2$ and $\vec{R}_3$ are the vectors connecting the emission point and each vertex of the given triangle, respectively, as it is illustrated in a scheme in Figure 2.21 [59]. For the first triangle $\Delta A_S B_S C_S$ in the current slit geometry, the three vectors are the following:

- $\vec{R}_1 = \overrightarrow{A_S} - \overrightarrow{X'_\iota}$
- $\vec{R}_2 = \overrightarrow{B_S} - \overrightarrow{X'_\iota}$
- $\vec{R}_3 = \overrightarrow{C_S} - \overrightarrow{X'_\iota}$

(14)

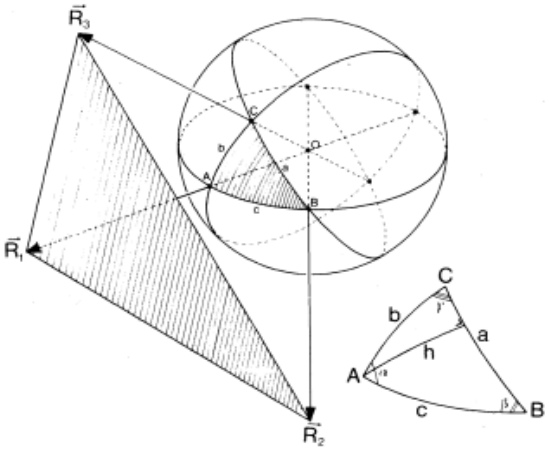

Figure 2.21: Diagram illustrating the Van Oosterom and Strackee formula and the parameters involved in the calculation of the solid angle [59].

On the other hand, for the second triangle $\Delta C_S D_S A_S$, the three vectors are the following:

- $\vec{R}_1 = \overrightarrow{C_S} - \overrightarrow{X'_i}$
- $\vec{R}_2 = \overrightarrow{D_S} - \overrightarrow{X'_i}$ (15)
- $\vec{R}_3 = \overrightarrow{A_S} - \overrightarrow{X'_i}$

From that, it is then possible to calculate the solid angle $\Omega_i = \Omega_{i1} + \Omega_{i2}$ of each point X'_i.

The resulting geometric sensitivity profile along the FOV for the designed aperture system is reported in Figure 2.22, together with its mean value.

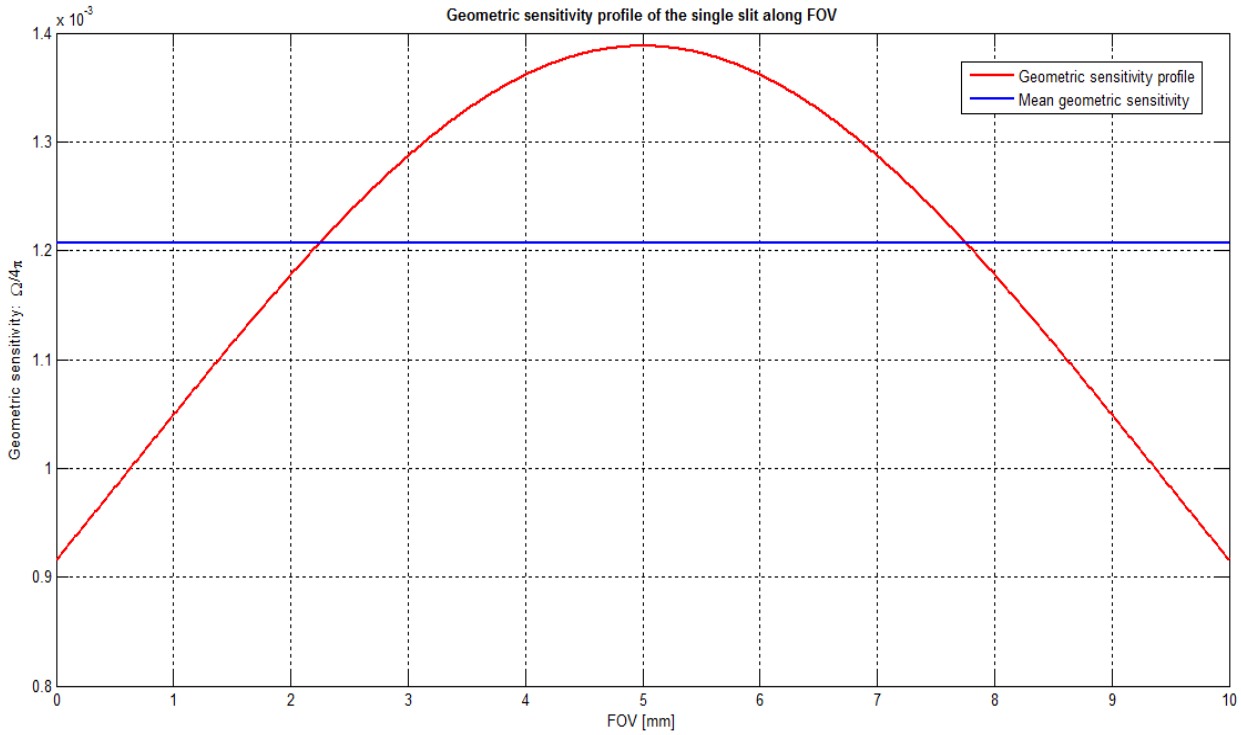

Figure 2.22: Geometric sensitivity profile of the single-slit aperture along the entire FOV (=1 cm). The red curve is the actual profile, while the blue curve is its mean value.

As expected, the geometric sensitivity profile of the single-slit aperture is symmetric respect with the midpoint of the FOV and it resembles a parabola, with a maximum in the middle of the object LOI. Such result is expected, because the distance between each emission point X'_i and the slit plane increases for points further and further away from the midpoint of the FOV, which is aligned with the center of the slit; thus, as the distance gets larger, the solid angle becomes smaller.

The mean value $\bar{\epsilon}$ of the geometric sensitivity profile calculated in such way, for an arbitrary large number of emission points $N = 10{,}000$, results equal to:

$$\bar{\epsilon} = 1.2075 \cdot 10^{-3}$$

The maximum value ϵ_{max} of the geometric sensitivity profile, corresponding to the peak of the trend, is also calculated and it is the following:

$$\epsilon_{max} = 1.3879 \cdot 10^{-3}$$

A tradeoff is established between spatial resolution and geometric sensitivity, for such configura-

tion, because in order to increase the latter, the width of the slit would have to be enlarged, as one of the way to enhance the number of photons passing through the collimator. Another solution to improve the geometric sensitivity profile and flatten its mean value would involve increasing the number of slits (from *single-slit* to *multiple-slits* aperture). However, in such case, the aperture must be designed as to prevent overlapping (also known as *multiplexing*) of the projections on the detector area.

3. Data processing and analysis of XF and XL signal for quantification and imaging

After the design and the physical construction of the XFCT/XLCT system (as described in the previous Chapter), an efficient and reliable set of data processing and analysis methods and algorithms has been conceived and developed. Such apparatus is necessary and fundamental to start imaging studies and experimental investigations, being a complementary part of the data acquisition process. In particular, a methodology for the processing and the quantification of the signal from x-ray luminescence, acquired with the EMCCD plus DM tube, has been implemented, using a previous data analysis and noise correction code (primary used for different applications regarding gamma ray detection). Moreover, a model and mathematical framework for the geometric calibration of the XFCT part of the system has been created and computationally verified.
Finally, the XFCT/XLCT system has been designed to be used with specific XFET geometries [11], whose basis and rationale have been explained in Chapter 1. In particular, two different imaging configurations have been realized in the setup and they will be explained in the following paragraphs. In addition to the improvements in the image acquisition procedure and in the performances of the system, such geometries are specifically useful because they allow volumetric image reconstruction without the need for complex and computationally dispendious algorithms, such as *the Maximum Likelihood Estimation* (MLE) or the *Maximum A Posteriori* (MAP) algorithm. The way to perform such quicker reconstruction for XF and XL imaging will be reported, as well.

3.1 Geometric calibration of the XFCT system for imaging

Although XFET geometries permit XFCT tomographic image formation without the use of reconstruction algorithms, the development and creation of a geometric calibration model and procedure for XFCT imaging has been carried out. Such calibration is meant to be used in the future for different data acquisition configurations (rather than XFET), which may require a more accurate and more detailed knowledge of the exact geometry of the XFCT part of the system. A similar calibration for the XLCT part of the system based on the same procedure may be also developed, but first it would require the implementation of precise models for light propagations, which goes beyond the primary purposes and goals of this thesis project.
The XFCT geometric calibration model here proposed is based on the geometry and the modeling framework that has been described in Chapter 2, although with few important differences. Such changes in the model were required in order to obtain the initial known data of the XFCT geometry. The detailed scheme of the XFCT system geometry based on the previous modeling, to which the

geometric calibration procedure is referred, can be seen in Figure 3.1.

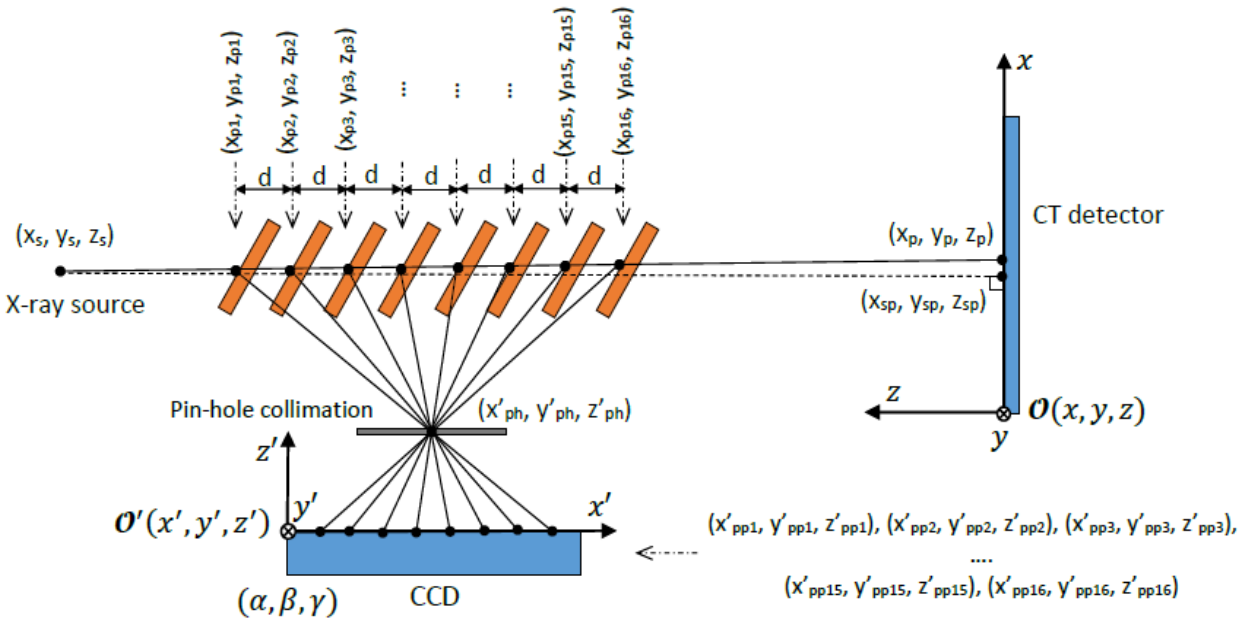

Figure 3.1: Scheme of the geometric calibration model and procedure for the XFCT system, complete with all the parameters involved in the calculations.

The main purpose of the geometric calibration of the XFCT is to correlate all the parameters that determine the geometry of the setup (reported in the previous figure) and to estimate their numerical values, which cannot be possibly known *a priori* from physical measurements. The knowledge of all these geometric parameters permits the complete characterization of the XFCT configuration. The estimation of the unknown parameters can be performed using the experimental measurement of x-ray fluorescence projections on the CCD camera in a particular configuration, established in the geometric calibration procedure. All the unknown parameters can be directly related to each other and to such measured projections by calculating a specific function, usually called *forward projector* $\mathcal{F}$. This particular function analytically computes the values of any XF projection in the geometric calibration procedure, given arbitrary values of the initial parameters. From that, a minimization problem (using a MLEM algorithm, for example) can be used as an inverse process on the forward projector, as to estimate the parameters of the geometry from measured input values of the XF projections.

The experimental procedure used to obtain and measure this input XF projections (as schematized in Figure 3.1) involves the excitation, with a pencil beam of x-rays, of a copper plate mounted on the sample support assembly. The x-ray fluorescence photons produced by the stimulation of a certain voxel of the copper plate will project on the CCD camera sensor, after being collimated by a pinhole located in front of the detector. By translating the copper plate with constant distance steps along the x-ray beam, several distinct and spaced circular projections can be measured on the CCD camera, in a number large enough (here 16 projections are taken) for the convergence of

the minimization problem (using the forward projector) and the final estimation of all the parameters of the geometry.

Firstly, the definition and the description of all these main parameters of the geometric calibration (as labelled in the figure) are reported in the following list:

- $\mathcal{O}(x, y, z)$ is the origin of the right hand global system of coordinates on the CT detector, located on the top right corner of the top right pixel of its sensor, viewed from the x-ray source;
- $\mathcal{O}'(x', y', z')$ is the origin of the right-hand local system of coordinates of the CCD camera, located on the top right corner of the top right pixel of the CCD camera sensor, viewed from the sample location (the copper plate in this case);
- $(\mathrm{x}_1, \mathrm{y}_1, \mathrm{z}_1)$ are the coordinates of the origin $\mathcal{O}'$ of the local system of coordinates of the CCD camera referred to the global system of coordinates. Such coordinates correspond to the components of the displacement vector between the two reference frames;
- (α, β, γ) are the Euler angles of the system of coordinates of the CCD camera with respect to the global system of coordinates on the CT detector;
  - → α is the rotation angle around the *z*-axis, also called *precession angle*;
  - → β is the rotation angle around the new *x*-axis, also called *nutation angle*;
  - → γ is the rotation angle around the *z'*-axis, also called *spin angle*;
- $(\mathrm{x}_\mathrm{s}, \mathrm{y}_\mathrm{s}, \mathrm{z}_\mathrm{s})$ is the position of the source point of the central x-ray beam emitted by the x-ray source, in the global system of coordinates;
- $(\mathrm{x}_{\mathrm{sp}}, \mathrm{y}_{\mathrm{sp}}, \mathrm{z}_{\mathrm{sp}})$ is the position of the center of the orthogonal projection of the central x-ray beam on the CT detector plane, in the global system of coordinates;
- $(\mathrm{x}_\mathrm{p}, \mathrm{y}_\mathrm{p}, \mathrm{z}_\mathrm{p})$ is the position of the center of the measurable projection of the central x-ray beam on the CT detector plane, in the global system of coordinates;
- $(\mathrm{x}_{\mathrm{ph}}, \mathrm{y}_{\mathrm{ph}}, \mathrm{z}_{\mathrm{ph}})$ is the position of the center of the circular pin-hole collimator used in front of the CCD camera, in the global system of coordinates;
- $(\mathrm{x}_{\mathrm{p1}}, \mathrm{y}_{\mathrm{p1}}, \mathrm{z}_{\mathrm{p1}}), (\mathrm{x}_{\mathrm{p2}}, \mathrm{y}_{\mathrm{p2}}, \mathrm{z}_{\mathrm{p2}}), \ldots (\mathrm{x}_{\mathrm{p16}}, \mathrm{y}_{\mathrm{p16}}, \mathrm{z}_{\mathrm{p16}})$ are the positions of the centers of the sixteen projections of the x-ray beam on the copper plate, for each shifting of such plate by a given distance d, in the global system of coordinates. Such positions also coincide with the emission points of the x-ray fluorescence projection lines towards the CCD camera;
- $(\mathrm{x}'_{\mathrm{pp1}}, \mathrm{y}'_{\mathrm{pp1}}, \mathrm{z}'_{\mathrm{pp1}}), (\mathrm{x}'_{\mathrm{pp2}}, \mathrm{y}'_{\mathrm{pp2}}, \mathrm{z}'_{\mathrm{pp2}}), \ldots (\mathrm{x}'_{\mathrm{pp16}}, \mathrm{y}'_{\mathrm{pp16}}, \mathrm{z}'_{\mathrm{pp16}})$ are the positions of the centers of the sixteen projections of the emission XF beams on the CCD sensor, after interaction with the copper plate and for each shifting of it by a given distance d, referred to the local system of coordinates of the CCD camera detector;

- Δ_1 is the initial distance, along the central x-ray beam line, of the first emission point (x_{p1}, y_{p1}, z_{p1}) on the copper plate from the measured projection (x_p, y_p, z_p) of the central x-ray beam on the CT detector plane;
- d is the constant distance along the x-ray central beam line by which the copper plate is shifted, for each consecutive measurement of the projections, starting from $\Delta_1 + d$ and so on, until the last emission point $(x_{p16}, y_{p16}, z_{p16})$;

It is important to state that such model needs a preexisting geometric calibration of the CT detector used in the setup, i.e. the Zyla sCMOS camera in the current case (anyway, the flat panel may also be used). This is fundamental because the CT geometric calibration will provide the piece of information about the starting known parameters, on which the entre geometric calibration is built on. Such starting parameters are the position of the source (x_s, y_s, z_s) of the central beam of x-rays and the position of its two projections: the one perpendicular to the CT detector plane (x_{sp}, y_{sp}, z_{sp}) and the physical and measurable projection on the same plane (x_p, y_p, z_p). For such reason, as it can be seen in scheme of the model, the global system of coordinates that has been used is the reference frame of the upper level of the XFCT/XLCT system, which is the one refereed to the CT detector (differently from the model described in Paragraph 2.2).

At this point, it is possible to calculate systematically the form of the forward projector, by setting up its constituent equations. Firstly, it can be noticed that the position of the orthogonal projection (x_{sp}, y_{sp}, z_{sp}) of the central beam, which is known from CT calibration, is a point belonging to the CT detector plane, i.e. the *xy*-plane of the global system of coordinates. Then, it is possible to conclude that $z_{sp} = 0$. Therefore:

$$(x_{sp}, y_{sp}, z_{sp}) \equiv (x_{sp}, y_{sp}, 0) \equiv (x_{sp}, y_{sp}) \tag{16}$$

Moreover, the position of the source point (x_s, y_s, z_s) of the central beam, known again from the CT geometric, shares the same *x* and *y* coordinates of its orthogonal projection (x_{sp}, y_{sp}, z_{sp}) on the CT detector surface and has a *z*-coordinate that is equal to the distance between the central beam source position and the CT detector plane. This is due to the orthogonality of the central beam projection resulting in the point (x_{sp}, y_{sp}, z_{sp}). Therefore $x_s = x_{sp}$ and $y_s = y_{sp}$.

Similarly as before, also the position $(x_p, y_p, z_p)$of the measured projection of the central beam on the same CT detector plane, known again due to the direct measurement on the CT detection system, belong to the CT detector plane (i.e. the *xy*-plane of the global panel system of coordinates). Thus, it is possible to conclude, as well, that:

$$(x_p, y_p, z_p) \equiv (x_p, y_p, 0) \equiv (x_p, y_p) \tag{17}$$

From these revelations, the length *L* of the central x-ray beam from the source point position to the

CT detector plane can be calculated, by firstly deriving the distance between the two previously discussed projections, (x_{sp}, y_{sp}) and (x_p, y_p), respectively:

$$p = \sqrt{(x_{sp} - x_p)^2 + (y_{sp} - y_p)^2} \tag{18}$$

Afterwards, by applying the Pythagoras's theorem on the right triangle that is formed by the points (x_s, y_s, z_s), (x_p, y_p) and (x_{sp}, y_{sp}), the length L is given by the following:

$$L = \sqrt{p^2 + z_s{}^2} = \sqrt{(x_{sp} - x_p)^2 + (y_{sp} - y_p)^2 + z_s{}^2} \tag{19}$$

Going further, the Cartesian equation that describes the central beam line in the 3D space can be written from two points belonging to it, which in this case are the position of the source point of the central beam (x_s, y_s, z_s) and the position of the its measured projections (x_p, y_p) on the CT detector. Therefore, such equation can be written as:

$$\frac{x - x_p}{x_s - x_p} = \frac{y - y_p}{y_s - y_p} = \frac{z}{z_s} \tag{20}$$

The parametric form of the previous is following (for the parameter t):

$$\begin{pmatrix} x \\ y \\ z \end{pmatrix} = \begin{pmatrix} x_p \\ y_p \\ 0 \end{pmatrix} + t \begin{pmatrix} x_s - x_p \\ y_s - y_p \\ z_s \end{pmatrix} \tag{21}$$

Now, it is evident that all the emission points (x_{p1}, y_{p1}, z_{p1}), (x_{p2}, y_{p2}, z_{p2}), ... $(x_{p16}, y_{p16}, z_{p16})$, which give the positions of the consecutive x-ray projections on the copper plate (shifting it by a distance d at each measurement), belong to the central x-ray beam line, whose equation has just been defined. Therefore, each one of these points (x_{pi}, y_{pi}, z_{pi}), for i =1, …16, satisfies the following identities, obtained by substituting such points in the equation of the central beam line:

$$\begin{pmatrix} x_{pi} \\ y_{pi} \\ z_{pi} \end{pmatrix} = \begin{pmatrix} x_p \\ y_p \\ 0 \end{pmatrix} + t \begin{pmatrix} x_s - x_p \\ y_s - y_p \\ z_s \end{pmatrix} \qquad \text{for } i = 1, \ldots 16$$

By converting the parametric equation into its Cartesian form, then:

$$\frac{x_{pi} - x_p}{x_s - x_p} = \frac{y_{pi} - y_p}{y_s - y_p} = \frac{z_{pi}}{z_s} \qquad \text{for } i = 1, \ldots 16$$

From such identities, sixteen algebraic systems of three equations in the three unknowns coordinates (x_{pi}, y_{pi}, z_{pi}) can be written as following:

$$\begin{cases} \dfrac{x_{pi} - x_p}{x_s - x_p} = \dfrac{y_{pi} - y_p}{y_s - y_p} \\ \dfrac{x_{pi} - x_p}{x_s - x_p} = \dfrac{z_{pi}}{z_s} \\ \dfrac{y_{pi} - y_p}{y_s - y_p} = \dfrac{z_{pi}}{z_s} \end{cases} \qquad \text{for } i = 1, \ldots 16$$

Nevertheless, all the three equations of each one of these algebraic systems are linearly dependent by twos. Thus, an additional condition (for each system i) is necessary to resolve the abovementioned systems. Such condition can be determined by the formula of all the sixteen distances Δ_i, along the collimated beam line, of each one of the emission points (x_{pi}, y_{pi}, z_{pi}) from the measured projection (x_p, y_p, z_p) of the central x-ray beam on the CT detector plane. Such distances Δ_i is easy to calculate in the 3D space, as it can be seen clearly in the diagram in Figure 3.2.

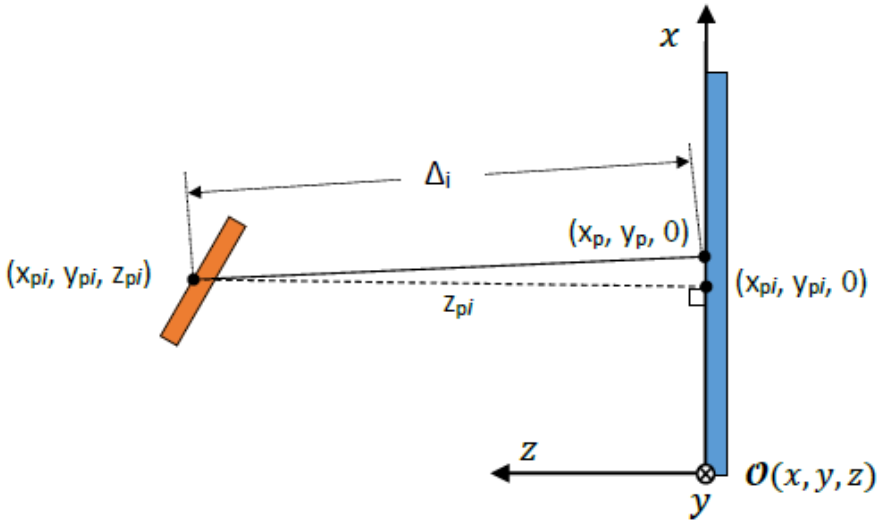

Figure 3.2: Illustration of the distances, along the central x-ray beam line, of each one the emission points (x_{pi}, y_{pi}, z_{pi}) from the CT detector plane. The way to calculate them can also be inferred from the picture.

Therefore, all these distances Δ_i, along the collimated beam line, of each one of the emission points (x_{pi}, y_{pi}, z_{pi}) from the measured projection (x_p, y_p, z_p) of the central x-ray beam on the CT detector plane, in the 3D space, are given by the following sixteen equations:

$$\Delta_i = \sqrt{(x_{pi} - x_p)^2 + (y_{pi} - y_p)^2 + (z_{pi})^2} \qquad \text{for } i = 1, \ldots 16$$

From these sixteen equations, it is possible to rewrite each one of the previous algebraic systems by substituting one of its equations with the corresponding newly found condition, as:

$$\begin{cases} \dfrac{x_{pi} - x_p}{x_s - x_p} = \dfrac{y_{pi} - y_p}{y_s - y_p} \\ \dfrac{x_{pi} - x_p}{x_s - x_p} = \dfrac{z_{pi}}{z_s} \\ \Delta_i = \sqrt{(x_{pi} - x_p)^2 + (y_{pi} - y_p)^2 + (z_{pi})^2} \end{cases} \qquad \text{for } i = 1, \ldots 16$$

Finally, it can be noticed that all the distances Δ_i are also related to each other, because the copper plate is shifted by a given distance d for each measurement. Therefore:

$$\Delta_{i+1} = \Delta_i - d \qquad \text{for } i = 1, \ldots 16$$

Hence, it is possible to derive all these distances from just two parameters, i.e. the initial distance

Δ_1 from the first emission point (x_{p1}, y_{p1}, z_{p1}) on the copper plate and the distance step d, by which the copper plate is shifted at each consecutive measurement.

After the derivation of the set of mathematical equations that determine all the sixteen emission points (x_{p1}, y_{p1}, z_{p1}), (x_{p2}, y_{p2}, z_{p2}), ... $(x_{p16}, y_{p16}, z_{p16})$, it is now possible to calculate the equations of the sixteen XF projection lines from such points, through the collimation pinhole, onto the CT detector plane. Introducing the position of the center (x_{ph}, y_{ph}, z_{ph}) of the pinhole, referred to the global system of coordinates, the sixteen equations of the XF projection lines, in Cartesian form, are given by the following equations, for i =1, …16:

$$\frac{x - x_{pi}}{x_{ph} - x_{pi}} = \frac{y - y_{pi}}{y_{ph} - y_{pi}} = \frac{z - z_{pi}}{z_{ph} - z_{pi}} \qquad \text{for } i = 1, \ldots 16$$

The parametric form of the previous equations is the following (again for the parameter t):

$$\begin{pmatrix} x \\ y \\ z \end{pmatrix} = \begin{pmatrix} x_{pi} \\ y_{pi} \\ z_{pi} \end{pmatrix} + t \begin{pmatrix} x_{ph} - x_{pi} \\ y_{ph} - y_{pi} \\ z_{ph} - z_{pi} \end{pmatrix} \qquad \text{for } i = 1, \ldots 16$$

The equations of the projection lines are fundamental in order to calculate the sixteen centers of the projection points $(x_{pp1}, y_{pp1}, z_{pp1})$, $(x_{pp2}, y_{pp2}, z_{pp2})$, ... $(x_{pp16}, y_{pp16}, z_{pp16})$ of the emitted XF beams on the CCD sensor plane. It must be stated that the previous notation means that the abovementioned coordinates pf the projection points are referred to the global system of coordinates (no prime symbol is used). Such points can be derived as the result of the intersections of the previously described projection lines with the *x'y'*-plane of the local system of coordinates of the CCD camera. Such plane is described in the CCD reference frame by the following equation:

$$x'y': \qquad z' = 0$$

Being such equation of the *x'y'*-plane referred to the local system of coordinates of the CCD detector and not to the global one, a transformation of coordinates from a reference frame to the other is required, in order to calculate the intersection points. Therefore, being (x_1, y_1, z_1) the coordinates, referred to the global system of coordinates, of the origin $\boldsymbol{O}'(x', y', z')$ of the local system of coordinates of the CCD camera (i.e. the displacement vector between the two reference frames), the transformation of coordinates between the two systems can be written as:

$$\begin{bmatrix} x' \\ y' \\ z' \end{bmatrix} = R \begin{bmatrix} x \\ y \\ z \end{bmatrix} - \begin{bmatrix} x_1 \\ y_1 \\ z_1 \end{bmatrix} \qquad (22)$$

where:

- $\begin{bmatrix} x \\ y \\ z \end{bmatrix}$ is the position of a given point in the global system of coordinates;
- $R = R(\alpha, \beta, \gamma)$ is the Eulerian rotational matrix of the transformation between the two coordinate systems;

- (α, β, γ) are the Euler angles between the two reference frames (as previously defined);
- $\begin{bmatrix} x' \\ y' \\ z' \end{bmatrix}$ is the position of a given point in the local system of coordinates of the CCD camera;
- $\begin{bmatrix} x_1 \\ y_1 \\ z_1 \end{bmatrix}$ is the displacement vector of the origin of the local system of coordinates of the CCD camera, with respect to the global system of coordinates.

The rotational matrix R can be calculated as the composition of three rotations about the z axis first, of an angle α, then about the new x of an angle β, and finally of an angle γ about the z' axis:

$$R = R(\alpha, \beta, \gamma) = R_1(\alpha) R_2(\beta) R_3(\gamma) \tag{23}$$

All these rotations and the corresponding Euler angles are shown schematically in Figure 3.3.

The rotation $R_1(\alpha)$ around the z-axis of the global system of coordinates is defined as:

$$R_1(\alpha) = \begin{bmatrix} \cos\alpha & \sin\alpha & 0 \\ -\sin\alpha & \cos\alpha & 0 \\ 0 & 0 & 1 \end{bmatrix}$$

The rotation $R_2(\beta)$ around the new x-axis after the previous transformation is defined as:

$$R_2(\beta) = \begin{bmatrix} 1 & 0 & 0 \\ 0 & \cos\beta & \sin\beta \\ 0 & -\sin\beta & \cos\beta \end{bmatrix}$$

The rotation $R_3(\gamma)$ around the z'-axis of the local system of coordinates of the CCD camera is defined as:

$$R_3(\gamma) = \begin{bmatrix} \cos\gamma & \sin\gamma & 0 \\ -\sin\gamma & \cos\gamma & 0 \\ 0 & 0 & 1 \end{bmatrix}$$

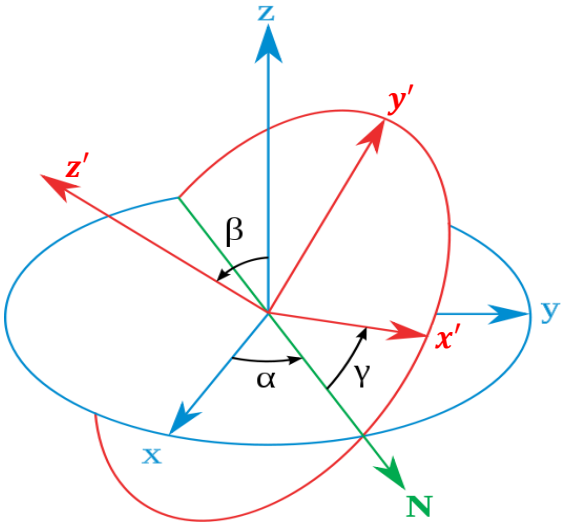

Figure 3.3: Depiction of the three rotations, about the Euler angles (α, β, γ), that compose the transformation matrix R.

Therefore, the rotational matrix R is calculated as the product of these three rotational matrices:

$$R = R_1(\alpha) R_2(\beta) R_3(\gamma) = \begin{bmatrix} \cos\alpha & \sin\alpha & 0 \\ -\sin\alpha & \cos\alpha & 0 \\ 0 & 0 & 1 \end{bmatrix} \begin{bmatrix} 1 & 0 & 0 \\ 0 & \cos\beta & \sin\beta \\ 0 & -\sin\beta & \cos\beta \end{bmatrix} \begin{bmatrix} \cos\gamma & \sin\gamma & 0 \\ -\sin\gamma & \cos\gamma & 0 \\ 0 & 0 & 1 \end{bmatrix}$$

$$= \begin{bmatrix} \cos\alpha\cos\gamma - \sin\alpha\cos\beta\sin\gamma & \cos\alpha\sin\gamma + \sin\alpha\cos\beta\cos\gamma & \sin\alpha\sin\beta \\ -\sin\alpha\cos\gamma - \cos\alpha\cos\beta\sin\gamma & -\sin\alpha\sin\gamma + \cos\alpha\cos\beta\cos\gamma & \cos\alpha\sin\beta \\ \sin\beta\sin\gamma & -\sin\beta\cos\gamma & \cos\beta \end{bmatrix}$$

From the definition of the rotational matrix R and of the displacement vector given by (x_1, y_1, z_1), it is now possible to transform the equation of the $x'y'$-plane referred to the local system coordinates of the CCD in its corresponding form in the global system of coordinates. By applying the above-mentioned transformation of coordinates, then:

$$\begin{bmatrix} x' \\ y' \\ z' \end{bmatrix} = R \begin{bmatrix} x \\ y \\ z \end{bmatrix} - \begin{bmatrix} x_1 \\ y_1 \\ z_1 \end{bmatrix} \tag{24}$$

Hence, for $z' = 0$, i.e. the equation of the CCD camera plane, such transformation is reduced to:

$$z' = (\sin\beta \sin\gamma)x - (\sin\beta \cos\gamma)y + (\cos\beta)z - \mathrm{z}_1 = 0 \tag{25}$$

In the end, it is found that the equation of the *x'y'*-plane of the CCD camera in the global system of coordinates is determined by the following equation:

$$(\sin\beta \sin\gamma)x - (\sin\beta \cos\gamma)y + (\cos\beta)z - \mathrm{z}_1 = 0 \tag{26}$$

Therefore, the intersection points $(\mathrm{x_{pp1}}, \mathrm{y_{pp1}}, \mathrm{z_{pp1}}), (\mathrm{x_{pp2}}, \mathrm{y_{pp2}}, \mathrm{z_{pp2}}), \ldots (\mathrm{x_{pp16}}, \mathrm{y_{pp16}}, \mathrm{z_{pp16}})$ of the sixteen projection lines with such plane can be calculated by substituting the three components of the parametric equations of each of these projection lines (calculated previously), for i =1, …16:

$$\begin{aligned}&(\sin\beta \sin\gamma)\left[\mathrm{x_{pi}} + t\left(\mathrm{x_{ph}} - \mathrm{x_{pi}}\right)\right] - (\sin\beta \cos\gamma)\left[\mathrm{y_{pi}} + t\left(\mathrm{y_{ph}} - \mathrm{y_{pi}}\right)\right] \\ &+ (\cos\beta)\left[\mathrm{z_{pi}} + t\left(\mathrm{z_{ph}} - \mathrm{z_{pi}}\right)\right] - \mathrm{z_1} = 0\end{aligned} \tag{27}$$

From these identities the values of the parameter t corresponding to the sixteen intersection points can be derived as given in the following formulas, for i =1, …16:

$$t = -\frac{(\sin\beta \sin\gamma)\mathrm{x_{pi}} - (\sin\beta \cos\gamma)\mathrm{x_{pi}} + (\cos\beta)\mathrm{z_{pi}} - \mathrm{z_1}}{(\sin\beta \sin\gamma)\left(\mathrm{x_{ph}} - \mathrm{x_{pi}}\right) - (\sin\beta \cos\gamma)\left(\mathrm{y_{ph}} - \mathrm{y_{pi}}\right) + (\cos\beta)\left(\mathrm{z_{ph}} - \mathrm{z_{pi}}\right)}$$

Finally, the substitution of such values of the parameter t in the sixteen equations of the projection line, previously determined, provides the sixteen sets of three equations each that derive the positions of the sixteen projection points $(\mathrm{x_{pp1}}, \mathrm{y_{pp1}}, \mathrm{z_{pp1}}), (\mathrm{x_{pp2}}, \mathrm{y_{pp2}}, \mathrm{z_{pp2}}), \ldots (\mathrm{x_{pp16}}, \mathrm{y_{pp16}}, \mathrm{z_{pp16}})$. These sets of equations are the following, for i =1, …16:

$$\begin{pmatrix}\mathrm{x_{ppi}} \\ \mathrm{y_{ppi}} \\ \mathrm{z_{ppi}}\end{pmatrix} = \begin{pmatrix}\mathrm{x_{pi}} \\ \mathrm{y_{pi}} \\ \mathrm{z_{pi}}\end{pmatrix} - \frac{(\sin\beta \sin\gamma)\mathrm{x_{pi}} - (\sin\beta \cos\gamma)\mathrm{x_{pi}} + (\cos\beta)\mathrm{z_{pi}} - \mathrm{z_1}}{(\sin\beta \sin\gamma)\left(\mathrm{x_{ph}} - \mathrm{x_{pi}}\right) - (\sin\beta \cos\gamma)\left(\mathrm{y_{ph}} - \mathrm{y_{pi}}\right) + (\cos\beta)\left(\mathrm{z_{ph}} - \mathrm{z_{pi}}\right)} \begin{pmatrix}\mathrm{x_{ph}} - \mathrm{x_{pi}} \\ \mathrm{y_{ph}} - \mathrm{y_{pi}} \\ \mathrm{z_{ph}} - \mathrm{z_{pi}}\end{pmatrix}$$

At this point, from the positions of such points $\left(\mathrm{x_{ppi}}, \mathrm{y_{ppi}}, \mathrm{z_{ppi}}\right)$ calculated in the global system of coordinates, it is possible then to derive the positions $\left(\mathrm{x'_{ppi}}, \mathrm{y'_{ppi}}, \mathrm{z'_{ppi}}\right)$ of the same projections points referred to the local system of coordinates of the CCD camera. This can be done by simply using again the transformation of coordinates that has been previously determined. Moreover, considering that all these points belong to the *x'y'*-plane of the CCD camera reference frame (i.e. $z' = 0$), then:

$$\left(\mathrm{x'_{ppi}}, \mathrm{y'_{ppi}}, \mathrm{z'_{ppi}}\right) \equiv \left(\mathrm{x'_{ppi}}, \mathrm{y'_{ppi}}, 0\right) \equiv \left(\mathrm{x'_{ppi}}, \mathrm{y'_{ppi}}\right) \qquad \text{for } i \text{ =1, …16}$$

Therefore, by applying the abovementioned transformation, it follows that:

$$\begin{bmatrix}\mathrm{x'_{ppi}} \\ \mathrm{y'_{ppi}} \\ 0\end{bmatrix} = R \begin{bmatrix}\mathrm{x_{ppi}} \\ \mathrm{y_{ppi}} \\ \mathrm{z_{ppi}}\end{bmatrix} - \begin{bmatrix}\mathrm{x_1} \\ \mathrm{y_1} \\ \mathrm{z_1}\end{bmatrix} \qquad \text{for } i \text{ =1, …16}$$

In conclusion to the entire mathematical procedure here exposed, the forward projector $\mathcal{F}$ can be ultimately obtained by substituting the calculated form of the rotational matrix R and of the proje-

ction points $(x_{ppi}, y_{ppi}, z_{ppi})$ referred to the global system of coordinates (as previously calculated). Therefore, it results, for i =1, …16:

$$\begin{bmatrix} x'_{ppi} \\ y'_{ppi} \\ 0 \end{bmatrix} = \begin{bmatrix} \cos\alpha\cos\gamma - \sin\alpha\cos\beta\sin\gamma & \cos\alpha\sin\gamma + \sin\alpha\cos\beta\cos\gamma & \sin\alpha\sin\beta \\ -\sin\alpha\cos\gamma - \cos\alpha\cos\beta\sin\gamma & -\sin\alpha\sin\gamma + \cos\alpha\cos\beta\cos\gamma & \cos\alpha\sin\beta \\ \sin\beta\sin\gamma & -\sin\beta\cos\gamma & \cos\beta \end{bmatrix} \left[\begin{pmatrix} x_{pi} \\ y_{pi} \\ z_{pi} \end{pmatrix} - \frac{(\sin\beta\sin\gamma)x_{pi} - (\sin\beta\cos\gamma)x_{pi} + (\cos\beta)z_{pi} - z_1}{(\sin\beta\sin\gamma)(x_{ph} - x_{pi}) - (\sin\beta\cos\gamma)(y_{ph} - y_{pi}) + (\cos\beta)(z_{ph} - z_{pi})} \begin{pmatrix} x_{ph} - x_{pi} \\ y_{ph} - y_{pi} \\ z_{ph} - z_{pi} \end{pmatrix} \right] - \begin{bmatrix} x_1 \\ y_1 \\ z_1 \end{bmatrix}$$

This full set of sixteen triplets of equations giving the projection points $(x_{ppi}, y_{ppi}, z_{ppi})$, together with the previous sixteen algebraic systems in three unknowns used to determine the emission points (x_{pi}, y_{pi}, z_{pi}), for i =1, …16, constitutes the forward projector $\mathcal{F}$, in the form:

$$\mathcal{F}\begin{pmatrix} x_{pi}, y_{pi}, z_{pi} \\ \alpha, \beta, \gamma \\ d \\ \Delta_1 \\ x_1, y_1, z_1 \\ x_{ph}, y_{ph}, z_{ph} \end{pmatrix} = (x'_{ppi}, y'_{ppi}, z'_{ppi}) \qquad \text{for } i = 1, \ldots 16$$

The mathematical model for the forward projector $\mathcal{F}$, which has just been described, is also implemented in a MATLAB code, in order to produce a 3D visualization of the geometric calibration procedure. This can be used to verify and validate the correctness of the current model, assessing its coherence with the simulated geometry. To do that, a set of arbitrary parameters, which have been chosen to be conform to the real experimental geometry and to be representative of the current setup as close as possible, was used in the MATLAB code. Such input arbitrary values of those parameters that have been described and used for the model are reported in Table 3.1.

Parameter:	**Arbitrary value in the code:**
(x_s, y_s, z_s)	(60, 63, 860) mm
(x_p, y_p, z_p)	(65, 61.5, 0) mm
(x_1, y_1, z_1)	(-100, 25, 100) mm
(α, β, γ)	(-π/2, -π/2, π/2) rad
(x_{ph}, y_{ph}, z_{ph})	(-60, 62, 460) mm
Δ_1	700 mm
d	40 mm

Table 3.1: Arbitrary input parameters for the validation of the geometric calibration model with MATLAB code.

The results of the code are thus reported in Figure 3.4. As it can be seen, the 3D visualization of the application of the forward projector $\mathcal{F}$ is coherent with the expected geometry (it must be noted that the axis are not using the same scale). All the XF emission points are aligned along the central

x-ray beam line, while the XF projection points are all spaced and belongs to the CCD detector plane. The calculated transformation of coordinates using the rotational matrix R also performs the predicted change of reference frames.

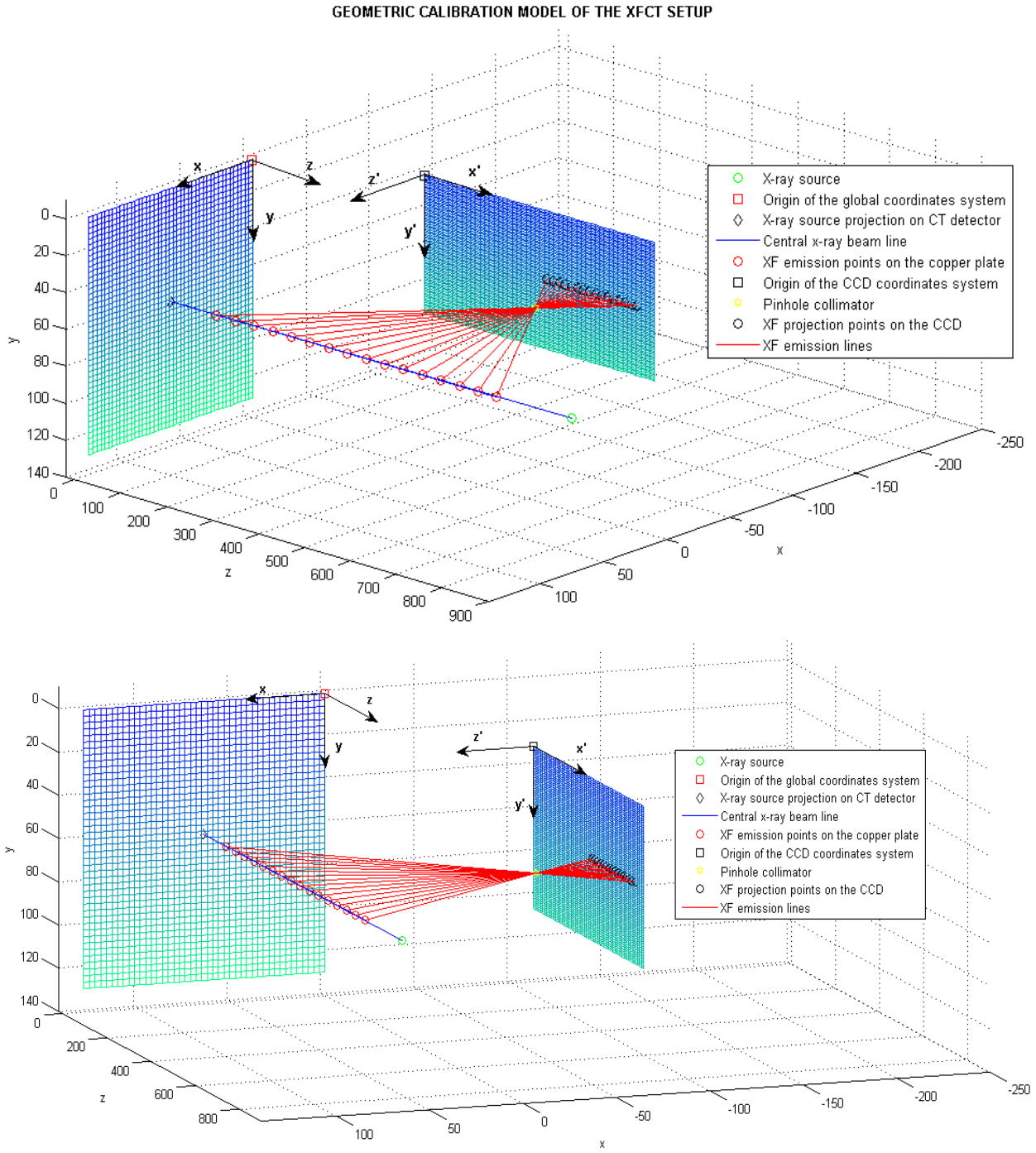

Figure 3.4: Results of the implementation on MATLAB code of the geometric calibration model for the XFCT setup. Two isometric views are shown, depicting also the planes of the sensors of the two detectors (CT on the left and CCD on the right).

As mentioned previously, the verified forward projector $\mathcal{F}$ can be minimized through an optimization algorithm, in order to calculate the values of the unknown parameters composing it. The optimization process can be performed through an algorithm (such as *fmincon* in MATLAB, using MLE), so that the difference between the measured projection points $\left(x'_{ppi}, y'_{ppi}, z'_{ppi}\right)_{measured}$ and

those expected from the application of the forward projector $\mathcal{F}$, called $(x'_{ppi}, y'_{ppi}, z'_{ppi})_{\mathcal{F}}$, using the optimized parameters as inputs, is smaller or equal than a certain tolerance ε. Therefore:

$$\begin{pmatrix} x_{pi}, y_{pi}, z_{pi} \\ \alpha, \beta, \gamma \\ d \\ \Delta_1 \\ x_1, y_1, z_1 \\ x_{ph}, y_{ph}, z_{ph} \end{pmatrix} = \text{argmin}_{i=1\ldots16}(\mathcal{F}) \text{ such that } \left[(x'_{ppi}, y'_{ppi}, z'_{ppi})_{\mathcal{F}} - (x'_{ppi}, y'_{ppi}, z'_{ppi})_{measured} \right] \leq |\varepsilon|$$

3.2 Methodology for processing and analysis of XL data

A methodology and analysis procedure for the processing of the x-ray luminescence data acquired with the EMCCD plus DM tube of the XFCT/XLCT system has been developed and implemented in a suite of codes, written in C language and MATLAB. Such methodology is necessary for the correction of the raw data frames (composed by 512 by 512 pixels) taken with the EMCCD assembly during experiments, either for imaging or just for quantification of the final net XL signal. The data processing procedure was based on a preexisting code, written in C by L.J. Meng [52] [54], for gamma ray detection and imaging application of the EMCCD camera with the DM tube. In such applications, the input window of the demagnifier was coupled with a scintillator for ionizing radiation detection and successive conversion of the signal in visible light. However, in this case, the contribution of background radiation (coming mainly from ambient radioactivity and cosmic radiation) to the overall signal is generally minimal, compared to the contamination to the XL signal generated by ambient light and undesired sources of optical radiation in the range of wavelength allowed by the EMCCD camera. Furthermore, such background signal is usually not stationary and can change over time, as well as the pedestal noise contribution, due generally to electronic noise, dark currents in the detector and counting statistics. At the same time, even the signal detected by each pixel, measured in *analog-to-digital units* (ADU), is also variable, due to the unpredictable probability for an optical photon to reach a given pixel in a given frame at a specific time interval, and also due to the time and space variation of the pedestal noise contribution from pixel to pixel. All these aspects, in general, lead to a configuration where basically each pixel could behave independently and in a unique way respect with the others, as if it were a single detector itself. Therefore, a constant tracking of the variation of the signal, and of the pedestal noise as well, in each pixel, from frame to frame over the entire acquisition time, is necessary, in order to perform a correct pedestal noise identification and correction from the detected XL signal. The tracking of the background and of the pedestal noise is performed during experimental measurements with the EMCCD by simply acquiring alternated sets of frames with x-ray excitation (X-ray ON) and sets with no x-ray excitation (x-ray OFF). Analyzing each sets of frames in both the configurations permits a constant updating of the pedestal noise correction (every given number

of frames) per pixel. Moreover, successive corrections can be made by updating multiple times within nested loops (first order correction, second order correction and so on).

The XL data processing procedure here proposed has three main tasks concerning the correction of the acquired x-ray luminescence frames, which are illustrated in the following list:

1) Pedestal noise calculation, with first and second order correction due to tracking and updating of the processed frames over time, and subtraction of it from the raw XL data frame;
2) Identification and elimination from the frames of those pixels, commonly known as *bad pixels*, which behave abnormally in a very large number of frames. Such pixel may have either a very large signal (*hot pixels)* or negative/null signal (*dead* pixels) constantly for a consistent number of frames in the whole measurement.
3) Identification and elimination of pixel clusters that have been saturated (the saturation value for the EMCCD is 2^{14} ADUs = 16,384 ADUs) due to sudden electric discharge of the cathode of the DM tube. Such clusters are visible in the raw XL data frames as relatively wide and unusual bright spots.

A typical raw XL data frame acquired for 0.5 seconds and its pixel map distribution are shown in Figure 3.5. Such frame has been taken during the XL signal quantification experiment described in the next Chapter, with LaF_3:Tb nanoparticles using the polychromatic source at 50 kVp of tube voltage and 1 mA of current for the x-ray excitation.

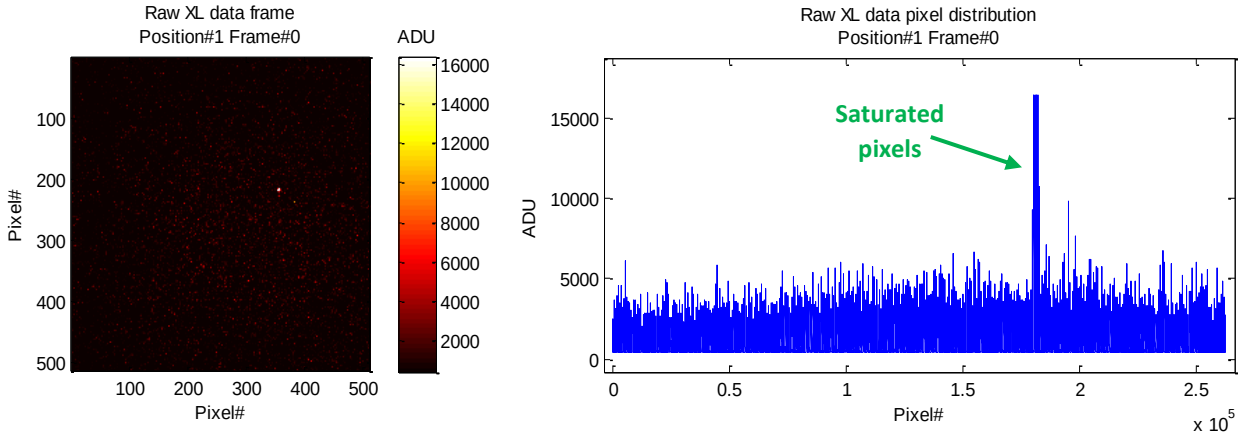

Figure 3.5: Raw XL data frame (512x512 pixels) acquired with the EMCCD plus DM tube (left) and its corresponding pixel distribution (right).

It can be seen both in the raw frame and in the pixel distribution that a cluster of saturated pixels is present. Moreover, the contribution of the pedestal noise is also visible in the pixel distribution, shifting the baseline of the 1D map from zero to around 450 ADUs. It must also be noted that the raw data frame includes both the XL signal coming from the nanoparticles and the background signal coming from elsewhere in the setup.

The XL data processing for the correction of the above-described exemplary raw frame (and that can be extend to all the acquired frames) is composed of several steps, which are described and di-

scussed in details as following:

1) A preliminary calculation of the pedestal noise value for each pixel is performed, by analyzing a given number of sets of frames, depending on the number of frames for each set (usually 400-500 frames in total). The analyzed frames are only those that have been acquired with no x-ray excitation (X-ray OFF), in order to have the minimum amount of signal coming from sources that are not noise. For each pixel of the EMCCD (from 1 to 512x512), a histogram, with bin size equal to 4, of the ADU intensity distribution of the given pixel over all the considered frames is determined. The histogram shows the pedestal noise peak of each pixel, which is centered on the value of its signal baseline (at about 450 ADUs, as mentioned before, if the considered pixel is not a bad pixel). An example of such histogram is shown in Figure 3.6. The centroid value x_0 of the pedestal noise peak in the frame distribution of each pixel is calculated. Then, again for each pixel, all the frames in which a given pixel has a ADU intensity ranging between the centroid value plus or minus a specific threshold x^* (usually 10 ADUs) is identified, as:

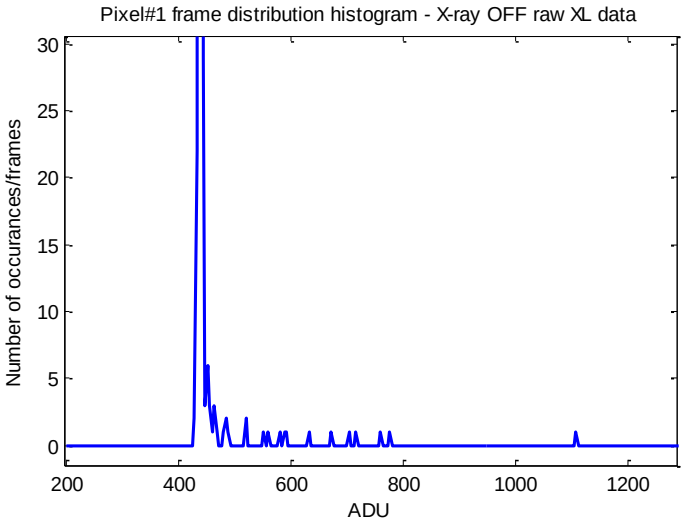

Figure 3.6: Example of frame distribution histogram for an arbitrary pixel, for 300 X-ray OFF frames considered. The pedestal noise peak is clearly visible.

$$x_0 - x^* \leq \text{pixel intensity in the frame} \leq x_0 + x^*$$

The ADU intensities of the given pixel in each of these identified frames are recorded and finally the pedestal noise value of each pixel is estimated by averaging all these ADU intensities over all the frames identified in such way (sum of all the ADU intensities divide by the total number of identified frames). Such preliminary evaluation of the average pedestal noise contribution to each pixel returns a 1D pixel value map, as the exemplary one depicted in Figure 3.7. The baseline related to the pedestal noise level can be evidently seen. This represents the 1D form of the basic pedestal noise frame that is the starting point for the subsequent tracking and updating of the pedestal noise in the successive steps. Simultaneously to the preliminary pedestal noise calculation, the identification of the bad pixels is also performed. Such operation is simply done by considering as bad each pixel, in the resulting pedestal noise map, that has an intensity higher than a certain threshold. This threshold is usually set at 500 ADUs. This operation is also visible in the previous figure,

where the threshold is depicted as a dashed red line. Each pixel whose intensity is above that line is identified as a bad pixel.

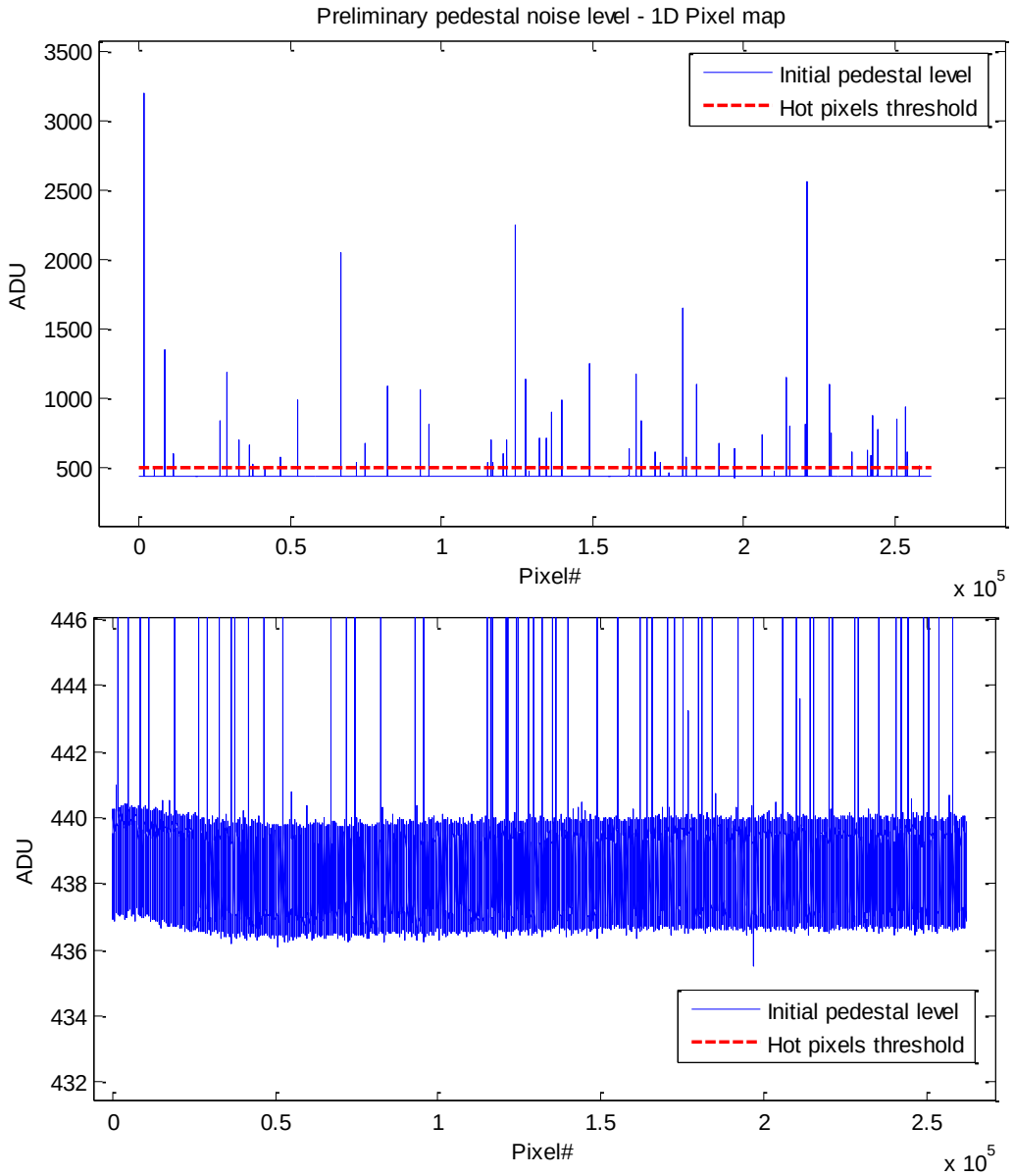

Figure 3.7: Preliminary pedestal noise level calculation for a number of frames equal to 300. The pedestal noise baseline is clearly visible (top). The same graph is also enlarged to depict the oscillation of the pedestal noise baseline, due to thresholding at 10 ADUs (bottom). The threshold for the identification of bad pixels is also reported as a dashed red line.

The bad pixels estimated in such way are recorder in a 2D map (512 by 512) that will be used in the next steps to perform the bad pixel correction of the noise-subtracted frame.

2) At this point, the preliminary pedestal noise frame calculated in the previous step is subtracted, pixel by pixel, by each raw data frame, either with x-ray ON or X-ray OFF, starting from the very first sets of frames acquired. During this operation the pedestal noise variation from frame to frame over time is tracked and two correction are performed in the meantime on it: a *first order correction*, where, every ten analyzed frames, if the subtracted ADU intensity of a given pixel, at the considered frame, is included in a range between

$\pm x^*$ (i.e. the pedestal noise threshold used in the preliminary calculation, which is usually equal to 10 ADUs), such pixel is considered a true noise pixel in that particular frame and its original ADU intensity (before the correction) is recorded; then, a *second order correction*, where, every five frames after the first order correction, the pedestal noise level of each pixel is recalculated by summing all the ADU intensities of that given pixel recorded during the first order correction (when it was considered a true noise pixel) and by dividing such sum for the number of frames, until the considered one, in which such pixel was identified as a true noise pixel. After the processing of all the acquired frames and the application of the abovementioned corrections, the final pedestal noise frame is obtained. An example of this final pedestal noise frame is shown in Figure 3.8, considering the same initial raw data frame as in Figure 3.5.

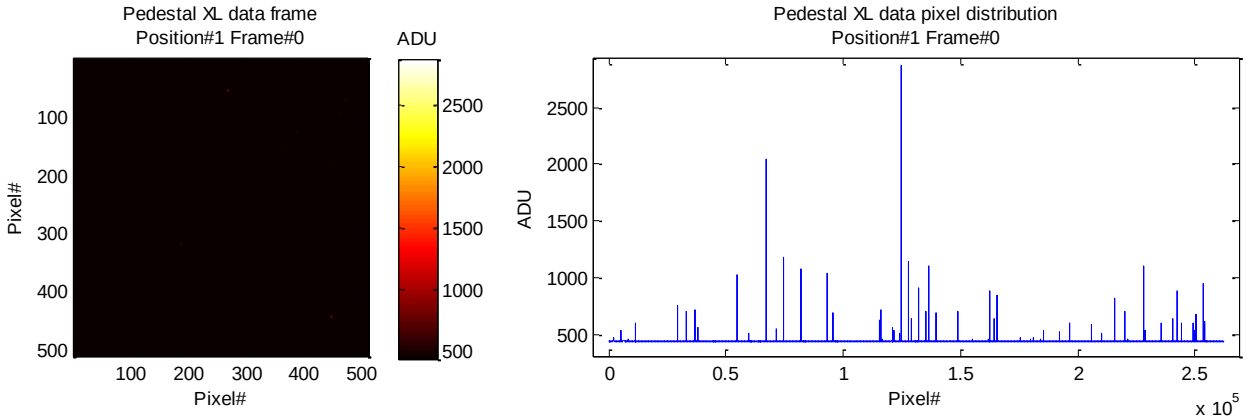

Figure 3.8: Final pedestal noise XL data frame (512x512 pixels) (left) and its corresponding pixel distribution (right), after the whole pedestal noise correction procedure.

As it can be seen in the previous figure, the bad pixels are still clearly present in the 1D distribution, because their correction will be performed only in the next step. The final noise-subtracted frame is also calculated, as it can be seen in Figure 3.9 for the same arbitrary raw data frame that has been considered for the previous figures.

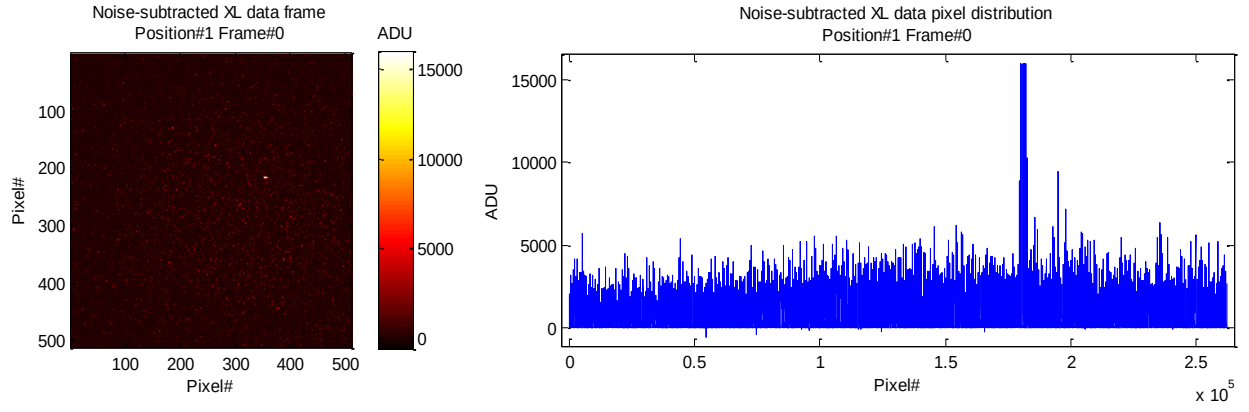

Figure 3.9: Final noise-subtracted XL data frame (512x512 pixels) (left) and its corresponding pixel distribution (right), after the whole pedestal noise correction procedure.

The noise-subtracted pixel distribution demonstrates that the signal baseline has been shif-

ted back to zero, as a confirmation of the accuracy of the noise correction. However, some pixels clearly have a relatively consistent negative ADU intensity, even as larger as hundreds of ADUs. Such pixel are those that have been identified as abnormal or bad pixels, so after the noise subtraction they need to be corrected in the next step of the processing procedure. Furthermore, it is evident, from both the 2D frame and its corresponding 1D pixel distribution, that the cluster of saturated pixels is still present. Such abnormality in the signal will also be eliminated in the successive step.

3) Finally, the noise-subtracted frame is furtherly corrected by first applying the bad pixel map that has been calculated in step 1). Figure 3.10 illustrates such 2D map and the corresponding 1D pixel distribution for the same arbitrary data as the previous figures.

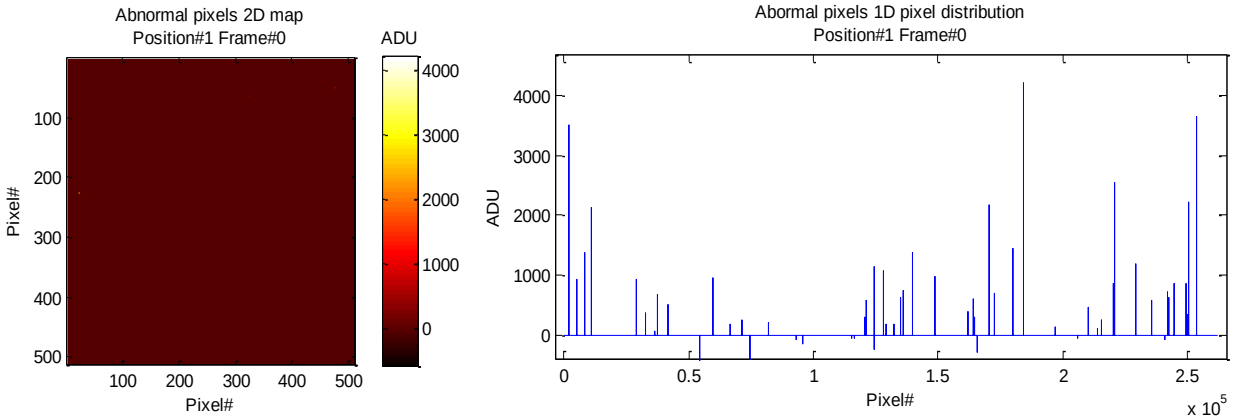

Figure 3.10: Abnormal pixel 2D map (512x512 pixels) (left) and its corresponding 1D pixel distribution (right). The bad pixels are those whose ADU intensities are different from zero.

The ADU intensity of those pixels that have been identified previously as abnormal, and thus recorded in the bad pixel map, is set equal to zero, in order to eliminate them from all the final 2D frames. Afterwards, each noise-subtracted frame is ultimately corrected by identifying and eliminating the clusters of saturated pixels, which are generated by electric discharges of the cathode of the DM tube. It must be considered that the discharge of the DM tube generally creates a Gaussian distribution of pixels with abnormally high intensity. Such distribution is centered on one or to pixels that has reached an ADU intensity equal to the pixel saturation value of the EMCCD (i.e. 16,384 ADUs). The identification process of the saturated centroids of the abovementioned distribution is the first action performed in the final correction. Hence, each pixel in a given frame that has an ADU intensity in a range between a lower threshold value, usually 10,000 ADU and the pixel saturation value is considered. Its ADU intensity is then compared with that of those pixels in a 9x9 region surrounding the considered pixel. If no pixel in such region has a higher ADU intensity than the considered pixel, the such pixel is identified as the centroid of the saturation cluster. Otherwise, a new search of the centroid in a surrounding 9x9 region is done in the same

way for the newfound pixel that has a higher ADU intensity than the considered one, until the centroid is univocally identified. Once that all the pixels in a given frame are analyzed and compared in such way and a certain number of saturated centroid pixels may be found, the ADU intensities of these centroid pixels and of all the pixels in a 9x9 region surrounding them are set equal to zero, in order to eliminate them from the final corrected frame.

In conclusion, after the just-described data processing procedure is terminated, the final corrected 2D frame is obtained. An example of such final frame and its corresponding 1D pixel map is depicted in Figure 3.11, again for the same initial raw data frame as previously shown in all the figures regarding the single correction steps.

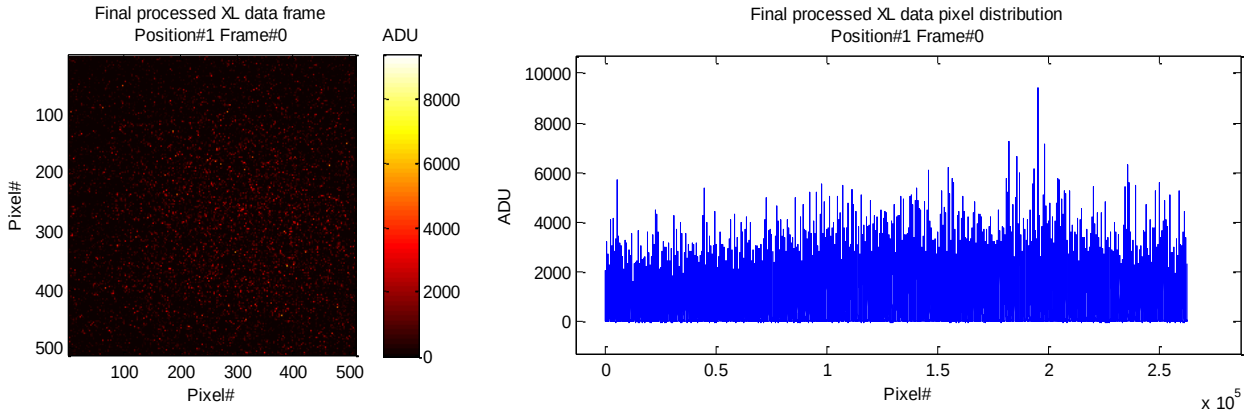

Figure 3.11: Final processed XL data frame (512x512 pixels) (left) and its corresponding pixel distribution (right), after the whole XL signal processing methodology.

The final processed 2D frame clearly shows the pedestal noise correction, as mentioned and explained before, Moreover, it can be seen that the abnormal pixel contribution, which mainly generated relatively large negative ADU intensities for such pixel, has been eliminated. Similarly, the cluster of saturated pixels has been removed from the final XL data, as evident in both the 2D frame (the bright spot is not present anymore) and the 1D pixel distribution. These aspects are even more manifest if the previous figure is compared with the corresponding initial raw XL data, shown at the beginning in Figure 3.5.

At this point, the final processed frames, obtained with the application of the methodology previously described, can be used as they are for XLCT imaging, by reconstructing them into a slice. Such procedure will be illustrated and explained in the next Paragraph. Otherwise, the final processed frames can also be used to quantify the x-ray luminescence intensity over a certain time, by calculating the net ADU intensity rate of a given set of acquired frames. Such quantification will be performed in an experiment that is going to be described in the next Chapter.

Anyway, the XL signal quantification can be easily obtained by first summing all the ADU intensities of all the pixels in each frame. Afterwards, the average ADU intensity of a given XL measurement can be calculated by averaging such summed total intensities of all the frames over the

total number of frames. Finally, by subtracting the XL quantified signal with x-ray OFF from the same quantity with x-ray ON, and dividing the resulting overall ADU intensity for the total acquisition time, the ultimate ADU intensity rate of a given XL measurement can be derived. The result of the abovementioned quantification operation is depicted in Figure 3.12, for 10 sets of 300 XL frames with x-ray ON and 10 sets of 300 XL frames with x-ray OFF. Each frame has been acquired for 0.5 seconds. Such result is again referred to a measurement explained in the next Chapter, regarding x-ray luminescence from LaF_3:Tb nanoparticles excited with the polychromatic x-ray tube at 50 kVp of tube voltage and 1 mA of tube current.

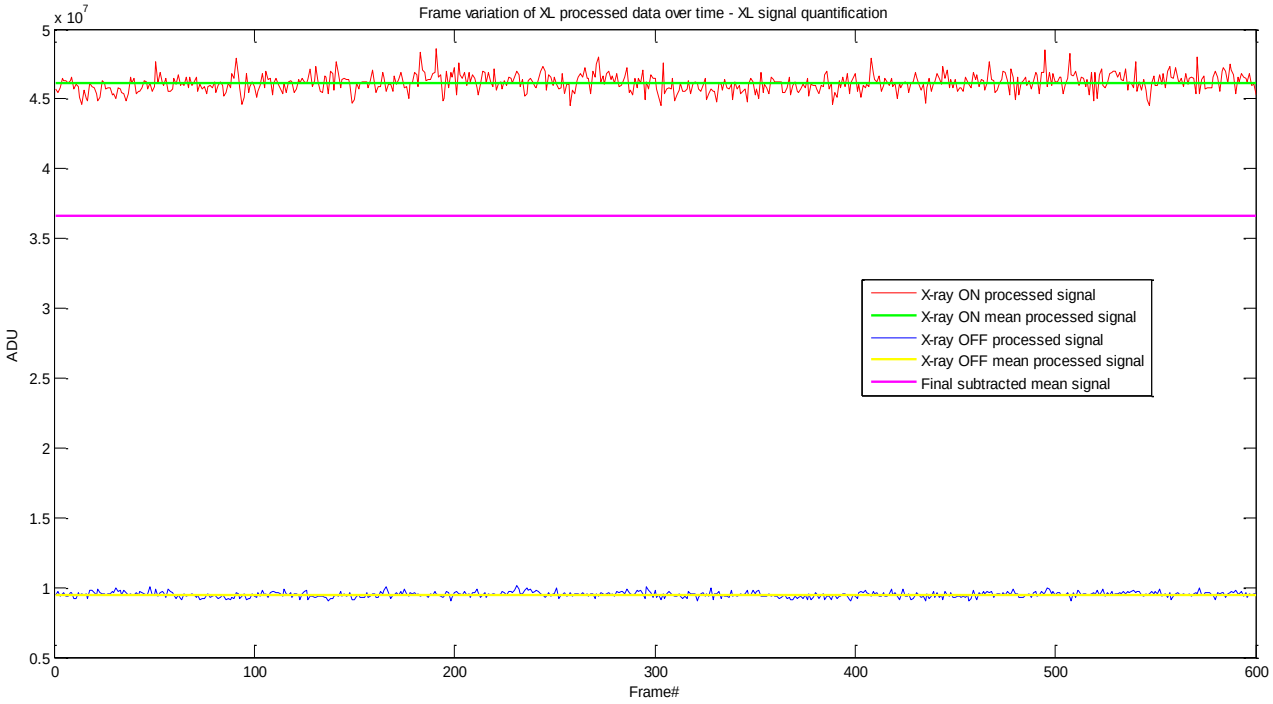

Figure 3.12: Graph showing the time-variation of the total processed XL signal of each frame, with x-ray ON (in red) and x-ray OFF (in blue). Quantification of such signal is done by averaging over the total number of frames for both x-ray ON (in green) and x-ray OFF (yellow). The subtracted mean XL signal between the two configurations is also depicted in magenta.

In the figure, it can be clearly seen that the time-variation of the total ADU intensity of each frame, for both the configurations with x-ray ON and with x-ray OFF (the former curve in red and the latter in blue), is relatively flat and stationary over time. It is also centered on its corresponding mean value over all the measurement time (horizontal lines in green and yellow, respectively), with no particularly relevant oscillations or identifiable periodic trends. Such behavior is a good index of the correctness of the XL data processing procedure and of the subsequent XL quantification. It must also be noted that the XL signal with x-ray ON is consistently higher than that with x-ray OFF, as expected. The magenta horizontal line corresponds to the subtraction between the two mean values and thus represents the final quantification of the XL signal during a given acquisition time span. Such final quantification value is the one that will be used for the forthcoming XL quantification experiments described in Chapter 4.

3.3 Imaging geometries and reconstruction for combined XFCT and XLCT

In Chapter 1, the concepts and ideas behind X-ray Fluorescence Emission Tomography (XFET) imaging geometries have been introduced. Such techniques, whose name recalls emission tomography modalities that are typical of nuclear medicine (SPECT, in particular) are based on the peculiar collimation of both the stimulating x-ray beam (before irradiating the object) and of the emitted x-ray fluorescence (before being detected by the camera). They have been applied to XFCT, in order to reduce the dimension of the source voxel from which the XF photons are emitted, by decreasing both the field of view of the detector through the collimation and the volume of the excited region in the object. This without excessively compromising the sensitivity of the modality and greatly enhancing its spatial resolution performances. Moreover, as primary advantage, the amount of imaging information carried by each XF photon is maximized and then the total imaging acquisition time of an XFCT scan is significantly lowered. An important result, directly connected to the reduction of the imaging time, regards the substantial reduction in the ionizing radiation dose absorbed by the imaged target [11] [16] [60].

As mentioned, such XFET imaging geometries has been applied mainly to XFCT in the current state-of-the-art, by L. J. Meng *et al* [11] [16] [60]. However, they can be used with the same exact principle for XLCT, by simply collimating the x-ray luminescence signal before detection, as it is done for XFCT. Therefore, XFET (which can also be called XLET at this point) imaging geometries are used in this project and implemented in the combined XFCT/XLCT system here described for all the imaging studies reported, as they will be described in the next Chapters.

In particular, two different imaging geometries have been chosen for the XFCT/XLCT system. The first one involves the use of a very small pencil beam of x-rays, with size up to 300 μm, for the excitation and of a slit collimator, with maximum size similar to the stimulation beam, in order to collect the XF or XL signal before it reaches the CCD camera or the EMCCD plus DM tube assembly. The pencil beam is used to irradiate a volumetric line across the object and by scanning it line by line 3D image information can be collected for successive tomographic reconstruction. Such configuration is perfectly suited for the GeniX^{3D} monochromatic source, as described in Chapter 2, but it can be also applied to the polychromatic x-ray tube, by simply using a small pinhole to collimate the cone beam. Moreover, the single-slit aperture, designed and explained in Paragraph 2.3, has been engineered exactly to be used for this imaging geometry and to fit with the dimensions and characteristics of the x-ray CCD used in the XFCT/XLCT system. In fact, as it will be seen in Chapter 4, this first imaging configuration will be used for an XF imaging study.

The second XFET/XLET imaging geometry that has been implemented in the XFCT/XLCT system consists of a thin sheet beam of x-rays, with thickness up to 200 μm, coupled with a pinhole collimator in front of the detector. This configuration has been used (see Chapter 4) for both XFCT

and XLCT imaging, by attaching a slit collimator in front of the polychromatic x-ray source and thus reduce the cone beam to a vertical plane of x-ray photons. Such sheet beam irradiates the object through a single vertical plane and then scan the target object, slice by slice, to collect the volumetric information. A single pinhole, with diameter ranging between 100 to 300 μm, has been mounted in front of both the x-ray CCD and the DM tube, according to the desired spatial resolution. Both the two above-described XFET/XLET imaging geometries used in the XFCT/XLCT system are schematized in Figure 3.13 [60], showing their respective process of image formation.

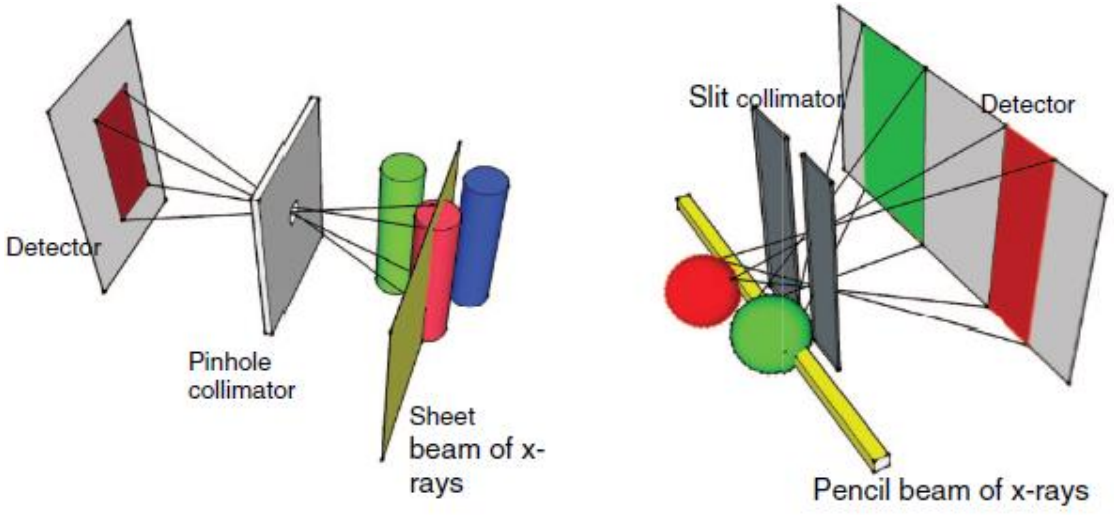

Figure 3.13: Diagram showing the two XFET/XLET imaging geometries implemented in the XFCT/XLCT system and used in the investigations and experimental studies. In the first, a sheet beam of x-rays irradiates a single plane the object and the resulting emission photons are transmitted through a pinhole (left). In the second, a pencil beam of x-rays illuminates a line across the object and the resulting emission radiation is collected through a slit aperture (right) [60].

It can be seen for the schematic representation of the image formation process for both the two geometries, that in the case of the pencil beam plus slit, the acquired image is collapsed along the column direction (vertically) in order to obtain a direct image of the illuminated line. While this approach involves more object motion, the sensitivity of the slit collimator is much larger than that of the pinhole, because of the greater area of collimation allowed. However, the sheet beam of x-rays permits a quicker image acquisition procedure, due to the larger volume of object scanned per beam position.

L. J. Meng *et al* has shown in an extensive Monte Carlo study [11] that both geometries potentially offer benefits over the current synchrotron-based line by-line approach. The pencil beam irradiation coupled with the slit aperture could provide an improvement of about an order of magnitude to the imaging speed, without increasing radiation dose rate. Moreover, the use of slit-apertures also offers reasonable detection efficiency, even with very thin widths of the aperture. On the other hand, the combination of sheet illumination with pinhole collimators can lead to a much lower imaging time, for the reasons previously mentioned. This helps to counter the lower detection efficiency of the pinhole. However, the improvement in imaging speed is reached at the cost of a

greater dose rate to the object. The first imaging geometry with the pencil beam and the slit collimator results to be better suitable for high-resolution XFCT and XLCT studies. This is also because of the challenges related to the second imaging geometry with the sheet beam and the pinhole, due to difficulties and high cost in fabricating micrometer-scale collimators and their extremely low sensitivity. Experimental demonstration of these two novel geometries have also been carried out by G. Fu *et al* [60].

Finally, reconstruction of the signal collected from XFCT and XLCT with both this two XFET/XLET imaging geometries must be discussed and it is necessary in order to obtain a whole 3D tomographic image with the XFCT/XLCT system here proposed. Hence, a very valuable characteristic of these imaging configurations is represented by the simplicity and straightforwardness in 3D image reconstruction, with no need of complex and computationally expensive algorithms. In fact, in the case of the sheet beam of x-rays coupled with the pinhole, each projection on the detector that has been transmitted though the collimator is already corresponding to a vertical slice of the imaged object, with thickness equal to that of the excitation x-ray planar beam. Multiple and consecutive frames during a given acquisition time, per beam position, can be acquired and then summed, pixel by pixel, to obtain the final slice. After scanning plane by plane the object through its entire transversal size, the final 3D image can be built by simply stacking each slice along the scanning direction. A scheme of this procedure is shown in Figure 3.14.

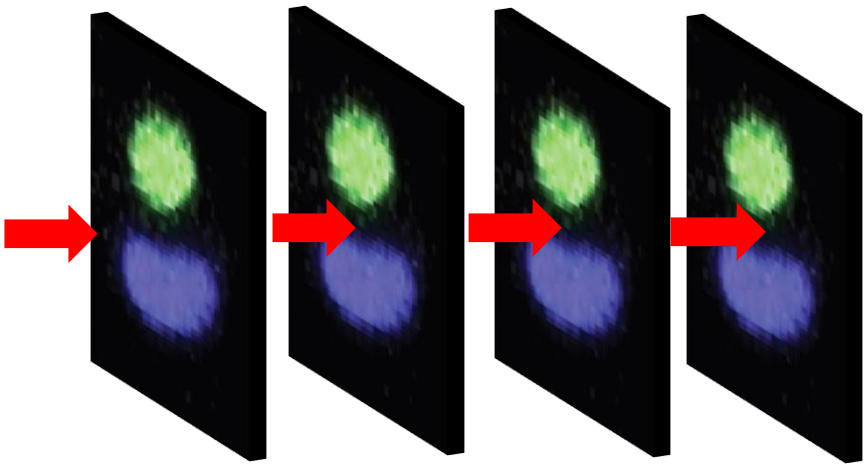

Figure 3.14: Simple reconstruction of a 3D image from the data acquired with the sheet beam of x-rays plus pinhole imaging geometry. The volumetric image of the scanned object is purely obtained by piling all the slices acquired along one direction (depicted in red). The slice image has been modified from G. Fu *et al* [60].

The 3D image reconstruction for the data acquired with the pencil beam plus slit aperture configuration is just a bit more complex and time-consuming than that just described, but it does not require any particular computational effort. Being the projection of the emitted radiation on the detector through the slit just a magnified representation of the irradiated line voxel, stretched along the vertical direction, the image of the volume line can be obtained by summing all the ADU intensities of each pixels in the given projection along the columns in the same vertical direction,

row by row. Such operation would create thin slices of thickness equal to the size of the pencil beam and of length equal to the horizontal dimension of the detector. From that, the tomographic image of a transversal slice of the object can be built by stacking all these thin line slices along the scanning direction. Finally, as in conventional CT, the entire 3D volumetric image can be compose by piling up all such slices along the vertical direction. The above-described reconstruction procedure is summarized as a diagram in Figure 3.15, showing all the steps just mentioned.

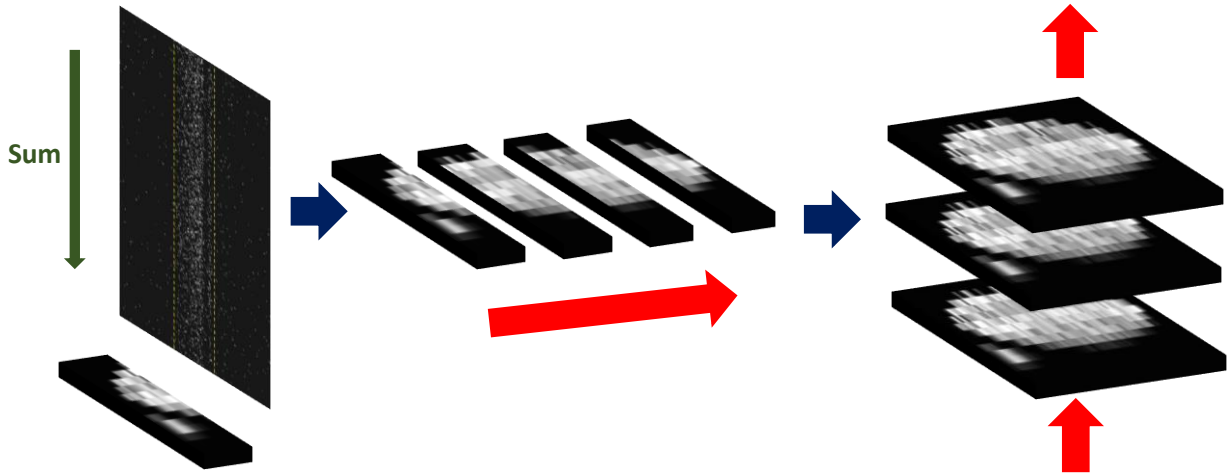

Figure 3.15: Reconstruction of a 3D image from the data acquired with the pencil beam of x-rays plus slit imaging geometry. After summing each pixel intensity along the vertical direction to obtain a line voxel of the object, all these voxels are stacked first along the transverse direction and then piled up, slice by slice. The projection and the slice images have been modified from A. Groll *et al* [16].

It is evident that the ease and relative effortlessness in 3D reconstruction offered by the application of XFET/XLET geometries, such as the two configurations just described, provides substantial benefits to the XFCT/XLCT system of this project and it is clearly favorable in any clinical or preclinical imaging technique.

4. Experimental studies from applications of the XFCT/XLCT system

Once the design and the construction of the XFCT/XLCT system, described in Chapter 2, was ultimately finished and all the tools necessary for data processing and image reconstruction were develop and tested, as illustrated in Chapter 4, experimental studies and investigations have been conducted with the setup. This was done with the objective of evaluating the performances of the system and demonstrating its imaging capabilities, but also to study the feasibility of using such technology for theranostic applications, like those explained in Chapter 1.

Regarding such last aspect, a first experimental study has been conducted with the aim of quantifying the XL and XF signal from two samples of different nanoparticles for theranostic purposes, as to compare such agents and their features for XFCT and XLCT. Different excitation energies and strategies, such as using filters or the monochromatic source, have also been used, in order to establish which may be the best and more suitable for x-ray induced therapies, such as XPDT (see Chapter 1). Moreover, an evaluation of the excitation energy that is necessary to produce both XF and XL in such two nanoparticles was also performed by measuring their corresponding x-ray attenuations through the x-ray transmission energy spectra.

Afterwards, two imaging studies have been also conducted, with different phantoms filled with metal-based compounds, using both XFCT and XLCT. Such two different studies have great importance and relevance to assess the capabilities of the system in terms of spatial resolution, sensitivity and other characteristics, such those illustrated in Chapter 1, which are essential for molecular imaging.

4.1 XF and XL signal quantification study of x-ray stimulated nanoparticles

The aim of the quantification study of the XF and XL signal from x-ray stimulated nanoparticles has a simple premise: to perform a quantitative comparison of the amount of x-ray fluorescence and x-ray luminescence produced by two of those nanoparticles illustrated in Chapter 2, i.e. LaF_3:Tb and Y_2O_3:Eu(III), and to investigate how such signal varies with different x-ray stimulation configurations, such as using different energies of the x-ray photons, using different sources or applying different filters to the excitation beam. In a perspective of XPDT as a potential theranostic application of the XFCT/XLCT system here proposed, the results of this kind of investigations could determine which nanoparticle is more suitable for XPDT and which excitation strategy, among those abovementioned, is able to produce the larger amount of XF and XL signal. In particular, the intensity of x-ray luminescence photons can be used as an index of the amount

of therapeutic effect that is delivered with nanoparticle-mediated XPDT, because it is directly related to the magnitude of the potential cytotoxic effect created in cancer cells. On the other hand, a large signal for both XF and XL is always desirable, as to increase the signal to noise ratio and the sensitivity in XFCT and XLCT imaging with the current system. However, an evaluation of the excitation energy absorbed by each nanoparticle is also necessary, as to estimate the amount of XF and XL signal produced per unit energy. Such quantity is more reliable and useful for a comparison between the two samples and an evaluation of their characteristic for XPDT and XFCT/XLCT imaging, because it can also take into account the dose that is delivered to the object. A quantification of this excitation energy using different x-ray stimulation strategies will be described in the next paragraph.

The quantification study of the XF and XL signal has been conducted using three samples:

1) A capillary tube filled with LaF_3:Tb nanoparticles in powder form;
2) A capillary tube filled with Y_2O_3:Eu(III) nanoparticles in powder form;
3) An empty capillary tube.

All the three capillary tubes were of the same type and model (Drummond Microcaps® 1-000-1000 [61]). They were made of borosilicate glass and had a volume of 100 µL. The inner dimeter of the tubes was equal to 1049.02 µm, while the outer diameter was 1435.10 µm. Thus, the thickness of glass of the tubes was 193.04 µm. A picture of the type of capillary tube used for the samples in the study is shown in Figure 4.1. As it can be seen in the figure, a thin foil of copper was wrapped around ne of the edges of the capillary tubes, in order to simplify its alignment with the collimated x-ray beam. Because of the unavoidable presence of the capillary tube as container of the samples, the XF and XL signal from an empty tube was also measured, quantified and subtracted from the signal emitted by the two other samples, as it was a sort of control group. This was done in order to correct for any contribution to the final XL and XF quantified signal coming from the glass, especially regarding metal impurities that may be present in its composition.

Figure 4.1: Example of glass capillary tube used in the quantification study.

Three main groups of excitation strategies were used during the quantification study, as to stimulate the production of XF and XL signal from the samples:

1) Using the polychromatic x-ray tube of the setup, at its maximum tube current equal to 1 mA, all the three samples were irradiated at different values of tube voltage, from 10 kVp to 50 kVp with increment steps of 5 kVp each time. Therefore, nine sets of tube voltage were used (10, 15, 20, 25, 30, 25, 40, 45 and 50 kVp) and, consequently, the shape and the

values of the energy spectrum of the cone beam of x-rays coming from the polychromatic tube changed. In particular, the maximum flux of photons, the maximum energy of the photons, the average energy of the photons and the fraction of photons having such energy in the spectrum vary with different tube voltages [29].

2) The x-ray cone beam of the polychromatic source was filtered with three different materials, in some cases combined together and using different thicknesses to attenuate the beam, before illuminating all the three samples. The three materials used were cerium (Z=58, ρ = 6.77 g/cm^3, K-edge = 40.41 keV), aluminum (Z=13, ρ = 2.70 g/cm^3, K-edge = 1.56 keV) and tungsten (Z=74, ρ = 19.25 g/cm^3, L-edge = 12.92 keV). They were chosen to attenuate and shape the x-ray cone beam and to make it as monochromatic as possible around the energies of the K-edges of the two nanoparticles (38.92 keV for La and 17.03 keV for Y), in order to maximize the x-ray absorption of the samples.

   Seven configurations of filters were used, as described in the following list:

   - A filter of 100 µm of cerium;
   - A filter of 200 µm of cerium;
   - A filter composed of 200 µm of cerium and 5 mm of aluminum;
   - A filter composed of 200 µm of cerium and 10 mm of aluminum;
   - A filter of 100 µm of tungsten;
   - A filter composed of 100 µm of tungsten and 3 mm of aluminum;
   - A filter composed of 100 µm of tungsten and 5 mm of aluminum;

   It must be considered that the filtering not only changes the energies of the photons of the x-ray cone beam, by mainly attenuating the low energy ones and those at K-edges or L-edges of the filters, but it also reduce the total flux of radiation illuminating the sample.

   The settings of the polychromatic x-ray tube were maintained constant during all the measurements with the filters and for each one of the samples, using the tube maximum values (50 kVp of tube voltage and 1 mA of tube current).

3) Using the monochromatic source (17.48 keV), at 50 kVp of tube voltage and 1 mA of tube current, all the three samples were irradiated with a pencil beam of size equal to 300 µm.

It is necessary to report that in all the measurements using the polychromatic x-ray tube, either with or without the filters, the x-ray cone beam coming out from the source was collimated with a 300 µm pinhole, before reaching the samples. Such operation was done to reduce the scattering of the primary x-rays in the surrounding environment and to minimize the probability that such scattered photons from the excitation beam may reach the detectors and the samples. On the contrary, no collimation was used in front of the detectors, to avoid contamination of the signal (mainly the XF signal) from the materials on which the apertures are made.

The XL signal was measured with the EMCCD plus DM tube assembly in the XFCT/XLCT system, alternating acquisition of frames with x-ray excitation of the sample (x-ray ON) and with no excitation (X-ray OFF), in equal numbers. Such procedure was applied accordingly to the XL data processing methodology described in Paragraph 3.1, as to track and update, from frame to frame, the calculated pedestal noise and to perform a better correction of the raw data. 10 sets of frames with x-ray ON and 10 sets of frames with x-ray OFF were thus acquired, for each single excitation strategy (i.e. for all the nine kVps, all the seven filters and for the monochromatic irradiation) and for all the three samples (LaF_3, Y_2O_3 and the empty tube). For LaF_3 and the empty tube, 60 frames per set were acquired at 0.5 seconds per frame, while for Y_2O_3, 300 frames per set at 0.1 seconds per frame were measured. A shorter acquisition time per frame was used for Y_2O_3, because of its higher luminescence intensity per unit time, thus to avoid saturation of the pixels of the EMCCD. Anyway, in the end each set of frames for all the three samples was acquired for the same time span, equal to 30 seconds. Hence, the total number of frames acquire, for either LaF_3 and the empty tube, was equal to 1200 frames (600 frames with x-ray ON and 600 frames with x-ray OFF), while for Y_2O_3 was 3000 frames (1500 frames with x-ray ON and 1500 frames with x-ray OFF).

All the XL raw data frames, acquired in such a way, were then processed and corrected using the XL data processing methodology explained in Paragraph 3.1. The final quantification of the mean subtracted signal over all the frames measured in each excitation configuration (i.e. for all the nine kVps, all the seven filters and for the monochromatic irradiation) were then derived from the final corrected frames (see Paragraph 3.1 for description of the XL quantification procedure), for all the three samples. In this way, the mean ADU intensity of the XL signal emitted from LaF_3, Y_2O_3 and the empty tube, in each collected frame, was determined, for all the investigated excitation strategies. Such mean ADU intensity was then normalized to the acquisition time of each frame (according to the different frame rate of each samples), in order to obtain the final ADU intensity rate (ADU/s) of the three samples in each configuration. Finally, the values of the ADU intensity rates for the empty tube were subtracted from the corresponding values of ADU intensity rates for the both the two nanoparticles, thus ultimately quantifying the total XL signal from LaF_3:Tb and Y_2O_3:Eu(III), as the main result.

On the other hand, the XF signal from the three samples, for each excitation strategy, was measured using the CdTe spectroscope of the XFCT/XLCT setup. After proper energy calibration of the CdTe detector, using an Iron-55 source (5.85 keV of gamma ray emission) and the energy of the monochromatic source (17.48 keV), an energy spectrum of the x-ray fluorescence emitted by each sample (LaF_3, Y_2O_3 and the empty tube) was collected and recorded. This was done for each strategy (i.e. for all the nine kVp, all the seven filters and for the monochromatic irradiation). Each of these XF energy spectra were measured for the same acquisition time, equal to 120 seconds.

Then, the XF counts per energy channel, in all the energy spectra collected in this way, were normalized to such common acquisition time. Thus, each XF energy spectra represented the count rate, per energy channel, of the detected x-ray fluorescence photons emitted by the three samples. At this point, the counts in each XF energy spectra taken from the empty tube, for all the excitation strategies, were subtracted, channel by channel, from the corresponding XF energy spectra of both the two nanoparticles. Thus, the resulting XF energy spectra, obtained is such way, measure the detected x-ray fluorescence (and relative scattered radiation) emitted only from the nanoparticles, eliminating the contribution from the glass capillary tube.

Finally, the XF signal of each nanoparticle, in each configuration, was calculated by first isolating the fluorescence peaks in the subtracted XF energy spectra (knowing their corresponding energies) and then summing all the counts in the channels that include such peaks. An example of this procedure and of the XF energy spectra collected in such way during the quantification study is shown in Figure 4.2, for the irradiation of LaF_3 with the polychromatic source at 50 kVp and 1 mA.

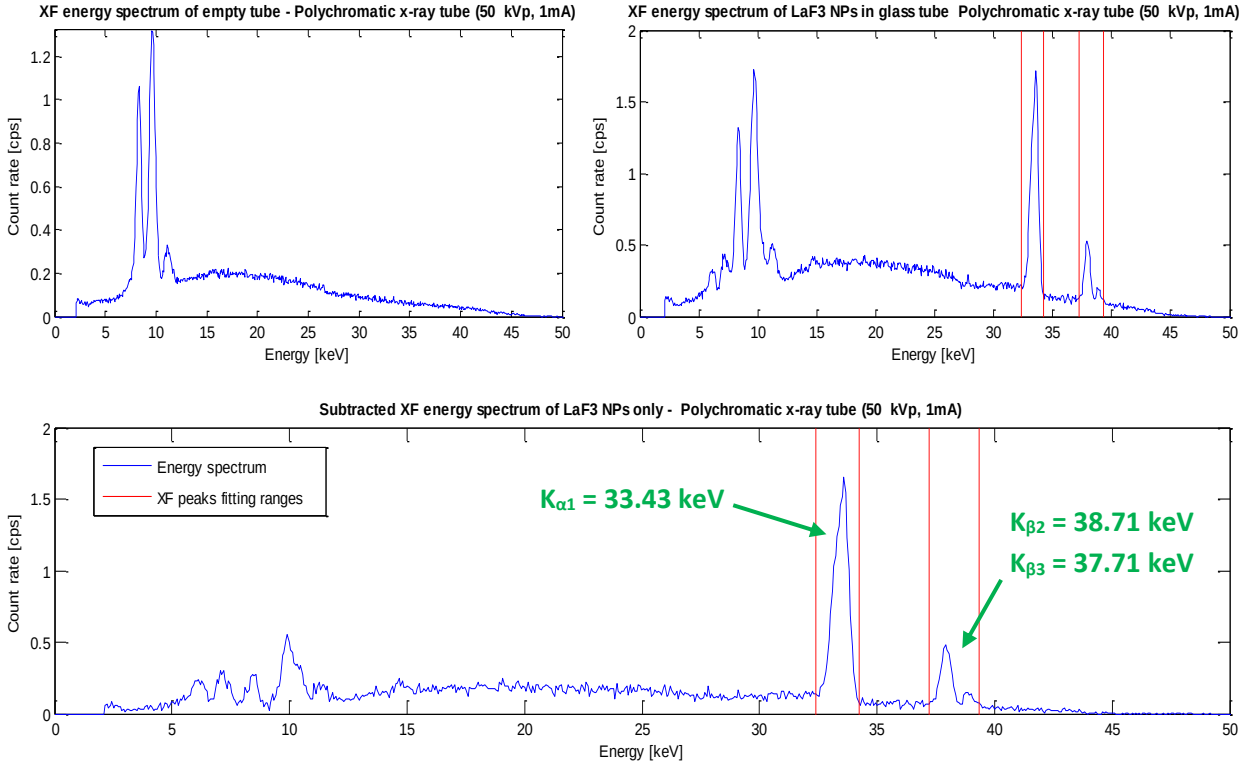

Figure 4.2: XF energy spectra for the empty tube (top left), the LaF_3 nanoparticles in the tube (top right) and the subtraction between the two (bottom). The isolation of the K-fluorescence peaks of lanthanum is visible (in red).

The three K-edge fluorescence peaks are evident in the figure, while the L-fluorescence peaks are difficult to discriminate, because of the presence of the characteristic x-rays peaks from the tungsten anode of the polychromatic source. Therefore, they have been ignored in the final quantification of the XF signal and only the K-fluorescence peaks were quantified. It must be noted that, although most of the contribution of the scattered photons to the spectra has been eliminated with

the subtraction of the empty tube (because the glass is the primary cause of such scattering, through coherent scattering and Compton scattering), a consistent fraction remains in the final spectrum. A similar example, still for the irradiation of LaF_3, is also reported in Figure 4.3, with the use of the filter composed of 100 µm of tungsten plus 3 mm of aluminum. This time, only the subtracted XF energy spectrum is shown in the figure.

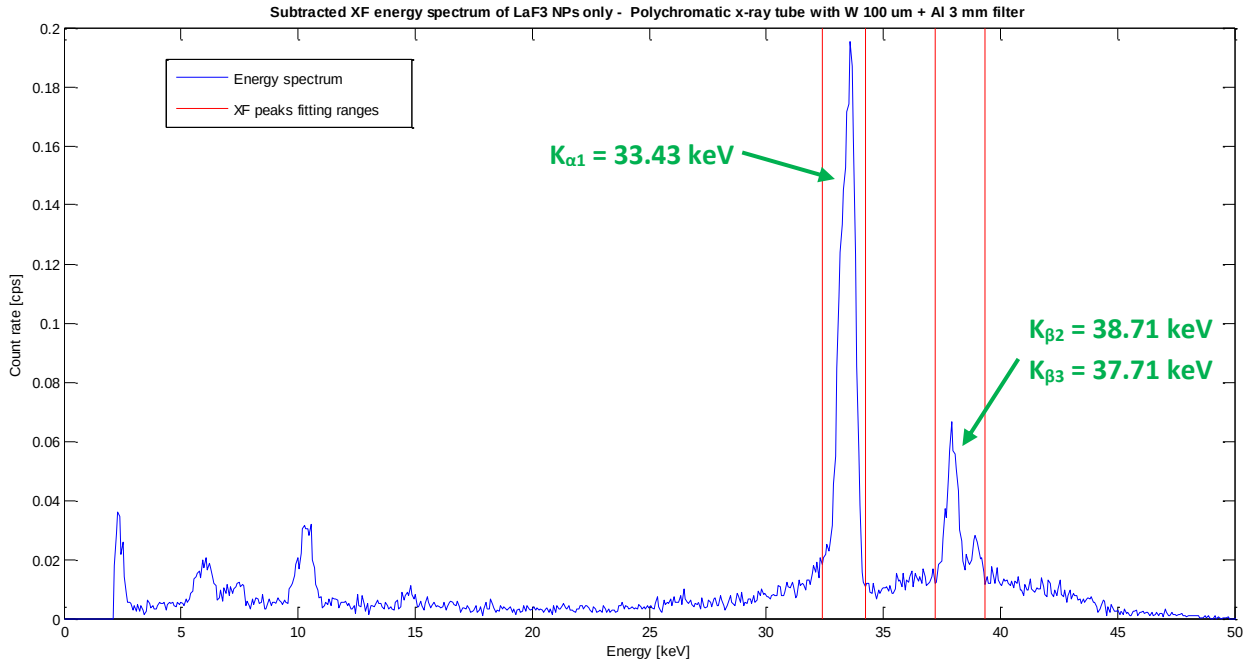

Figure 4.3: XF energy spectrum for the LaF_3 nanoparticles after subtraction of the XF signal from empty tube. The isolation of the K-fluorescence peaks of lanthanum is visible (in red). The excitation beam has been filter with tungsten and aluminum.

The same exemplary cases for the XF spectra are also reported for Y_2O_3, first showing the irradiation with the polychromatic source at 50 kVp and 1 mA. This is depicted in Figure 4.4.

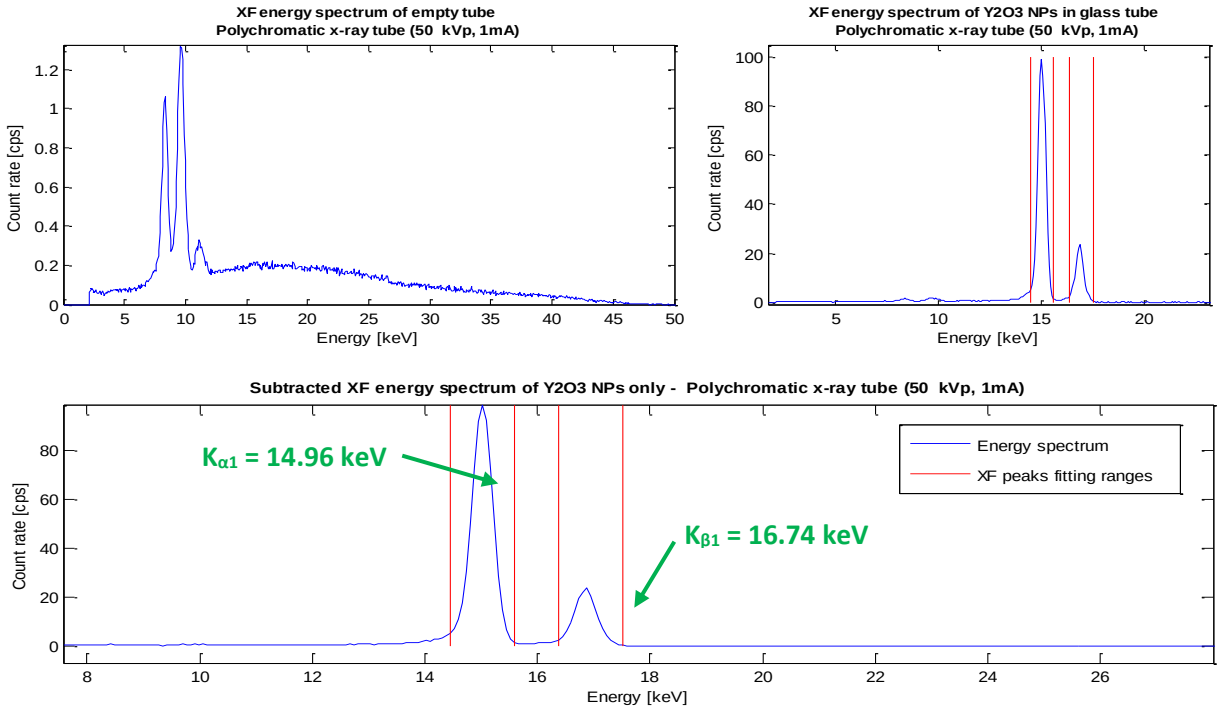

Figure 4.4: XF energy spectra for the empty tube (top left), the Y_2O_3 nanoparticles in the tube (top right) and the subtraction between the two (bottom). The isolation of the K-fluorescence peaks of yttrium is visible (in red).

The K-fluorescence peaks can be seen in the picture, which has been scaled in order to focus only on such features of the spectrum. Again, the XF spectrum for the irradiation of Y_2O_3, is also reported in Figure 4.5, with the use of the filter composed of 100 µm of tungsten plus 3 mm of aluminum, as previously (only the subtracted one is shown, as well).

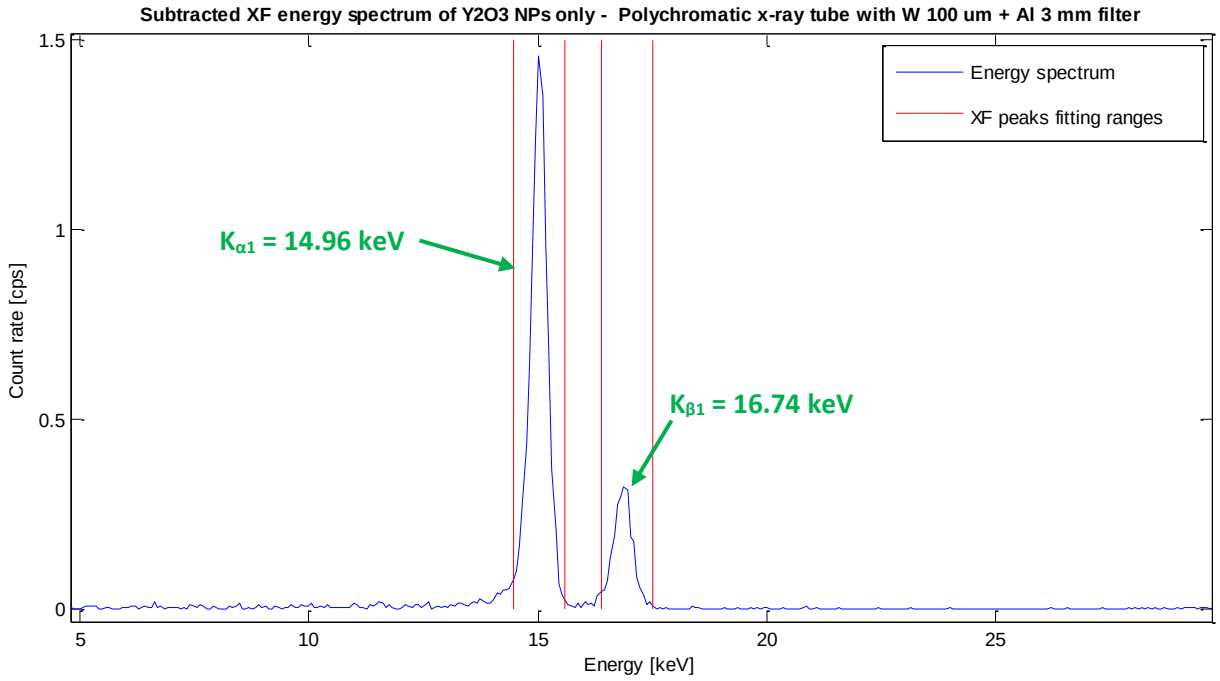

Figure 4.5: XF energy spectrum for the Y_2O_3 nanoparticles after subtraction of the XF signal from empty tube. The isolation of the K-fluorescence peaks of yttrium is visible (in red). The excitation beam has been filter with tungsten and aluminum.

Finally, an example of the XF energy spectrum for the irradiation of Y_2O_3 nanoparticles with the monochromatic source at 50 kVp and 1 mA is also reported in Figure 4.6.

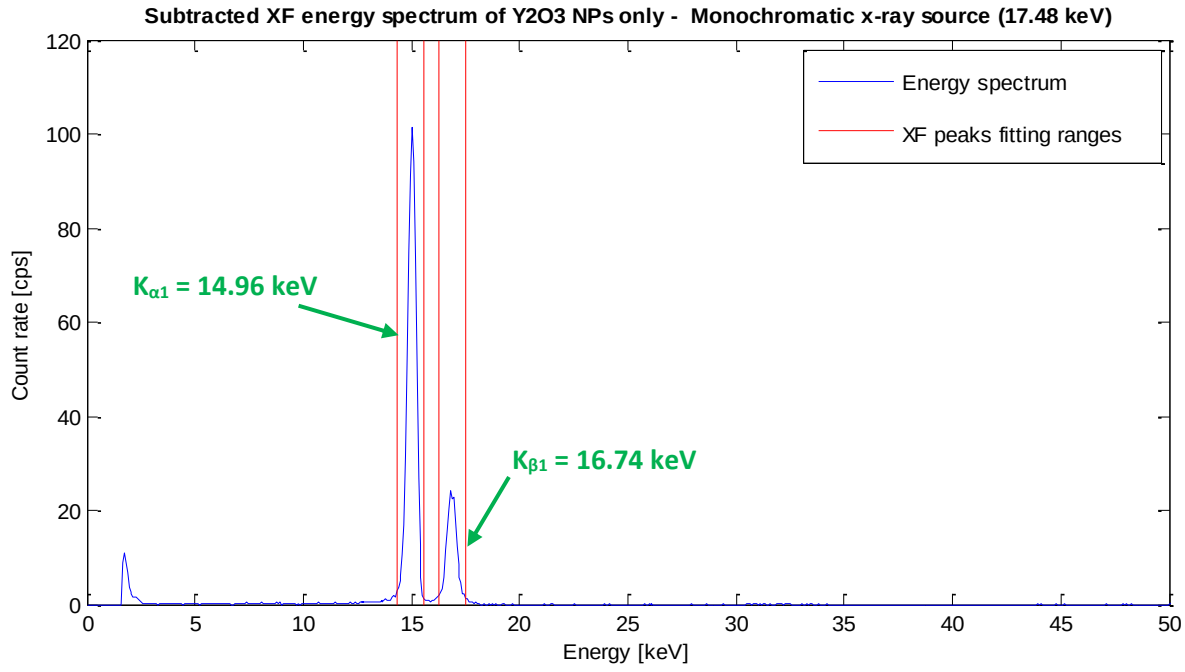

Figure 4.6: XF energy spectrum for the Y_2O_3 nanoparticles after subtraction of the XF signal from empty tube. The isolation of the K-fluorescence peaks of yttrium is visible (in red). The excitation beam was produced by the monochromatic source at 17.48 keV.

The results of the quantification study of the XF and XL signal from the two nanoparticles, which has been described previously, will be shown and discussed in details in the following Chapter, primarily focusing on what explained before about the evaluation of the applicability of the system to theranostics and the assessment of the different excitation strategies.

4.2 Quantification study of the excitation energy for theranostic XFCT/XLCT

As introduced at the beginning of this Chapter, a quantification of the excitation absorbed by LaF_3:Tb and Y_2O_3:Eu(III) nanoparticles, which was necessary to produce the XF and Xl signal quantified in the previous measurements, has been performed. This study is directly related and perfectly complementary to the quantification of the XL and XF signal illustrated in the preceding Paragraph. Hence, the same exact three samples in the glass capillary tubes have been used. Moreover, the absorbed energy was measured for all the excitation strategies mentioned in the Paragraph 4.1 (i.e. for all the nine kVp of tube voltage used with the polychromatic source, for all the seven filters and also for the monochromatic irradiation). This was done in order to correlate with high precision the XF and XL intensities (measured as count rates and ADU intensities, respectively) calculated from the signal quantification study and the amount of energy required to excite the two nanoparticles and to produce such signal. It is important to consider that the geometry of the setup used in the quantification study was maintained, without moving the sample and the source, in order to preserve the exact excitation occurred for the measurement of the XF and XL signal. In fact, the x-ray beam in each excitation strategy during the production of the XF and XL signal was required to illuminates the exact same region of the three samples, as to allow an accurate correlation between the XF and XL signals and the energy essential to produce them.

Therefore, during this quantification study of the excitation energy, the same irradiation configurations used for the previous measurements were repeated, in the exact same geometry inside the XFCT/XLCT system. This time, the CdTe spectroscope was used to measure the x-ray photons from the primary beam that has been transmitted across each one of the three samples. Thus, a single transmission energy spectrum of all the samples (LaF_3, Y_2O_3 and the empty tube) and for each excitation strategy (i.e. for all the nine kVp, all the seven filters and for the monochromatic irradiation) was collected and recorded. The acquisition time for these transmission energy spectra was the same in all the measurements and equal to 120 seconds.

The counts per channel recorded in each one of the transmission spectra represent the number of primary x-ray photons that have not been attenuated from the beam by the sample (or the air in between) and having an energy, after the transmission, included within the energy window of the corresponding channel. In order to collect only those photons that directly belong to the path of the primary x-ray beam and that have not been scattered outside the beam with wide scattering

angles, the CdTe detector was located at a relatively large distance (few centimeters) from the samples and a pinhole collimator of 1 mm was also mounted in front of its active area. This was done to further reduce the scattering and also to eliminate any possible x-ray fluorescence photon emitted by the sample along the same path of the primary beam. Anyway, the XF flux would be greatly lower than that of the excitation beam, so their contribution to the transmission spectra can be assumed as negligible. Hence, for all these reasons, it can be stated that the x-ray flux measured by the CdTe spectroscope was an accurate estimate of the amount of x-ray photons from the primary excitation beam that have not been attenuated by the samples during the irradiation.

At this point, all the transmission energy spectra collected in such way were first normalized to the acquisition time, as to obtain the count rates per channel of each of them. From that, a subtraction, channel per channel, of the count rates in the transmission energy spectra of the two nanoparticles (inside the glass tubes) from the corresponding count rates in the same spectra for the empty tube only would represents the amount of x-ray photons attenuated only by the nanoparticles thmeselves. This operation eliminates the contribution to the attenuation of the glass capillary tubes. Hence, it is possible to consider that the resulting subtracted energy spectra provide an indirect measure of the amount of x-ray photons per unit time attenuated from the primary excitation beam by the nanoparticles.

The count rates determined by the subtracted energy spectra calculated in such way are also with a good precision and correctness an estimate of the theoretically maximum rate of x-ray photons completely absorbed by the nanoparticles from the excitation beam, if all the occurred interactions were photoelectric absorptions. Moreover, such maximum estimate is not severely far from the actually rate of excitation x-ray photons really absorbed by the nanoparticles. This can be assumed because both LaF_3 and Y_2O_3 have large photoelectric cross sections for the photon energies used in all the excitation strategies of the described measurements. Anyway, such assumption cannot be properly verified without a Monte Carlo simulation or a model for the x-ray interactions and transport. Therefore, in this discussion, it will be assumed that the count rates in the subtracted energy spectra represents the rate of x-ray photons attenuated from the primary excitation beam by the nanoparticles, and at most the theoretically maximum rate of absorbed ones.

The rate of excitation energy, in keV/s, attenuated by the nanoparticles from the primary x-ray photons can then be calculated from the subtracted energy spectra discussed previously, for all the excitation strategies tested in the measurements. To do this, the count rates CPS_i in each energy channel i of all the energy spectra are multiplied for corresponding the energy centroid E_i of such channel, and then all these quantities resulting from the multiplication are summed, channel by channel, to obtain the total rate of attenuated excitation energy Φ_E. The total number of channels (or bins) in the spectra taken with the CdTe spectroscope is equal to 2048, for the Amptek detector

used in the XFCT/XLCT system. Thus, it can be written that:

$$\Phi_E = \sum_{i}^{2048} \mathrm{CPS}_i \cdot \mathrm{E}_i \tag{28}$$

As previously stated, such rate Φ_E for each set of tested excitation strategies is measured in keV/s. An example of the transmission energy spectra collected during the quantification study and the resulting subtracted spectra is shown in Figure 4.7, for the irradiation of LaF_3 with the polychromatic source at 50 kVp and 1 mA.

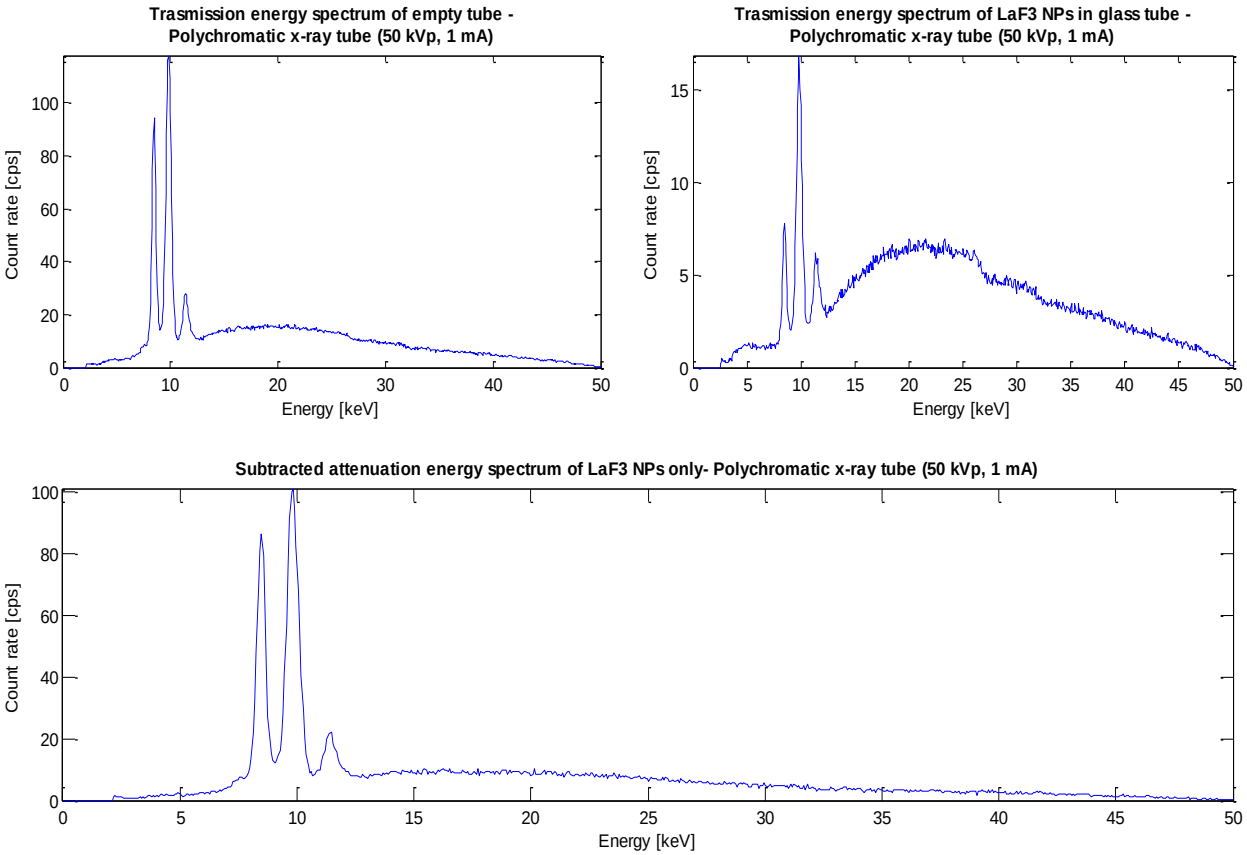

Figure 4.7: Transmission energy spectra for the empty tube (top left), the LaF_3 nanoparticles in the glass tube (top right) and the subtracted attenuation spectra (bottom), which is given by the first spectrum minus the second one. The polychromatic x-ray tube at 50 kVp and 1 mA was used for the irradiation.

The transmission energy spectra of both the empty tube and the nanoparticles in the glass tube clearly have the typical shape of the spectrum of a polychromatic x-ray tube. The peaks generated by characteristic x-rays from the tungsten anode of the source are also present. Comparing these two transmission energy spectra and also analyzing the resulting subtracted attenuation energy spectrum, it is evident that the nanoparticles are attenuating a large fraction of the x-ray photons from the primary beam, compared to the empty glass tube. Such aspect may be used to enforce the assumption, previously proposed, that the nanoparticles predominantly interact with the x-rays through photoelectric absorption, or at least via Compton scattering with large scattering angles, thus depositing almost all their energies in the sample.

It must also be noted from the figure, that the fraction of x-ray photons from the excitation beam having energies above the K-edge of lanthanum (around 40 keV) is very small, therefore the preferential absorption of these energy is not particularly manifest in the transmission spectra.
The same image is also provided for the irradiation of the same type of nanoparticles, using the filter composed of 200 µm of cerium plus 5 mm of aluminum, in Figure 4.8.

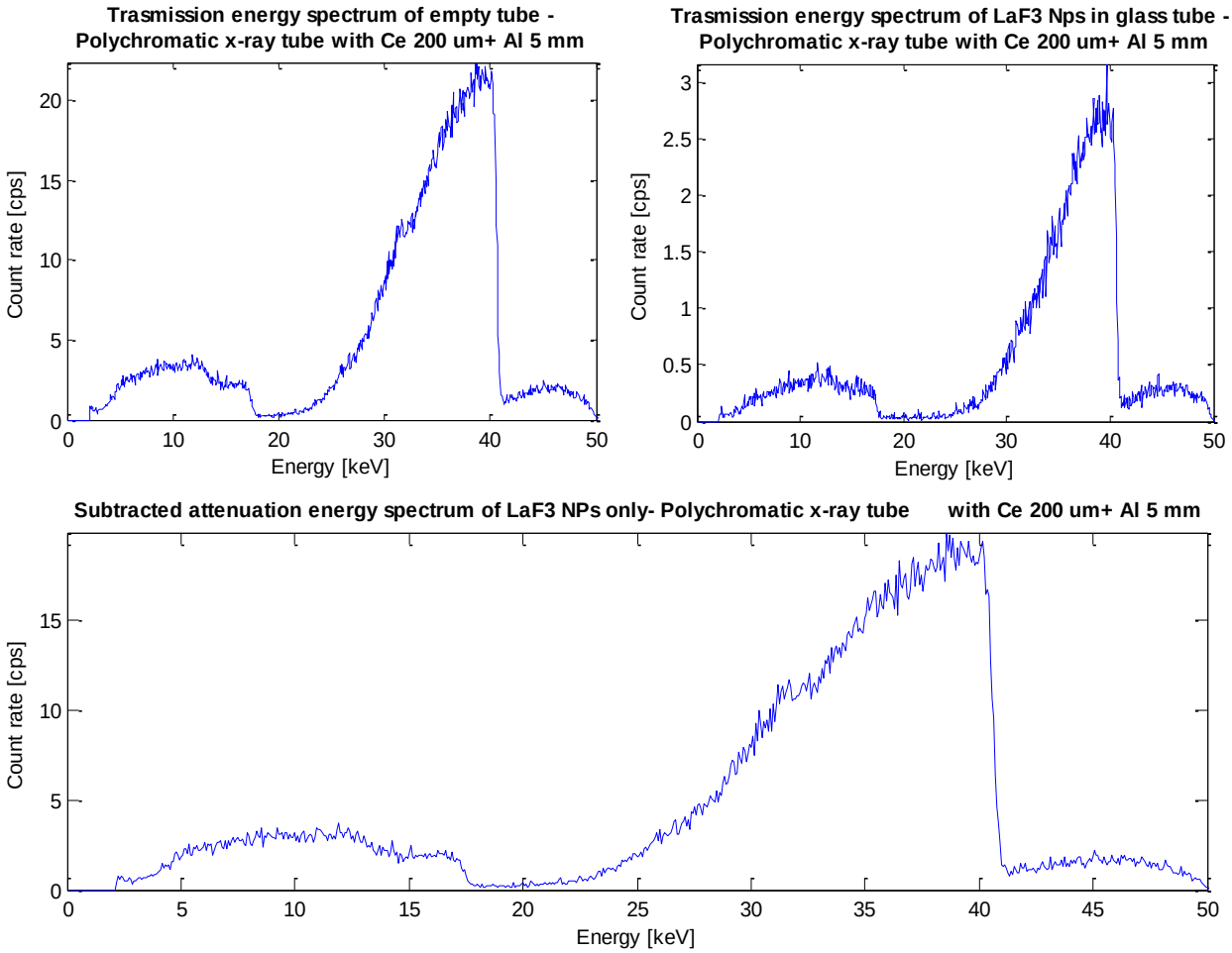

Figure 4.8: Transmission energy spectra for the empty tube (top left), the LaF_3 nanoparticles in the glass tube (top right) and the subtracted attenuation spectrum (bottom), which is given by the first spectrum minus the second one. The polychromatic x-ray tube at 50 kVp and 1 mA was used for the irradiation, filtering the beam with cerium and aluminum.

It can be seen form the transmission energy spectra that the polychromatic x-ray beam has been greatly modified by the filtering, hugely diminishing the flux of x-ray photons at the lower energies (with a larger fraction in correspondence of the tungsten characteristic x-rays) and also the energies above the K-edge of cerium (40.41 keV). The overall flux is also greatly reduced, in comparison with the previous, in Figure 4.7, without the filtering action and at the same tube voltage and tube current. Again, it is evident that the LaF_3 nanoparticles attenuate the primary beam photons more than the empty tube, as demonstrated by the large difference in the net count rates from the transmission energy spectrum of the empty tube only and that of the nanoparticles plus the empty tube. This further corroborates the assumption made previously about the absorbed photons,

Another example of transmission energy spectra acquired during the quantification study of the x-ray excitation energy is reported in Figure 4.9, for the Y_2O_3 nanoparticles, showing this time the irradiation with the polychromatic source at 35 kVp and 1 mA.

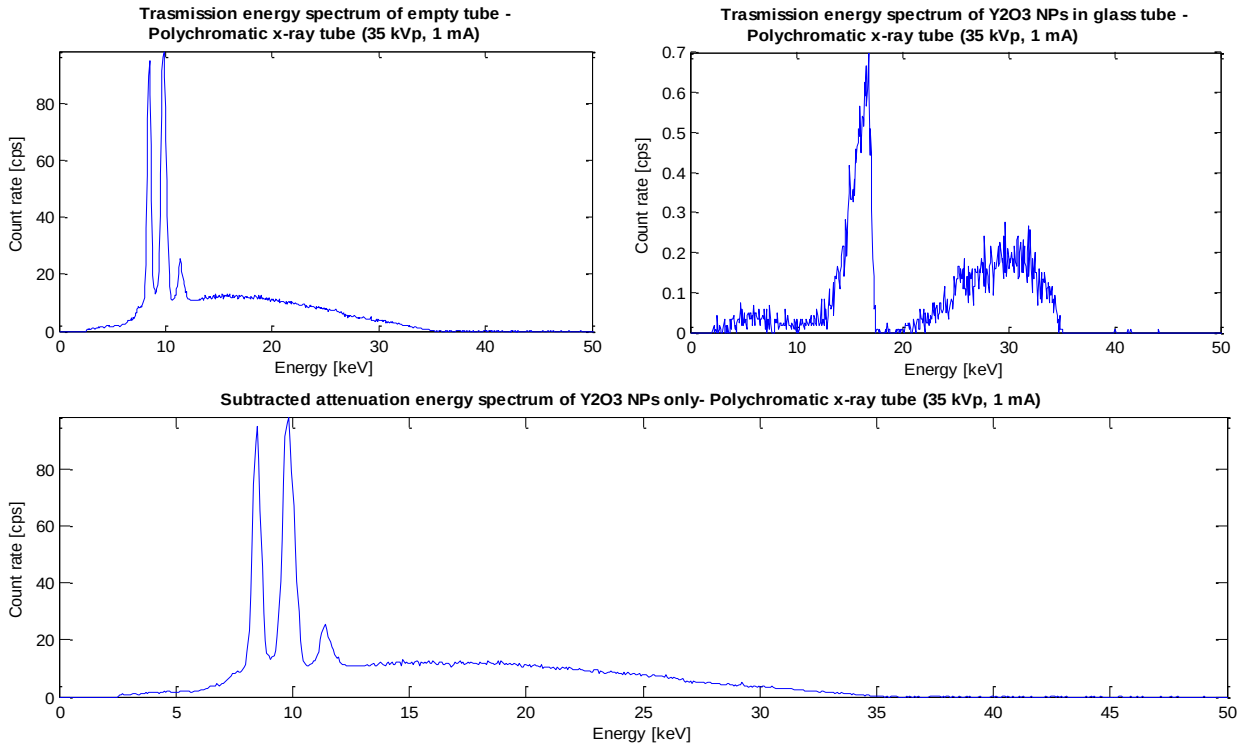

Figure 4.9: Transmission energy spectra for the empty tube (top left), the Y_2O_3 nanoparticles in the glass tube (top right) and the subtracted attenuation spectrum (bottom), which is given by the first spectrum minus the second one. The polychromatic x-ray tube at 35 kVp and 1 mA was used for the irradiation.

This time, the transmission energy spectra of Y_2O_3:Eu(III) clearly show that, at the energy of the K-edge of yttrium (17.03 keV), a large fraction of x-ray photons from the primary beam is absorbed by the nanoparticles, in comparison with what happened previously with the spectra from LaF_3:Tb.

Finally, Figure 4.10 illustrates the same transmission energy spectra and attenuation spectra, again for Y_2O_3, with irradiation using the monochromatic x-ray beam at 17.48 keV. In

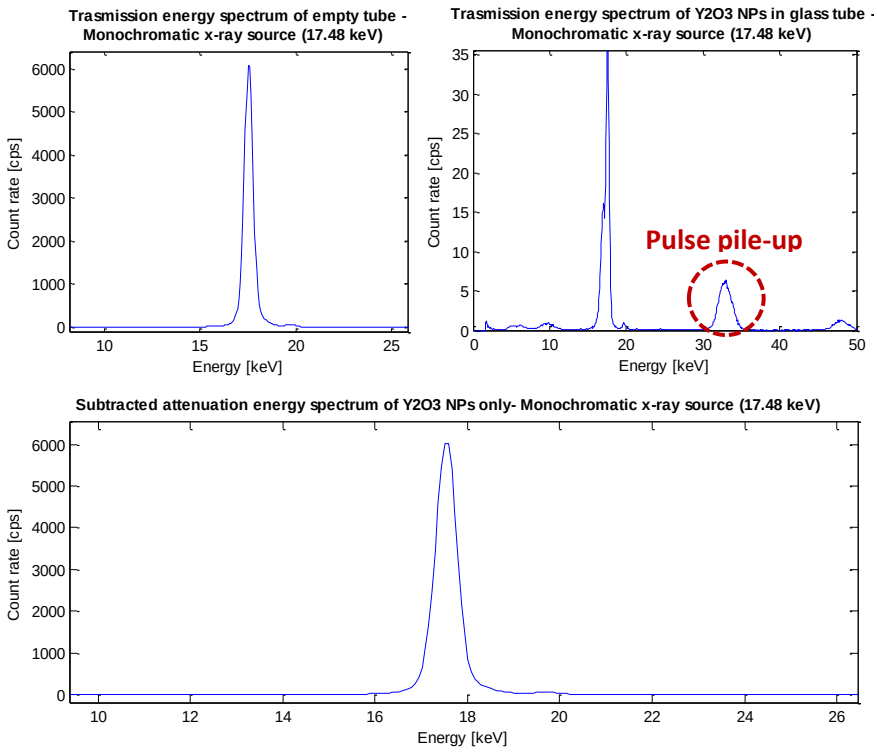

Figure 4.10: Transmission energy spectra and subtracted attenuation spectrum for irradiation of Y_2O_3 with monochromatic x-ray source at 17.48 keV.

the case of the monochromatic x-ray source, pulse pile-up peaks due to the very high flux of photons is visible (in the red circle). This is caused by the simultaneous detection of two events by the detector, without being able to discriminate them.

In addition to the previously discussed rates of excitation energy, in keV/s, attenuated by each nanoparticle from the primary x-ray photons, in the various tested stimulation strategies, the average attenuated energy was also calculated, for each of the same measured excitation configurations. Such average attenuated energy $\overline{\mathrm{E}}_{\mathrm{att}}$ was derived from the subtracted attenuation spectra (calculated as it was explained previously) by simply dividing the total attenuated energy rate Φ_E, for each energy spectrum, by the total count rate in the whole spectrum, i.e. the sum of all the count rate per energy channel over the total number of channels (equal to 2048). Thus:

$$\overline{\mathrm{E}}_{\mathrm{att}} = \frac{\Phi_E}{\sum_i^{2048} \mathrm{CPS}_i} = \frac{\sum_i^{2048} \mathrm{CPS}_i \cdot \mathrm{E}_i}{\sum_i^{2048} \mathrm{CPS}_i}$$

The average attenuated energy (in keV) can also be considered an estimate of the mean excitation energy absorbed by the nanoparticles, if all the occurred interactions were photoelectric effects, in the same way as assumed for the attenuated energy rates. An example of such calculation with the transmission and the attenuation energy spectra, for the irradiation of Y_2O_3 with the polychromatic source filtered with 100 µm of tungsten plus 5 mm of aluminum, is shown in Figure 4.11.

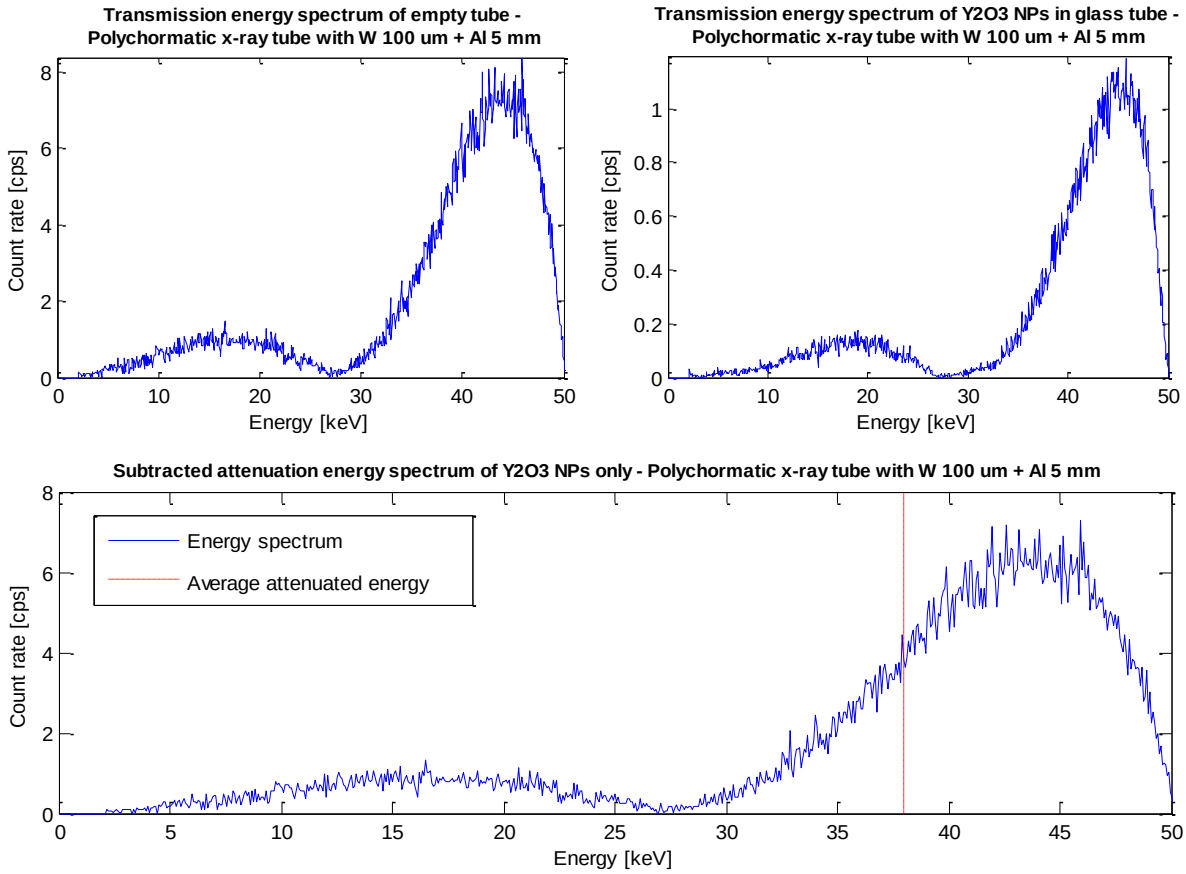

Figure 4.11: Transmission energy spectra for the empty tube (top left), the Y_2O_3 nanoparticles in the glass tube (top right) and the subtracted attenuation spectrum (bottom). The polychromatic x-ray tube at 50 kVp and 1 mA was used for the irradiation, filtering the beam with cerium and aluminum. The dashed red line shows the average attenuated energy that has been calculated.

The average attenuated energy calculated with the previous procedure is labelled in the figure using a dashed vertical line in red.

The result from the quantification of the excitation energy attenuated from the primary beam by the two investigated nanoparticles will be presented and discussed in Chapter 5, in combination with the outcomes of the XF and XL signal quantification study of the previous Paragraph.

4.3 XFCT imaging study of a mouse phantom loaded with metal compounds

The first of the two imaging studies, which has been performed with the XFCT/XLCT system proposed and described in this thesis work, involved the use of a plastic phantom, modeled as a mouse head and loaded with some of the nanoparticles and metal-based compounds, among those illustrated in Chapter 1 for theranostic applications [62]. The main purpose of this imaging study regards the testing of the feasibility of XFCT at molecular or near-molecular imaging levels using the current system, with also the evaluation of its performances, mainly in terms of spatial resolution, sensitivity and capability of multiplexed imaging.

Considering such objectives, the imaged phantom was designed in order to stress and challenge these aforementioned characteristics of the XFCT/XLCT system, in particular for what concerns its size, its geometric features and details and the concentrations of the target material used. Hence, two identic double-tube cylinders, each one composed by two borosilicate capillary tubes concentrically put one inside the other, were prepared and filled with different metal-based compounds. The external capillary tube (Drummond Microcaps® 1-000-1000 [61]) had an inner dimeter equal to 1049.02 µm, while the outer diameter was 1435.10 µm. Thus, the thickness of glass of the tube was 193.04 µm. On the other hand, the internal capillary tube (Drummond Microcaps® 1-000-0010 [61]) had an inner dimeter equal to 200.66 µm and an outer diameter of 660.40 µm. Thus, the thickness of glass for this tube was 229.87 µm. Considering such dimensions, then the inner annular gap between the two capillary tubes was equal to 194.31 µm. The metal-based compounds were inserted both in such annular gap and in the inner capillary tube. A scheme of such configuration for both the double tube cylinders is schematized in Figure 4.12. The dimension of the capillary tubes were chosen also accordingly to the mean free path and the attenuation of the XF photons produced by the compounds that were put inside them.

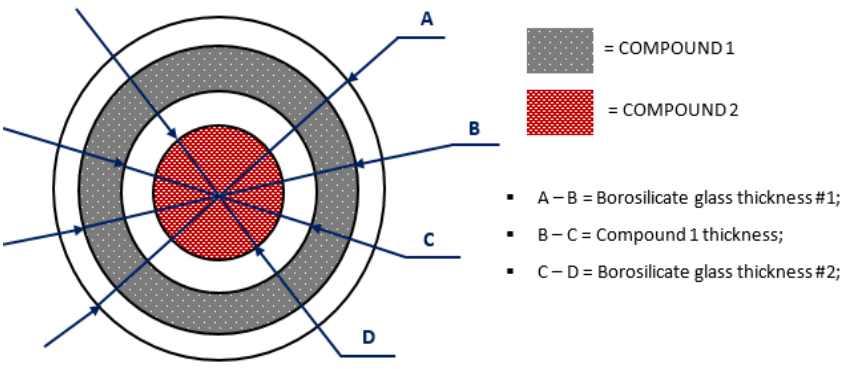

Figure 4.12: Scheme of the cross section of the double tube cylinders used in the imaging study.

One of the two double tube cylinders was filled on the inside region with LaF_3:Tb nanoparticles in powder form (compound 2 in Figure 4.12) and in the annular region with Cisplatin in water solution (compound 1 in Figure 4.12), at a concentration of 1mM, corresponding to 300 µg/mL. A picture of such double tube cylinder is shown in Figure 4.12 [62].

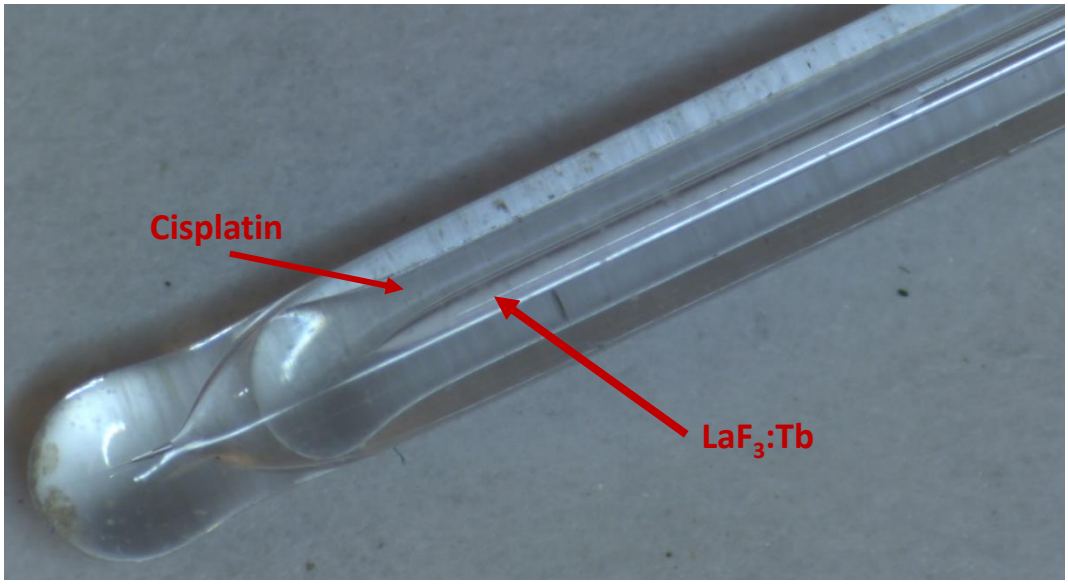

Figure 4.12: Glass double tube filled with LaF_3:Tb nanoparticles in powder form (inside) and 300 µg/mL of Cisplatin solution in water (outside) [62].

The other double tube cylinder was filled on the inside region with Y_2O_3:Eu(III) nanoparticles in powder form (compound 2 in Figure 4.12) and in the annular region with HfO_2 nanoparticles dissolved in water solution (compound 1 in Figure 4.12), at saturation. A picture of such double tube cylinder is also reported, in Figure 4.14 [62].

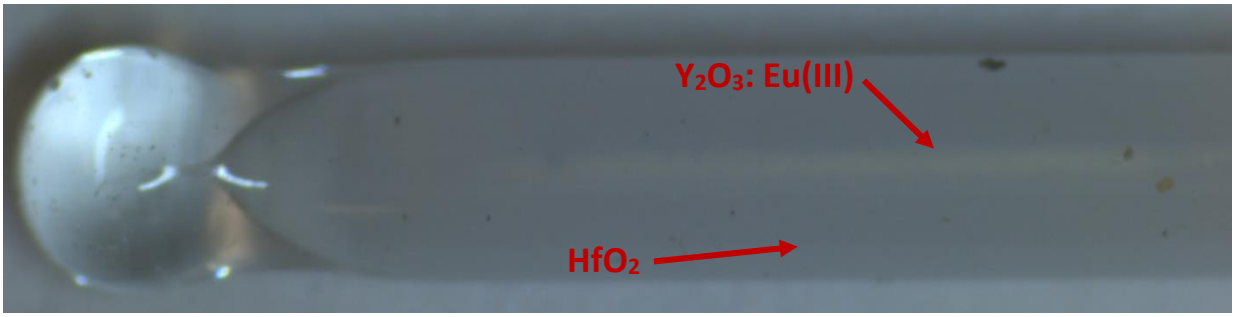

Figure 4.14: Glass double tube filled with Y_2O_3:Eu(III) nanoparticles in powder form (inside) and HfO_2 nanoparticles in water solution at saturation (outside) [62].

All the four metal-based compounds used in the two double tube cylinders have been introduced in Paragraph 2.4 and are suitable agents for theranostic applications, such as XPDT, x-ray induced Auger therapy and x-ray induced radiosensitization of tumors.

The two double tube samples just described were then glued to an optically transparent phantom made of plastic, which was 3D-printed using the model of a mouse head. Such phantom had approximate dimensions equal to about 15 mm x 11 mm for the height and the transversal diameter, respectively. The model for the phantom, using a head of a mouse, was chosen to simulate as much

as possible small animal imaging, which is the closest application for future developments of the XFCT/XLCT system. Different views of such mouse head with attached the two double tube cylinders arereported in Figure 4.15 [62], showing also the position and the arrangement of these two samples.

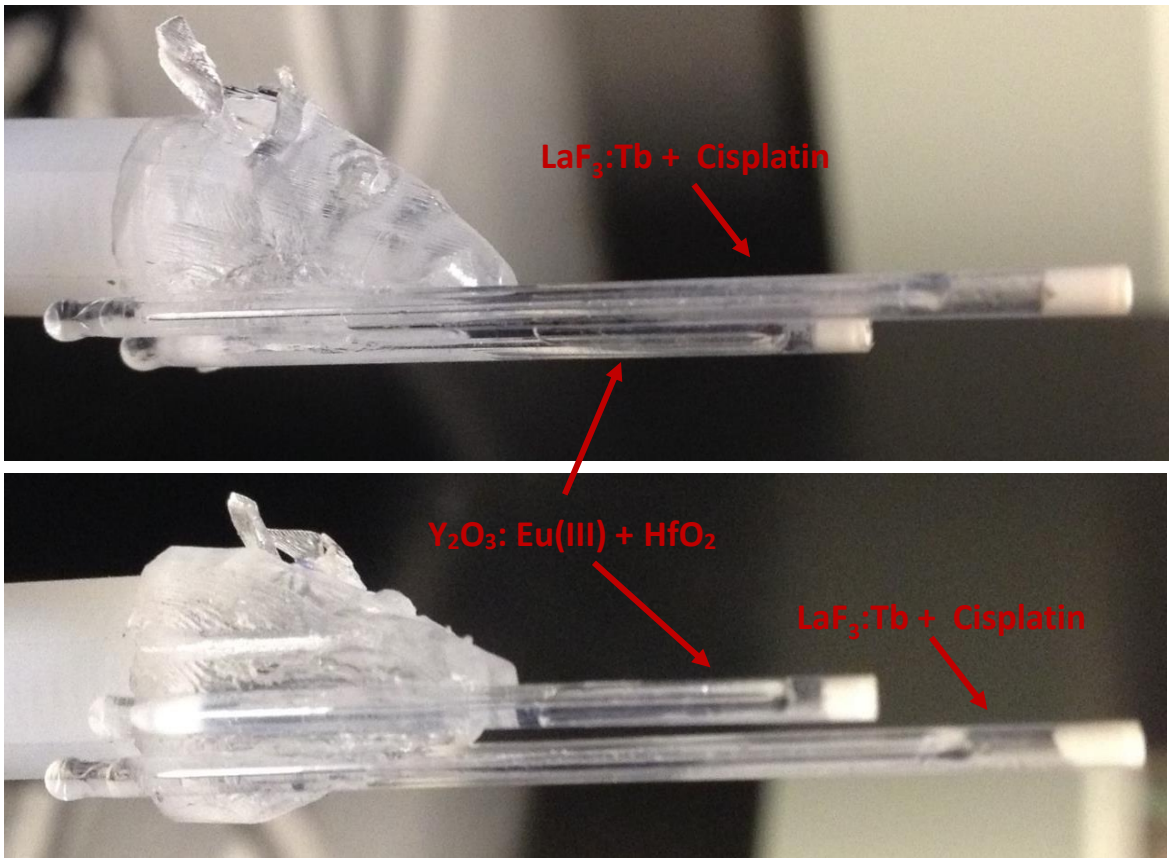

Figure 4.15: Lateral view (top) and frontal view (bottom) of the mouse head phantom with the two double tube cylinders loaded with metal-based compounds. The respective compositions of the cylinders are labelled in red [62].

The XFCT imaging study of the mouse head sample just described was performed inside the XFCT/XLCT system, which has been illustrated and discussed multiple times, especially in Chapter 2. The XFET imaging geometry using a pencil beam and a slit collimator (as described in Paragraph 3.3) was chosen, due to the small size of the imaged object and the low concentrations of the samples involved. In fact, such geometry, as written previously, is the one with the highest sensitivity and detection efficiency. Moreover, the longer acquisition time of such configuration was compensated by the limited size of the phantom to be scanned.

The monochromatic GeniX^{3D} source, at 17.48 keV, was used for the x-ray excitation of the samples, with a pencil beam of size equal to 200 µm. The diameter of the x-ray beam was chosen to be roughly the same dimension of the four regions in the two double tubes filled with the metal-based compounds, as to potentially be able to spatially resolve the geometric features of the whole phantom. The mouse and the pencil beam of x-rays were aligned using the Zyla sCMOS camera, by qualitatively measuring the variation in the attenuation through the different sample materials,

and also using the CdTe spectroscope, in order to detect changes in the XF signal from the compounds, when differrent regions of the phantom were irradiated by the excitation source. In addition, the CdTe spectroscope was also actively used to collect the energy spectra at different excitation positions, during the scanning of the phantom throughout the entire XFCT imaging study. Finally, the x-ray CCD camera of the system was employed to collect and record the projections of the x-ray fluorescence photons emitted by the various material in the phantom. The single slit aperture that has been designed in Paragraph 2.3 were created and mounted in front of the CCD, to collimate the XF photons emitted by the samples before they reach the detector. As described in the abovementioned Paragraph, the slit had a width of 100 μm. A photo of the single slit aperture that was made and used for the XFCT is reported in Figure 4.16 [62].

Figure 4.16: Picture of the 100 μm-single slit aperture used in the XFCT imaging study [62].

During the XFCT imaging study, 16 scanning irradiation positions of the x-ray pencil beam were acquired for each tomographic slice, having a thickness equal to the size of the beam (200 μm). Translational steps of 200 μm were applied to move from one position to the successive, in order to cover the entire volume that included the two double tube cylinders. 6 of the 16 scanned positions covered the first double tube cylinder filled with Y_2O_3:Eu(III) and HfO_2, acquiring 200 frames at 2 seconds per frame for each of these positions. Therefore, the total imaging time per position for the cylinder filled with Y_2O_3:Eu(III) and HfO_2 was equal to 5 minutes. Similarly, other 6 of the 16 total scanned positions also covered the cylinder filled with LaF_3:Tb and Cisplatin, this time acquiring 600 frames at 2 seconds per frame for each of such positions. Hence, the total imaging time per position for the cylinder filled with LaF_3:Tb and Cisplatin was four times as long as that for the other cylinder, being equal to 20 minutes. This was because of the weak XF signal being produced by Cisplatin, having the lowest concentration involved in the study. As said before, XF energy spectra were collected with the CdTe detector per each position. The XF signal from each frame acquired with the CCD during this imaging procedure was then used for reconstruction of a single tomographic slice of 200 μm, using the methodology already described in Paragraph 3.3. Multiplexed imaging of the slice was also obtained by isolating the XF signal from each target compound in the mouse head phantom, using the XF energy spectra collected with the CdTe spectroscope.

The final results of this XFCT imaging study just described, with the mouse head phantom filled with metal-based compounds, will be presented and discussed in details in the next Chapter.

4.4 Combined XFCT and XLCT imaging study of double tube with metal compounds

The second imaging study presented in this thesis work, again using the XFCT/XLCT system here described and developed, involved the use of a double tube glass cylinder, with bigger dimensions than those of the previous experiment, yet loaded again with metal-based compounds. Such sample was imaged through combined XFCT and XLCT, with the aim of test the feasibility of such simultaneous dual-modality with the current setup and evaluates its performance for potential molecular imaging. The capability to perform multicolored imaging with two different radiation signals, the x-ray fluorescence and x-ray luminescence, was also one of the main objective of the study. In fact, it would demonstrate the fitness of the system to detect multiple agents at the same time, even in the case such agents are concurrently producing either x-ray fluorescence, x-ray luminescence or both. In addition, the detection of simultaneous XF and XL signal could demonstrate the applicability of such system for theranostics, in particular for delivering and monitoring XPDT, where the x-ray luminescence provides the therapeutic effect and the x-ray fluorescence the detectable signal for imaging. For this reason, the double tube cylinder used in the imaging study was filled with some of the compounds discussed in Paragraph 2.4, which have been proved to suitable for the abovementioned kind of theranostic application [62].

The sample used in this imaging study was composed of two borosilicate glass test tubes, the smaller one inserted concentrically inside the bigger one, as to form a double tube cylindrical structure with an internal region and an external annular region, as for the previous configuration of the capillary tube samples shown in Figure 4.12. The internal glass tube had an inner diameter of 3 mm, while the external tube had an inner diameter of 5 mm. The annular region between the two tubes had a thickness of 1 mm. The inner region was then filled with Y_2O_3:Eu(III) in powder form, which produces both XF and XL signal (as investigated in the previous paragraphs and Chapters), while the annular region was loaded with sodium bromide (NaBr) in water solution. NaBr is capable of emitting x-ray fluorescence with external x-ray excitation, due to the presence of bromine (Br, Z=35, K-edge = 13.48 keV), with $K_{\alpha 1}$-fluorescence at 11.92 keV and $K_{\beta 1}$-fluorescence at 13.29 keV. A picture of the final double tube sample is shown in Figure 4.17 [62].

Figure 4.17: Glass double tube filled with Y_2O_3:Eu(III) nanoparticles in powder form (inside) and NaBr in water solution (outside) [62].

The combined XFCT and XLCT imaging study of the abovementioned double tube sample was conducted using the proposed XFCT/XLCT system. For this second study, the imaging geometry using a sheet planar beam of x-rays and a pinhole collimator (as described in Paragraph 3.3) was chosen this time, for both XFCT and XLCT, mainly because of the larger dimensions of the samples that implies a longer acquisition time and a greater number of scanned positions. The excitation with the planar x-ray beam reduces the scanning time by irradiating a larger volume. However, such improvements is counterbalanced by the lower sensitivity provided by the pinhole.

The polychromatic x-ray tube, at 50 kVp of tube voltage and 1 mA of tube current, provided the x-ray stimulation of the sample. Its cone beam was collimated with a tungsten single slit aperture, having a width equal to 200 μm, in order to create the thin sheet beam of x-rays required by the imaging geometry. For the detection of the x-ray luminescence signal, the EMMCD plus DM tube assembly of the system was used, while the x-ray CCD camera performed the detection of the x-ray fluorescence signal. Single tungsten pinholes of 300-μm were attached in front of both the CCD camera and the DM tube, as to collect and transmit the XL and XF projections of the photons emitted by the various material in the phantom. Finally, the CdTe spectroscope was used again to collect the XF energy spectra at different excitation positions, during the entire scanning of the sample. Pictures of the slit collimator for the x-ray cone beam and of the type of pinhole used in front of the two detectors are reported in Figure 4.18 [62].

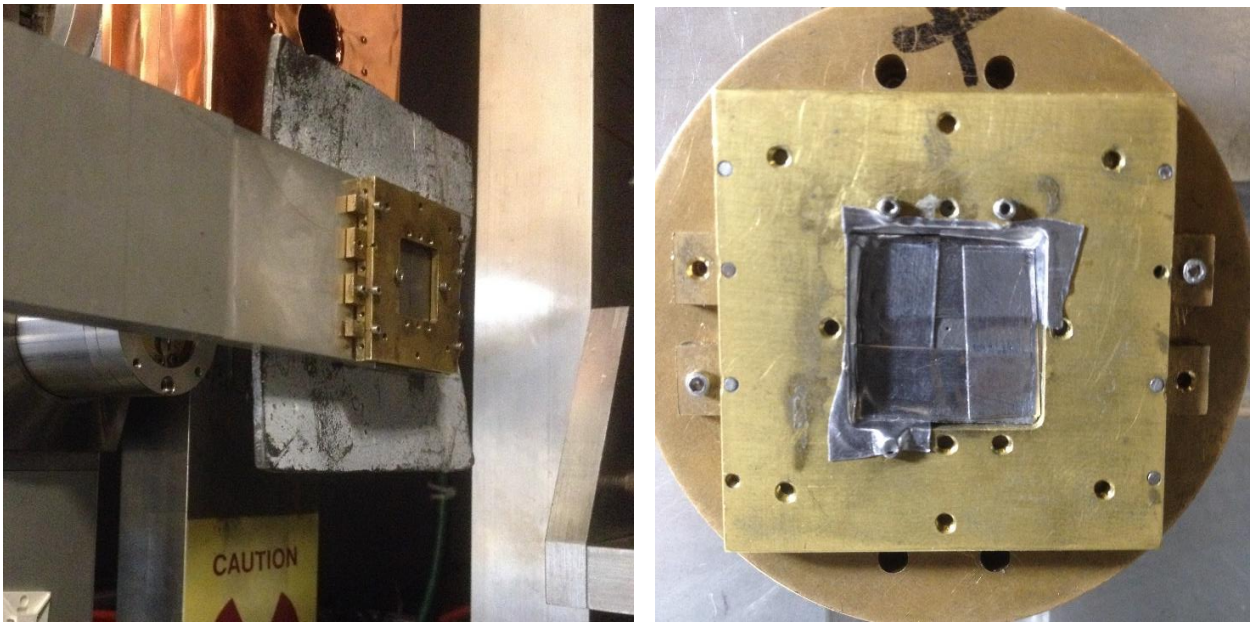

Figure 4.18: Pictures of the 200-μm single slit aperture used to collimate the x-ray cone beam into a plane (left) and of the 300-μm pinhole for the two detectors in the XCFT/XLCT study [62].

During the combined XFCT and XLCT imaging study, 27 total scanning positions of the x-ray sheet beam irradiating vertical slices of the double tube cylinder were acquired, composing the tomographic slices for the volumetric reconstruction. Each slice have a thickness equal to that of the plane beam (200 μm). Translational steps of 200 μm were applied to move from one position

to the successive, in order to cover the entire volume of the sample. For each position, 3600 frames were acquired with the CCD camera, at 2 seconds per frame, while for the EMCCD plus DM tube assembly, 7200 frames were acquired at 1 second per frame. The total imaging time was then equal to 2 hours per position. Such long acquisition time was required due to the bigger size pf the sample, compared to the previous imaging study, and because of the reduced sensitivity provided by the single pinholes collimators. Moreover, XF energy spectra were also collected with the CdTe spectroscope, per each position. All the frames per position were summed, for both the two detectors, to create the respective XF and XL slice projections. Such slices were combined together for the reconstruction of the 3D volumetric image of the entire double tube cylinder, using the methodology already described in Paragraph 3.3. Multiplexed imaging with x-ray fluorescence was also obtained by isolating the XF signal from each of the two target compounds in the sample, using the XF energy spectra collected with the CdTe spectroscope. The resulting images from both XF and XL signal were then superimposed to obtain multimodal multicolored 3D information.
The ultimate results and outcomes of this aforementioned combined XFCT and XLCT imaging study, using a double tube sample loaded with metal-based compounds, will also be presented and discussed in details in Chapter 5.

5. Results from the experimental studies with the XFCT/XLCT system

In this Chapter, the main and most important results of the experimental studies and investigations, which have been performed with the XCFT/XLCT system (the subject of this thesis work) and that has been described in their procedures and purposes in the previous paragraphs, will be shown and discussed in details.

First, the outcomes of the quantification study of the x-ray fluorescence and x-ray luminescence signal from theranostics nanoparticles will be presented, discussing how such signal varies with the different excitation strategies used. Then these results will be combined with those produced by the experimental evaluation and quantification of the excitation energy used for the abovementioned measurements, analyzing how it relates to the generated signal and its intensity. An efficiency and yield evaluation of the XF and XL signal for both the nanoparticles, LaF_3:Tb and Y_2O_3:Eu(III), will be proposed, based on the estimated excitation energy. Finally, a comparison both between the two different nanoparticles and between the respective XF an XL signal will be discussed, always in a perspective of their theranostic applicability. Conclusions about the best excitation strategies to perform therapy and imaging will be drawn from these data.

Afterwards, the results from the two imaging studies carried out with the XFCT/XLCT system designed and developed during this project will also be produced, as explained in Chapter 4. The outcomes of these studies will permit to assess the performances of the system, mostly in terms of spatial resolution, sensitivity and capability of multiplexed and multimodal imaging. Again, the potentials to use the system for theranostics applications, such those described in Paragraph 2.4, will be derived and evaluated from the data gained from the two imaging studies.

5.1 Quantification of XL and XF signal from x-ray stimulated nanoparticles

The quantification study described in Paragraph 4.1 was conducted using two nanoparticles, LaF_3:Tb and Y_2O_3:Eu(III), which are considered suitable for theranostics applications, such as x-ray induced and monitored XPDT, to be performed with the XFCT/XLCT system here proposed. Various excitation strategies were tested, in order to find the best way to stimulate the two theranostic agents. The emitted XF and XL signal from those different excitations were subsequently collected and then quantified from the corresponding detectors in the setup, following the procedure and the modalities explained in the previous Chapter, and considering the attenuated excitation energies involved.

The first major group of excitation strategies that has been investigated was represented by the

nine increasing tube voltages, from 10 to 50 kVp with 5 kVp incremental steps, at which the polychromatic x-ray tube was ran for the stimulation of the nanoparticles. Such tube voltages corresponds, for the energy spectra of the polychromatic source, to the maximum energies, in keV, of the x-ray photons of the excitation beam. Therefore, they can be compared also with the corresponding data from the excitation with the monochromatic x-ray source, which has an energy of 17.48 keV. In Figure 5.1, the resulting trends for the XL intensity rate (ADU/s) with the variation of source maximum energy are reported, for both the nanoparticles.

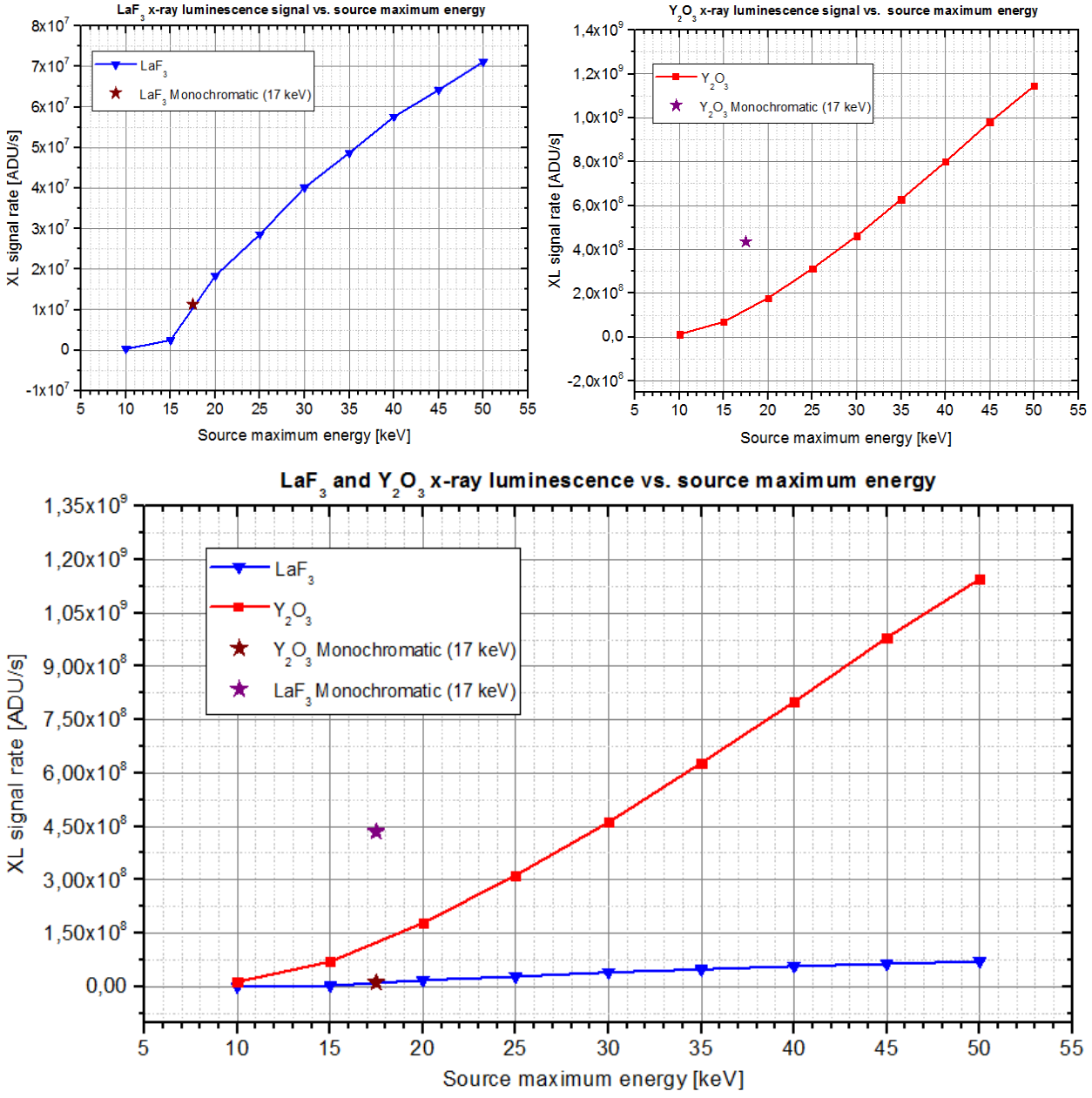

Figure 5.1: Variation of the XL signal rate with source maximum energy, for LaF_3 (top left) and Y_2O_3 (top right). A comparison on the same scale of the two curves is also reported (bottom).

First, it can be seen clearly from the graphs that the XL signal rate emitted by Y_2O_3:Eu(III) is at least one order of magnitude larger than that emitted by LaF_3:Tb, for the same maximum energy of the source. Moreover, the difference between the two rates becomes greater and greater as the

source maximum energy increases. In general, both the two curves show an approximately quadratic growth of the XL signal with the source maximum energy, although with different slopes and different curve concavity. Such trend may be expected, as the photon flux become higher with the rise of the source tube voltage, which in turn is directly correlated to the maximum source energy shown in the plots. For the LaF_3:Tb nanoparticles, an asymptotic behavior may be reached for higher energies, but such hypothesis cannot be confirmed due to the lack of data for energies above 50 keV. Regarding the data points for the monochromatic excitation, it is evident that, while the XL signal stimulated by the monoenergetic beam at 17.48 keV and emitted by LaF_3:Tb follows the tendency of the other data points, for Y_2O_3:Eu(III) a sharp increase in the luminescence signal is present. This may be because of the enhanced photoelectric absorption in correspondence of the K-edge of Yttrium (17.03 KeV).

The same types of plots are reported, in Figure 5.2, also for the XF intensity rates (in counts/s).

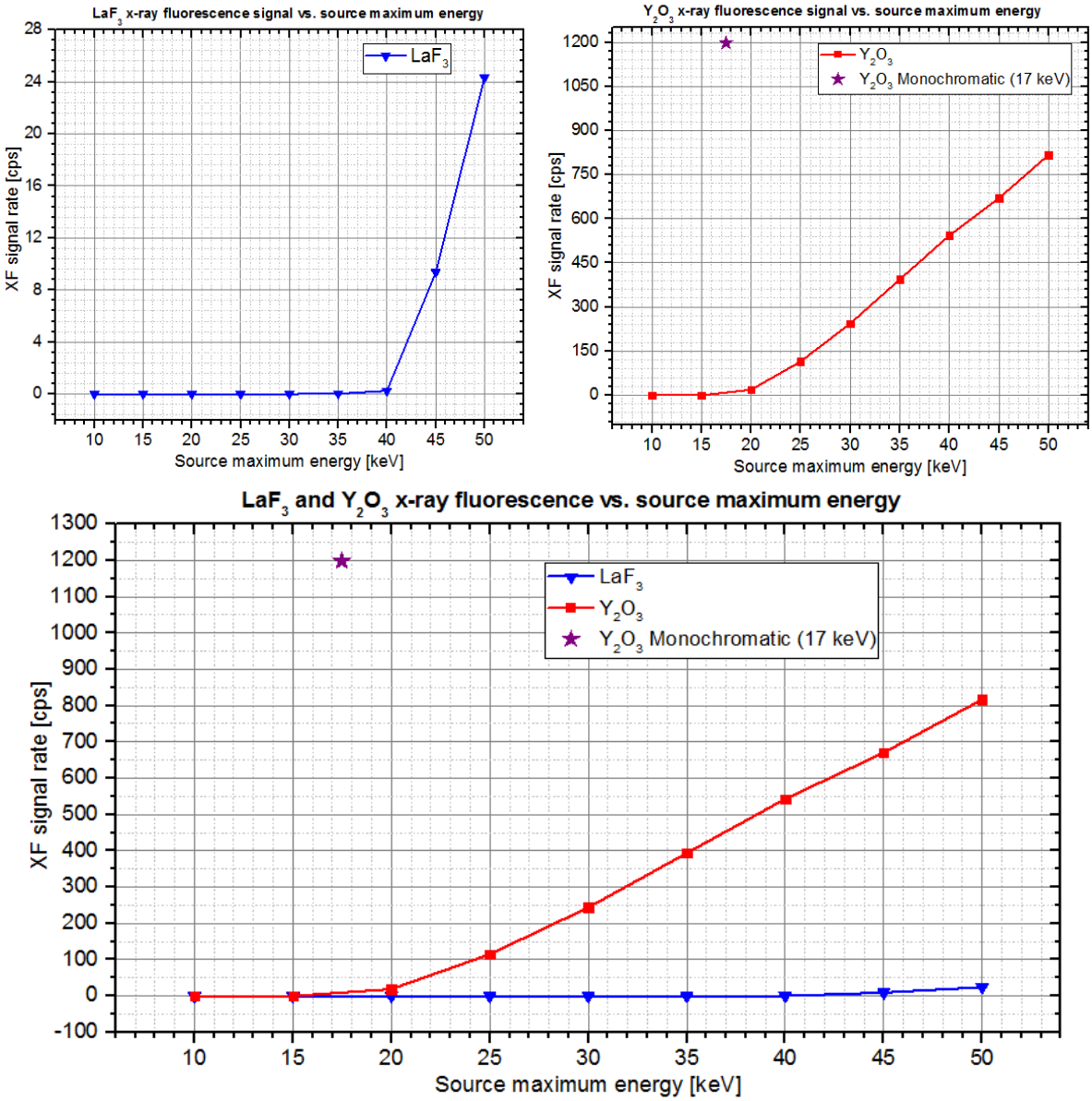

Figure 5.2: Variation of the XF signal rate with source maximum energy, for LaF_3 (top left) and Y_2O_3 (top right). A comparison on the same scale of the two curves is also reported (bottom).

The curves in the previous figure visibly show the onsets of the x-ray fluorescence for both the two nanoparticles, approximately in correspondence of their respective K-edges, as expected. Before such energies, the X signal is totally negligible, because no photon in the polyenergetic beam form the x-ray tube has an energy above the maximum energy of the source (which is below the K-edges in these circumstances). Furthermore, also in the case of x-ray fluorescence, the XF intensity rates of both the two nanoparticles increase almost quadratically with the maximum energy of the polychromatic source and the XF signal of Y_2O_3:Eu(III) is much higher than that of LaF_3:Tb, almost by two orders of magnitude, as the maximum energy grows. Again, this may be due to the increase in the gross photon flux (which is also usually quadratic with source tube voltage), and thus in the overall photoelectric absorptions by the nanoparticles, beyond their respective K-edges.

For what concerns the excitation with the monochromatic source, it must be noted that no data are shown for the x-ray stimulation of LaF_3:Tb with the monoenergetic beam at 17.48 keV. This is obviously because the energy of such beam is far lower than the K-edge of lanthanum (38.92 keV), thus no K-fluorescence signal is produced. In fact, it must be remembered, as said in the previous chapter, that the L-edge fluorescence from LaF_3:Tb has not been considered because of its overlapping in the XF energy spectra with the characteristic x-rays peaks from tungsten in the source anode). On the other hand, the data point from the excitation of Y_2O_3:Eu(III) with the monochromatic beam displays a very high XF signal emitted by yttrium under such stimulation, as expectable due to the tuning of the monoenergetic beam with the K-edge of such element (17.03 keV). The XF signal rate produced by Y_2O_3:Eu(III) with the monochromatic excitation is about three thousand times greater than the corresponding on at the same energy using the polychromatic source, and even higher than the XF signal with maximum energy equal to 50 keV. An explanation to such event can be derived considering: (1) that the monochromatic source has a higher x-ray photon flux than the polychromatic one, at equal maximum source energy; (2) that for the monochromatic source, all the photons have an energy equal to about the maximum energy of the beam (with a small standard deviation), while only a small fraction of photons in the polychromatic beam of the x-ray tube have the same energy of the maximum of the energy spectrum, due to its shape.

Instead of using the maximum values of the energies of the x-ray excitation beams, a better evaluation and comparison of the XL and XF signal of the two nanoparticles can be done by considering the average attenuated energy of the primary x-ray photons, as it has been calculated in Paragraph 4.2. While there is no difference for the monochromatic source between these two energies, for the polychromatic beam of the x-ray tube, the average attenuated energy take into account the net attenuated flux of stimulating x-ray photons, per keV, and thus is more

representative of the effective excitation energy that generated the XF and XL signal. Moreover, using the average attenuated energy, the results from the quantification of the XF and XL signal produced with the filtered polychromatic source (the third major group of tested excitation strategies) can also be taken into account and compared with the others. Hence, in Figure 5.3, the resulting trends for the XL intensity rates with the variation of the average attenuated energy are depicted in plots, for both the two nanoparticles and for each different excitation strategy.

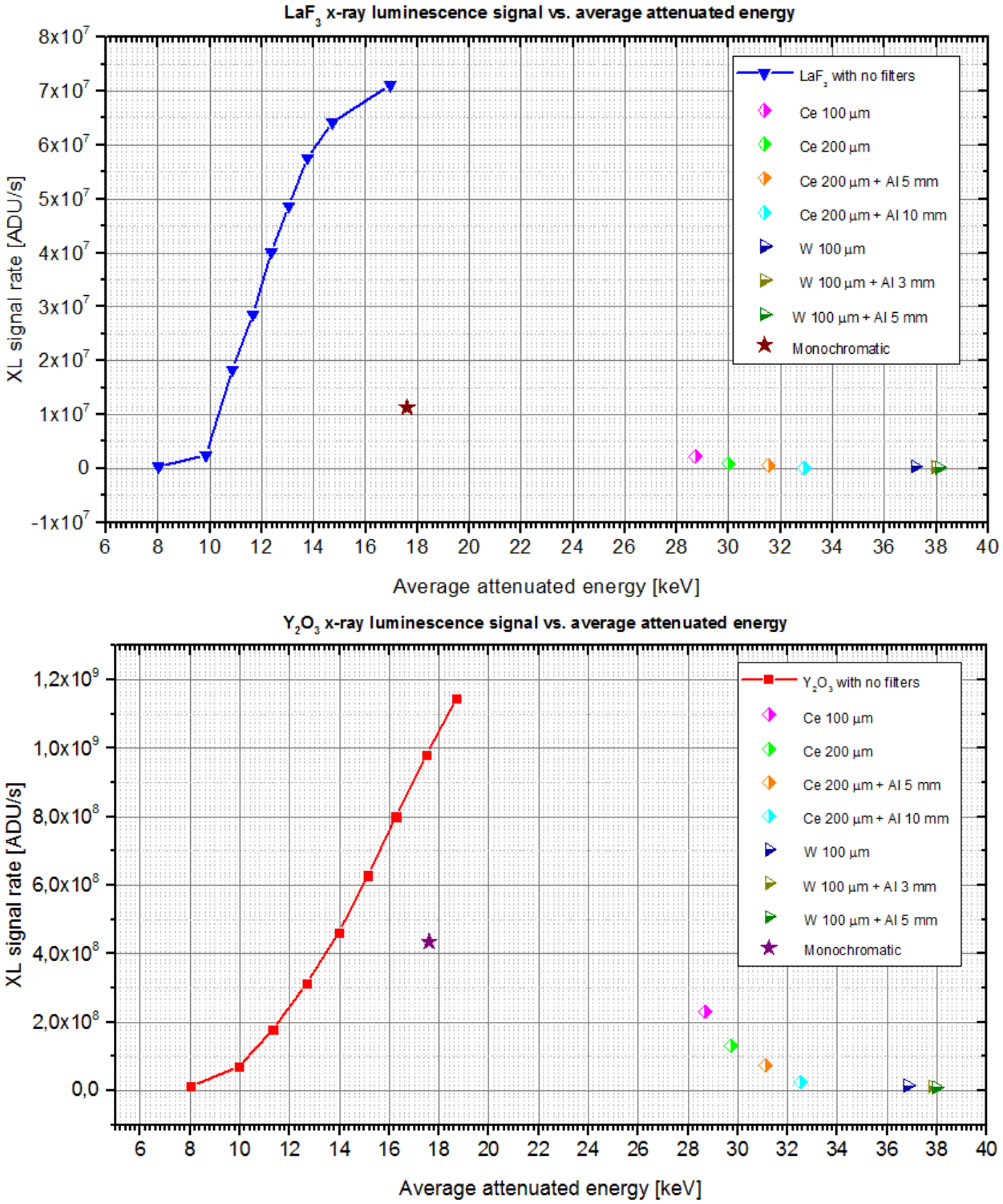

Figure 5.3: Variation of the XL signal rate with average attenuated energy, for LaF_3 (top) and Y_2O_3 (top bottom) and for all the excitation strategies that have been measured.

From the previous plots, it can be first noticed that XL signal rates for the different excitations with the unfiltered polychromatic beam have still increasing trends also with the average attenuated energy. The maximum men attenuated energy calculated in these cases results equal to about 17 keV for LaF_3:Tb and around 19 keV for Y_2O_3:Eu(III), both in correspondence of the maximum tube voltage of 50 kVp. This demonstrates that the yttrium-based nanoparticles attenuates higher energy values of the primary x-ray photons. Moreover, it is evident that the XL signal rates produced by both the nanoparticles with the filtered excitation beam are generally lower than those regarding the unfiltered excitations, although the average attenuated energies are higher, ranging between 28 and 38 keV, according to the filtering. In particular, it can inferred from the graphs that, for both the two nanoparticles, the filtered data shows a decreasing tendency of the XL signal rates with the average attenuated energy, as the degree of filtering increases. A reason for that, as mentioned previously, may be the decreasing x-ray photon flux produced by the filtering, which eliminates more and more photons per each layer of filters added. However, such assumption seems not to agree with the monoenergetic excitation data points, which, as the plots show, present a lower XL signal rate, even if the total x-ray photon flux produced by the monochromatic source is generally higher than that form the polychromatic x-ray tube. From such results, it is possible to start to assume that for x-ray luminescence, the tuning of the excitation energy with the K-edge may not be fundamental in the physical emission process. The same types of plots are also reported for the XF signal rates, in Figure 5.4 and 5.5 for LaF_3:Tb and Y_2O_3:Eu(III), respectively.

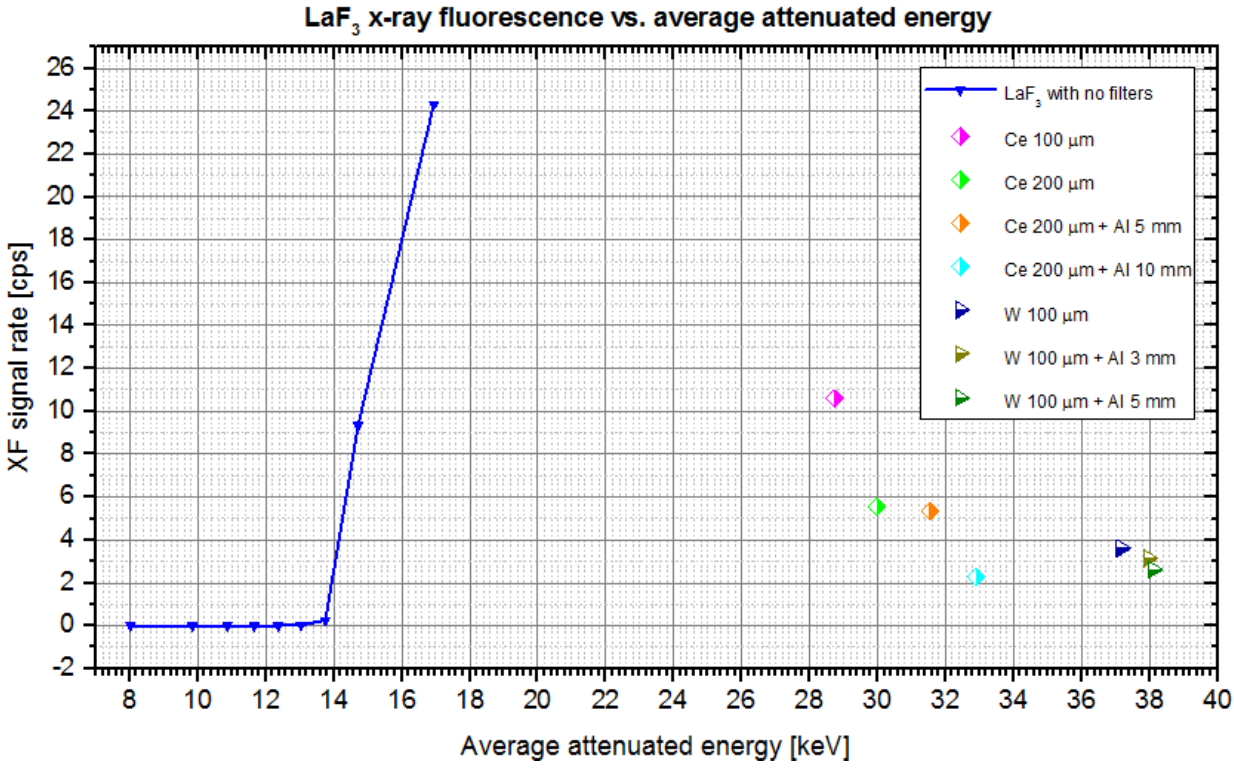

Figure 5.4: Variation of the XF signal rate with average attenuated energy, for LaF_3 and for all the excitation strategies that have been measured.

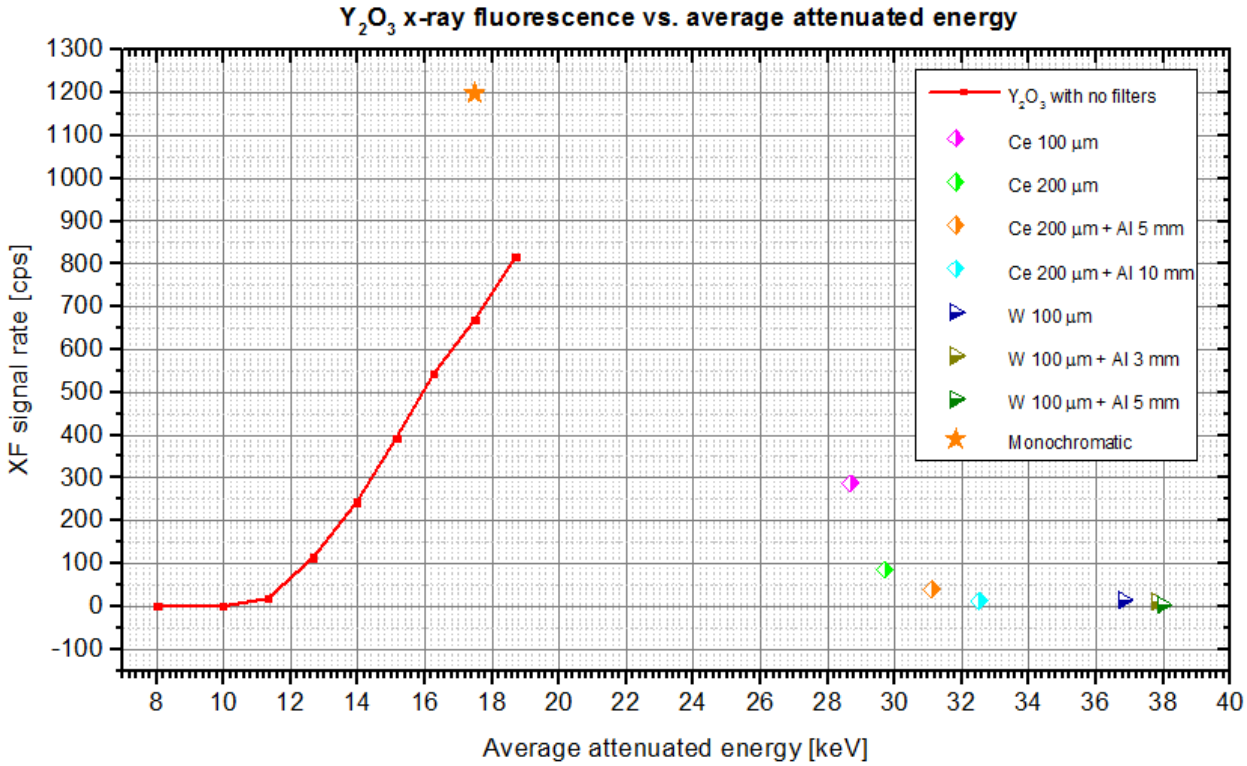

Figure 5.5: Variation of the XF signal rate with average attenuated energy, for Y_2O_3 and for all the excitation strategies that have been measured.

For the x-ray fluorescence data, the same decreasing trends of the XF signal rates with the average attenuated energy can be found, for both the two nanoparticles, regarding the excitation with the different filters before the primary beam. Such tendency seems to be almost quadratic, especially for the Y_2O_3:Eu(III) data. The same consideration about the decreasing x-ray photon flux as a possible cause for such tendencies may be proposed in this case, as well. Furthermore, for the fluorescence data, the XF signal rate produced by the monoenergetic excitation strategy is in agreement with such assumption, being far higher that the corresponding signal with all the stimulations using the polychromatic x-ray tube. Again, it can be assumed that the K-edge tuning of the excitation energy of the primary beam may have fundamental importance in the production of x-ray fluorescence, but not the same influence for x-ray luminescence. Such aspect will be elaborated and examine in depth in the next paragraph. Finally, it must be reported that no monoenergetic excitation data has been considered for LaF_3:Tb, as explained before. Furthermore, it can be seen, also in the case of x-ray fluorescence, that the XF signal for the filtered data is not as high as the signal produced with the other excitation configurations. For XF, this may be related not only to the decrease in the primary photon flux, but also to the fact that photoelectric absorption is disadvantaged for the filtered excitations, due to two different reasons, according to the considered nanoparticle. For Y_2O_3:Eu(III), it may be because at higher and higher energies above the K-edge, the photoelectric cross section of yttrium decreases exponentially. On the other hand, for LaF_3:Tb, it may be due to the fact that the average energy attenuated by each one of the filters

is always lower than the K-edge of lanthanum, thus photoelectric absorption is not favored in such excitation configurations.

At this point, the rates of attenuated energy (in keV/s) calculated during the experiments, as described in Paragraph 2.2, can be considered and combined with the quantified XL and XF signal rate data. Therefore, the plots of the variations of the XL intensity rates with the corresponding attenuated energy rates are shown, in Figure 5.6 for LaF_3:Tb and in Figure 5.7 for Y_2O_3:Eu(III).

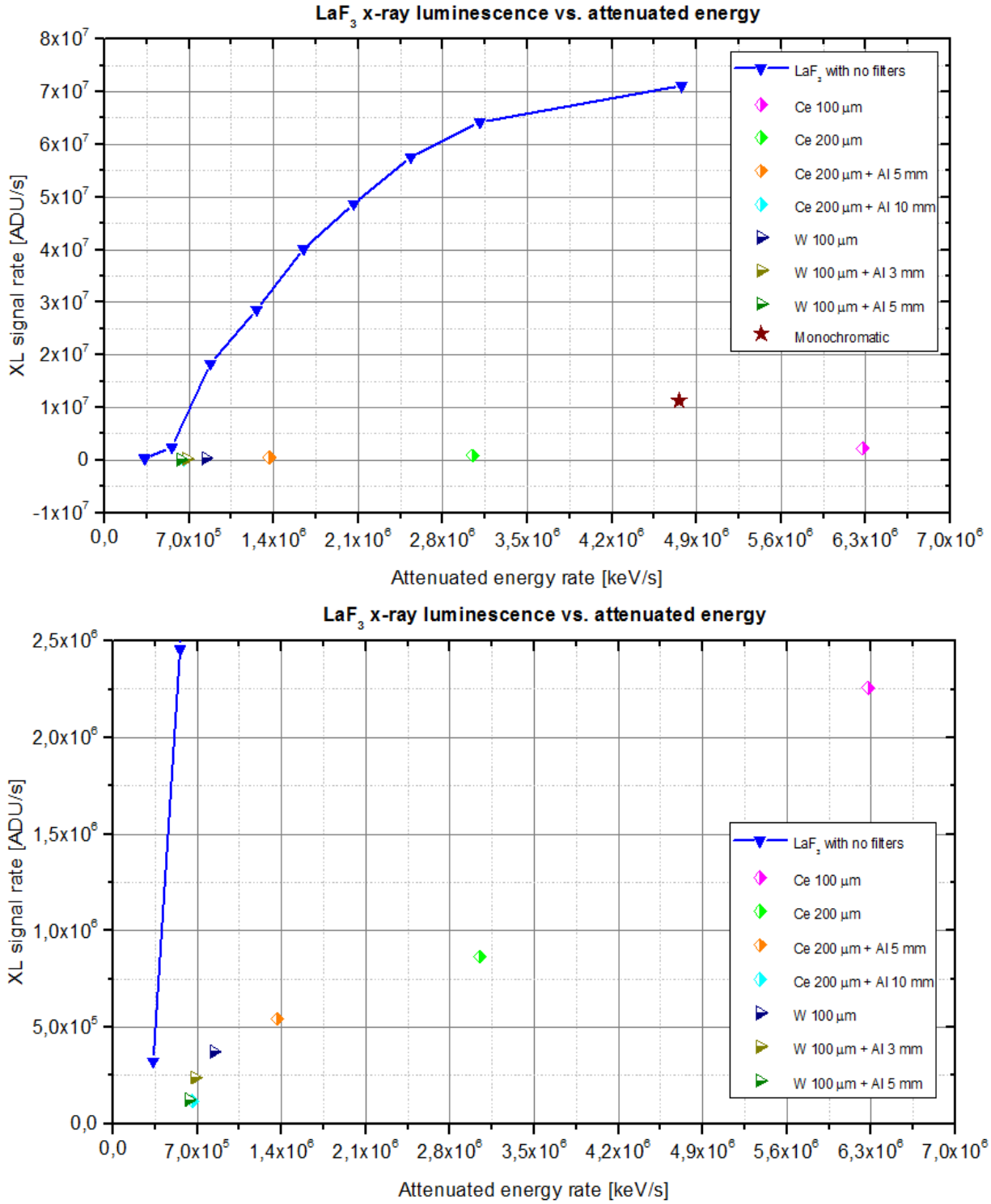

Figure 5.6: Variation of the XL signal rate with attenuated energy rate, for LaF_3 (top) and for all the excitation strategies that have been measured. The plot is also enlarged to highlight the filtered data (bottom).

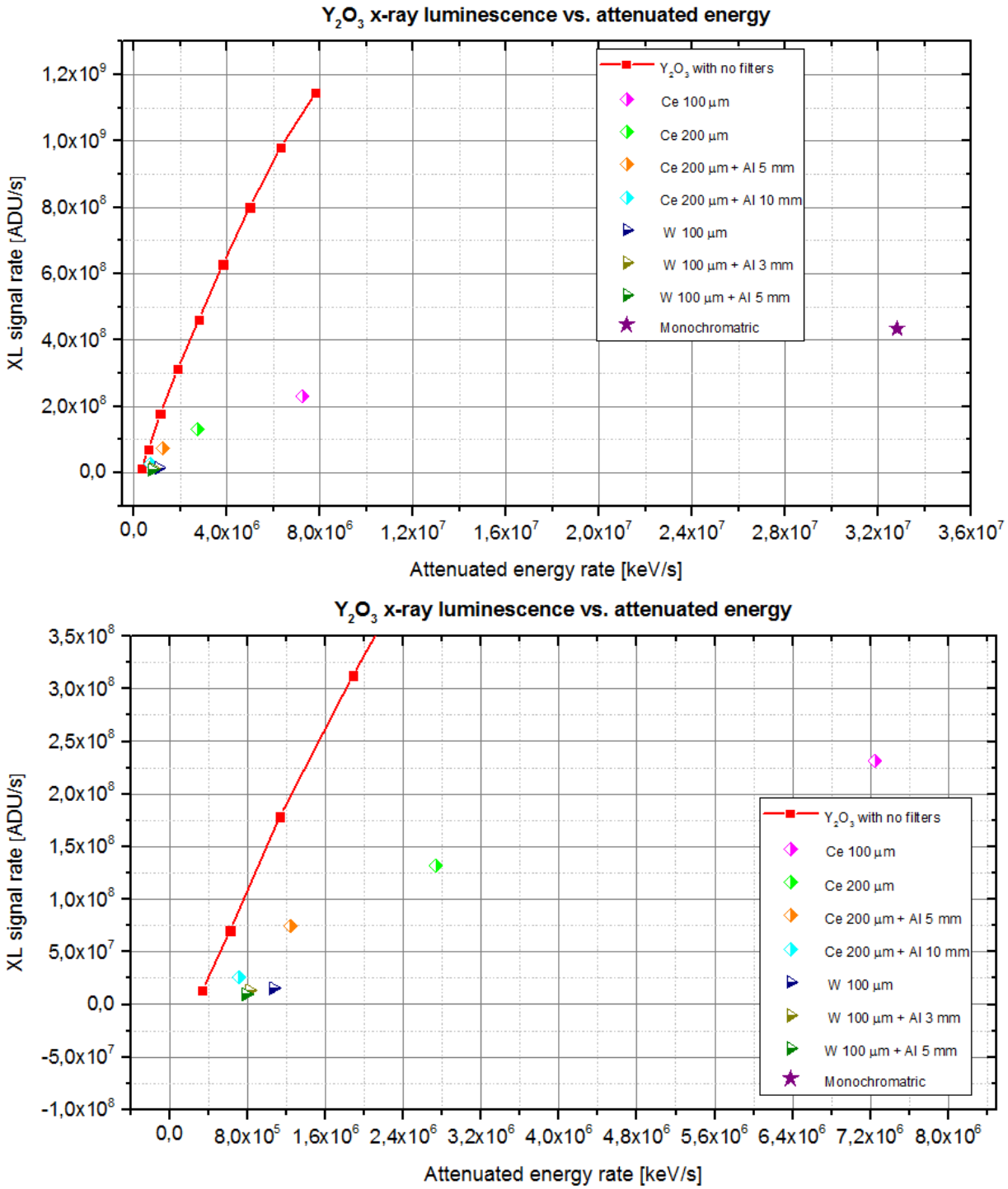

Figure 5.7: Variation of the XL signal rate with attenuated energy rate, for Y_2O_3 (top) and for all the excitation strategies that have been measured. The plot is also enlarged to highlight the filtered data (bottom).

The first thing to appear clearly from the graphs is that the attenuated energy rates of all the excitation strategies, for both the two nanoparticles, are not always comparable and do not lie on the same ranges of keV/s. For example, the monochromatic data point for Y_2O_3:Eu(III) is at least one order of magnitude higher than the rest of the data. This is due to the enhanced energy absorption per unit time of yttrium at 17.48 keV, which is just above its K-edge. Furthermore, for both the two nanoparticles, the XL signal rates associated with the data with the tungsten filters are those showing the lowest attenuated energy rates. An explanation to this can be given by

looking back at the average attenuated energies shown in Figure 5.3, Figure 5.4 and Figure 5.5. In fact, the tungsten filter data are associated with the highest average attenuated energy, thus the x-ray absorption cross section of both the nanoparticles for highest energies are generally smaller than those for lower energies. Finally, it can be seen that, when the attenuated energy rates are considered, the trends of the XL signal with the unfiltered polyenergetic excitation are quadratic, but seems to tend towards asymptotic values towards the highest attenuated energy rates. This is valid for both the two nanoparticles.

The same kind of graphs are also shown for the XF signal rates, in Figure 5.8.

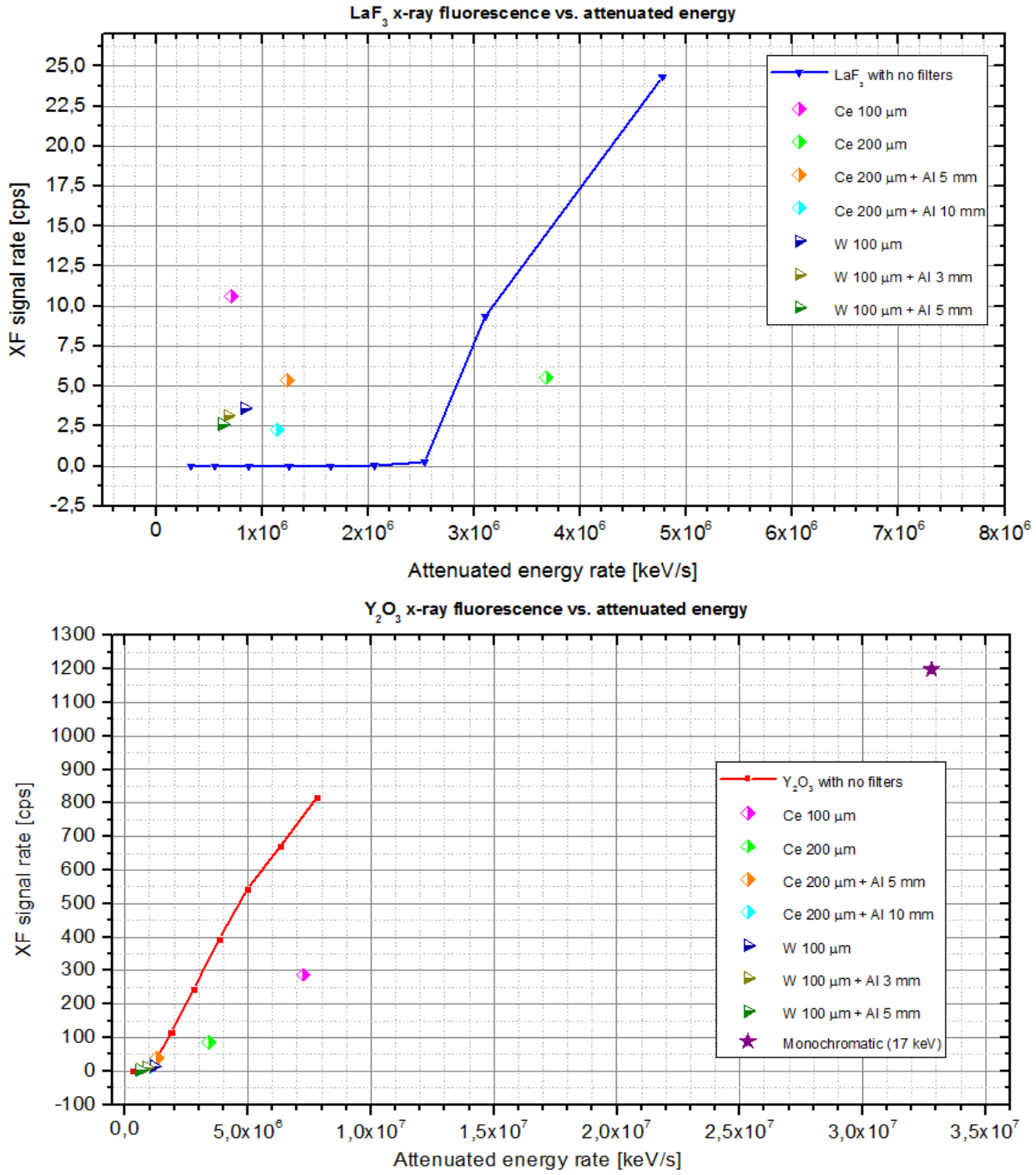

Figure 5.8: Variation of the XF signal rate with attenuated energy rate, for LaF_3 (top) and Y_2O_3 (bottom) and for all the excitation strategies that have been measured.

Again, the onset of the x-ray fluorescence is present, for the polyenergetic excitation data at different tube voltages, and it can be correlated to the corresponding attenuated energy rate, for each of the nanoparticles. Furthermore, it can be clearly seen that the monochromatic excitation for Y_2O_3:Eu(III) provides the highest XF signal rate, but also has by far the largest attenuated energy rate, meaning that the process may not be so efficient in term of XF yield per unit energy. Such aspect will be discussed an analyzed in details in the next paragraph. Moreover, for LaF_3:Tb, the excitation with the filtered polyenergetic beam seems to produce a higher XF signal at the same rate of attenuated energy, while it is not the case for Y_2O_3:Eu(III). This may be because, at the considered attenuated energy rates, the unfiltered polyenergetic beam has always a maximum energy of its photons below the onset of fluorescence due to K-edge. On the other hand, the filtered stimulation, although having a mean attenuated energy always below the K-edge of lanthanum (39.82 keV), has a maximum energy of the primary photons (50 keV) above the k-edge, because the source is ran at 50 kVp of tube voltage. Hence, a fraction of photons from the unfiltered excitation beams, yet small, has energies above the K-edge of lanthanum, producing a non-negligible XF signal, as it can be seen in the figures. In the case of Y_2O_3:Eu(III), the filtered excitation data are usually in the same increasing quadratic trend of the unfiltered data and for the lowest energies, they account for about the same XF signal rates, especially for all the tungsten and the cerium plus aluminum filter data . However, as the attenuated energy rates increasing, the unfiltered polyenergetic excitation produces a higher XF signal than the unfiltered one, thus having a steeper increasing tendency. This can be seen in a better way by looking at the same plot, enlarged in the region of the filtered data, as in Figure 5.9.

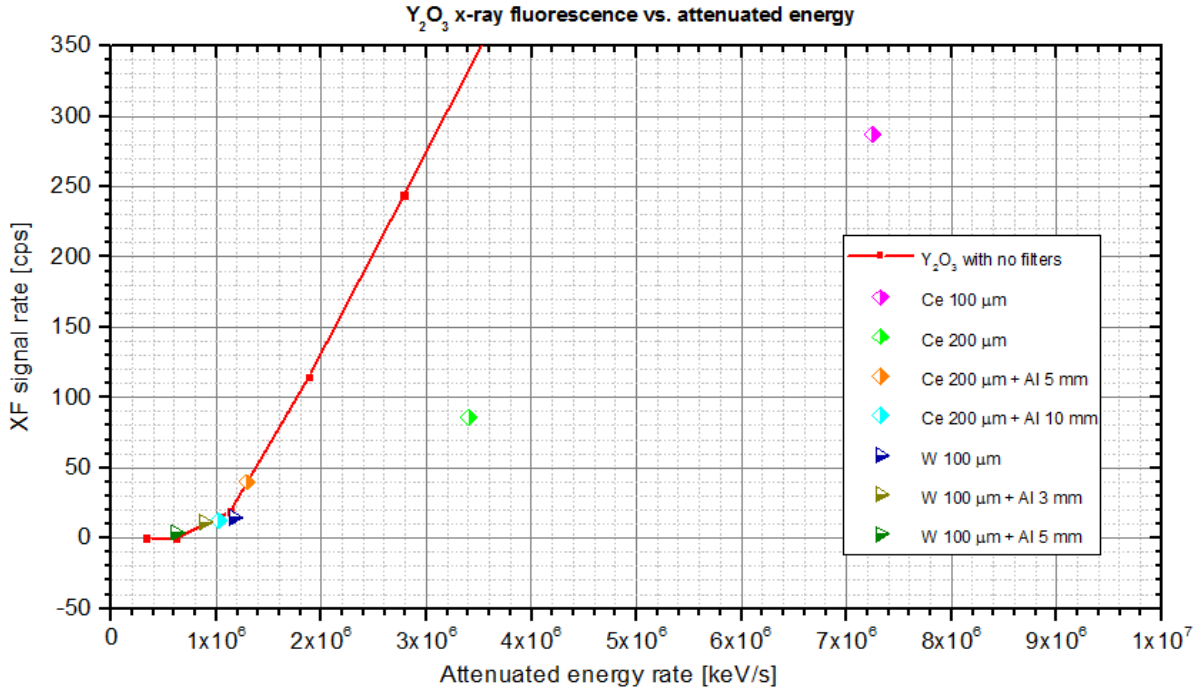

Figure 5.9: Enlarged plot of the variation of the XF signal rate with attenuated energy rate, for Y_2O_3 and for all the excitation strategies, as to highlight the filtered data.

As to briefly summarize the main conclusions and outcomes derived from the results of the quantify-cation of the XF and XL signal just described, it can be stated that:

1) Both the x-ray fluorescence and the x-ray luminescence intensity rates produced by Y_2O_3:Eu(III) are generally even order of magnitude higher than those emitted by LaF_3:Tb, for all the excitation configurations. Such comparison will be extended in Paragraph 5.3;
2) The XL signal seems no to strictly depend on the K-edge energy tuning of the primary excitation beam, while it is clearly a major factor for the XF signal, although the mono-energetic excitation may not be energetically efficient. Also this point will be analyzed further and deeper, in the next Paragraph;
3) The filtered polychromatic excitation mainly produces a lower signal rate for both XF and XL and for all the nanoparticles, except for the case of LaF_3:Tb below the K-edge, where it is the only predominant XF signal, yet lower than for the other excitation strategies when considered above that energy value.

5.2 Best excitation strategies and XF-XL signal yields for x-ray stimulated nanoparticles

In the analysis of the quantified XF and XL signal from LaF_3:Tb and Y_2O_3:Eu(III) nanoparticles presented in the previous paragraph, a preliminary evaluation of the different tested excitation strategies has been proposed. This was done by taking into account the net XF and XL signal rate production in the different configurations, according to either the average attenuated energy or the attenuated energy rates. However, a better assessment of which type of excitation is the most suited and advantageous for producing x-ray fluorescence and x-ray luminescence for imaging and theranostics applications (such as XPDT) van be performed by considering an estimate of the amount of both XF and XL signal per unit of attenuated energy. Such estimates will give an understanding of the XL and XF signal yields, in ADU/keV and counts/keV respectively, representing the efficiency of a given excitation strategy to produce x-ray fluorescence and/or x-ray luminescence according to the energy necessary to generate it. Such evaluation is fundamental because it can provide a general index of the XF and XL signal produced per unit dose related to each from of stimulation. These would be the best factor to be used to compare such different excitation strategies in a perspective of medical applications, especially molecular imaging and theranostics, where dose efficient modalities are strongly required. It will also help to understand how to improve both the XF and XL signal emission during imaging and the treatment delivery during therapy, for the current XFCT/XLCT system. This will also provide information about how to furtherly develop such system, according to such results.

Therefore, an estimate of the just proposed the XL and XF signal yields per unit energy can be calcula-ted by simply dividing the XF and XL signal rates for the corresponding attenuated energy

rates, in each excitation configuration and for both the two nanoparticles. Thus:

$$\text{Signal energy yield [intensity/keV]} = \frac{\text{Signal intensity rate [Intensity/s]}}{\text{Attenuated energy rate [keV/s]}}$$

From that, the variation of such energy-normalized signal, for the case of x-ray luminescence, with the rates of attenuated energy is reported in Figure 5.10, for LaF_3:Tb.

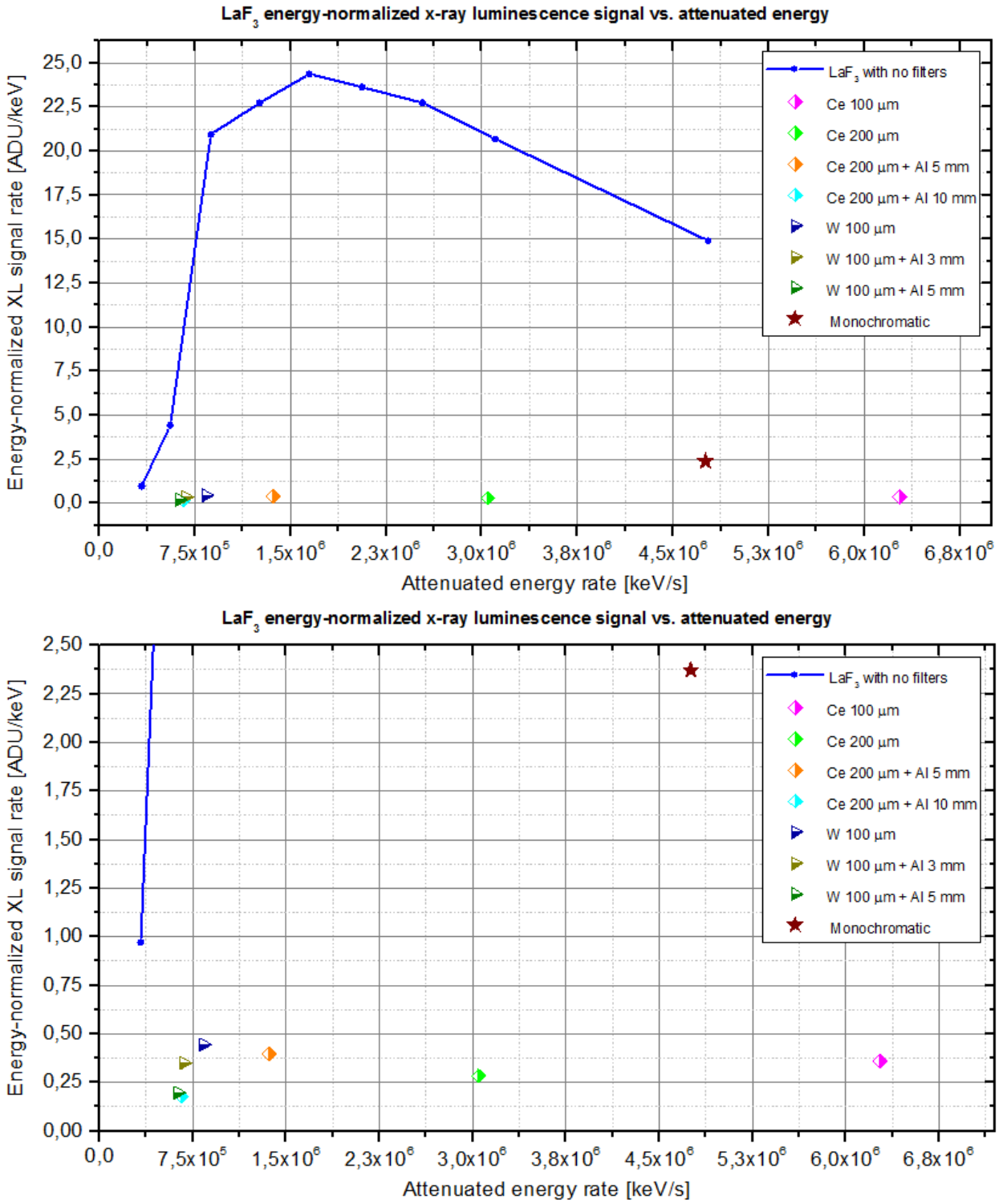

Figure 5.10: Variation of the energy-normalized XL signal rate with attenuated energy rate, for LaF_3 (top) and for all the excitation strategies that have been measured. The plot is also enlarged to highlight the filtered data (bottom).

The same kind of results are also shown for and Y_2O_3:Eu(III), in figure 5.11.

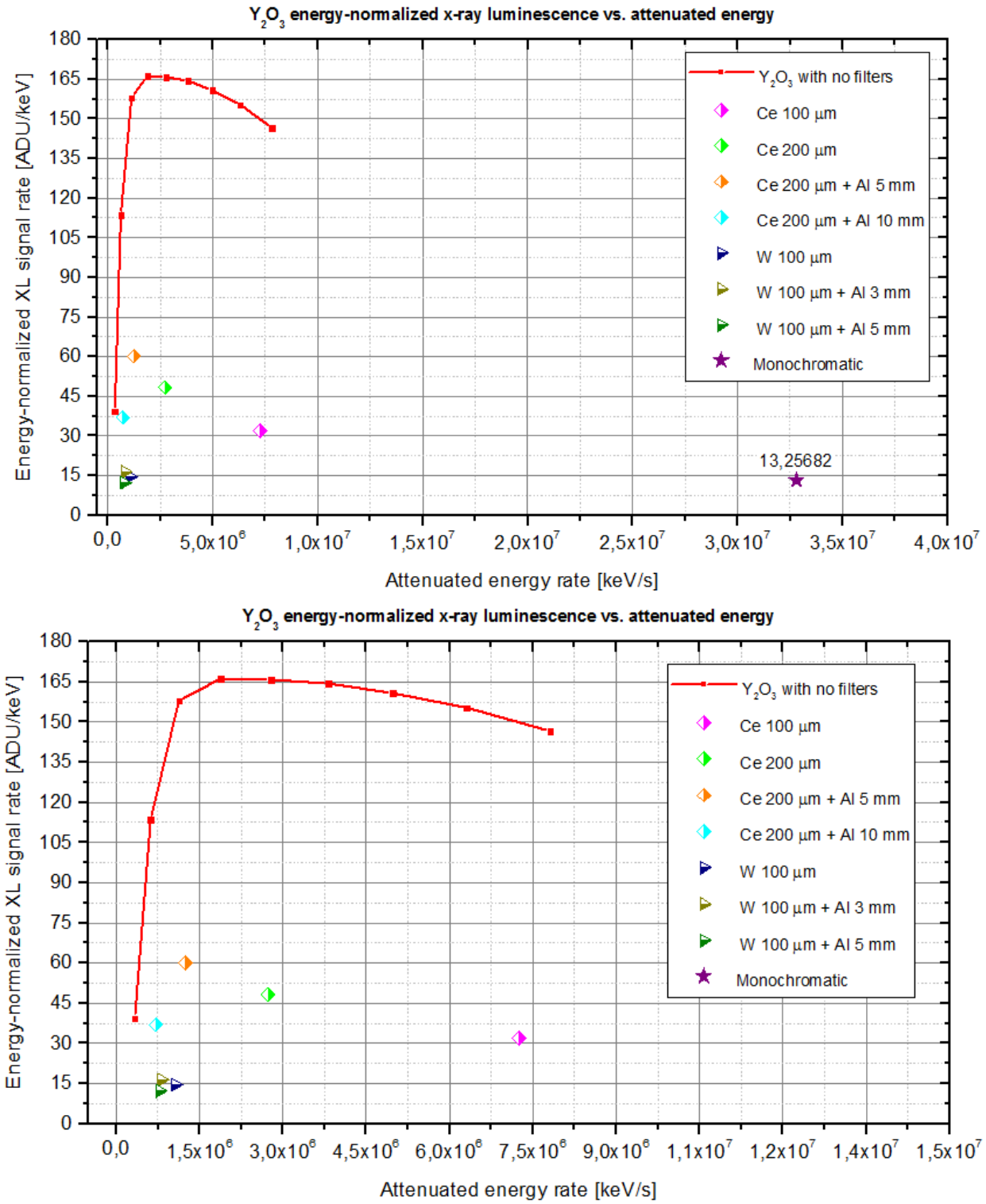

Figure 5.11: Variation of the energy-normalized XL signal rate with attenuated energy rate, for Y_2O_3 (top) and for all the excitation strategies that have been measured. The plot is also enlarged to highlight the filtered data (bottom).

The first and most interesting result that emerges from the two previous figures is the presence of local maximum points in the curves for the energy-normalized XL signal, for both the nanoparticles. Such maximum peaks are visible in the polyenergetic excitation plots, ranging between $1.5x10^6$ and $2x10^6$ keV/s for both LaF_3:Tb and Y_2O_3:Eu(III), but also in the filtered data.

In fact, both the excitation strategy using filters with cerium and that using tungsten filters have this type of local maxima, although in a slightly lower range of the attenuated energy rates (around $1x10^6$ keV/s). The very similar results for the maxima and the values of the attenuated energy rates shared by the two different nanoparticles are greatly interesting, introducing the possible existence of an optimal rate of attenuated energy that is required to produce XL signal in the most energy-efficient way, thus to maximize the signal yield. It is also important to notice that for both the nanoparticles, the estimated XL signal yield given by the monoenergetic excitation is consistently lower than that produced by the poly-energetic excitation. In fact, it is quite comparable with the XL signal yield from the filtered data, and in the case of Y_2O_3:Eu(III) has surprisingly almost the lowest yield value among all the data points. Therefore, it can be assumed that the monochromatic source is possibly inefficient to produce XL signal compared to the energy attenuated by the nanoparticles. In particular, for LaF_3:Tb, the monoenergetic excitation deliver almost the same rate of attenuated energy as the unfiltered polyenergetic stimulation at 50 kVp, although producing as much as a sixth of XL signal yield. This may be dependent on the composition of the excitation beam in the two different configuration, with the polyenergetic one, having photons with various and diverse energies in a large range, being the more suitable for an efficient XL signal generation. Even in this case, by analyzing the monochromatic data for Y_2O_3:Eu(III), it seems that the K-edge tuning is not playing a pivotal role in the energy-efficient production of x-ray luminescence.

Same sets of curves can be plotted also for the XF signal yield, as shown in Figure 5.12, for LaF_3:Tb.

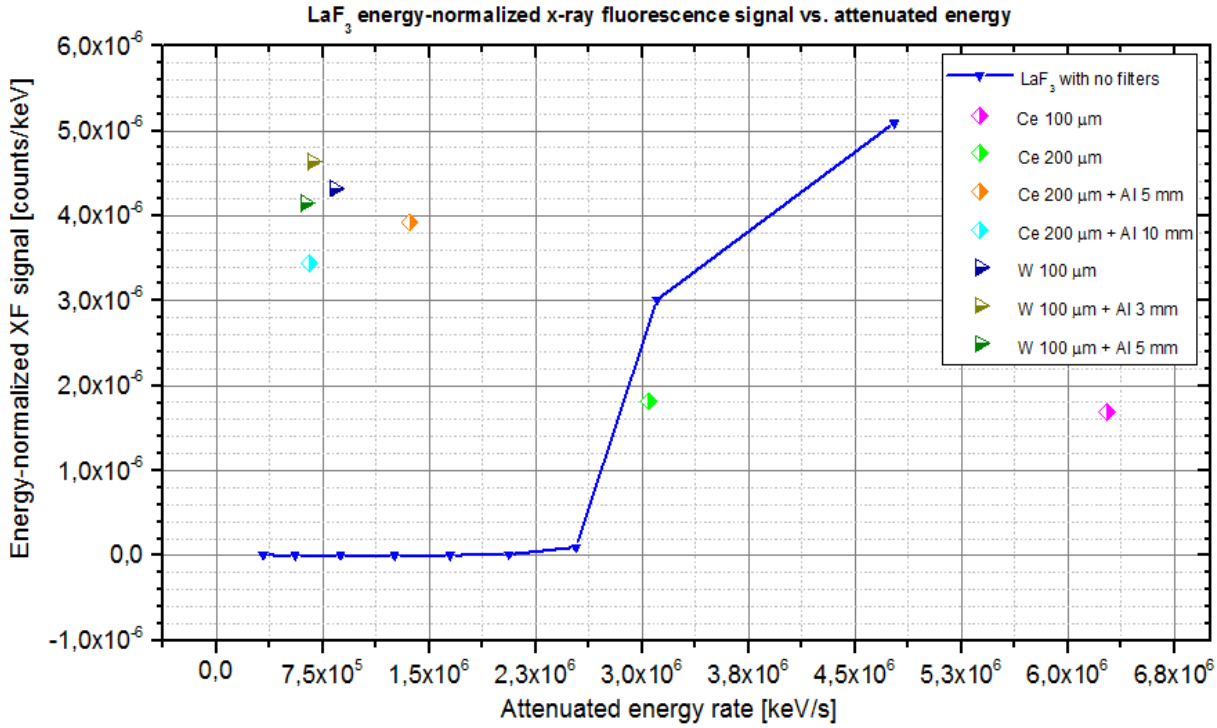

Figure 5.12: Variation of the energy-normalized XF signal rate with attenuated energy rate, for LaF_3 and for all the excitation strategies that have been measured.

Likewise, the curves and data points of the energy normalized XF signal with the attenuated energy rate are depicted also for Y_2O_3:Eu(III), in Figure 5.13.

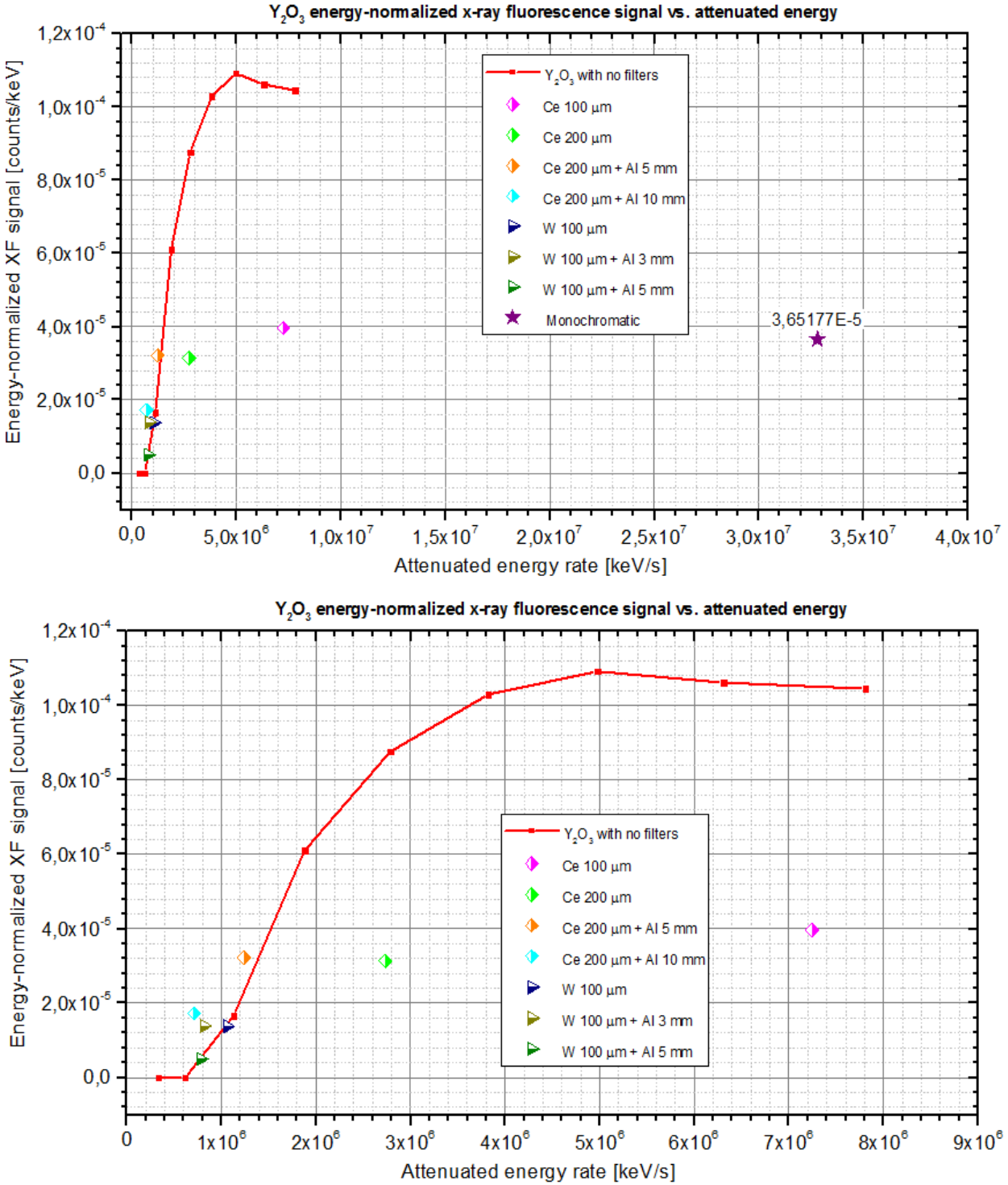

Figure 5.13: Variation of the energy-normalized XF signal rate with attenuated energy rate, for Y_2O_3 (top) and for all the excitation strategies that have been measured. The plot is also enlarged to highlight the filtered data (bottom).

For both the two nanoparticles, the curves of the data for the unfiltered polyenergetic excitation pre-sent again the well-established onset of x-ray fluorescence at the K-edge and seem to have a quadratic increase above such value, as the attenuated energy rate increases. However, the XF signal yield curve for Y_2O_3:Eu(III) shows, as for XL, a local maximum peak at around $5x10^6$

keV/s. Such result is again interesting because it suggest the presence of an optimum value of energy also for the most efficient stimulation of the XF signal, as it has been assumed for the XL signal. This aspect is also hinted by looking at the filtered excitation data for both the two nanoparticles, especially for LaF_3:Tb. In particular, it must be noted that, for such type of nanoparticle, the highest XF signal yield at the lowest attenuated energy rate is provided by the excitation with the tungsten filter, with a local maximum corresponding to the stimulation with the polychromatic beam filtered with 100-µm thick tungsten plus 3 mm of aluminum. Moreover, after the value of the attenuated energy rate corresponding to the onset of K-edge fluorescence in LaF_3:Tb, it seems that the unfiltered polyenergetic data become the ones with the highest XF signal yield. Such event does not happen in the case of Y_2O_3:Eu(III), where the XF signal yield from the unfiltered stimulation is always the highest. This result appears unusual and further investigations may be necessary. Finally, it can be seen that unexpectedly the monoenergetic excitation of Y_2O_3:Eu(III) at 17.48 keV, although tuned to the K-edge of yttrium, is not as efficient as the polyenergetic excitation, because of the large rate of attenuated energy triggered by the monochromatic source. Even this aspect was not predicted, though it can be inferred from the graphs that the monoenergetic excitation data point may be following the general trend of the polyenergetic curve, which decreases beyond the local maximum as the attenuated energy rate increases. A better understanding of all these aspects may be given by the analysis of the variation of the XF and XL signal yields with the calculated average attenuated energy (as seen in Paragraph 4.2). Such results for the XL signal and first for the Y_2O_3:Eu(III) nanoparticles are illustrated in Figure 5.14.

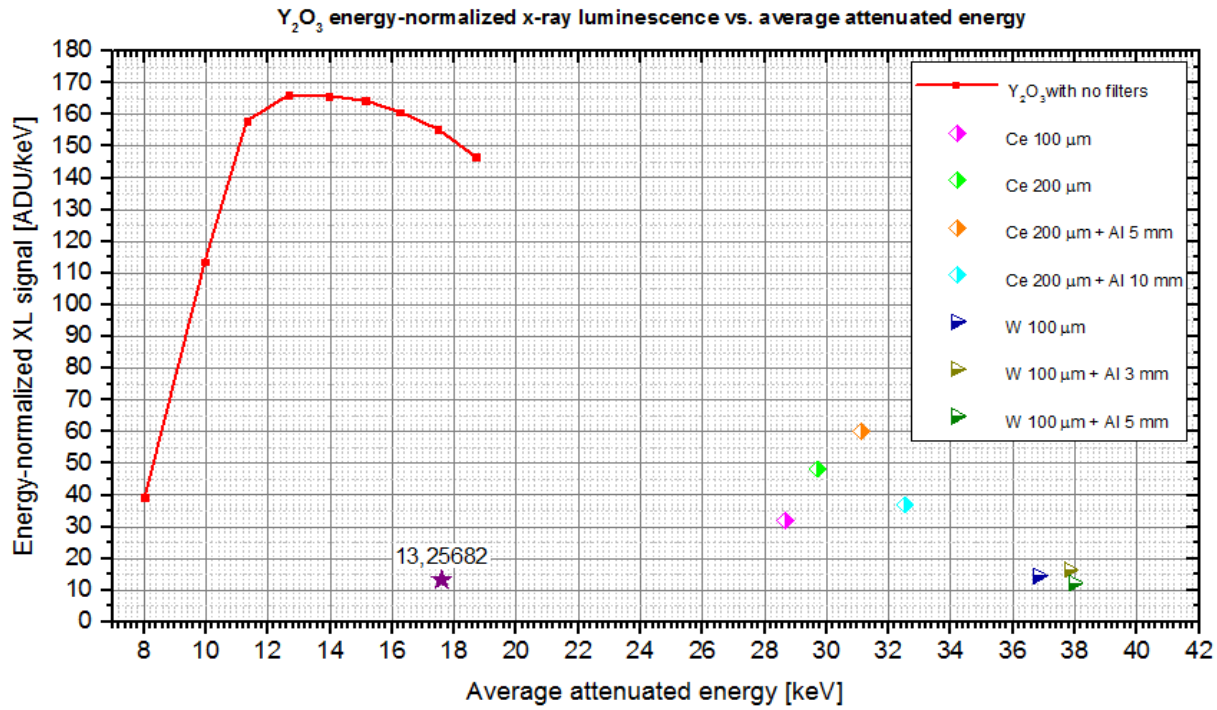

Figure 5.14: Variation of the energy-normalized XL signal rate with average attenuated energy, for Y_2O_3 and for all the excitation strategies that have been measured.

Then, the same curves for LaF_3:Tb are also reported as well, in Figure 5.15.

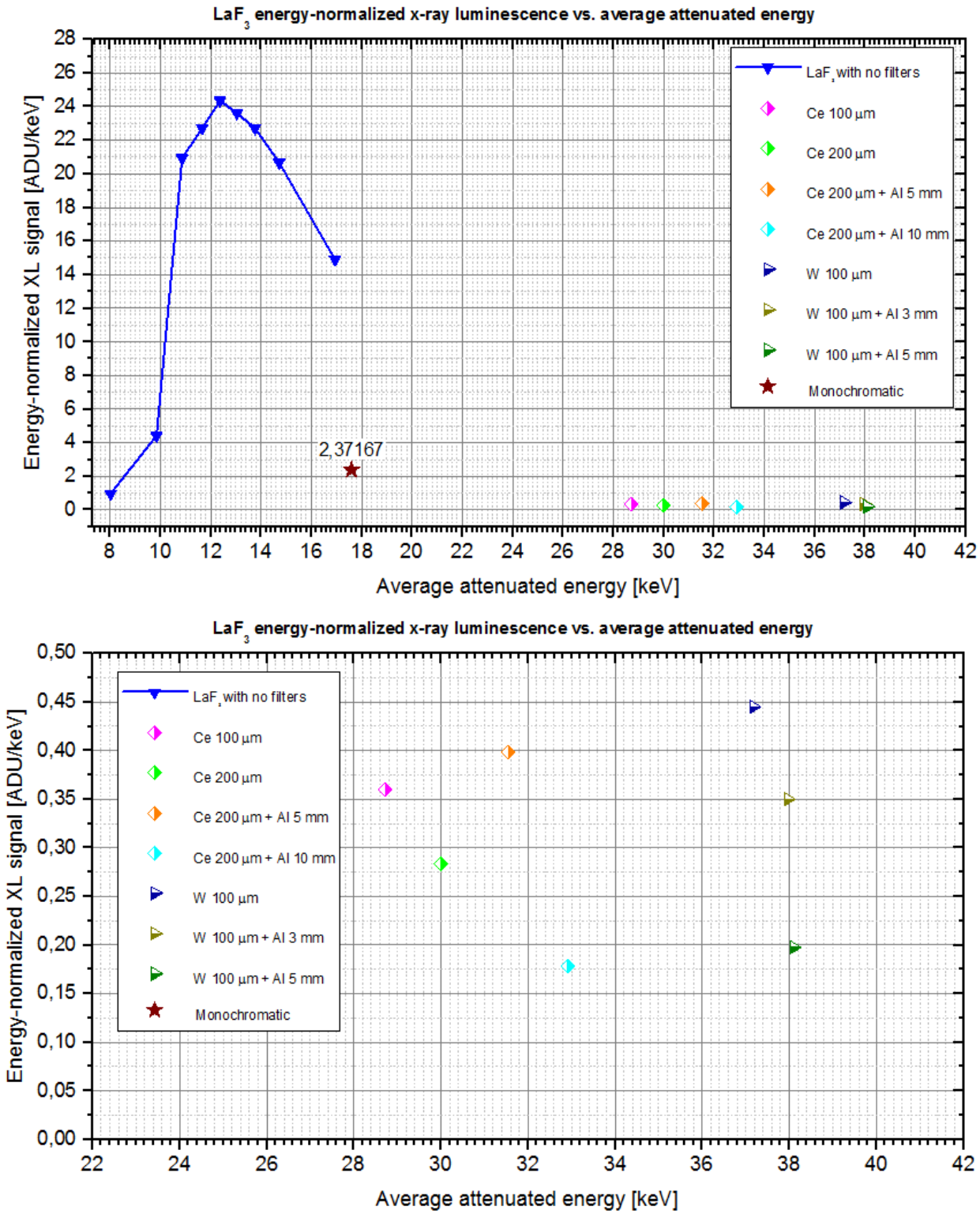

Figure 5.15: Variation of the energy-normalized XF signal rate with average attenuated energy, for LaF_3 (top) and for all the excitation strategies that have been measured. The plot is also enlarged to highlight the filtered data (bottom).

The plots of the XL signal yield with the average attenuated energy confirm the presence of local maximum points in the curves for the unfiltered polyenergetic excitation, which are actually even more emphasized, especially for LaF_3:Tb. Both the two nanoparticles reach the maximum XL signal yield among all the excitation strategies with the polychromatic source without filters, in a

range of average attenuated energies between 12 and 14 keV. For the other excitation configurations, the XL signal yield is always far lower, even for the monoenergetic excitation with Y_2O_3:Eu(III). This seems to confirm the hypothesis that the tuning of the excitation source with the K-edge of the target does not have a positive influence on the amount of luminescence per unit energy produced. Generally decreasing values of the XL signal yield are reported for the highest values of attenuated energies, but also for energies below 10-11 keV. Thus, it may be concluded that the optimal range of excitation energies for the most efficient production of x-ray luminescence with the polychromatic source lies between 12 and 14 keV for both the two nanoparticles. Maximum peaks can be identified also for the filtered polyenergetic excitation of Y_2O_3:Eu(III), with a local maximum for the 200 µm cerium plus 5 mm aluminum filter, at around 31 keV and another maximum for 100 µm tungsten plus 3 mm aluminum at slightly below 38 keV. Such aspect shows a discontinuity with the previous sets of data considering the attenuated energy rates, where all the maximum points were centered on the same range of rates. The difference in the net x-ray photon fluxes from on excitation strategy to the other could be the reason of such behavior, although deeper investigations may be needed. On the other hand, all the filtered data for LaF_3:Tb does not show particular peaks and has a decreasing tendency of the XF signal yield with the average attenuated energy, except for the data point corresponding to filtering with 200 µm cerium plus 5 mm aluminum. This may be due to an error in the acquisition of the transmission energy spectra for this particular data point.

The same plots can be obtained also for the XF signal yield, as shown in Figure 5.16 for LaF_3:Tb.

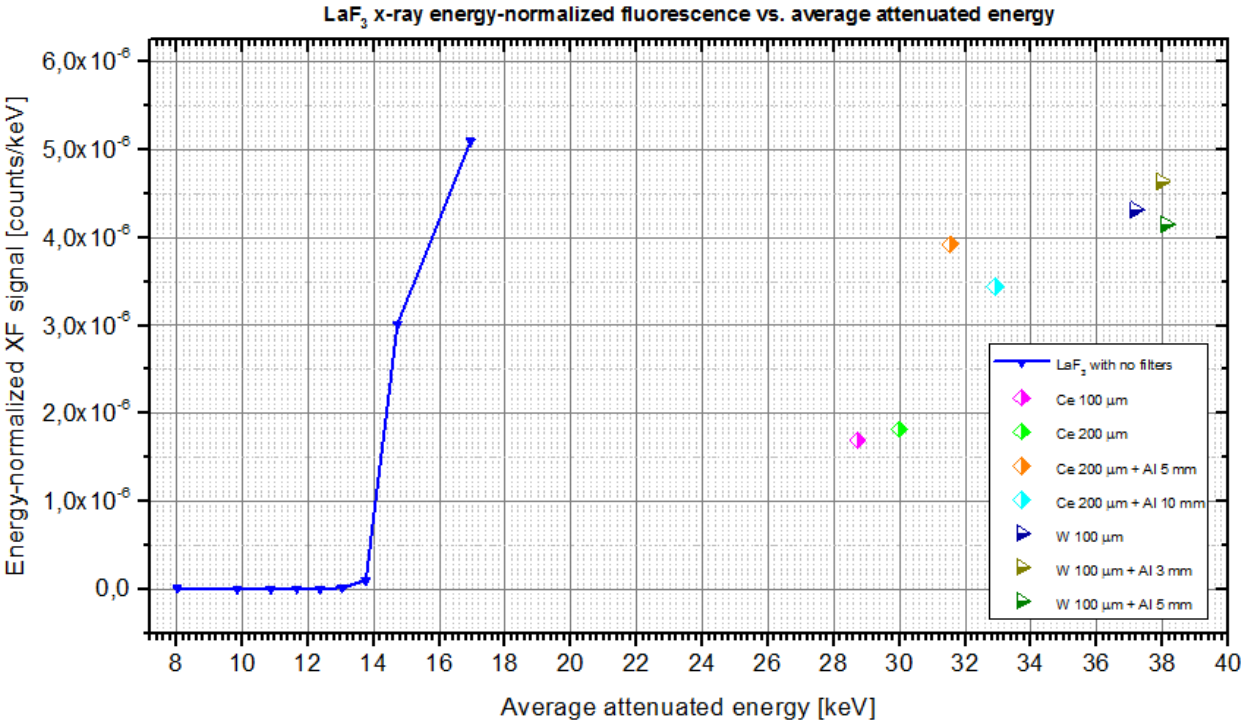

Figure 5.16: Variation of the energy-normalized XF signal rate with average attenuated energy, for LaF_3 and for all the excitation strategies that have been measured.

Figure 5.17 depicts the same plots for the other nanoparticle, Y_2O_3:Eu(III).

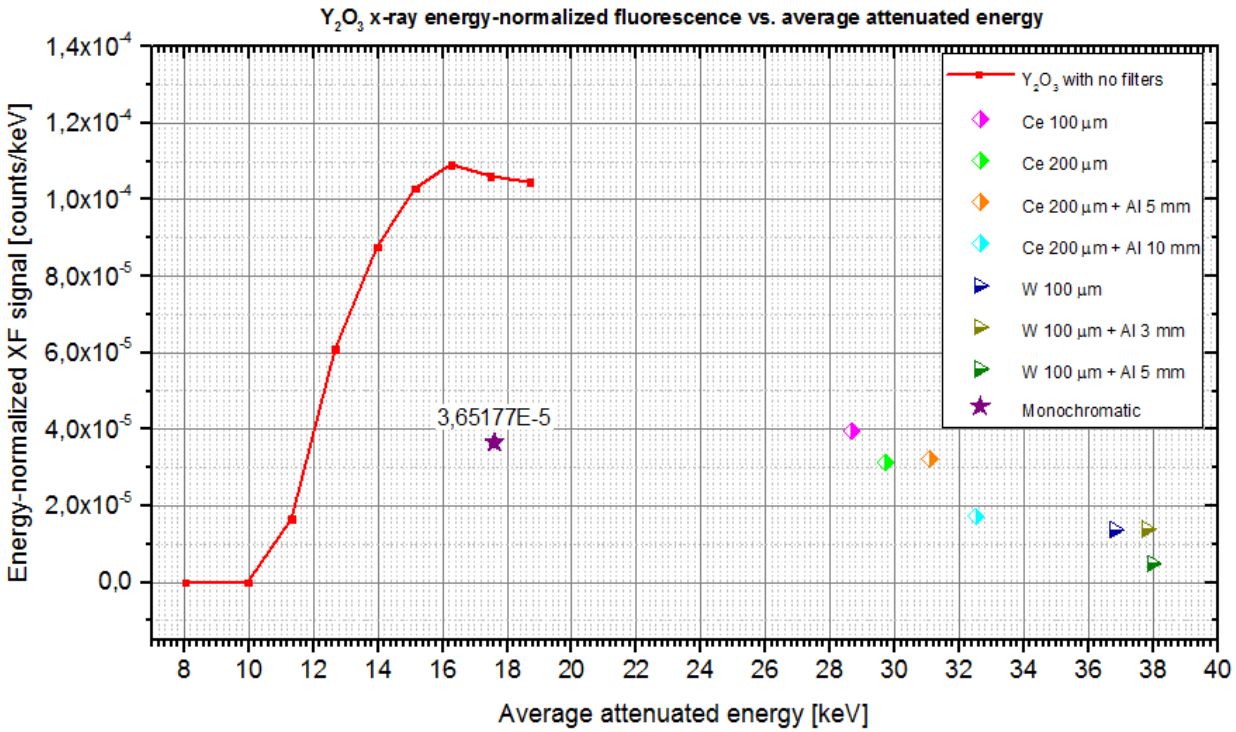

Figure 5.17: Variation of the energy-normalized XF signal rate with average attenuated energy, for Y_2O_3 and for all the excitation strategies that have been measured.

The first important and expected result that can be evinced from the graph in Figure 5.17, referred to Y_2O_3:Eu(III), is the location of the previously identified maximum in the energy-normalized XF sig-nal for the unfiltered polyenergetic excitation, which has the highest XF signal yield among all the data. Such maximum seems to occur with an average attenuated energy almost in correspondence of the K-edge of yttrium, as expectable. This means that the most efficient excitation configuration for maximizing the XF signal yield is the one where the average attenuated energy matches the K-absorption energy of the nanoparticle. Such excitation is provided by the unfiltered polychromatic x-ray tube at 45 kVp. However, this aspect cannot be confirmed for LaF_3:Tb as well, due to the lack of a local maximum in the unfiltered data. Anyway, all such attenuated energies are far below the K-edge of lanthanum. Therefore, data points for excitation at higher energies are required. In addition, the filtered data for Y_2O_3:Eu(III) seems again to follow the tendency of the unfiltered ones, as after the local maximum the XF signal yield with the polyenergetic excitation appears to decrease with the rise of the average attenuated energy. On the other hand, the filtered excitation data points for LaF_3:Tb provides an opposite behavior, with an increasing trend towards the higher energies. A local maximum is also present, for the 200 µm cerium plus 5 mm aluminum filter, but even in this case the attenuated average energy may have been calculated from a wrong or inaccurate transmission energy spectrum. Moreover, it is interesting to notice that all this points may have followed the same XF signal yield, as the unfiltered data if the x-ray photon flux of the filtered excitation beam were high enough, thus

producing a greater net XF signal rate. For the filtered data related to the excitation LaF_3:Tb, it can be also hypnotized that a maximum in this increasing trend may be reached at the K-edge of lanthanum, but without further data for higher energies this cannot be confirmed. Finally, the surprisingly low XF signal yield from the excitation of Y_2O_3:Eu(III) with the monochromatic source tuned at the K-edge of yttrium must be reported. This fact shows that, although the monochromatic source produces by far the highest XF signal rate among all the excitation energies (as seen in the previous paragraph), it is not an efficient stimulation process, because a high attenuated energy rate seems to be required to generate such signal. The XF signal yield of the monoenergetic excitation exactly demonstrate this. This controversial aspect would need further studies and more experimental data to be analyzed.

Important conclusions can be drawn from the analysis of the XL and XF energy-normalized data from the two nanoparticles and all the sets of excitation configurations that has been tested. These conclusions can be summarized in the following major points:

1) For x-ray luminescence, the most efficient excitation strategy, in terms of maximum XL signal yield is always provided by the unfiltered polychromatic source for both the two nanoparticles. In particular, a maximum of such yield can be found for attenuated energy rates ranging between $1.5x10^{-6}$ and $2.5x10^{-6}$ keV/s, which correspond to an average attenuated energy provided by the polienergetic beam at about 12-14 keV. Thus, low energy photons in this range may be to be more efficient and suitable in producing x-ray luminescence with the lowest energy rates. Such result could be important in a perspective of therapeutic delivery using the XL signal, such as in XPDT. An optimal XL signal yield at low dose rates of radiation is in fact highly favorable and advantageous for theranostics applications, especially in clinical human imaging and therapy;
2) For x-ray luminescence, the monoenergetic excitation, even if a high photon flux is used, seems to be energetically inefficient and leads to low XL signal yields. It may not be advantageous for maximizing the XL signal production, because of the high attenuated energy rates required for that, which in terms of related dose rates are not favorable neither for molecular imaging nor for theranostics;
3) For x-ray fluorescence, the unfiltered polychromatic excitation seems to be the best and most energetically efficient strategy to stimulate both the two nanoparticles. For Y_2O_3:Eu(III) a maximum in the XF signal yield has also been found, in correspondence of an average attenuated energy very close to the K-edge of yttrium. Tuning the x-ray beam to the K-edge of the target material may be fundamental to maximize the XF signal at low dose rates, as expectable theoretically. Even the filtered data for LaF_3:Tb seems demonstrated that, but no average attenuated energies above the K-edge of lanthanum was

available to further confirm that. As discussed multiple times, the x-ray photon flux may be crucial in establishing such aspect;

4) For x-ray fluorescence, it was unexpectedly found from the experimental data that the mono-energetic excitation tuned with the K-edge of Y_2O_3:Eu(III) was not as energetically efficient as the unfiltered polyenergetic one, producing a lower XF signal yield per unit energy. Although the monochromatic source generates by far the greatest XF signal rate (as shown in the results in the previous paragraph), the attenuated energy rates required for such rates are incredibly high, thus implying consistent dose rates for potential theranostic applications.

5.3 Comparison between XF and XL signal from different nanoparticles

A direct comparison between the x-ray fluorescence and x-ray luminescence signals can be performed in a quantitative way, from the sets of data that has been shown and discussed in a large part previously. Such comparison is conducted not only amongst the two types of nanoparticles that has been tested in this quantification study, but also between the two kind of signal, the x-ray fluorescence and x-ray luminescence, that each nanoparticle is able to produce. The first important comparison above-mentioned will permit to furtherly evaluate which nanoparticle is more suited for theranostics applications using the XFCT/XLCT system described in this work. A brief assessment of such aspect has been already proposed in Paragraph 5.1, when the XL and XF signal rates generated by the two nanoparticles has been analyzed and compared. However, this time also the energy signal yields calculated and reported in the previous Paragraph will be taken into account. The second comparison, considering the XF and XL signal produced by each single nanoparticle in all the configurations, will allow to estimate which type of emission is the most favorable or the most predominant during the simultaneous x-ray stimulation, according to the type of excitation used.

First of all, for the comparison between the two nanoparticles, the ratio of the XL signal rate (in ADU/S) emitted by Y_2O_3:Eu(III) over the XL signal rate produced by LaF_3:Tb has been calculated from the previous data. Considering that each nanoparticle involves different rates of attenuated energies and also different average attenuated energies (as they have been derived in Paragraph 4.2), the variation of the ratio between the XL signal rates of the two compounds were plotted only in dependency of the changes in the maximum energy of the excitation beam (see Paragraph 5.1). Therefore, only the data from the unfiltered polychromatic source and those from the monochromatic source has been considered, because they maximum beam energies were known. For the filtered excitations, this is not possible, because the all the data have been acquired using the polychromatic source at 50 kVp. Hence, all those data share the same maximum energy of the

excitation source, but the distri-bution of the energies of their x-ray photons, given by their energy spectra, is hugely variable and cannot be represented only by the maximum value. Then, the graph for the ratio between the Xl signal rates of Y_2O_3:Eu(III) over LaF_3:Tb, with the variation of the maximum energy of the source, is re-ported in Figure 5.18.

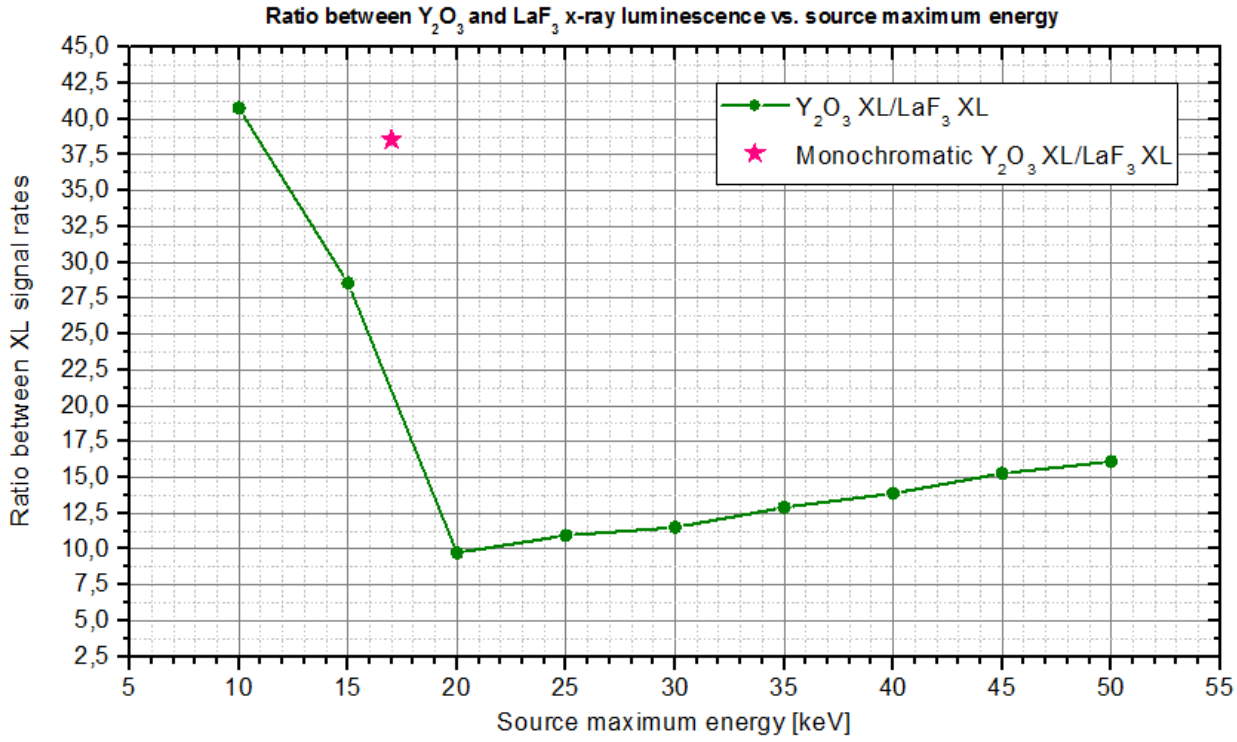

Figure 5.18: Variation of the ratio between the XL signal rates of Y_2O_3 over LaF_3 with the source maximum energy, for the polychromatic and monochromatic excitation.

The graph in the previous figure has a decreasing trend until a discontinuity point of local minimum at 20 keV, after which the curve shows a smooth growth of the ratio between the XL signal rates of the two nanoparticles, as the source maximum increases. It is evident that the XL signal rate of Y_2O_3:Eu(III) is always as high as at least ten times that of LaF_3:Tb, confirming what it has been already inferred from the results in Paragraph 5.1. However, the local minimum indicates a possible reversal in such tendency, as the source maximum energy increases. It is interesting to notice that the local minimum is just above the K-edge energy of yttrium, maybe hinting that after such energy and by approaching the K-edge of lanthanum, the Xl signal produced by LaF_3:Tb could become predominant over Y_2O_3:Eu(III). Anyway, although there are no data above keV enough to enforce that, the fact that, around the K-edge of lanthanum (39.82 keV), the curve is still very flat may already dis-courage such hypothesis.

It can also be seen from the plot that for the monoenergetic excitation, the ratio between the XL signal rates of Y_2O_3:Eu(III) over LaF_3:Tb is almost at its maximum value and it is higher than the corresponding values at the same source maximum energy for the polyenergetic excitation. This is because of the tuning of the monochromatic x-ray beam with the K-edge of yttrium, which maximizes the absorption of x-ray photons by Y_2O_3:Eu(III). Thus, the XL signal produced in this

case can be influenced by this enhanced absorption, rather than in the case of LaF_3:Tb. Nevertheless, the previous results from the quantification of the XL signal yields has shown a low or even negligible impact of the monoenergetic excitation on the production of x-ray luminescence. This fact seems to disagree with the data point in Figure 5.18 about the monochromatic source. To resolve such issue, it may be useful to calculate and analyze the ratio between the XL signal yields, instead of the signal rates. Such ratio has been derived, again for Y_2O_3:Eu(III) over LaF_3:Tb. The results are shown in Figure 5.19, as the source maximum energy changes from 10 to 50 keV.

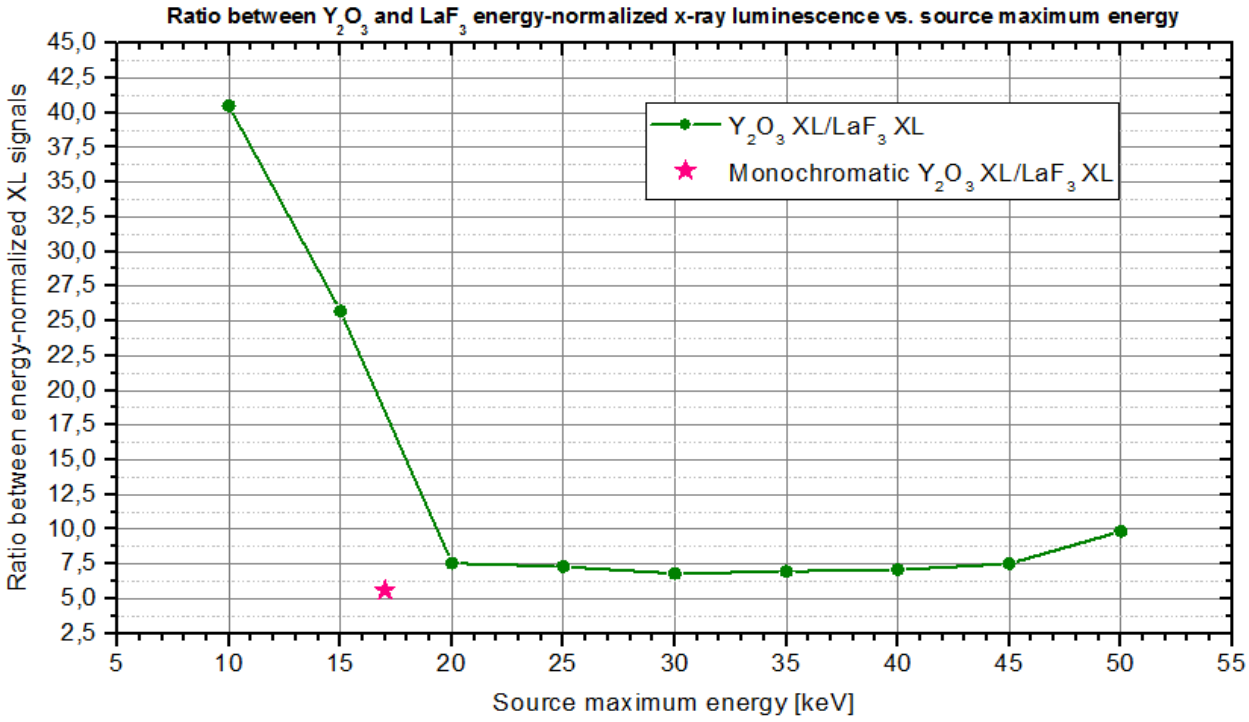

Figure 5.19: Variation of the ratio between the energy-normalized XL signal rates of Y_2O_3 over LaF_3 with the source maximum energy, for the polychromatic and monochromatic excitation.

It can be seen that the first part of the curve, blow the minimum point, has not changed drastically from the previous plot regarding the signal rates. However, the local minimum now has a lower value than before (about 7.5 instead of 10). In addition to that, the second part of the curve beyond such point is now even more flat and almost constant, until a slightly increase at 50 keV. Therefore, it can be stated that Y_2O_3:Eu(III) reaches the greatest difference in XL signal yield, with respect to LaF_3:Tb, for the lowest values of the source maximum energy. It may be possible that this is connected to the presence of the local maximum in the XL signal yields for both the nanoparticles exactly for energies between 10 to 12 keV. Anyway, further understanding of such aspect is required to confirm this. Finally, the resulting ratio between the XF signal yields for the monoenergetic excitation resolves the previous issue emerged from Figure 5.18. In fact, the data point for the monochromatic source has the lowest value among all and it confirms the assumed negligible influence of the monochromatic excitation over the produced XL and especially over

the corresponding XL signal yield.

The same kind of graphs, as those shown in Figure 5.18 and Figure 5.19 for x-ray luminescence, can be derived for x-ray fluorescence, showing both the ratio between the XF signal rates and the ratio between the XF signal yields of Y_2O_3:Eu(III) over LaF_3:Tb, again for the variation of the source maximum energy. Such plots are reported in Figure 5.20.

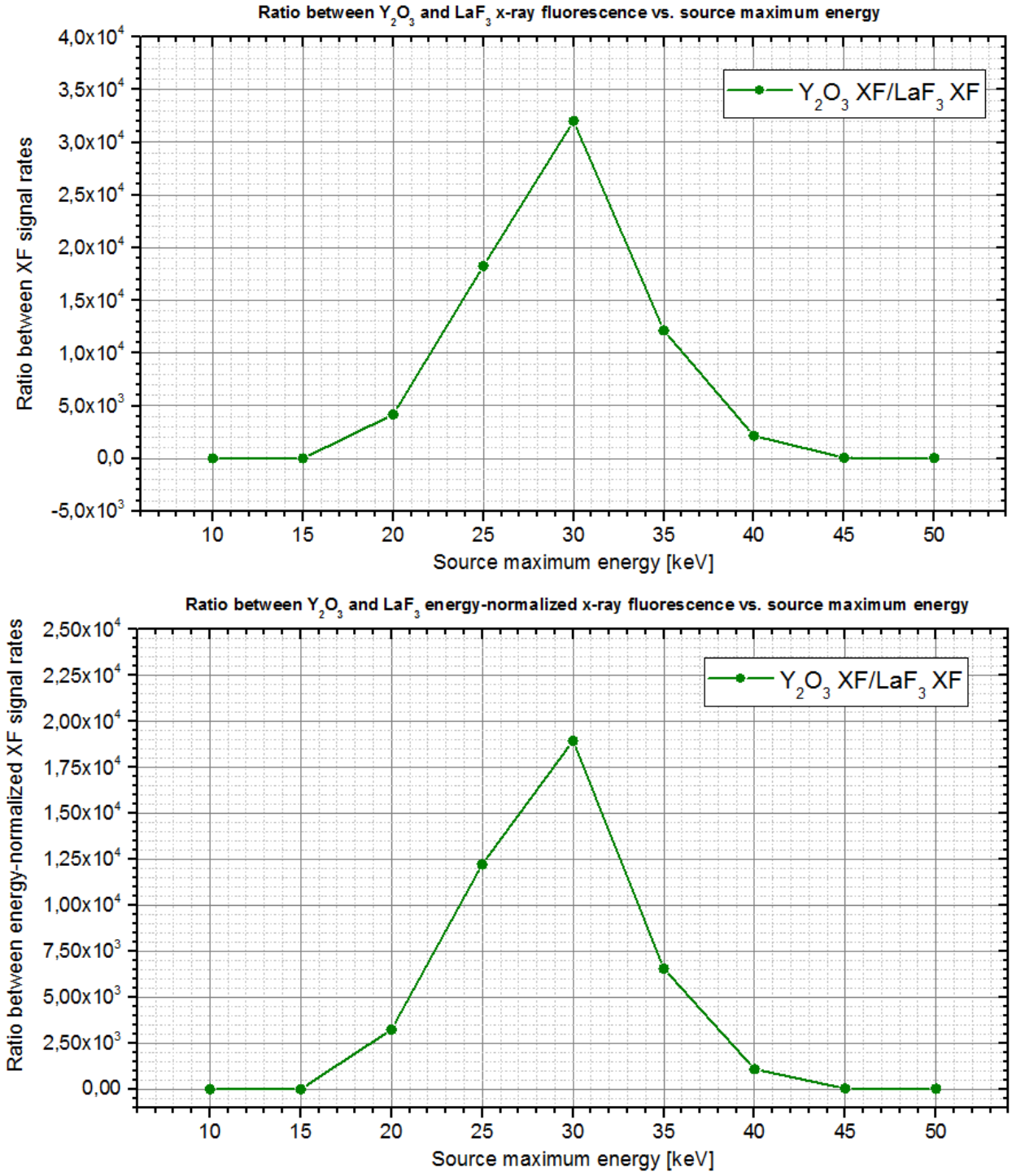

Figure 5.20: Variation of the ratio between the XF signal rates (top) and of the ratio between energy-normalized XL signal rates (bottom) of Y_2O_3 over LaF_3, with the source maximum energy.

The two curves in the figure, for both the ratio between the XF signal rates and the ratio between the XF signal yields, show almost perfectly identical trends, with the only difference being in the

scale of the respective values. In fact, the ratio between the XF signal rates is almost twice as the ratio between the XF signal yields. However, the similarity between the tendencies of the plots may suggest a negligible influence of the attenuated energy in the comparison between the x-ray fluorescence signals of the two nanoparticles. By looking carefully at the both the two curves, it can be clearly seen that a maximum peak is present, at 30 keV. Below such point, both the two XF ratios increases from almost zero to such maximum value. This is because the XF signal of both Y_2O_3:Eu(III) and LaF_3:Tb is negligible until the onset of x-ray fluorescence at the K-edge, which happens first for yttrium. Hence, beyond such value (between 15 and 20 keV in the curve), the XF signal of Y_2O_3:Eu(III) is predominant, as shown by the two ratios, until the maximum peak. After such value, the onset of x-ray fluorescence for lanthanum occurs and then the ratio between the XF signals of the two nanoparticles becomes lower and lower, due to the increasing production of x-ray fluorescence by LaF_3:Tb. However, the quantification data from the results in Paragraph 5.1 have clearly shown that the XF signal of Y_2O_3:Eu(III) is always higher than that of LaF_3:Tb, at least of one order of magnitude.

The second comparison of the data discussed in this Paragraph, between the XL and the XF signals of each nanoparticle, can be easily estimated by calculating the ratio between the XL signal rate and the XF signal rate (in ADU/counts) of both Y_2O_3:Eu(III) and LaF_3:Tb. Such ratio can be calculated for all the excitation strategies that has been tested in the experimental studies. Furthermore, such ratio is the same for both the signal rates and the signal yields, due to the same attenuated energy rates. The first graph is shown in Figure 5.21, for LaF_3:Tb, with the average attenuated energy.

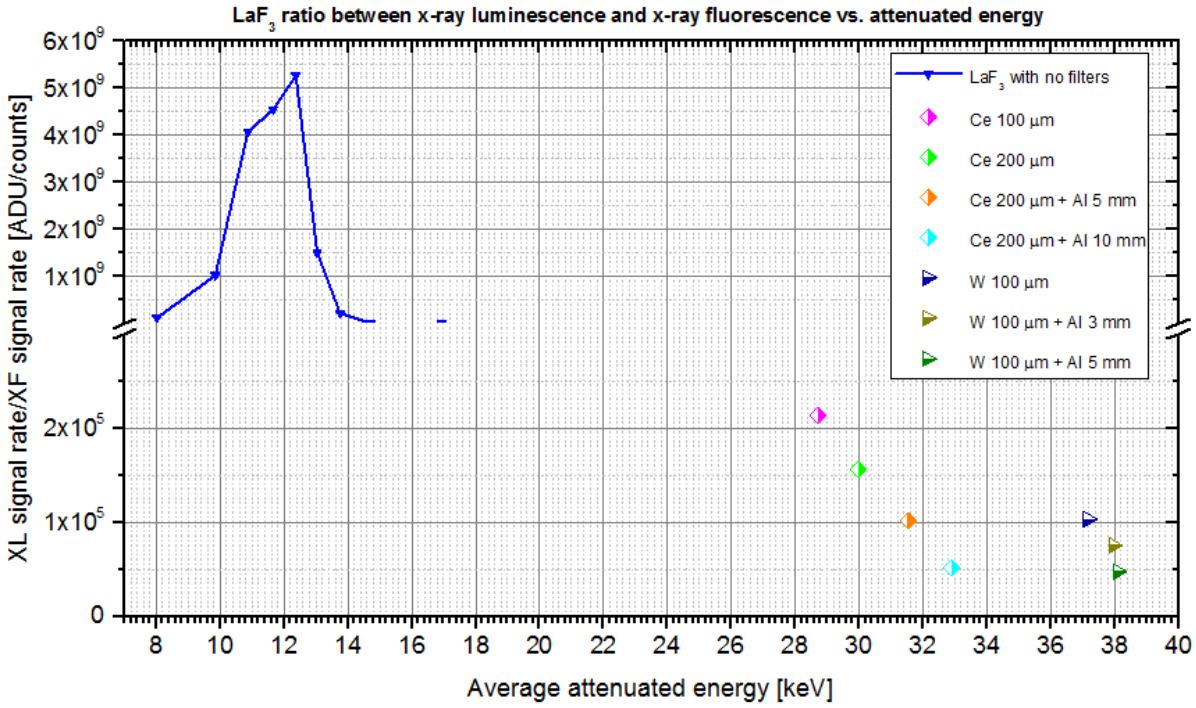

Figure 5.21: Variation of the ratio between the XL signal rate and the XF signal rate of LaF_3, with the average attenuated energy and for all the excitation strategies that have been measured.

The most evident aspect emerging from the plot for LaF_3:Tb is the predominance of the XL signal over the XF signal for this nanoparticle, which is from five to nine orders of magnitudes higher than the x-ray fluorescence emitted by the same compound. This result is expected, because of the lower energy required to produce a visible light photon (few eV), compared to that required to generate a characteristic x-ray photon. The lowest values for the ratio are presented by the characteristic x-rays, which have average attenuated energies closer to the K-edge of lanthanum. The curve for the unfiltered polyenergetic data also show a maximum value of the ratio center on about 12-14 keV. Such value corresponds almost to the energy that maximized the XL signal yield, as shown in the previous Para-graph, thus enforcing the hypothesis about the most efficient action of these lower energies for the production of x-ray luminescence. The ratio between XL and XF signal rates tends to decrease as the average attenuated energy increases, moving toward the K-edge of lanthanum, as noticed previously.

An equivalent graph is also depicted for the second nanoparticle, i.e. Y_2O_3:Eu(III), in Figure 5.22.

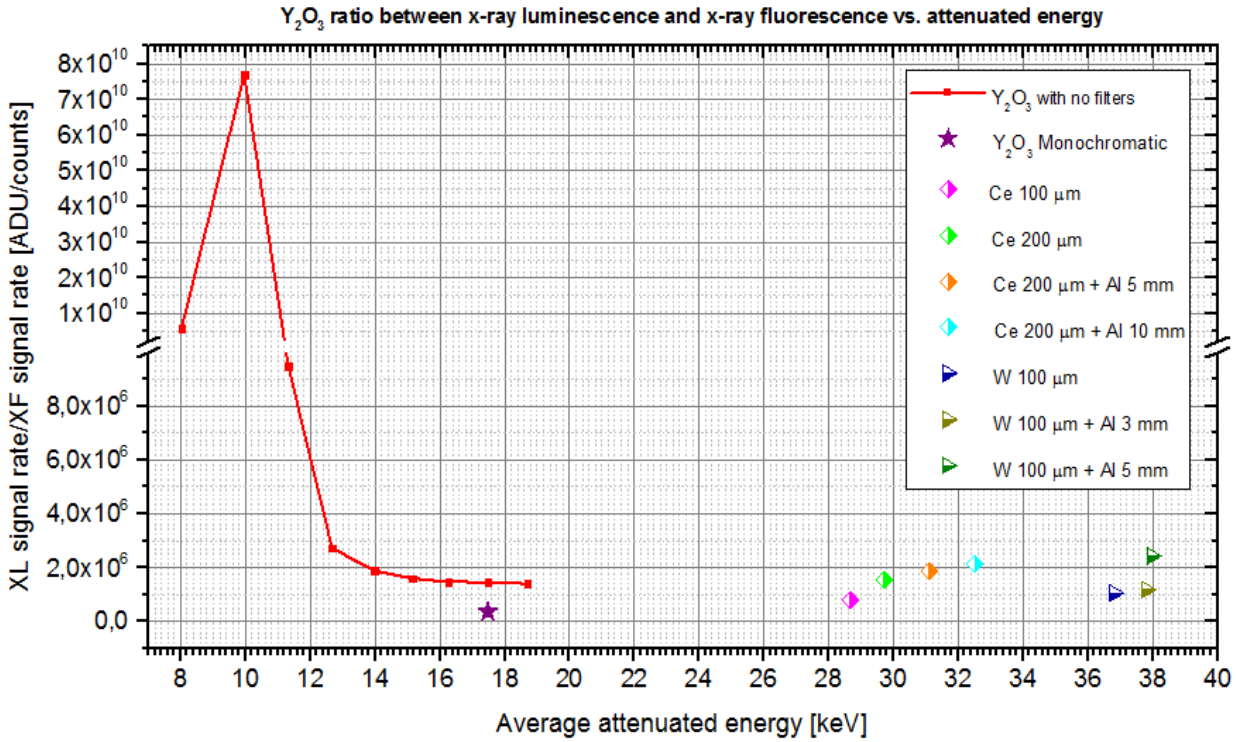

Figure 5.22: Variation of the ratio between the XL signal rate and the XF signal rate of Y_2O_3, with the average attenuated energy and for all the excitation strategies that has been measured.

As it was seen previously for the case of LaF_3:Tb, the graph of the ratio between the XL and the XF signal of Y_2O_3:Eu(III) with the unfiltered polyenergetic excitation shows a maximum value, at around 10-12 keV, approximately in correspondence of the range of energies that was found to maximize the XL signal yield (see Paragraph 5.2). Beyond such value, the XL over XF signal ratio greatly decreases and becomes almost flat beyond the K-edge of yttrium. It is interesting to see that the ratio between the XL and XF signal for the monoenergetic excitation is the lowest value depicted, as to demonstrate the great influence on the XF signal production given by the tuning of

the monochromatic source with the K-edge of yttrium. Furthermore, the filtered excitation data for Y_2O_3:Eu(III) shows an increasing trend with the average attenuated energy, as the degree of filtering grows. This is a fact that dis-agree with the previous plot for LaF_3:Tb, where a decreasing trend for the same configuration was visible. The decreasing trend for LaF_3:Tb was explained considering the proximity with the K-edge of lanthanum. On the contrary, for the case of yttrium, the increase in the average energy reduces the probability of having photoelectric effect, thus decreasing the production of x-ray fluorescence for the XL over XF ratio. Finally, it can be noticed that, in general, the ratio between XL and XF signals is greater for Y_2O_3:Eu(III), rather than for LaF_3:Tb.

In the end, the major conclusion that can be inferred by the previous graphs and the analyzed data from the different comparisons of the result of the quantification study is related, as already seen, to the predominance of the XF and XL signal produced by Y_2O_3:Eu(III), as compared to that emitted by LaF_3:Tb, for all the various excitation strategies. In a perspective of molecular imaging and theranostics, Y_2O_3:Eu(III) nanoparticles can be considered the most suitable and favorable among the two types considered, especially for XPDT, for these kinds of applications with the current XFCT/XLCT system of this work.

5.4 Results from XFCT imaging of metal-based compounds in the mouse phantom

The results from the first imaging study carried out with the XFCT/XLCT system are now discussed and presented [62]. As illustrated previously n Paragraph 4.3, a mouse head phantom with two double tube cylinders loaded with metal-based compounds was used in such XFCT imaging study. One of the cylinders was filled with Y_2O_3:Eu(III) and HfO_2 nanoparticles, while the other with LaF_3:Tb and Cisplatin. The XFCT study was performed applying the first XFET geometry involving a pencil beam of x-rays for the excitation and a single slit aperture for the collection of the XF signal before of the x-ray CCD camera. Simultaneously to the detection of the x-ray fluorescence projections through the slit with the CCD, the CdTe spectroscope was used to acquire the XF energy spectra emitted by the samples in each scanned position. These spectra were used later to isolate the peaks of each of the x-ray fluorescence emitting compounds, in order to create a multicolored image by superimposition of the single slices for each target material.

Therefore, an example of such XF energy spectra is shown in Figure 5.23, for all the compounds in both the two double tube cylinders. Such specific XF spectra were acquired in positions where both the two materials filling each tube were irradiated simultaneously, as for all the x-ray fluorescence peaks emitted by the targets to appear. The only exception is for lanthanum in the LaF_3:Tb nanoparticles. Such lack of the XF peak of lanthanum is obviously due to the use of the monochromatic source at 17.48 keV for the imaging study. Thus, the energy of the x-ray photons

emitted by the source was lower than the K-edge of lanthanum, while the L-fluorescence peaks have energies that were too low to be detected clearly in the XF spectra [62].

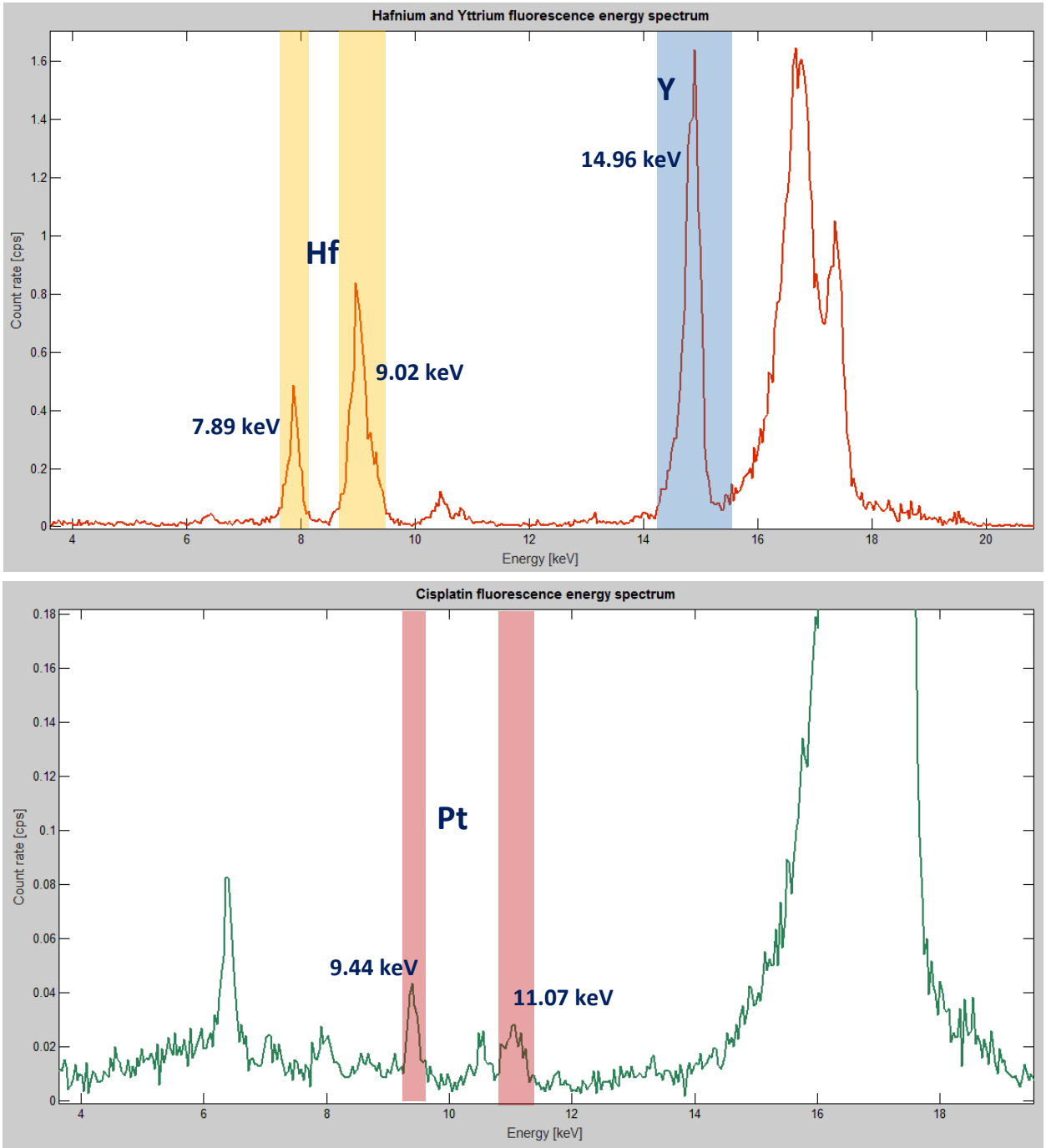

Figure 5.23: XF energy spectra acquired in arbitrary positions, at which the mouse head phantom was scanned during the XFCT study. The energy-isolated peaks for the compounds in the first double tube cylinder, containing Y_2O_3:Eu(III) and HfO_2 (top), and those for the second cylinder, loaded with LaF_3:Tb and Cisplatin (bottom), are identified and labelled [62].

In the first spectra, the two L-fluorescence peaks of hafnium (7.89 keV and 9.02 keV) and the K-fluorescence peak of yttrium (14.96 keV) have been isolated. In the second spectra, the same was done for the two L-fluorescence peaks of platinum (9.44 keV and 11.07 keV). The peak generated by the scattering (mainly coherent and Compton scattering) of x-ray photons from the primary beam is also evident in both the XF spectra, showing the great contribution to the noise of such

process. Peaks from undesired x-ray fluorescence emitted by various materials in the surrounding environment are also present, mainly due to iron (6.40 keV) and lead (10.52 keV).

The net count rates associated with the XF signal of all the three compounds is relatively low and the scattering is predominant in the energy spectra. This is due to the very low concentrations of materials filling the samples that has been used for the imaging study. However, the counting statistics for all the peaks and the energy resolution of the CdTe detector is favorable enough to perform energy isolation of such XF peaks, as to reconstruct a single 200-µm tomographic slice of the imaged target. The procedure for the image reconstruction has been explained in Paragraph 3.3. A 4 x 4 binning of the pixels of the x-ray CCD camera was chosen, in order to increase the net amount of signal per unit area in the slice, at the cost of spatial resolution. At this point, the results from the energy isolation of each x-ray fluorescence peak form the various compounds and their reconstruction into monocolored transversal slices are reported in figure 5.24, including the energy isolation of the peak produced by the scattering from the primary beam [62].

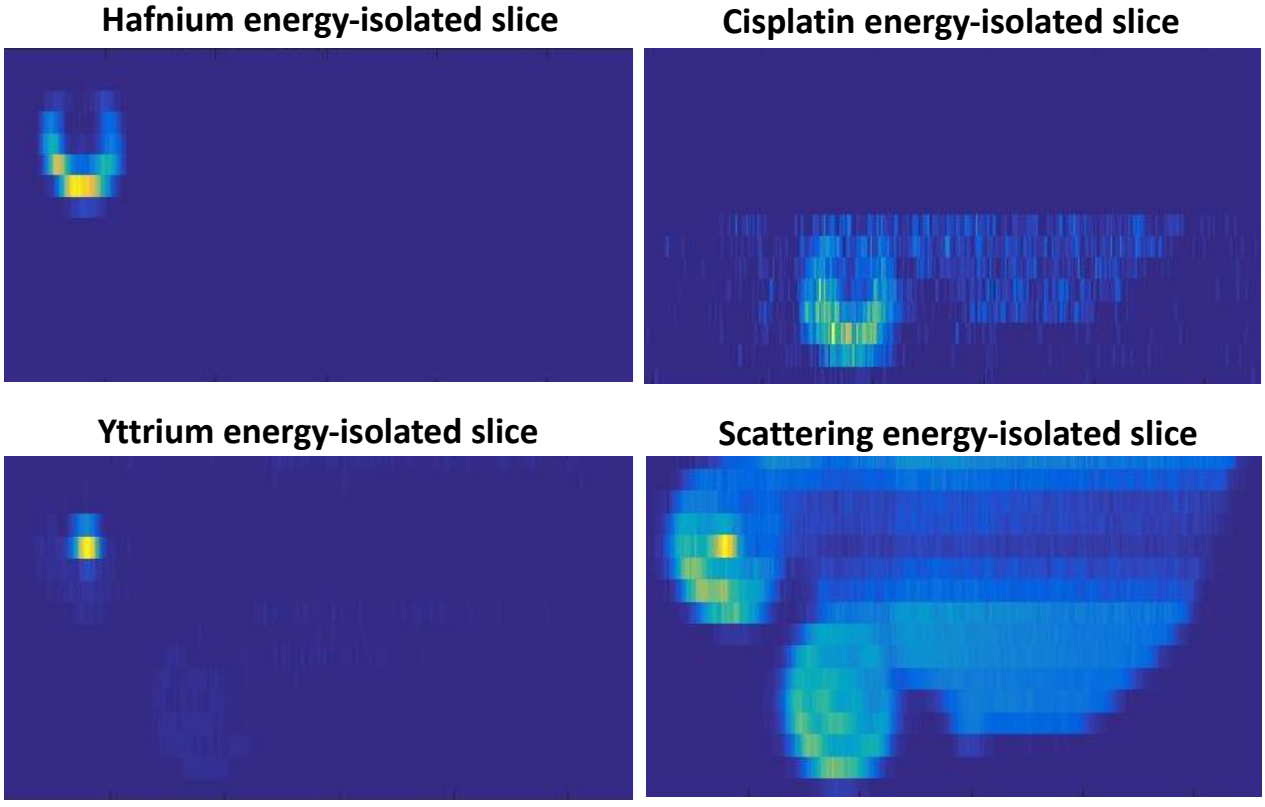

Figure 5.24: Energy-isolated slices for each of the three main compounds of the XFCT imaging study, i.e. hafnium (top left), cisplatin (top right) and yttrium (bottom left). The energy-isolated slice for the scattering is also shown (bottom right) [62].

The results from the reconstructed slices show that all the features of both the double tube cylinders are clearly resolved and distinguishable. Thus, it is demonstrated that the XFCT/XLCT system is able to reach a spatial resolution of about 200 µm, the size of the smallest region resolved. The energy-isolated slice of platinum, and slightly also the energy-isolated slice for yttrium, presents noise perturbations due to scattering contaminating the isolated signal from the XF peaks. Anyway,

even the lowest concentration of target material, i.e. 300 µg/mL for Cisplatin, has been detected, tough the not-negligible presence of noise. The sensitivity performances of the XFCT/XLCT system are then assessed for x-ray fluorescence.

Finally, the four energy-isolated slices previously shown are combined and superimposed to create a single 200-µm multicolored slice, visible in Figure 5.25 [62].

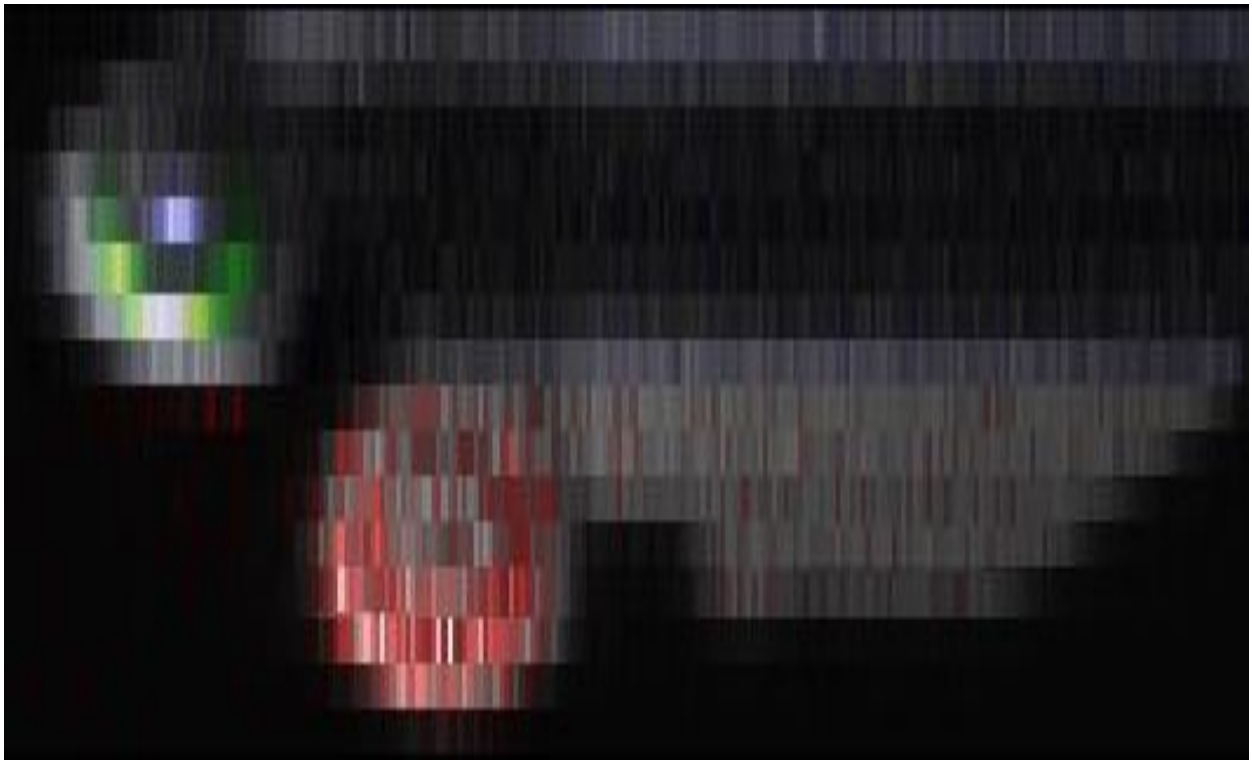

Figure 5.25: Multicolored slice resulting from the XFCT imaging study. The scattering contribution (in gray) and the signal from yttrium (blue), hafnium (green) and platinum (red) are visible [62].

In the multicolored image, the scattering slice has been used as a sort of structural frame for the entire image, because of the visibility of the shapes and contour of the mouse head phantom. All the main features of the sample at 200-µm size are again clearly visible and spatial resolved, even after the superimposition of the energy-isolated slices. This demonstrates the feasibility of multiplexed XFCT imaging at high resolution with the proposed XFCT/XLCT system.

5.5 Results from XFCT and XLCT imaging of metal-based compounds in the double tube

Finally, this paragraph will introduce and discuss the 3D imaging results from the combined XFCT and XLCT study of a double tube cylinder, loaded with metal-based compounds [62]. As described in Paragraph 4.4, the glass double tube (of 1 to 3 mm-size) was filled on the inside with Y_2O_3:Eu(III) in powder form and on the annular region with NaBr in water solution.

The imaging study was carried out using an XFET/XLET imaging geometry, which involved an excitation with a sheet x-ray beam, produced by collimating with a slit the cone beam of the polychromatic x-ray tube, and the collection of the XF and XL signal coming from the materials

with a pinhole. Two different pinholes were mounted in front of both the x-ray CCD camera, for XF detection, and the EMCCD plus DM tube assembly, for XL detection.

Single vertical slices corresponding to the XF and XL projections of the irradiated plane in the double tube cylinder were acquired. From such slices, a 3D volumetric image was then reconstructed by stacking them all together, as explained in Paragraph 3.3. The CdTe spectroscope was used to acquire XF energy spectra from the two metal-based compounds, in order to isolate the XF peaks of each of the imaged materials and perform multiplexed imaging of different emitters. The XF slices were then combined with the corresponding slices obtained from the XL projections. Afterwards, the final multicolored and multimodal 3D image was obtained. Such final volumetric image and two single slices, one for XF only and the other with the combination of XF and XL signal, are reported in Figure 5.26, as the main results of the abovementioned imaging study with the proposed XFCT/XLCT system [62].

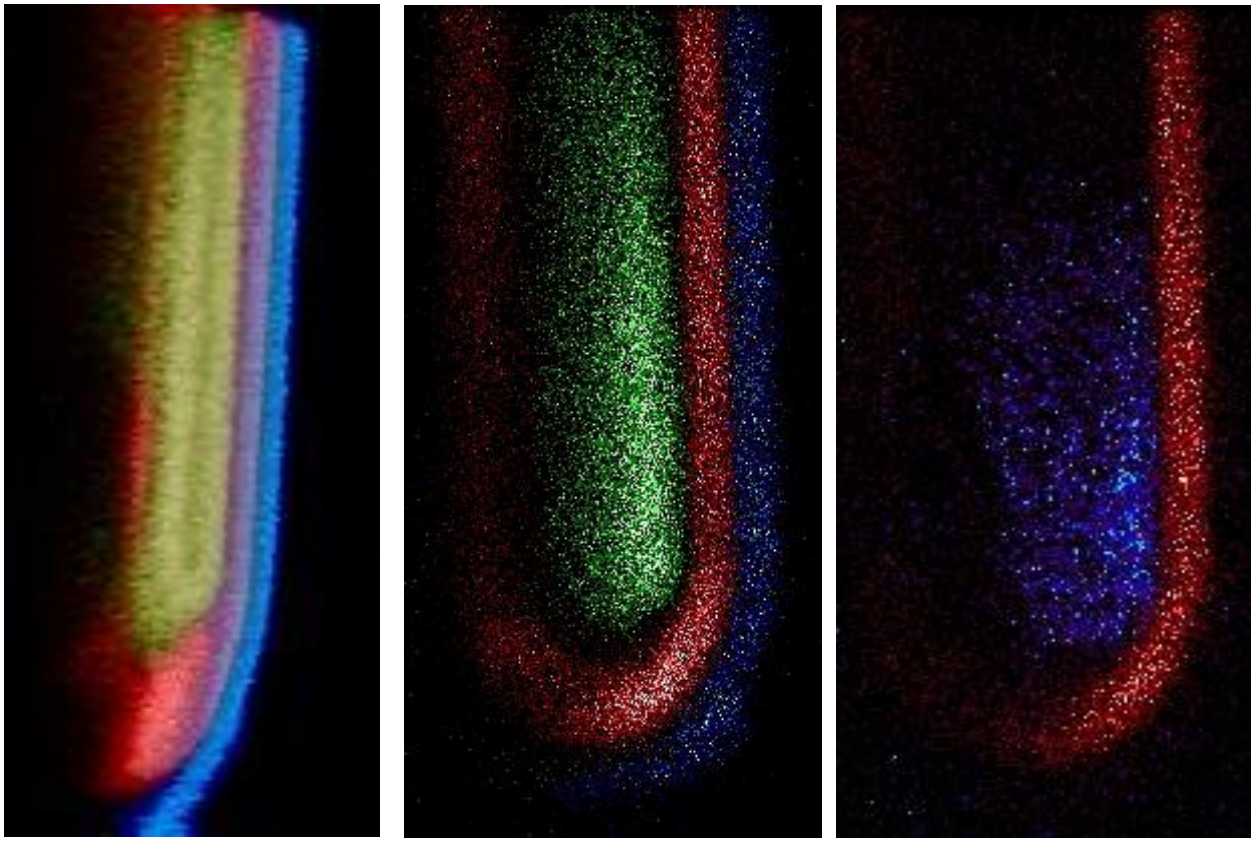

Figure 5.26: Main results of the combined XFCT and XLCT imaging study. A 3D XFCT volumetric image is shown (left), where Y_2O_3 (in yellow) and NaBr (in red) are visible. The outer layer (in blue) is XF signal coming from zinc impurities in the glass. A complete XF slice is also reported (center), with again Y_2O_3 (in green), NaBr (in red) and zinc (in blue) clearly present. Finally, a combined XF and XL slice (right) is also presented, showing XF signal from NaBr (in red) and XL signal from Y_2O_3 (in blue) [62].

The 3D image clearly shows all the major contributors for the XF signal emitted by the double tube cylinder: the XF signal isolated from Y_2O_3:Eu(III) in yellow and the XF signal isolated from NaBr in red. A third XF signal is visible as an outer layer in blue. The glass, from impurities of zinc, emits such XF signal. Anyway, the zinc XF signal provide structural information about the

outer contour and thick-ness of the double tube cylinder. It is evident from the image that all the three major features have been clearly and sharply resolved in the XFCT study, with excellent spatial resolution. This is also due to the bigger dimensions of such sample compared to the mouse head phantom used in the previous study (1 mm rather than 200 μm). The slice reported in Figure 5.26 showing the three major XF projections from the sample enforces such statement and demonstrates the good performances of the XFCT/XLCT system. Finally, the last slice reported in the figure, shows the combination of the imaged XL projection emitted by Y_2O_3:Eu(III) and again the XF projection from NaBr. Again, all the details of the double tube sample are perfectly resolved and distinguishable. Moreover, the multiplexed and multimodal image openly demonstrates the feasibility of combined XFCT and XLCT with the system proposed in this thesis work. Attenuation correction, using a transmission x-ray detector, such as the Zyla sCMOS, has not been performed on the final resulting images, thus some area in the pictures appears less resolved and with a lower amount of signal. This is due to the gradual attenuation of both the primary x-ray beam across the thickness of the double tube, and also of the corresponding XF and XL photons emitted by regions deep within the sample. Attenuation correction may have furtherly improved the quality of the final images.

6. Conclusions and future work

As mentioned multiple times throughout all the previous Chapters, the main motivation behind this work has been the design, creation and development of a smart, advanced and innovative XFCT and XLCT imaging system, as to investigate potential theranostic applications of this type of technology, such as x-ray induced and monitored XPDT. The system has also been characterized in details and various experimental studies have been conducted to test and evaluate its performances. Spatial resolution, sensitivity and capability of multiplexed and multimodal imaging were among the main features that has been assessed. Furthermore, an extended quantification study for the x-ray fluorescence and x-ray luminescence signals was one of the core targets of the experimental applications of such XFCT/XLCT system. Various x-ray excitation strategies has been tested and evaluated, in combination with nanoparticle agents as the main targets and vehicles for theranostics.

At this point, the current Chapter will first summarized the entire work that has been here described and illustrated, highlighting the most important aspects, the fundamental basis of the XFCT/XLCT system and the primary results obtained from the experiments. Afterwards, future directions for this thesis project, together with potential developments and improvements of the current XFCT/XLCT system proposed here, will be discussed briefly.

6.1 Summary of the work and relevant conclusions

The key features and aspects concerning the design, construction and development of the XFCT/XCT system can be summarized through the main points in the following list:

1) The system has been primarily designed for combined XFCT and XLCT imaging. The main purpose of the system is assessing the feasibility of using such emission techniques also to deliver therapeutic effects, triggered by x-ray selective stimulation, and to simultaneously monitor and image such treatments with suitable molecular imaging performances;
2) The system is embodied in a benchtop laboratory setup, compose of commercial and custom-made detectors. Such aspect is important, as to demonstrate the practicability of XFCT and XLCT technology outside synchrotron facilities and its potential for future commercial pre-clinical and even clinical applications;
3) The system implements XFET (x-ray fluorescence emission tomography) and XLET (x-ray fluorescence emission tomography) imaging geometries, in order to perform the scanning of the target object with the x-ray beam and to acquire the final XL and XF

signals. XFET/XLET geometries involves the use of collimated x-ray beam with specific shapes for x-ray stimulation and also the collimation of the emitted XF/XL signal with different apertures to collect and transmits the respective projections to the detectors. Their main objective is to reduce the image acquisition time of both XFCT/XLCT, to maximize the tradeoff between spatial resolution and geometric sensitivity of the setup, and finally to allow image reconstruction without complex algorithms or the necessity to calculate any sinogram;

The XFCT/XLCT has been used to conduct experimental investigations on the applicability of x-ray fluorescence and x-ray luminescence in nanoparticle-mediated therapy, with simultaneous monitoring of the treatment via tomographic treatment. Nanomaterials were chosen as potential theranostics agents with XFCT/XLCT, because of their versatility and unique properties. In particular, two types of nanoparticles were tested and studied: LaF_3:Tb and Y_2O_3:Eu(III). A quantification study of the XF and XL signal produced by these two nanoparticles under different x-ray excitation strategies were per-formed. The tested excitation strategies carried with the XFCT/XLCT system includes:

- Excitation with a polyenergetic x-ray cone beam produced by the polychromatic source of the setup, using different sets of tube voltage (from 10 to 50 kVp with 5 kVp increment steps);
- Excitation with a high-flux monoenergetic x-ray beam at 17.48 keV, produced by the mono-chromatic source of the setup;
- Excitation with a filtered and *hardened* polyenergetic x-ray cone beam, using different seven filters that involves various thicknesses of cerium, tungsten and aluminum. The x-ray beam was produced again by the same polychromatic source of the setup.

An estimate of the energy attenuated by the nanoparticles in each excitation strategy was also calcula-ted, using the measured x-ray transmission energy spectra of the primary beam passing through the samples. It can be assumed that such estimated attenuated energy is the theoretical maximum energy absorbed by the nanoparticles in such configurations, if all the interactions occurred as photoelectric effects. Moreover, it can be proposed that such energy is also not so far from the real absorbed energy, due to the high photoelectric cross sections of the nanoparticles involved.

The first important result emerged from the quantification study regards the preponderance of both the XF and XL signal produced by Y_2O_3:Eu(III), over that emitted by LaF_3:Tb for all the excitation strategies. This was demonstrated considering both the XL and XF intensity rates of the two signals and their energy-normalized intensity rates, which give indexes of the signal yields per unit energy of the two nanoparticles. Therefore, it can be concluded from such study that Y_2O_3:Eu(III) is

definitely more suitable and efficient to be used as theranostics agents for combined XFCT/XLCT therapy and imaging, in particular for light-based therapies such as the aforementioned XPDT.

Secondly, other results of the quantification study has suggested that the unfiltered polyenergetic source was the best and most energy-efficient among the tested excitation strategies for x-ray luminescence production, in particular using the minimum attenuated energy rates to stimulates the nanoparticles. The highest XL signal rate was achieved with the polychromatic source at its maximum tube voltage (50 kVp) and the trends of the intensity rates curves hinted to a possible further increase in the XL signal as the maximum energy of the source grows. However, such excitation was not the most efficient in terms of rate of energy attenuated by the samples. In particular, for all the excitation strategies, XL signal production of both the nanoparticles presented maxima points of its energy-yield in correspondence of relatively low rates of attenuated energy, ranging between $1.5 \cdot 10^6$ and $2.5 \cdot 10^6$ keV/s. Similarly, XL signal yields for both the nanoparticles with unfiltered polyenergetic beam presented a maximum peak in efficiency for average attenuated energies at 12-14 keV. Hence, it can be concluded that excitation with low-energy photons may be the most efficient in stimulating XL production with the lowest energy involved in the process.

Such result is greatly interesting and important, in a perspective of theranostics applications of x-ray luminescence. In fact, optimizing XL signal production per unit of attenuated energy is equivalent to reducing to the minimum the dose rates involved in the stimulation, during both the therapeutic and the imaging procedure. Such aspect should be furtherly investigated in the future. However, a hypothesis on the physical causes of such maximization at low energies may be introduced: low-energy x-ray photons may be more suitable to produce x-ray luminescence because the generally produce photoelectrons with low kinetic energy, during interaction with the nanoparticles. Hence, low kinetic energy electrons are more advantaged in recombining within scintillation centers in the light-emitting materials, compared to electron with high kinetic energy, produce by high-energy photons. Such electrons, in fact, have first to lose part of their energy through collisions before reaching the proper energy for recombination inside luminescence centers for XL production.

For what concerns x-ray fluorescence, the quantification study has confirmed the expected importance and influence of using x-ray excitation energies that are tuned to the absorption edges (in particular the K-edge) of the target materials. In fact, the highest XF signal rate measured was produced by the stimulation of Y_2O_3:Eu(III) with the monoenergetic beam at 17.48 keV, just above the K-edge of yttrium (17.03 keV), thus maximizing the photoelectric absorption of x-ray photons in the material. In the same way, for LaF_3:Tb, the filtered excitations, which were designed to harden the x-ray stimulating beam towards energies as close as possible to the K-edge of lanthanum, were found to produce a consistent XF signal. Specifically, they were the best

excitation strategies in maximizing the XF signal yield of LaF_3:Tb at the lowest attenuated energy rates. The maximum net XF signal rate, for LaF_3:Tb, was still produced by unfiltered polyenergetic excitation with energies above the K-edge, yet the highest photon flux produced by such strategies is probably the cause of that. In fact, beam hardening through filtering reduces the net x-ray photon flux of the stimulating source.

Lastly, it was surprisingly and unexpectedly found that the monoenergetic excitation tuned at the K-edge of Y_2O_3:Eu(III) was not the most energy-efficient stimulation strategy for maximizing the XF signal yield at the lowest attenuated energy rates. In fact, the monoenergetic excitation produced by far the greatest rate of attenuated energy, almost an order of magnitude higher than those of the other strategies. This may be due effectively to the enhanced photoelectric absorption with the K-edge tuning, thus corresponding to very high energy deposition rates in the target materials. However, it seems that an equivalent increase in the XF signal production is not corresponding to such heightened energy absorption. Hence, it can be assumed that a large fraction of this energy is not used for x-ray fluorescence generation and then it can be considered as "wasted", in a perspective of XFCT.

As a last significant result, it must be reported also that a comparison between the XL signal and the XF signal produced simultaneously by the same nanoparticle has shown, for both Y_2O_3:Eu(III) and LaF_3:Tb, that x-ray luminescence is by far the type of radiative emission produced in the largest quantity. The x-ray luminescence signal (in ADU/s) was even as high as a million time the x-ray fluorescence one (in count/s). Anyway, such result is not startling, because it is known that a much lower photon energy is required to produce an optical photon of few eV, compared to a characteristic x-ray of even tents of keV. It can be noticed that the ratio between the required energies is exactly in the order of 10^9-10^{10}, as the comparison between the two signals has found.

Furthermore, the outcomes of the two imaging studies performed with the XFCT/XLCT system has provided important conclusions and evaluations regarding the imaging performances of the current setup. The first XFCT study with the mouse head phantom and the double tube cylinders has demonstrated the excellent spatial resolution achievable with the XFCT/XLCT system using x-ray fluorescence and the XFET imaging geometries. In fact, all the 200-μm features of the sample were resolved and distinguishable, although a not-negligible noise contribution primarily coming from scattered radiation was present. Such spatial resolution level is already an order of magnitude higher than that achievable with clinical nuclear medicine techniques and even higher than the respective preclinical modalities (as shown in Paragraph 1.3). It is also comparable to the best state-of-the art modalities for high-resolution imaging, such as micro-CT and micro-MRI. Similarly, the sensitivity of the system was high enough to detect even the lowest concentration used, which was equal to 300 μg/mL of Cisplatin in water solution. Such result is promising,

although it is still order of magnitude lower than conventional molecular imaging modalities such as PET and SPECT. Moreover, the clinical concentrations of Cisplatin found in tumor during chemotherapy are still ten times lower (around 30 μg/mL) than the sensitivity limit of the system. Such concentrations are the necessary sensitivity targets for the XFCT/XLCT system, in order to be used for Auger therapy or radiosensitization of conventional chemotherapy. However, as it will be described in the next Paragraph, there is a large margin of improvement of the system sensitivity with further development of the XFCT/XLCT setup, in particular regarding its geometry and detection efficiency. Capability of performing multiplexed XFCT with different compounds was also proved by these imaging results.

On the other hand, the second imaging study has mainly demonstrated the feasibility of combined XFCT and XLCT with the current system of this thesis work. The results also confirm the good spatial resolution performances of the system even for simultaneous XFCT/XLCT, with optimum visuali-zation of all the details of the millimeter-sized double tube cylinder imaged in the experiment. Multi-modal and multicolored imaging with both XFCT and XLCT was also proven.

In conclusion, this thesis project has demonstrated and shown the promising potentials of XFCT and XLCT for both molecular imaging and theranostics, following the premises illustrated in the very introduction to this work. The system here proposed is based on a preliminary design and it was thou-ght for research applications and tests. However, several improvements can be implemented in the current setup and such system can be an optimal and solid starting point from more advanced proto-types with possible commercial purposes, beginning with preclinical applications. This will be briefly discussed and considered in the next Paragraph about the future directions of this work.

6.2 Future work and directions

Although important results has been achieved with the XFCT/XLCT system design proposed in this thesis work and the excellent potential of this technology has been preliminary assessed and proven, several improvements and further developments can be proposed to the current setup.

First and most, x-ray transmission CT can be considered and tested in future imaging studies, as to demonstrate the feasibility of tri-modal XFCT, XLCT and traditional CT in a single setup. The system is already capable to perform an imaging study of this type, by using either the Zyla sCMOS camera or the flat panel. This will add an important and helpful benefit to the system, allowing it to combine molecular and functional imaging with structural and anatomical information provided by x-ray CT.

Similarly, x-ray CT can be used to estimate x-ray attenuation of the primary beam through the imaged object. Such attenuation estimate can be used to correct the lack of homogeneity of the

signal at different values of the thickness of the sample, thus furtherly improving the quality of the resulting XFCT/XLCT images.

In terms of system performances, spatial resolution of the XFCT/XLCT system can be pushed farther towards smaller and smaller values, by trying to collimate the x-ray excitation beam with pinholes and slits of sizes below 200 μm, or even below 100 μm. On the other hand, sensitivity can be also improved by minimizing as much as possible background signal. In the case of x-ray fluorescence, this can be done by shielding any radiation produced by metals or high Z material in the surroundings, while for x-ray luminescence, by using more efficient optical filters and furtherly prevent ambient light to contaminate the XL signal.

The quantification study can be repeated to confirm the results obtained in this thesis. For example, a more accurate estimation of the energy absorbed by the nanoparticles can be directly acquired using dosimeters, such as gel or liquid dosimeters. Specific phantoms with dosimetric gel can be prepared and filled with nanoparticles or other theranostics compounds, in order to measure the dose rate absorbed by the samples. Moreover, additional excitation strategies can be tested, such as using different filters, sources with higher flux or with different values of their maximum energy.

XPDT feasibility with the proposed XFCT/XLCT system and using the types on nanoparticles tested in this thesis work can be assessed by directly measuring the amount of cytotoxic effect induced in biological tissues. This can be done by incorporating water solutions or tissue-mimicking phantoms in the setup together with the nanoparticles. Then the production of free radicals, such as singlet oxy-gen $^1O_2$ by x-ray luminescence can be quantified using specific chemical markers and dyes, like *singlet oxygen sensor green* (SOSG).

In addition to that, new and different theranostics and imaging agents can be tested with the current XFCY/XLCT setup, envisioning even other theranostics applications, such as x-ray mediated drug release or Cherenkov radiation PDT [4] [32] [35] [36].

Finally, the XFCT/XLCT system proposed and discussed in this project can be a promising starting point for more advanced and commercially focused designs and versions. In fact, a novel XFCT full-ring detection system with small pixel CdTe detectors for nanoparticle-mediated theranostics appli-cations has been recently proposed by L. Giannoni et al. [62]. Such design will incorporate multiple cadmium telluride detectors in a full ring assembly. The system design is based, as it is reported in the figure, on the MRC-SPECT I system developed in the Radiation Imaging and Detection Group at the University of Illinois at Urbana-Champaign (UIUC) [63]. Detection efficiency and overall sensitivity of the setup will be greatly enhanced, compared with the XFCT/XLCT system of this thesis work, thanks to the full-ring geometry. Room-temperature CdTe detectors, such that used for the spectroscope in the XFCT/XLCT setup, have been chosen because of their good detection performances and high energy resolution with x-ray photons. This is due

to their high density, atomic number and capability of creating pixelated arrays with micron-size pixel pitch. The full-ring XFCT system would also implement the same XFET geometries described in this thesis work, but furtherly improving geometric sensitivity and imaging skills by using multiple-slits apertures or multiple pinholes, instead of single ones. The main targets for such a commercial system will be preclinical and small animal imaging, using a field of view (FOV) of few centimeters, which is perfectly suitable for mouse brain imaging. Such design of a full-ring CdTe detection assembly for XFCT is introduced in Figure 6.1 [62] [63].

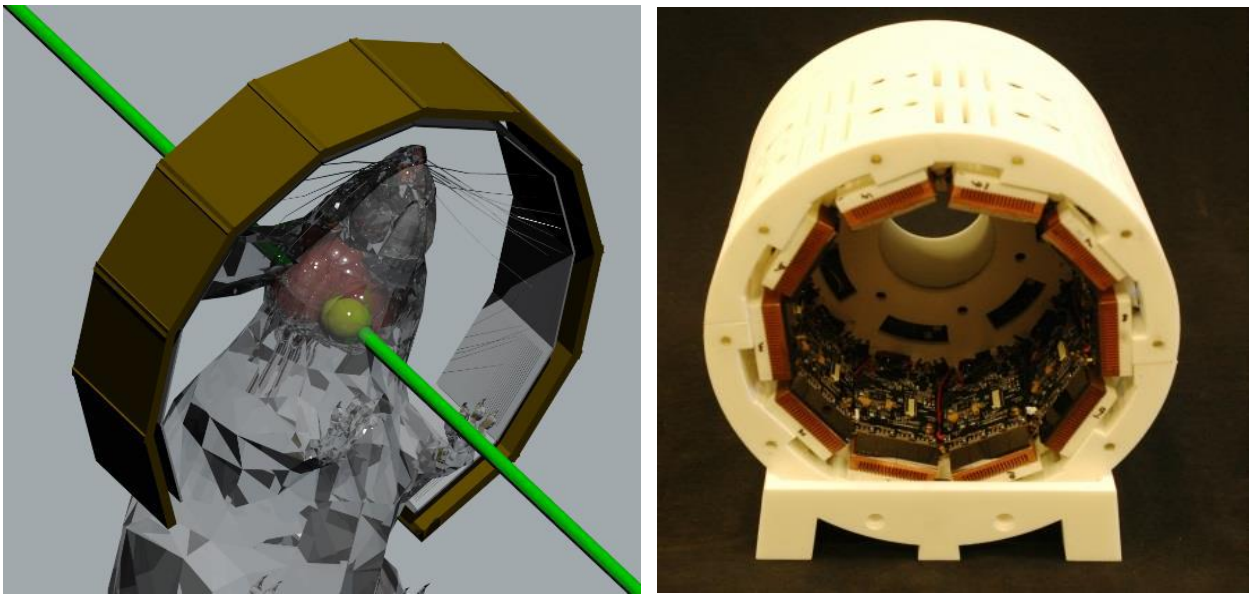

Figure 6.1: Design of a full-ring XFCT detection system composed on small-pixelated CdTe detectors (left). It is based on the MRC-SPECT I model developed at UIUC (right) [62] [63].

REFERENCES

[1] T. F. Massoud, S. S. Gambhir, "Molecular imaging in living subjects: seeing fundamental biological processes in a new light", in *Genes & Dev.*, vol. 17, pp. 545-580, 2003.

[2] J. Tian, "Molecular Imaging", Springer-Verlag, China, 2013.

[3] M. Ahmad, G. Pratx, M. Bazalova and L. Xing, "X-ray Luminescence and X-ray Fluorescence Computed Tomography: new molecular imaging modalities", in *IEEE Access*, vol. 2, pp. 1051-1061, 2014.

[4] S. S. Kelkar, T. M. Reineke, "Theranostics: combining imaging and therapy", in *Bioconjugate Chem.*, vol. 22 (10), pp. 1879-1903, 2011.

[5] C. M. O'Connor, J. U. Adams, "Essentials of cell biology", NPG Education, MA, 2010.

[6] H. Nikjoo, S. Uehara, D. Emfietzoglou, "Interaction of radiation with matter", CRC Press, 2012.

[7] K. S. Krane, "Introductory nuclear physics", 3rd ed., Wiley, NY, 1987.

[8] G. F., Knoll, "Radiation detection and instrumentation", 4th ed., Wiley, NY, 2010.

[9] R. Cesareo, S. Mascarenhas, S. Crestana, A. Castellano, "New tomographic methods using X-ray tubes", in *Nucl. Instr. and Methods in Physics, Res. Sect. A*, vol. 299, pp.440-443, 1990.

[10] P. Boisseau, L. Grodzins, "Fluorescence tomography using synchrotron radiation at the NSLS", in *Hyperfine Interactions*, vol. 33, pp. 283-292, 1987.

[11] L. J. Meng, N. Li, P. J. La Riviere, "X-ray Fluorescence Emission tomography (XFET) with novel imaging geometry – a Monte Carlo study", in *IEEE Trans. Nucl. Science*, vol. 58 (6), pp. 3359-3368, 2011.

[12] M. Chukalina, A. Simionovici, S. Zaitsev, C. J. Vanegas, "Quantitative comparison of X-ray Fluorescence Microtomography setups: standard and confocal collimator apparatus", in *Spectrochimica Acta Part B*, vol. 62 (6-7), pp. 544-548, 2007.

[13] B. Vekemans, L. Vincze, F. E. Brenker and F. Adams, "Processing of three-dimensional microscopic x-ray fluorescence data", in *J. Anal. At. Spectrom.*, vol. 19, pp. 1302-1308, 2004.

[14] S. K. Cheong, B. L. Jones, A. K. Siddiqi, F. Liu, N. Manohar, and S. H. Cho, "X-ray Fluorescence Computed Tomography (XFCT) imaging of gold nanoparticle-loaded objects using 110 kVp X-rays", in *Phys. Med. Biol.*, vol. 55 (3), pp. 647-662, 2010.

[15] M. Bazalova, Y. Kuang, G. Pratx, and L. Xing, "Investigation of X-ray Fluorescence Computed Tomography (XFCT) and K-edge imaging", in *IEEE Trans. Med. Imag.*, vol. 31 (8), pp. 1620-1627, 2012.

[16] A. Groll, J. George, P. Vargas, P. J. La Riviere and L. J. Meng, "Element mapping in organic

samples utilizing a benchtop X-ray Fluorescence Emission tomography (XFET) system", in *IEEE Trans. Nucl. Science*, vol. 62 (5), pp. 2310-2317, 2015.

[17] M. Ahmad, M. Bazalova, L. Xiang and L. Xing, "Order of magnitude sensitivity increase in X-ray Fluorescence Computed Tomography (XFCT) imaging with an optimized spectro-spatial detector configuration: theory and simulation," in *IEEE Trans. Med. Imag.*, vol. 33 (5), pp. 1119-1128, 2014.

[18] H. Zaidi, K. F. Koral, "Scatter modelling and compensation in emission tomography", in *Eur. J. Nucl. Med. Molecular Imag.*, vol. 31 (5), pp. 761-782, 2004.

[19] R. Cesareo, S. Mascarenhas, "A new tomographic device based on the detection of fluorescent x-rays", in *Nucl. Instr. and Methods in Physics, Res. Sect. A*, vol. 277, pp. 669-672, 1989.

[20] S. K. Cheong, B. L. Jones, A. K. Siddigi, F. Liu, N. Manhoar and S. H. Cho, "X-ray fluorescence computed tomography (XFCT) imaging of gold nanoparticle-loaded objects using 110 kVp X-rays", in *Phys. Med. Biol.*, vol. 55 (3), pp. 647–662, 2010.

[21] N. Manhoar, S. H. Cho, "Quality of micro-CT images acquired from simultaneous micro-CT and benchtop X-ray Fluorescence Computed Tomography (XFCT): a preliminary Monte Carlo study", in *2013 IEEE NSS Conference Record*, 2013.

[22] P. Lecoq, A. Annenkov, A, Getkin, M. Korzhik, C. Pedrini, "Inorganic scintillators for detector systems: physical principles and crystal engineering", Springer-Verlag, NY, 2006.

[23] G. Praxt, C. M. Carpenter, C. Sun and L. Xing, "X-ray Luminescence Computed Tomography via selective excitation: a feasibility study", in *IEEE Trans. Med. Imag.*, vol. 29 (12), pp. 1992-1999, 2010.

[24] G. D. Luker, K. E. Luker, "Optical imaging: current applications and future directions, in *J. Nucl. Med.*, vol.49, pp. 1-4, 2008.

[25] G. Praxt, C. M. Carpenter, C. Sun, R. P. Rao and L. Xing, "Tomographic molecular imaging of x-ray excitable nanoparticles", in *Opt. Lett.*, vol. 35 (20), pp. 3345-3347, 2010.

[26] D. Chen, S. Zhu, H. Yi, X. Zhang, D. Chen, J. Liang and J. Tian, "Cone beam x-ray luminescence computed tomography: a feasibility study", in *Med. Phys.*, vol. 40 (3), pp. 1-14, 2013.

[27] X. Liu, Q. Liao and H. Wang, "Fast x-ray luminescence computed tomography imaging" in *IEEE Trans. Biomed. Eng.*, vol. 61 (6), pp. 1621-1627, 2014.

[28] H. M. Hertz, J. C. Larsson, U. Lundström, D. H. Larsson, and C. Vogt, "Laboratory x-ray fluorescence tomography for high-resolution nanoparticle bio-imaging", in *Opt. Lett.*, vol. 39 (9), pp. 2790-2793, 2014.

[29] S. R. Cherry, J. A. Sorenson, M. E. Phelps, "Physics in Nuclear Medicine", 4th Ed., Elsevier-Saunders, CA, 2012.

[30] A. Del Guerra, N. Belcari, "State-of-the-art of PET, SPECT and CT for small animal imag-

ing", in *Nucl. Instr. and Methods in Physics, Res. Sect. A*, vol. 583 (11), pp. 119-124, 2007.

[31] C. Vanhove, J. P. Bankstahl, S.D. Krämer, E. Visser, N. Belcari, S. Vandenberghe, "Accurate molecular imaging of small animals taking into account animal models, handling, anaesthesia, quality control and imaging system performance", in *EJNMMI Physics*, vol.2 (31), pp. 1-25, 2015.

[32] D. K. Chatterjee, T. Wolfe, J. Lee, A. P. Brown, P. K. Singh, S. R. Bhattarai, P. Diagaradjane, and S. Krishnan, "Convergence of nanotechnology with radiation therapy - insights and implications for clinical translation", in *Trans. Cancer Res.*, vol. 2 (4), pp. 256–268, 2013.

[33] J. George, **L. Giannoni**, A. Groll, D. Strat, B. Quigley, P. J. La Riviere, and L. J. Meng, "Experimental evaluation of a combined X-ray Fluorescence Emission Tomography and X-ray Luminescent Computed Tomography system towards quantifying and imaging therapeutic nanoparticles", in *2015 IEEE NSS-MIC*, San Diego, USA, November 1-8, 2015.

[34] J. George, **L. Giannoni**, K. Kim, J. Dutta, B. Yoon, A. Groll, Q. Li, P. J. La Riviere, P.J., and L. J. Meng, "Hybrid X-ray Fluorescence, Luminescence and Transmission Computed Tomography for image-guided nanoparticle-mediated X-ray Micro-Beam Therapy", in *2016 SNMMI Annual Meeting*, San Diego, USA, June 11-15, 2016.

[35] L. Benov, "Photodynamic Therapy: current status and future directions", in *Med. Prin. Pract.*, vol. 24 (suppl. 1), pp. 14-28, 2015.

[36] M. B. Vrouenraets, G. W. Visser, G. B. Snow, G. A. van Dongen, "Basic principles, applications in oncology and improved selectivity of photodynamic therapy", in *Anticancer Res.*, vol. 23 (1B), pp. 505-522, 2003.

[37] X. Zou, M. Yao, L. Ma, M. Hossu, X. Han, P. Juzenas, and W. Chen, "X-ray-induced nanoparticle-based photodynamic therapy of cancer", in *Nanomedicine*, vol. 9 (15) , pp. 2339-2351, 2014.

[38] M. Hamblin, L. Chiang, S. Lakshmanan, et al., "Nanotechnology for photodynamic therapy: a perspective from the Laboratory of Dr. Michael R. Hamblin in the Wellman Center for Photomedicine at Massachusetts General Hospital and Harvard Medical School", in *Nanotech. Rev.*, vol. 4 (4), pp. 359-372, 2015.

[39] XRF Research, Inc. "XRF spectra" at: http://www.xrfresearch.com/xrf-spectra/.

[40] H. A. A. Seed Ahmed, O. M. Ntwaeaborwa, R. E. Kroon, "The energy transfer mechanism in Ce, Tb co-doped LaF_3 nanoparticles", in *Curr. Appl. Phys.*, vol. 13, pp. 1264-1268, 2013.

[41] G. Liu, G. Hong, X. Dong, J. Wang, "Silica-coated Y_2O_3:Eu nanoparticles and their luminescence properties", in *J. Lumin.*, vol. 1 (26), pp.702-706, 2007.

[42] J. D. Carter, N. N. Cheng, Y. Qu, G. D. Suarez, and T. Guo, "Nanoscale energy deposition by x-ray absorbing nanostructures", in *J. Phys. Chem. Lett. B*, vol. 111, pp. 11622-11625, 2007.

[43] G. Choi, S. Seo, K. Kim, H. Kim, S. Park, J. Lim, and J. Kim, "Photon activated therapy (PAT) using monochromatic Synchrotron x-rays and iron oxide nanoparticles in a mouse tumor model: fea-
sibility study of PAT for the treatment of superficial malignancy", in *Rad. Oncol.*, vol. 7 (184), pp. 1-10, 2012.

[44] L. Maggiorella, G. Barouch, C. Devaux, A. Pottier, E. Deutsch, J. Bourhis, E. Borghi, and L. Levy, "Nanoscale radiotherapy with hafnium oxide nanoparticles", in *Future Oncol.*, vol.8 (9), pp. 1167-1181, 2012.

[45] S. Lee, D. Tsai, V. A. Hackley, M. W. Brechbiel, and R. F. Cook, "Surface-engineered nanomaterials as X-ray absorbing adjuvant agents for Auger-mediated chemo-radiation", in *Nanoscale*, vol. 5, pp. 5252-5256, 2013.

[46] Newport, "Integrity VCS^{TM}, user's manual", Part No. 90047911 Rev. B, 2014.

[47] Xenocs, "GeniX^{3D} x-ray beam delivering system", Manual 2014

[48] Oxford Instruments, "Radiation shielded x-ray tube, Apogee 5000 Series", Technical datasheet, 2013.

[49] Andor, "iKon-L [Do]", Technical datasheet, 2015.

[50] Andor, "High energy detection: solutions beyond the visible", HEDB 1014, 2015.

[51] Andor, "iXon3", Technical datasheet, 2007.

[52] L. J. Meng, G. Fu, "Investigation of the intrinsic spatial resolution of an intensified EMCCD scintillation camera", in *IEEE Trans. Nucl. Science*, vol. 55 (5), pp. 2508-2517, 2008.

[53] Phototek, "Demagnifiers", Datasheet, 2001.

[54] L. J. Meng, "An intensified EMCCD camera for low Energy gamma ray imaging applications", in *IEEE Trans. Nucl. Science*, vol. 53 (4), pp. 2376-2383, 2006.

[55] Andor, "Zyla sCMOS", Technical datasheet, LZYLASS 0216 R1, 2015.

[56] Varian, "Paxscan 1313", Technical datasheet, 2012.

[57] Amptek, "X-ray and gamma ray detector high resolution CdTe, XR-100T-CdTe", Technical datasheet, 2011.

[58] J. H. Hubbel and S. M. Seltzer, "Tables of x-ray mass attenuation coefficients and mass energy-absorption coefficients from 1 keV to 20 MeV for elements Z=1 to 92 and 48 additional substances of dosimetric interest", in *NIST Standard Reference Database 126*, last update 2014.

[59] A. Van Oosterom and J. Strackee, "The solid angle of a plane triangle", in *IEEE Trans. Biomed. Eng.*, vol. 30 (2), pp. 125-126, 1983.

[60] G. Fu, L. J. Meng, P. Eng, M. Newville, P. Vargas and P. J. La Riviere, " Experimental demonstration of novel imaging geometries for x-ray fluorescence computed tomography", in *Med. Phys.*, vol. 40 (6), pp. 1-11, 2013.

[61] Drummond Scientific Company, "Microcaps®: catalog information", at: http://www.drummondsci.com/product.cfm?cat=capillary-micropipets&prod=microcaps.

[62] **L. Giannoni**, J. George, X. Lai, and L. J. Meng, "Design and feasibility study of a full-ring x-ray fluorescence emission computed tomography system based on small-pixel CdTe detectors for real-time monitoring of x-ray induced and nanoparticle mediated radiation therapy, in *2016 SNMMI Annual Meeting*, San Diego, USA, June 11-15, 2016.

[63] L. Cai, X.Lai, Z. Shen, C. Chen and L. J. Meng, "MRC-SPECT: A sub-500 μm resolution MR-compatible SPECT system for simultaneous dual-modality study of small animals", in *Nucl. Inst. Met. A.*, vol. 734 (B), pp. 147-151, 2014

ACKNOWLEDGEMENTS

Many people deserves all my gratitude for the contributes, both direct and indirect, they have provided me with for the accomplishment of this Master Thesis work.

First, I would like to thank greatly all my supervisors, Prof. Ing. Francesco d'Errico and Ing. Valerio Giusti, at Università di Pisa, and Prof. Ling-Jian Meng, at the University of Illinois at Urbana-Champaign. In particular, a special thanks goes to Prof. d'Errico, for mentoring me and for introducing me to the great discipline of the medical applications of nuclear technologies.

This thesis work has been carried out at the Department of Nuclear, Plasma and Radiological Engineering (NPRE) of the University of Illinois at Urbana Champaign. I wish to thank all the faculty members and the staff at NPRE, in particular Prof. James F. Stubbins and Becky Meline, for welcoming me so cheerfully and kindly to this great "nuclear family", and for always helping me with all the possible aspects and issues of my thesis and exchange study experience in the USA.

I would also like to express my immense gratitude to all my friends and unchangeable colleagues in the Radiation Detection and Imaging Group at NPRE: to Jon George, for being my second mentor with this thesis project and for collaborating with me side by side, for teaching me and for all the long days and nights spent working together inside that box in the laboratory; to Andrew Groll, for being a sort of professional model for me and always being present whenever I need him, inside and outside the office; to Byung-Hui Yoon, for being my "desk buddy" and sharing with me the same experience as first-year grad students, with all its difficulties but also satisfactions; to Elena Maria Zannoni, for supporting me even before joining the group with advises from her past experience and for being a friendly Italian voice inside a US department; to Dan Strat, for being so welcoming and friendly from the very first time we met, like if we had knew each other for years; to Xiaochun Lai, for being patient with me and always keep me up with its smile and positivity.

I also own a huge debt and gratitude to my Alma Mater, Università di Pisa, my department Dipartimento di Ingegneria Civile e Industriale (DICI) and above all to my degree course in Nuclear Engineering, for my formation, education and all my knowledges and fro teaching me the most important qualities that an excellent engineer and scientist should have. I wish to thank all my professors and colleagues in the degree course of Nuclear Engineering, particularly the President, Prof. Walter Ambrosini, for the outstanding work he carries every single days for the benefits if the degree course and of the students. I could have never asked for a best teacher and professional as him, during my entire academic career. I would also like to express my gratitude to Prof. Marino Mazzini, for being my Bachelor Thesis supervisor, for mentoring me and for bringing me to my

first professional conference at ICONE22 in Prague.
I really hope to always carry on the good name of my Alma Mater and make it proud of my accomplishments. I really believe in the excellent education provided by Università di Pisa and I wish to be able to continue to work with it and for it in the future.
Last, but absolutely not least, a very heartfelt thanks is for my family, my parents, all my friends and fellow students in Pisa, and to Giulia, who always supported me and never stopped to believe in me. This would have never been possible without you. In particular to Giulia, for these incredible yet suffering adventure in the USA we shared and lived together. Thanks, for always being at my side. We made it, finally.
Finally, this thesis work is dedicated to my grandfather Franco, who will look at my Master graduation proudly from a far better view.